VNIVERSITAT DE VALÈNCIA

Effective Field Theories in Hadron Physics

Doctoral Thesis by
Fernando Alvarado Alvarez

Director:
Luis Alvarez-Ruso, IFIC (CSIC-UV)

Departament de Física Teòrica
Institut de Física Corpuscular (CSIC-UV)

Programa de Doctorat en Física - 3126
Valencia, España, Abril, 2024

For my chemist grandmothers

Contents

Chapter 1

Introduction

1.1 Motivation and outline

Quantum Chromodynamics (QCD), the theory of the strong interaction, governs the dynamics of quarks and gluons, binding them in hadrons. The properties of the latter are very interesting, not only to investigate the underlying strong interaction, but also, since hadrons are omnipresent in particle physics processes, they are fundamental in any experimental analysis.

As composite particles, hadrons are extended bodies with a certain structure. Their composition can be probed experimentally, and in this regard nucleons, *i. e.* protons and neutrons, are special. The proton is the only stable hadron (within experimental limits) and the neutron is the second most stable one, with a mean lifetime of about 15 minutes. This makes the nucleon the most suitable target for scattering experiments, which is the most straightforward way to probe the internal structure. In particular, electron-nucleon elastic scattering is sensitive to the distribution of electric charge within this hadron, as well as to its magnetic properties. On the other hand, weak probes, such as neutrinos scattering quasi-elastically on nucleons, give access to the so-called axial structure of the nucleon. This is related to the spin distribution within the nucleon and is a key input for the analysis neutrino physics. In general, the cross sections of these processes are decomposed in functions of the momentum transfer, each of these different functions is called form factor (FF) and encodes the information on the hadron structure. Lately even

gravitational FFs, related to the mass distribution, are under study.

In this thesis we have studied the electromagnetic and the axial form factor of the nucleon at low energies, since they provide the following information: a determination of fundamental nucleon properties; insight on the underlying QCD interaction; necessary input for the analysis of many relevant experimental processes. However, there is a complication intrinsic to the QCD interaction: since the strong coupling is large at low energies, these form factors can not be calculated perturbatively. This is circumvented by simulating a discretized spacetime where hadronic matrix elements can be computed numerically, what is called lattice QCD (LQCD). The recent progress in LQCD is one of the main motivations of this thesis. This invaluable source of theoretical information suffers from some artifacts and systematic uncertainties. The emphasis of this work is put on the effective field theory (EFT) approach to these and other problems. An EFT is a theoretical framework which simplifies the problem of the fundamental theory. It does it by examining the scales at play and the symmetries of the problem, using the most convenient degrees of freedom in order to account only for the most relevant dynamics. In this way, one can escape from the complications of the complete theory and obtain a description which has two beneficial features: being model independent and systematically improvable.

The EFT of QCD at low energies is called Chiral Perturbation Theory (ChPT). It takes advantage of the chiral symmetry of the fundamental interaction, as will be explained below, and has been very successful in the analysis of hadron physics. In particular, it is useful to describe the dependence on lattice artifacts, such as the use of quark masses heavier than the physical ones to ease the computation. This dependence will be at the center of the thesis, however ChPT can also account for other LQCD effects due to the size (finite volume) of the simulated universe, the finite spacing between lattice points, among others. By means of this helpful theory, the nucleon axial form factor is studied in Ch. 2, extracting it from a combined set of several recent LQCD data.

Complementary to ChPT, dispersion theory, which exploits the unitarity and analyticity of amplitudes, is also a powerful tool to study nonperturbative dynamics in quantities such as the form factors. In particular, in Ch. 3 we assessed the electromagnetic FF of the nucleon, using dispersion theory in combination with ChPT to study LQCD data and its quark mass dependence.

Finally, also new physics (NP) contributions to hadronic processes are studied. The search of beyond the Standard Model phenomena is one of the main efforts in current fundamental physics, with no clear evidence found yet. In Ch. 4 we study how possible NP contributions may affect the decay of a charmed baryon, the Λ_c. We analyze the weak semileptonic decay, $\Lambda_c \to \Lambda\, \ell^+ \nu_\ell$, motivated in part by very recent results from the BESIII collaboration. Again the approach is to use EFTs to gain phenomenological knowledge. On the one hand, the NP is parametrized in a model independent way using the so-called Standard Model Effective Field Theory (SMEFT). On the other hand, to obtain the relevant hadronic matrix element, we also employ another effective theory approach: we start from the matrix element of the Standard Model current, which has been simulated in the lattice, and employ the heavy quark spin symmetry (HQSS) approximation, which exploits the large value of the charm quark mass, to estimate the matrix elements of the other currents accounting for the NP interaction.

Before discussing the results of our works, we start by introducing the theoretical framework in the current chapter.

1.2 Chiral Perturbation Theory

Hadrons are QCD bound and resonant states. Their qualities can not be calculated perturbatively because QCD is strongly coupled at low energies. However, in this regime the QCD Lagrangian of light quarks is approximately invariant under rotations in the flavor space, the chiral symmetry. In particular, the spontaneous breaking of this symmetry leads to a theory where the lowest lying mesons are the Goldstone bosons. This allows to build a perturbative effective field theory, where the hadrons are the degrees of freedom. Once the free parameters, *aka* low energy constants (LECs), are fixed experimentally or from LQCD, such theory has predictive power. This is Chiral Perturbation Theory (ChPT), the effective field theory of QCD at low energies. This formalism will be introduced throughout the section, and to do so, first some symmetry considerations are necessary.

1.2.1 The Lagrangian of light quarks

Quark currents in the massless limit: chiral symmetry

Before presenting the EFT it is important to study the symmetries of QCD. The somewhat intricate discussion of this section will pay off obtaining a very powerful effective theory. The QCD Lagrangian of the light quarks (u, d and s), in the limit in which they are massless (chiral limit) reads:

$$\mathcal{L}^0_{QCD} = i\overline{q}_L \not{D} q_L + i\overline{q}_R \not{D} q_R \ , \tag{1.1}$$

with $q^T = (u, d)$ or $q^T = (u, d, s)$ depending whether we are in the $n_f = 2$ or $n_f = 3$ scenario, $q_{L/R} = P_{L/R} q = \frac{1}{2}(1 \mp \gamma_5) q$, and D_μ contains the gluon interactions. This Lagrangian owns global $G \equiv \mathrm{SU}(n_f)_L \otimes \mathrm{SU}(n_f)_R$ so-called chiral symmetry, with n_f quark flavors. The transformations are:

$$q_L \longrightarrow g_L q_L, \quad q_R \longrightarrow g_R q_R, \tag{1.2}$$

with $g_L \in \mathrm{SU}(n_f)_L$, $g_R \in \mathrm{SU}(n_f)_R$. The group elements are $g_{L,R} = e^{i\epsilon^a_{L,R} \frac{T^a}{2}}$ with T^a the τ^a Pauli (λ^a Gell-Mann) matrices for $n_f = 2$ ($n_f = 3$).

On top of this symmetry, there is another invariance given by the singlet transformations: $q_{L,R} \longrightarrow g^{(s)}_{L,R} q_L$, with $g^{(s)}_{L,R} = e^{i\epsilon^{(s)}_{L,R}}$, and $\epsilon^{(s)}_L$, $\epsilon^{(s)}_R$ independent constants. This has no flavor structure, and makes the symmetry group be: $G \otimes \mathrm{U}(1)_L \otimes \mathrm{U}(1)_R = \mathrm{SU}(n_f)_L \otimes \mathrm{SU}(n_f)_R \otimes \mathrm{U}(1)_L \otimes \mathrm{U}(1)_R$.

The group G can be constructed joining vector and axial transformations, respectively:

$$q \longrightarrow e^{i\epsilon^a_V \frac{T^a}{2}} q, \quad q \longrightarrow e^{i\epsilon^a_A \frac{T^a}{2}\gamma_5} q \ . \tag{1.3}$$

From $e^{i\epsilon^a_V \frac{T^a}{2}} e^{i\epsilon^a_A \frac{T^a}{2}\gamma_5} q = g_L q_L + g_R q_R$ it follows that $\epsilon_{V,A} = (\epsilon_R \pm \epsilon_L)/2$. The same can be done for the singlet transformations, using $\epsilon^{(s)}_{V,A} = (\epsilon^{(s)}_R \pm \epsilon^{(s)}_L)/2$.

According to Noether's theorem, the symmetry implies the conservation of certain quantities. To extract the Noether current we promote the global transformation to a local one, as explained in Ref. [1], which yields $J^\mu = \frac{\partial \delta \mathcal{L}}{\partial \partial_\mu \epsilon}$ and $\partial_\mu J^\mu = \frac{\partial \delta \mathcal{L}}{\partial \epsilon}$. The conserved vector and axial(-

vector) currents[1] and charges of G are (if not stated differently, we study the $n_f = 3$ scenario):

$$\begin{aligned} V_\mu^a \equiv \overline{q}\gamma^\mu \frac{\lambda^a}{2} q, \quad A_\mu^a \equiv \overline{q}\gamma^\mu\gamma_5 \frac{\lambda^a}{2} q \ , \\ Q_V^a = \int d^3\overline{x} V^{a0}, \quad Q_A^a = \int d^3\overline{x} A^{a0}. \end{aligned} \tag{1.4}$$

Analogously, the conserved flavor-singlet currents are $V_\mu^{(s)} \equiv \overline{q}\gamma^\mu q$, $A_\mu^{(s)} \equiv \overline{q}\gamma^\mu\gamma_5 q$, where the latter is not conserved at loop level, what is called the $\mathrm{U}(1)_A$ anomaly.

Quark currents with mass: explicit symmetry breaking

We now introduce the light quark masses, which enter in the following term, which is added to the Lagrangian of Eq. (1.1):

$$\mathcal{L}_\mathcal{M} = -\bar{q}\mathcal{M}q = -\left(\bar{q}_R\mathcal{M}q_L + \bar{q}_L\mathcal{M}q_R\right) \ , \tag{1.5}$$

with the mass matrix $\mathcal{M} = \mathrm{diag}(m_u, m_d, m_s)$. This term breaks the chiral symmetry. It constitutes the so-called explicit breaking, not to be confused with the spontaneous symmetry breaking responsible of the appearance of Goldstone bosons, which will be discussed later.

The divergences of the currents are now:

$$\begin{aligned} \partial_\mu V_a^\mu &= i\bar{q}\left[\mathcal{M}, \frac{\lambda_a}{2}\right] q \ , \\ \partial_\mu A_a^\mu &= i\bar{q}\gamma_5\left\{\frac{\lambda_a}{2}, \mathcal{M}\right\} q \ , \\ \partial_\mu V^{(s)\mu} &= 0 \ , \\ \partial_\mu A^{(s)\mu} &= 2i\bar{q}\gamma_5\mathcal{M}q + \frac{3\alpha_s}{4\pi} F_{\mu\nu}^a \widetilde{F}^{a\mu\nu} \ . \end{aligned} \tag{1.6}$$

This leads us to the following remarks:

- The vector current V_a^μ is conserved in the limit of SU(3) symmetry, where the masses of the light quarks are all the same. Taking $m_u = m_d \neq m_s$ yields SU(2) isospin symmetry. Given that hadrons are composed by quarks, approximate isospin symmetry is inherited

[1] A current, J^μ, is said to be conserved if $\partial_\mu J^\mu = 0$.

by hadrons. However, it should be remarked, that SU(2) chiral symmetry, i.e. $m_{u,d} = 0$, is actually a more reasonable limit than isospin symmetry, $m_u = m_d \neq 0$. $m_u = m_d$ is approximately a 100% violated[2], and the discrepancy is much larger if one compares $m_{u,d}$ with m_s.

- The axial current, A_a^μ, is not conserved even in the aforementioned SU(3) limit. However the breaking, as for the rest of the currents, is proportional to the light quark masses and therefore relatively small (this is why it is denoted partial conservation of the axial current). A notable consequence of this is the pion decay, where a spin zero pion can be annihilated by a an axial vector weak current which has spin one (see discussion of Eq. 2.50 of [3]).

- The flavor-singlet vector current, $V^{(s)\mu}$, is conserved, given that the corresponding transformation is flavor independent and the two chiralities are transformed equally. This symmetry is the one that leads to baryon number conservation.

- The divergence of the flavor-singlet axial current, $A^{(s)\mu}$, receives a contribution from the quark masses and another from the aforementioned $\mathrm{U}(1)_A$ anomaly, given by the gluon field strength tensors (see definitions of Ref. [4]). This has implications for the masses of the η and η'[3].

- The current divergences are not only affected by the masses, but also by other external sources, such as the electroweak interactions. We will not discuss these corrections in detail, but we do introduce the coupling of quarks to the electroweak force in the following section. This leads to the definition of the form factors, which are central to this thesis.

Electroweak interaction

The Standard Model is built upon the symmetries of color SU(3), the weak isospin $\mathrm{SU}(2)_L$ and the hypercharge $\mathrm{U}(1)_Y$. The latter two groups

[2]From the ChPT Lagrangian that will be introduced in Eq. (1.41), one can extract that at leading order $(m_d - m_u)/(m_u + m_d) = (M^2_{K^0} - M^2_{K^\pm})/M^2_{\pi^0}$ which is approx. 0.3 experimentally, implying that $m_d \simeq 2m_u$ [2].

[3]This is not to be confused with the QED anomalous $\mathrm{SU}(n_f)_A$ breaking observed in $\pi^0 \to \gamma\gamma$.

are spontaneously broken to electromagnetic U(1) below the electroweak energy scale:

$$\mathrm{SU}(3)_C \otimes \mathrm{SU}(2)_L \otimes \mathrm{U}(1)_Y \to \mathrm{SU}(3)_C \otimes \mathrm{U}(1)_{\mathrm{EM}} \ . \tag{1.7}$$

The left handed components of the leptons and quarks are SU(2) doublets of the weak isospin, T:

$$\begin{pmatrix} \nu_l \\ \ell \end{pmatrix}_L \ , \quad \begin{pmatrix} q_u \\ q_{d'} \end{pmatrix}_L \ , \quad \ell_R \ , \quad q_{uR} \ , \quad q_{dR} \ , \tag{1.8}$$

structured in three families: $\ell = e,\ \mu,\ \tau$, $\nu_l = \nu_e,\ \nu_\mu,\ \nu_\tau$ for the charged leptons and neutrinos; $q_u = u,\ c,\ t$, $q_{d'} = d',\ s',\ b'$, for the up and down-type quarks. The primes indicate that the weak eigenstate quarks are combinations of the mass eigenstates, d, s, b, what is accounted by the Cabibbo-Kobayashi-Maskawa (CKM) matrix. The same can be said about ν_e, ν_μ and ν_τ, however their masses are negligible for our purposes, and they are considered massless in the simple SM.

The fermions couple to the electroweak interaction in the following way:

$$\mathcal{L} = -eJ^\mu_{\mathrm{EM}}A_\mu - \frac{g}{2\cos\theta_W}J^\mu_{\mathrm{NC}}Z_\mu - \frac{g}{2\sqrt{2}}\left(J^\mu_{\mathrm{CC}}W^\dagger_\mu + \mathrm{h.c.}\right) \ , \tag{1.9}$$

where A_μ is the photon field (not to be confused with the axial currents) and W_μ and Z_μ are the massive bosons. The J^μ indicates the corresponding currents, made by lepton and quark bilinears. The weak angle θ_W satisfies the following relation between the electron and the weak charges: $\sin\theta_W = e/g$, where e is the charge of the positron ($e > 0$).

For the charged leptons, the currents are:

$$\begin{aligned} J^\mu_{\mathrm{EM}} &= \bar{\ell}\gamma^\mu\ell \ , \\ J^\mu_{\mathrm{CC}} &= 2\bar{\nu}_l\gamma^\mu P_L\ell \ , \\ J^\mu_{\mathrm{NC}} &= \bar{\nu}_l\gamma^\mu P_L\nu_l + \frac{1}{2}\bar{\ell}\gamma^\mu\left(c_V - c_A\gamma_5\right)\ell \ , \end{aligned} \tag{1.10}$$

with $c_V = -1 + 4\sin^2\theta_W$, $c_A = -1$ and the same P_L as in Eq. (1.1).

With respect to the quarks, we restrict ourselves to the light ones, u, d and s, so that we employ the quark vector $q^T = (u, d, s)$. Therefore we present the electromagnetic (EM) quark current, which is given by:

$$J^\mu_{\mathrm{EM}} = \bar{q}Q\gamma^\mu q \ , \quad Q = \mathrm{diag}(2/3, -1/3, -1/3) \ . \tag{1.11}$$

The operator Q can be separated in terms of the third component of the u and d isospin, I_3, and the hypercharge, Y, as follows:

$$Q = I_3 + Y/2 \ . \tag{1.12}$$

Hypercharge is defined by the baryon and strangeness content: $Y = B + S$, which depended on the number of quarks and antiquarks, $B = (n_q - n_{\bar{q}})/3$, $S = -(n_s - n_{\bar{s}})$. In the (u, d, s) space one has: $I_3 = \lambda_3/2 = \mathrm{diag}(1/2, 1/2, 0)$, $Y = \lambda_8/\sqrt{3} = \mathrm{diag}(1/3, 1/3, -2/3)$ and $S = \mathrm{diag}(0, 0, 1)$. One can therefore define the vector currents of isospin and hypercharge as:

$$V_3^\mu = \bar{q} I_3 \gamma^\mu q \ , \quad V_Y^\mu = \bar{q} Y \gamma^\mu q \ , \quad V_S^\mu = \bar{q} S \gamma^\mu q \ , \tag{1.13}$$

and rewrite the Q decomposition (1.12) in terms of quark currents:

$$J_{\mathrm{EM}}^\mu = V_3^\mu + V_Y^\mu/2 \ . \tag{1.14}$$

Turning now to the so-called neutral current, we separate it in vector and axial components:

$$J_{\mathrm{NC}}^\mu = V_{\mathrm{NC}}^\mu - A_{\mathrm{NC}}^\mu \ , \tag{1.15}$$

where the vector term is

$$V_{\mathrm{NC}}^\mu = (1 - 2\sin^2\theta_W) V_3^\mu - 2\sin^2\theta_W \frac{1}{2} V_Y^\mu - \frac{1}{2} V_S^\mu \ , \tag{1.16}$$

while the axial one reads

$$A_{\mathrm{NC}}^\mu = A_3^\mu - \frac{1}{2} A_S^\mu \ , \tag{1.17}$$

with the axial isovector current A_a^μ defined in Eq.(1.4) and the axial strangeness current given by $A_S^\mu = \bar{q} S \gamma^\mu \gamma_5 q$.

Finally we will discuss the quark charged current, J_{CC}^μ, momentarily including the heavy quarks for completeness. The interaction is purely left-handed ($L = V - A$), but no longer diagonal in flavor: it couples up and down-type quarks. On top of that, one has to account for the fact that d, s and b are not weak eigenstates. The interaction term reads:

$$J_{CC}^\mu = 2\,(\bar{q}_u, \bar{q}_c, \bar{q}_t)\,\gamma^\mu P_L V_{\mathrm{CKM}} \begin{pmatrix} q_d \\ q_s \\ q_b \end{pmatrix} \ , \tag{1.18}$$

where $V_{\rm CKM}$ is the Cabibbo-Kobayashi-Maskawa matrix, accounting for the change of eigenstate basis, is given in Ref. [5]. In the light quark sector, V_{CKM} can be written in terms of the Cabibbo angle, θ_C, so that one gets:

$$J^{\mu}_{CC} = 2\bar{q}_u \gamma^{\mu} P_L (\cos\theta_C q_d + \sin\theta_C q_s) \ . \tag{1.19}$$

Form factors

Form factors describe the interaction between particles and external fields, such as electroweak bosons. They contain the dependence in momentum transfer of the vertex. Moreover, they provide information on the structure of composite particles. In this work we focus on the electroweak interaction on nucleons: on the one hand, we study the vector form factor (Ch. 3), which gives information relevant for the electromagnetic interaction, but also for the weak one, since the latter also has a vector part as we have seen; on the other hand, we investigate the axial form factor (Ch. 2), which is relevant for the weak interaction only.

Starting by the electromagnetic form factor, we study the EM current (1.11) with two flavors, $q^T = (u, d)$:

$$J^{\mu}_{\rm EM}(x) = \bar{q}(x) \left(\frac{1}{6} + \frac{\tau_3}{2} \right) \gamma^{\mu} q(x) \ . \tag{1.20}$$

The form factors are defined by the matrix element between on-shell nucleon states of four-momenta p, p'. According to the symmetries of the SM, one parametrizes the matrix element as (see Ref. [6] for detailed derivation):

$$\langle N(p') | J^{\mu}_{\rm EM}(0) | N(p) \rangle = \bar{u}(p') \left(\gamma_{\mu} F_1^{(N)}(q^2) + \frac{i\sigma^{\mu\nu} q_{\nu}}{2m_N} F_2^{(N)}(q^2) \right) u(p) \ , \tag{1.21}$$

where $-Q^2 = t = q^2 = (p'-p)^2$ and m_N and u are the nucleon respective mass and spinor. $F_1^{(N)}$ and $F_2^{(N)}$ are the Pauli and Dirac form factors of the proton and neutron, for $N = p, n$ respectively (they are real due to time reversal symmetry). In general we will refer to them as diagonal matrices $F_{1,2}$ in the isospin space. In our work we separate in isoscalar and isovector components, $F_i = \frac{1}{2} F_i^{(s)} + F_i^{(v)} \frac{\tau_3}{2}$, $F_i^{(s/v)} = F_i^{(p)} \pm F_i^{(n)}$, with $i = 1, 2$, and we calculate only the isovector one.

The Dirac and Pauli form factors are related to the electric and mag-

netic ones, $G_{\rm E}$, $G_{\rm M}$, as:

$$\begin{aligned} G_{\rm E} &= F_1 - \frac{Q^2}{4m_N^2} F_2, & G_{\rm M} &= F_1 + F_2 \ , \\ F_1 &= G_{\rm E} + \frac{Q^2}{4m^2} \frac{(G_{\rm M} - G_{\rm E})}{(1 + Q^2/(4m_N^2))}, & F_2 &= \frac{G_{\rm M} - G_{\rm E}}{(1 + Q^2/(4m_N^2))} \ . \end{aligned} \tag{1.22}$$

One has to notice that $G_E(0) = F_1(0) = (1 + \tau_3)/2 = \mathrm{diag}(1, 0)$ is the electric charge. In addition, the magnetic moment, $\mu^{(N)}$, is

$$\mu^{(N)} = G_M^{(N)}(0)\mu_N = (\mathrm{diag}(1, 0) + \kappa^{(\rm N)})\mu_{\rm N} \ , \tag{1.23}$$

with $\kappa^{(N)} = F_2^{(N)}(0)$, the anomalous magnetic moment, which is due to the nucleon extended structure (μ_N is the nuclear magneton).

Moreover, one can define the proton and neutron radii, which are related to the nucleon charge distribution and its magnetism. The Dirac and Pauli quadratic radii, $\langle r_i^{(s,v)2} \rangle$, in the isospin decomposition are defined by the following low energy expansion:

$$F_i^{(s,v)}(q^2) = F_i^{(s,v)}(0) \left[1 + \frac{1}{6} \langle r_i^{(s,v)2} \rangle \, q^2 + \mathcal{O}(q^4) \right] \ . \tag{1.24}$$

Particularizing for the different cases in the physical basis one has:

$$\begin{aligned} \langle r_{\rm E}^{(p)2} \rangle &= -\frac{6}{G_{\rm E}^{(p)}(0)} \left. \frac{{\rm dG_E^{(p)}(Q^2)}}{{\rm dQ^2}} \right|_{Q^2=0} , \\ \langle r_{\rm M}^{(p)2} \rangle &= -\frac{6}{G_{\rm M}^{(p)}(0)} \left. \frac{{\rm dG_M^{(p)}(Q^2)}}{{\rm dQ^2}} \right|_{Q^2=0} , \\ \langle r_{\rm E}^{(n)2} \rangle &= -6 \left. \frac{{\rm dG_E^{(n)}(Q^2)}}{{\rm dQ^2}} \right|_{Q^2=0} , \\ \langle r_{\rm M}^{(n)2} \rangle &= -\frac{6}{G_{\rm M}^{(n)}(0)} \left. \frac{{\rm dG_M^{(n)}(Q^2)}}{{\rm dQ^2}} \right|_{Q^2=0} , \end{aligned} \tag{1.25}$$

where $\langle r_1^{(N)2} \rangle = \langle r_E^{(N)2} \rangle - \frac{3}{2m_N^2}(\mu^{(N)}/\mu_N - 1)$ is a useful expression.

Finally, we turn to the axial form factor, F_A, which is relevant for CC as well as NC lepton scattering on nucleons. In Ch. 2 we study the current of Eq. (1.4) in SU(2), given by the isovector structure:

$$A_\mu^a(x) = \overline{q}(x)\gamma^\mu\gamma_5 \frac{\tau^a}{2} q(x) \ . \tag{1.26}$$

The form factor decomposition reads:

$$\langle N(p')|A^a_\mu(0)|N'(p)\rangle = \bar{u}(p')\left[F_A(q^2)\gamma_\mu + \frac{q_\mu}{2m_N}F_P(q^2)\right]\gamma_5\frac{\tau^a}{2}u(p)\ . \tag{1.27}$$

F_A and F_P are the axial and pseudoscalar isovector form factors. The latter is dominated by the pion pole, and at LO satisfies the so-called Goldberger-Treiman relation. On the other hand, focusing on the axial FF, which is receiving much attention, it can be decomposed in the axial charge, g_A, and the axial quadratic radius, $\langle r^2_A\rangle$, as

$$F_A(q^2) = g_A\left[1 + \frac{1}{6}\langle r^2_A\rangle q^2 + \mathcal{O}(q^4)\right]\ , \tag{1.28}$$

and therefore $g_A = F_A(q^2=0)$, and $\langle r^2_A\rangle = \frac{6}{g_A}\frac{\mathrm{d}}{\mathrm{d}q^2}\ F_A|_{q^2=0}$.

1.2.2 Spontaneous symmetry breaking and the σ model: a didactic introduction

We will now discuss the spontaneous symmetry breaking (SSB) and the effective field theory treatment that follows from it. As explained before, the QCD Lagrangian with massless quarks (1.1) is symmetric under the chiral group $G \equiv SU(n_f)_L \otimes \mathrm{SU}(n_f)_R$ (as well as under $\mathrm{U}(1)_L \otimes \mathrm{U}(1)_R$). However, the vacuum is not invariant under axial transformations, $Q^a_A\,|0\rangle \neq |0\rangle$, while it is under vector ones, $Q^a_V\,|0\rangle = |0\rangle$ (see Ref.[1]). Thus, it is said that the symmetry is spontaneously broken, with the pattern:

$$G \equiv \mathrm{SU}(n_f)_L \otimes \mathrm{SU}(n_f)_R \to H \equiv \mathrm{SU}(n_f)_V\ . \tag{1.29}$$

Evidence of this fact can be found in the hadronic spectrum: chiral symmetry, i.e. symmetry under G, which should be approximately good for the light u, d, s quarks, would imply degenerate mirror hadronic multiplets with opposite chiralities. But these are not present in nature. On top of that, another evidence of SSB is the fact that the quark condensate, $\langle 0|\,\overline{q}q\,|0\rangle$, an order parameter of this symmetry breaking, has a non zero vacuum expectation value (v.e.v.).

In consequence, due to the Goldstone Theorem [7, 8], for $n_f = 3$ the spectrum contains eight Nambu-Goldstone bosons (NGB)[4], as many as

[4]For $n_f = 2$ the NGB are just the three pions.

broken generators or charges. These particles have the same quantum numbers as Q_A^a: odd parity, and transform under the adjoint representation of SU(n_f). These correspond to the lightest octet of pseudoscalar mesons ($\pi^\pm$, π^0, η, $K^\pm$, K^0, $\overline{K}^0$). While NGB are massless, these mesons are pseudo-Goldstone bosons, because their masses are small compared with the scale of the SSB, $\Lambda_\chi \sim 1$ GeV. Their masses are proportional to the square root of the quark masses, and therefore are related to the aforementioned explicit symmetry breaking (explained in Sec.1.2.3).

Toy example: the σ model

Before discussing ChPT, we start with a toy example, the σ model, which describes the pions, the scalar meson σ and implements the chiral SSB in the $n_f = 2$ case[5]. According to their quantum numbers, the aforementioned mesons correspond to the following currents: $\sigma \sim \overline{q}q$, $\pi^a \sim i\overline{q}\tau^a\gamma_5 q$. From Eq. (1.2) they transform under G at LO as:

$$\pi^a \longrightarrow \pi^a - \epsilon_A^a \sigma - \epsilon_{abc}\epsilon_V^b \pi^c, \quad \sigma \longrightarrow \sigma + \epsilon_A^a \pi^a \ . \tag{1.30}$$

In a first step we study the parametrization in which the field transformations are lineal in the fields themselves (linear realization). This corresponds to embedding the mesons in a multiplet: $\Phi(x)^T = (\vec{\pi}, \sigma)$, therefore the Lagrangian of the so-called linear σ model reads

$$\mathcal{L}_\sigma = \frac{1}{2}\,\partial_\mu \Phi^T \partial^\mu \Phi - \frac{\lambda}{4}\left(\Phi^T\Phi - v^2\right)^2 \ , \quad v^2 > 0 \ . \tag{1.31}$$

The Lagrangian is invariant under G (with $n_f = 2$), which is an equivalent of the rotational group $SO(4)$. In fact, $\mathcal{L}$ is invariant under rotations of the four components.

At tree level, where one can think of Φ as a classical field, the potential is at its minimum when $\Phi^T\Phi = v^2$. This corresponds to a degenerate ground state, Φ_0. We then choose our vacuum to be the one satisfying $\langle 0|\,\sigma\,|0\rangle = v$ and $\langle 0|\,\vec{\pi}\,|0\rangle = 0$. Therefore the chosen ground state, $\Phi_0^T = (\vec{0}, v)$, is not invariant under the symmetry of the Lagrangian, but only under SO(3). In general, this symmetry rupture is called spontaneous symmetry breaking.

[5] See Ref. [9] for a review on theories with Nambu-Goldstone modes.

After this, one redefines the field $\hat{\sigma} = \sigma - v$ around its vacuum, obtaining

$$\mathcal{L}_\sigma = \frac{1}{2}\left(\partial_\mu \vec{\pi}\partial^\mu \vec{\pi} + \partial_\mu \hat{\sigma}\partial^\mu \hat{\sigma} - 2\lambda v^2 \hat{\sigma}^2\right) - \lambda v\, \hat{\sigma}\left(\hat{\sigma}^2 + \vec{\pi}^2\right) - \frac{\lambda}{4}\left(\hat{\sigma}^2 + \vec{\pi}^2\right)^2 . \tag{1.32}$$

One can see that three massless Nambu-Goldstone bosons $\vec{\pi}$ have arisen after the breaking. They correspond to the generators of the coset SO(4) / SO(3) , the three broken generators in the SSB. On the other hand $\hat{\sigma}$ has a mass $M^2 = 2\lambda v^2$.

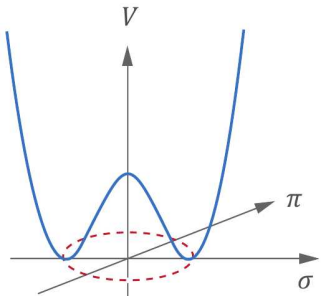

Figure 1.1: σ model potential of Eq. (1.32), where the three π^i are represented by the π axis (edited from Fig. 4.11 of Ref. [10]).

To see this in terms of the SU(2) group, one can rewrite $\mathcal{L}_\sigma$ as

$$\mathcal{L}_\sigma = \frac{1}{4}\langle \partial_\mu \Sigma^\dagger \partial^\mu \Sigma\rangle - \frac{\lambda}{16}\left(\langle \Sigma^\dagger \Sigma\rangle - 2v^2\right)^2 , \tag{1.33}$$

with $\Sigma(x) \equiv \sigma(x)\, I_2 + i\,\vec{\tau}\,\vec{\pi}(x)$ and $\langle ...\rangle$ a trace. According to Eq. (1.2), Σ transforms as $\Sigma \to g_L \Sigma g_R^\dagger$ under G. Now it is evident that $\mathcal{L}_\sigma$ is invariant under $G = \mathrm{SU}(2)_L \otimes \mathrm{SU}(2)_R$. The vacuum choice, $\langle 0|\Sigma|0\rangle = v\, I_2$, is unchanged only under $H = \mathrm{SU}(2)_V$. This corresponds to the SSB of QCD. The fact that we have just changed variables demonstrates the equivalence between $\mathrm{SU}(2)_L \otimes \mathrm{SU}(2)_R \to \mathrm{SU}(2)_V$ and $SO(4) \to SO(3)$. This breaking is key in the formulation of ChPT and its characteristics are an object of study in the realm of QCD at finite (non zero) temperature and chemical potential.

In order to walk towards ChPT, we introduce now another parameterization of the same model, the nonlinear realization. This comes through a change of variables which introduces the fields S (in the typical form

after SSB) and ϕ^a:

$$\begin{aligned} \Sigma &= (v+S)\,U\ , \\ U &= \exp\left\{ i\vec{\tau}\vec{\phi}\,\frac{\alpha(z)}{vz}\right\} = \cos\alpha(z) + i\vec{\tau}\vec{\phi}\,\frac{\sin\alpha(z)}{vz}\ , \end{aligned} \tag{1.34}$$

with $z^2 = \vec{\phi}^2$ and $\alpha(z)$ a function which encodes the particular representation. For instance for $\alpha(z) = z$ one gets the exponential form $U = \exp\left\{\frac{i\vec{\tau}\vec{\phi}}{v}\right\}$, whereas $\sin\alpha(z) = z$ corresponds to the square root one, $U = \sqrt{1-z^2} + \frac{i\vec{\tau}\vec{\phi}}{v}$. However, it is important to remark that all we have done is renaming the fields. Indeed one can show that on-shell scattering amplitudes obtained from the linear or any of the nonlinear representations are identical (equivalence theorem [11, 12, 13]).

The Lagrangian in this terms is:

$$\mathcal{L}_\sigma = \frac{v^2}{4}\left(1+\frac{S}{v}\right)^2 \langle\partial_\mu U^\dagger \partial^\mu U\rangle + \frac{1}{2}\left(\partial_\mu S\,\partial^\mu S - M^2 S^2\right) - \frac{M^2}{2v}\,S^3 - \frac{M^2}{8v^2}\,S^4\,. \tag{1.35}$$

The following remarks on SSB and the σ model are relevant at this point:

- Nonlinearity: An interesting feature of the nonlinear realization is that the scalar S and the new pions, i.e. the NGB ϕ^a, are no longer mixed by the chiral transformation G. From Eq. (1.2), S is invariant under G, while U transforms as Σ: $U \to g_L U g_R^\dagger$. The transformation is linear in U, however the model is called nonlinear because the transformation of ϕ^a is nonlinear in ϕ^a itself.

- Universality: In the nonlinear NGB sector, there are vertices with an arbitrary even number of external Goldstones, but these are always derivative vertices. Then the NGB scattering amplitudes vanish at zero momenta. As stated before, observables computed in the nonlinear realization are equal to the ones in the linear version. Therefore the nonlinear formulation has made explicit a cancellation that was happening among π^a scattering diagrams in the linear one (see Ref. [4] for an explicit calculation).

  In addition, given the transformation properties in the nonlinear model, it is straightforward to study the $M \to \infty$ limit and integrate

the scalar S in the Lagrangian[6]. If one does so, all that is left is the Goldstone Lagrangian:

$$\mathcal{L}_{M\to\infty} = \frac{v^2}{4}\langle \partial_\mu U^\dagger \partial^\mu U\rangle \ . \tag{1.36}$$

This Lagrangian is universal for the NGBs of theories with the pattern of symmetry breaking of Eq. (1.29) in the following sense: it is a model-independent interaction of the Goldstones at very low energies.

- The σ model is not realistic: the example presented here has been discarded by the community as a model of QCD. The main reason of this is that the attempts performed in the σ model do not agree well with experiment beyond the leading terms[7].

- Nonrenormalizability: In the nonlinear model, the separation of the transformations of S and ϕ^a and the integration[8] of S comes at a price. The couplings of the Goldstone vertices have negative mass dimension and therefore the Lagrangian (1.36) is not renormalizable. This means that one needs infinite renormalization conditions and has no predictive power.

- The effective field theory approach: The main conclusion of the discussion can be taken from Weinberg's *The Quantum Theory of Fields II* [15] p. 192-193. The model that will inspire ChPT is the one in which the fields transform nonlinearly under G (nonlinear σ model). When one builds an effective theory, instead of a model, one includes all operators allowed by the symmetries. A power counting is needed in order to retain only the relevant terms of the Lagrangian, and only the nonlinear realization has purely derivative Goldstone couplings, which correspond to a counting in powers of energy. Therefore, one can keep only the smaller powers in order to study low energy phenomena. This is the simplest motivation

[6] It is not possible to perform this integration in the linear model without breaking chiral symmetry in the Lagrangian.

[7] A one loop calculation in the linear σ model (see Ref. [14]) fails to describe the πN scattering data. Analogously, in the foundational work by Gasser and Leutwyler [2], the linear model fails to reproduce the experimental data in the pionic sector. It has to be said that in the latter calculation, the authors signal problems due to the value of the σ mass, M. They show that in the linear model the couplings scale with M, what is troublesome. Already $M = 500$ MeV would break perturbation theory at one loop, and integrating it out is problematic.

[8] Before the integration of S the linear and nonlinear Lagrangians are connected by field redefinition and both are renormalizable.

of the adoption of the nonlinear realization as the suitable for the description of the chiral symmetry breaking in Chiral Perturbation Theory. In fact, the Lagrangian of Eq. (1.36) is the leading order Lagrangian of ChPT (in the chiral limit)[9].

In addition, the renormalization problem is circumvented by the EFT. As will be shown, also the loops have a counting in terms of energy. At the loop order, also higher order terms of the Lagrangian enter the calculation, so that one can renormalize without problems. One can fix the necessary renormalization constants at that order and still have predictive power. This is how the next to leading order Lagrangian and its low energy constants (LECs) arise in Chiral Perturbation Theory.

1.2.3 Chiral Perturbation Theory for mesons

Chiral Perturbation Theroy is the effective field theory of QCD at low energies. It is almost 60 years ago that Steven Weinberg's seminal paper [16], which builds the Lagrangian of the nonlinear realization, came out (among different related works by others such as [17]). Ten years later, the same author elevated the model to a theory, by elucidating how to systematically compute quantities at one loop level [18]. Later, Juerg Gasser and Heinrich Leutwyler applied the theory calculating $\pi\pi$ scattering at one loop in their exhaustive work of Ref. [2]. Here it is not our intention to give a comprehensive explanation of the theory. One can find a very accurate one in Ref. [1]. We will present a brief overview of the main features.

The theory is based on the assumption of what Weinberg calls a *"theorem"* in Ref. [18]:

The "theorem" says that [...] *quantum field theory itself has no content beyond analyticity, unitarity, cluster decomposition*[10]*, and symmetry.* [...] *If one writes down the most general possible Lagrangian, including all terms consistent with assumed symmetry principles, and then calculates matrix elements with this Lagrangian to any given order of perturbation*

[9] Curiously, the electroweak symmetry breaking is analogous to the chiral pattern. We will present later the Standard Model Effective Field Theory, which is a linear realization of the symmetry breaking. Interestingly, there is a more general EFT which is a nonlinear realization, with a leading Lagrangian similar to Eq. (1.36). It is called Electroweak Effective Theory, and it does not assume the Higgs to be in a doublet with the gauge bosons (look [9] for a review).

[10] Cluster decomposition is equivalent to locality.

theory, the result will simply be the most general possible S-matrix consistent with analyticity, perturbative unitarity, cluster decomposition and the assumed symmetry principles.

ChPT follows this idea to build a Lagrangian where the degrees of freedom are the octet mesons, the Goldstone bosons of the spontaneous symmetry breaking. To construct it, all the independent operators invariant under Lorentz, charge conjugation, parity, and chiral transformations should be included.

However, as this makes an infinite set, an expansion rule must be used in order to retain the most relevant operators up to a given perturbative order. In ChPT, this ordering is given by Weinberg power counting theorem [18]. Since the NGB have derivative couplings, and derivatives correspond to momenta in the amplitude, one can expand the Lagrangian in terms of the number of derivatives. Let us denote $\mathcal{L} = \sum_d \mathcal{L}_d$ the ChPT Lagrangian, where $\mathcal{L}_d$ are the terms in the Lagrangian with vertices of d derivatives (or powers of the meson mass that will be introduced below). If a general amplitude depends on external meson momenta p_i, which set the small scale $p_i \sim p$, and on meson masses, which must be $M_\phi \sim \mathcal{O}(p)$, then the scaling D of the amplitude is defined by

$$\mathcal{A}(\lambda p, \lambda M_\phi) = \lambda^D \mathcal{A}(p, M_\phi) \ . \tag{1.37}$$

For illustrative purposes, one can study the scaling of the tadpole loop:

$$\mathcal{A}^{\text{tadpole}}(M_\phi) = \int \mathrm{d}^n k \frac{1}{k^2 - M_\phi^2} \ . \tag{1.38}$$

One scales M_ϕ and changes variables:

$$\begin{aligned} \mathcal{A}^{\text{tadpole}}(\lambda M_\phi) \quad &= \quad \int_{-\infty}^{\infty} \mathrm{d}^n k \frac{1}{k^2 - \lambda^2 M_\phi^2} \underbrace{=}_{k=\lambda k'} \int_{-\lambda\infty}^{\lambda\infty} \lambda^n \mathrm{d}^n k' \frac{1}{\lambda^2} \frac{1}{k'^2 - M_\phi^2} \\ &\underbrace{=}_{\lambda \neq 0} \quad \lambda^{n-2} \mathcal{A}^{\text{tadpole}}(M_\phi) \ . \end{aligned} \tag{1.39}$$

From this analysis, one sees that the internal line has an $n-2$ scaling, with n the number of dimensions. This is in fact general independently of the topology. It can be deduced from the fact that the only scales in a properly renormalized loop amplitude are p_i and M_ϕ, and therefore the dominant contribution of the loop momentum is also order p [15]. In consequence, the amplitude of a general loop graph will have the

Weinberg power counting (at $n = 4$ dimensions):

$$D = 4L - 2I + \sum_d d n_d = 2(1 + L) + \sum_d (d - 2) n_d \ , \tag{1.40}$$

where the diagram contains n_d vertices with d derivatives, $L \equiv\#$ loops, $I \equiv\#$ internal lines, and p represents a generic momentum. Notice that in the right hand side I has been eliminated thanks to the topological relation $L = 1 + I - \sum n_d$. Equation (1.40) determines which diagrams should be included to calculate up to a certain accuracy. It is straightforwardly related to the effective Lagrangian, which is organized in terms of a certain order.

The LO Lagrangian, $\mathcal{O}(p^2)$, is in fact [2, 1]:

$$\mathcal{L}_2 = \frac{F_0^2}{4} \langle D_\mu U \left(D^\mu U^\dagger \right) \rangle + \frac{F_0^2}{4} \langle \chi U^\dagger + U \chi^\dagger \rangle, \tag{1.41}$$

where $U = \exp\left\{ \frac{i\phi}{F_0} \right\}$ in line with (1.34) and $\phi = \phi^a T^a$, with T^a the Pauli or Gell-Mann matrices for $n_f = 2, 3$ respectively[11]. Including strangeness one has the following connection with the physical basis:

$$\phi = \phi^a \lambda^a = \begin{pmatrix} \pi^0 + \frac{1}{\sqrt{3}}\eta & \sqrt{2}\pi^+ & \sqrt{2}K^+ \\ \sqrt{2}\pi^- & -\pi^0 + \frac{1}{\sqrt{3}}\eta & \sqrt{2}K^0 \\ \sqrt{2}K^- & \sqrt{2}\bar{K}^0 & -\frac{2}{\sqrt{3}}\eta \end{pmatrix} \ . \tag{1.42}$$

The following gauge elements are also needed:

$$D_\mu U = \partial_\mu U - i r_\mu U + i U l_\mu \ , \quad \chi = 2B_0 (s + ip) \ , \tag{1.43}$$

where l_μ, r_μ, s and p are external c-number fields, the external currents used to couple the mesons to the electroweak interaction (promoting the global chiral symmetry to a local one [1]) and to introduce the meson masses. The Lagrangian has two LECs, F_0 is the pion decay constant in the chiral limit[12] and $B_0 = -\sum_{i=1}^3 \langle 0 | \bar{q}_i q_i | 0 \rangle / (3F_0^2)$. The transformation properties of these objects are given in Ref. [1].

The meson masses are introduced taking $s = \mathcal{M}$, with $\mathcal{M}$ =diag(m_u,m_d) or $\mathcal{M} = \mathrm{diag}(m_u, m_d, m_s)$ the mass matrix in the corresponding n_f case.

[11] The standard transformation convention is $U \to g_R U g_L^\dagger$, as in Ref. [1]. This is different than the one presented below Eq. (1.35) (the difference arises from the choice of left and right group representatives, $(U, 1)$ vs $(1, U)$).

[12] The parameter F_0 corresponds to v of the σ model in Eq. (1.31) at LO.

This explicitly breaks chiral symmetry, in the exact same way as it is broken in the QCD Lagrangian of Eq. (1.5). Therefore the effective theory implements realistically the symmetry breaking (electromagnetism and other interactions also break it). In the SU(2) isospin symmetric limit this leads to $M_\pi^2 = 2B_0 m_q$ (Gell-Mann–Oakes–Renner relation) and $\chi = M_\pi^2 I_2 + ...$. Given that the light-quark mass, m_q, and the pion mass, M_π, are related as stated, discussing the m_q or M_π will be interchangeable in what follows (up to higher orders).

1.2.4 Chiral Perturbation Theory for baryons

The theory can be extended to describe the lowest lying baryon octet, in what is called baryon ChPT (BChPT). The construction of the effective Lagrangian with two octet baryons resembles the one for the mesons. However the fact that the baryons are not chiral NGBs and that they carry a relatively large mass represents a theoretical challenge. Nevertheless, it has been shown that it is possible to extend the theory to this sector, as reported below. The Lagrangian should have the same symmetries as the mesonic one, with the chiral symmetry gauged analogously to introduce external currents.

We will restrict ourselves to the two flavor case here, i. e. nucleons, and direct the interested reader to Ref. [1] for $n_f = 3$. The pion-nucleon Lagrangian is discussed in Refs. [19] and [20] and the baryon transformation properties are discussed in Ref. [21]. We present now the LO, $\mathcal{O}(p)$, Lagrangian following Ref. [20][13]:

$$\mathcal{L}_{\pi N}^{(1)} = \bar{\Psi}\left(i\not{D} - \mathring{m} + \frac{\mathring{g}_A}{2}\not{u}\gamma_5\right)\Psi \ , \quad \Psi = \begin{pmatrix} p \\ n \end{pmatrix} \ . \tag{1.44}$$

The pions enter as $u = \exp\{i\phi/(2F_0)\}$. The baryon covariant derivative is given by $D_\mu \Psi = (\partial_\mu + \Gamma_\mu)\,\Psi$, and the so-called connection and chiral vielbein are

$$\begin{aligned} \Gamma_\mu &= \ \tfrac{1}{2} \ [u^\dagger(\partial_\mu - ir_\mu)u + u(\partial_\mu - il_\mu)u^\dagger] \ , \\ u_\mu &= \ i \ [u^\dagger(\partial_\mu - ir_\mu)u - u(\partial_\mu - il_\mu)u^\dagger] \ , \end{aligned} \tag{1.45}$$

[13] It is worth noting that there are some convention differences in the literature. In Ref. [20] $e < 0$, but we follow the opposite choice, which is more common. In Ref. [1] and [22] the external fields are presented separating them in isospin components, and some higher order couplings are different.

where also the vector/axial basis is sometimes used, with $v_\mu = (r_\mu + l_\mu)/2$, $a_\mu = (r_\mu - l_\mu)/2$. Finally $\mathring{m}$ and $\mathring{g}_A$ are the mass and the axial charge of the nucleon, both in the chiral limit. For instance, to couple to the photon field A_μ, one takes $v_\mu = -eA_\mu Q$, with $Q = (1+\tau^3)/2$ and $e > 0$, the charge of the positron.

By construction, ChPT is limited to the energy domain below the hadronic resonances, however, accounting for these as explicit degrees of freedom (instead of just absorbing its effect in the LECs) can result in a powerful extension of the theory. If such fields couple strongly to pions and nucleons and/or have relatively low masses, the convergence of the perturbative series can be improved including these relevant d.o.f.s. This is the case of the $\Delta(1232)$ resonance, which is known to couple strongly to π-N from phenomenology. The Δ is an $I(J^P) = 3/2(3/2^+)$ baryon which is close to the nucleon in mass and has a relatively large decay rate to photon. It is key that these states are relatively light: $\delta = m_\Delta - m_N \sim 300$ MeV. This allows to establish a power counting for the diagrams with intermediate resonances (the inclusion of resonant states beyond the baryon decouplet is problematic). The explicit inclusion of the Δ is beneficial [23, 24, 25, 26, 27] and can extend the range of applicability of ChPT. In general, the study of nucleon properties in ChPT (polarizabilities, couplings and form factors) is improved by the dynamical treatment of the Δ resonance, as can be appreciated from this, by no means exhaustive, list of references [28, 29, 30, 31].

Being a spin 3/2 particle complicates the treatment of its field. A massive fermion of spin 3/2 requires $2 \times 4 = 8$ independent complex fields to account for it. The Rarita-Schwinger formalism [32] allows to describe this kind of particle by means of a vector spinor Ψ^μ, with a Dirac field for each value of the Lorentz index μ. However, this encodes $4 \times 4 = 16$ complex fields, so that one needs to implement constraints in order to retain only the physical degrees of freedom. To this end, a Dirac's constraint analysis is performed for the $\pi\Delta$ Lagrangian in Ref. [33], resulting in the elimination of LECs g_2 and g_3 from it. Therefore, we follow Refs. [22, 1] and write:

$$\mathcal{L}^{(1)}_{\pi\Delta} = \bar{\Psi}_\mu \xi^{\frac{3}{2}} \Lambda^{(1)\mu\nu}_{\pi\Delta}(A = -1, g_{2,3} = 0) \xi^{\frac{3}{2}} \Psi_\nu \ , \tag{1.46}$$

where $\xi^{\frac{3}{2}}_{ij} = \delta_{ij} - \frac{\tau_i \tau_j}{3}$, $\Psi_\mu = \Psi_{\mu,i,r}$ has implicit SU(2) indices $i = 1, 2, 3$, $r = \pm 1/2$, and its relation to physical Δ states is given in Ref. [1].

A is a so-called off-shell parameter, related to a certain symmetry of the Lagrangian called point transformation. In line with [22, 1], we set $A = -1$. Consequently, $\Lambda^{(1)\mu\nu}_{\pi\Delta}$ is given by:

$$\Lambda^{(1)\mu\nu}_{\pi\Delta}(A=-1, g_{2,3}=0) = -\Big[(i\not{D} - \mathring{m}_\Delta)g^{\mu\nu} \\ -i(\gamma^\mu D^\nu + \gamma^\nu D^\nu - \gamma^\mu \not{D}\gamma^\nu) + \mathring{m}_\Delta \gamma^\mu\gamma^\nu + \frac{g_1}{2}\not{u}\gamma_5 g^{\mu\nu}\Big] \ , \quad (1.47)$$

and the covariant derivative reads, with explicit indices,

$$\begin{aligned} (D_\mu \Psi_\nu)_{i,r} &= \mathscr{D}_{\mu,ij,rs}\Psi_{\nu,j,s} \ , \\ \mathscr{D}_{\mu,ij,rs} &= \delta_{ij}\delta_{rs}\partial_\mu - 2i\epsilon_{ujk}\gamma_{\mu,k}\delta_{rs} + \delta_{ij}\left(\Gamma_\mu\right)_{rs} \ , \end{aligned} \quad (1.48)$$

with $\Gamma_{\mu,i} = \frac{1}{2}\langle \tau^i \Gamma_\mu \rangle$, and Γ_μ given in Eq. (1.45).

For the $\pi N\Delta$ interaction, there are two versions in the literature, called the consistent [34] and the simple interaction [35]. On the one hand, the consistent interaction is constructed such that only the spin 3/2 degrees of freedom are introduced, therefore it is consistent in the counting of d.o.f.s. On the other hand, the simple formalism includes spin 1/2 d.o.f.s. However, as shown in Ref. [36], the formalisms are equivalent in ChPT, up to changes in the values of LECs, because they are connected via field redefinition. Denoting $\mathcal{L}_{\rm RS}$ the free Δ Lagrangian, and $\mathcal{L}^{(\rm c)/(\rm s)}_{\pi N\Delta}$, the consistent/simple interaction Lagrangians respectively, there is a field redefinition which brings from the consistent formalism to the simple one,

$$\mathcal{L}_{\rm RS} + \mathcal{L}^{(\rm c)}_{\pi N\Delta} \longleftrightarrow \mathcal{L}_{\rm RS} + \mathcal{L}^{(\rm s)}_{\pi N\Delta} - \mathcal{L}_{\pi\pi NN} \ , \quad (1.49)$$

where $\mathcal{L}_{\pi\pi NN}$ corresponds to a $\pi\pi NN$ contact which arises from the field redefinition and satisfies the symmetries of ChPT. The details are givem in Ref. [36]. As explained there, one can then recall the equivalence theorem [11, 12, 13] mentioned in Sec. 1.2.2, which holds to arbitrary number of loops. Thanks to it, one can introduce the Δ in ChPT in the simple formalism, and ignore the $-\mathcal{L}_{\pi\pi NN}$, absorbing its contributions in the terms present in the chiral Lagrangian. In consequence, the parametrization of observables will be the same as if one would have used the consistent interaction, up to values of LECs, *i. e.* contact terms. This is the strategy that we follow. Consequently, we employ the simple interaction Lagrangian, $\mathcal{L}^{(1)}_{\pi N\Delta}$, of Ref. [1] with $A = -1$, but denoting the

$\pi N\Delta$ coupling as h_A[14] instead of g:

$$\mathcal{L}^{(1)}_{\pi N\Delta} = h_A\, \bar{\Psi}^i_\mu \xi^{\frac{3}{2}}_{ij} (g^{\mu\nu} - \tilde{z}\gamma^\mu\gamma^\nu) u_{\nu,j} \Psi + \text{h.c.}\,, \tag{1.50}$$

with $u_{\mu,i} = \frac{1}{2}\langle \tau^i u_\mu \rangle$ and $\tilde{z} \neq -1/4$ (see [1] for additional discussion).

1.2.5 Higher orders and loops in ChPT

So far we have presented only the ChPT LO Lagrangians. In order to make a more precise description and to extend the energy range, one needs to calculate higher order corrections. However, this comes with two main complications.

On the one hand, one needs NLO Lagrangians, which come with a higher number of new LECs, than the LO ones. More independent combinations of derivatives and external sources can be arranged in an operator of higher order in energy. For instance, only with $D_\mu U$ building blocks, $\mathcal{O}(p^2)$ allows for $\langle D_\mu U\,(D^\mu U)^\dagger \rangle$, whereas $\mathcal{O}(p^4)$ accommodates $\langle D_\mu U\,(D^\mu U)^\dagger \rangle^2$, $\langle D_\mu U\,(D_\nu U)^\dagger \rangle^2$ and $\langle (D_\mu U\,(D^\mu U)^\dagger)^2 \rangle$. These LECs add to the LO ones, and therefore more experimental or LQCD results are needed to fix their values, before one has predictive power. The NLO Lagrangians of meson and baryon ChPT can be found in Ref. [1]. The pion-nucleon Lagrangian in particular can be found in Ref. [20] up to $\mathcal{O}(p^4)$ (some of its terms are given here in Eqs. (2.5),(2.4), (3.14), (3.15) and (3.16)).

On the other hand, loops enter at this order. They carry divergent terms that are renormalized in dimensional regularization redefining the LECs. Here, baryon ChPT has an additional complication, the baryon mass in the loop propagators breaks the desired power counting. How to solve this problem is explained in the following section.

Extended on Mass Shell Renormalization Scheme

The fact that the baryon mass does not vanish in the chiral limit introduces a heavy scale in the propagator. At first sight, it seems that the correspondence between chiral and loop expansions is lost [19], [37]. Nevertheless, one can establish a power counting for the loops by separating the hard and soft components of the baryon momentum. This

[14] Note that h_A in Ref. [34] is two times the one here.

is called the heavy baryon-approach (HB) [38]. However it comes at a price: Lorentz invariance is lost (it is nonrelativistic) and the analytic structure of the amplitudes is distorted.

The HB propagator contains only the soft part of the baryon momentum in the denominator, so that it counts as $\mathcal{O}(p^{-1})$. The counting is therefore:

$$D = 4L - 2I_M - I_B + \sum_d d\, n_d \ , \tag{1.51}$$

where the only difference with Eq. (1.40) is the distinction between I_M and I_B indicating internal mesons and baryons respectively.

A more recent relativistic formalism that enforces the HB power counting without breaking Lorentz invariance and preserving the analytic structure is the so-called extended on mass shell (EOMS) renormalization scheme [39]. It has been successful in describing low energy baryon phenomenology in these years ([40], [41] among others). In this scheme, one first performs dimensional renormalization and then an additional renormalization. In the latter, the terms that break the HB ChPT power counting of Eq. (1.51) are absorbed in a redefinition of the LECs. This can be done because these terms are always analytic in the expansion parameters: energy and quark masses (or equivalently M_π^2).

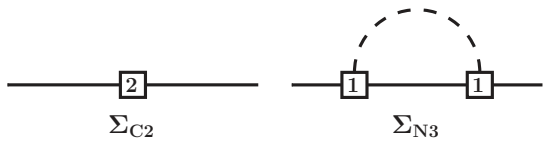

Figure 1.2: Nucleon selfenergy diagrams up to $\mathcal{O}(p^3)$ in ChPT (figure taken from Ref.[42]).

An example of this is given in Ref. [1] with the nucleon mass dependence on the pion mass, $m_N(M_\pi)$. If one calculates the nucleon mass including the Fig. 1.2 loop, which is $\mathcal{O}(p^3)$ according to Eq. (1.51), one obtains before renormalization:

$$m_N(M_\pi) = \mathring{m} - 4c_1 M_\pi^2 + \Sigma_{\mathrm{loop}}|_{\not{p}=\mathring{m}}(M_\pi) \ , \tag{1.52}$$

$$\Sigma_{\mathrm{loop}}|_{\not{p}=\mathring{m}}(M_\pi) = \frac{3\mathring{g}_A^2}{32\pi^2 F_0^2}\left[-\mathring{m}^3 R - \mathring{m} M_\pi^2 R + \mathring{m} M_\pi^2 - \pi M_\pi^3\right] + \mathcal{O}(M_\pi^4) \ ,$$

where c_1 corresponds to an insertion of the $\mathcal{O}(p^2)$ Lagrangian of Ref. [20] and Σ_{loop} is the $\mathcal{O}(p^3)$ loop (Σ_{C2} and Σ_{N3} in Fig. 1.2 respectively). Here

R is the divergent term which one subtracts in the $\widetilde{\rm MS} = \overline{\rm MS} - 1$ scheme redefining $\mathring{m}$ and c_1. After the dimensional renormalization, one performs the EOMS renormalization, where the third term in the bracket in Eq. (1.52), which breaks the power counting of Eq.(1.51), is subtracted in a redefinition of c_1. Therefore, in the end one has the following expression:

$$m_N(M_\pi) = \mathring{m} - 4c_1 M_\pi^2 - \frac{3\mathring{g}_A^2}{32\pi^2 F_0^2} M_\pi^3 + \mathcal{O}(M_\pi^4) \ , \tag{1.53}$$

where $\mathring{m}$ and c_1 have been redefined in $\widetilde{\rm MS}$ and c_1 additionally in EOMS, so that $m_N(M_\pi)$ is finite and respects the power counting. On top of this, if one writes Eq. (1.53) without expanding on M_π, the full analytic structure of the loop is preserved. Equation (1.53) describes the M_π dependence that can be observed in the lattice, especially the M_π^3 term, which is non-analytic in m_q, is a prediction of one loop ChPT from LO parameters.

Finally, with respect to the Δ, different power counting rules for the δ difference and therefore for the Δ propagator have been assumed depending on the situation under study. In this work, the small-scale expansion [24] is followed, according to which $\mathcal{O}(\delta) \sim \mathcal{O}(p)$. This leads to a counting of $\mathcal{O}(p^{-1})$ to the Δ propagator, and therefore, it is considered a regular baryon in our power counting in Eq. (1.51).

1.3 Unitarity and dispersion theory

1.3.1 The Optical Theorem

This section introduces some relevant features derived from the unitarity and analyticity of the S matrix. The dispersion theory that will be addressed constitutes a suitable framework to account for resonances and nonperturbative effects in general. This discussion is motivated by our work on the electromagnetic form factor of the nucleon (Ch. 3), where the ρ resonance plays a key role. The ρ meson is an $I = 1$, $J = 1$ resonance which appears in elastic $\pi\pi$ scattering around $m_\rho \simeq 770$ MeV (as the Δ does in πN scattering). It decays almost exclusively to $\pi\pi$. Therefore, from the point of view of S-matrix theory with its focus on asymptotic states, the ρ meson can be included in $\pi\pi$ scattering via the two-pion p-wave phase shift, as we will see. In fact, it can be implemented in this

fashion to other observables, as long as one couples correctly the external states to the pions. This is what we will do in the calculation of the electromagnetic form factor. It is worth mentioning here the existence of a simplified picture, the so-called vector meson dominance, in which the ρ can be seen as interpolating between two nucleons and a photon. This simplification is not completely unrealistic, and gives an idea of the importance of the ρ meson in the EM form factor.

One speaks of unitarity because, given that probability is conserved, the S matrix is unitary, $S^\dagger S = 1$, with its element denoted $\langle f|\, S\, |i\rangle \equiv S_{fi}$. If one writes S in terms of an interaction matrix, $\langle f|\, T\, |i\rangle \equiv T_{fi}$,

$$S_{f_i} = \delta_{fi} + i(2\pi)^4 \delta(p_f - p_i) T_{fi} \ , \tag{1.54}$$

with $p_{i,f}$ the momentum of the initial and final states, unitarity can be rewritten as a sum over all possible intermediate states, n:

$$\mathrm{Im}\, T_{fi} = \frac{1}{2} \sum_n (2\pi)^4 \delta(p_f - p_i) T^*_{fn} T_{ni} \ . \tag{1.55}$$

This is known as the optical theorem. In perturbation theory, an immediate consequence of this is that one can calculate the imaginary part of an NLO amplitude from an LO one, i.e. to partially compute a loop from tree level. We will discuss how this is realized in the case of scalar $\lambda\phi^4$ theory, by the calculation of the $2 \to 2$ scattering amplitude at $\mathcal{O}(\lambda^2)$, $\mathcal{A} = \mathcal{A}^{\text{tree}} + \mathcal{A}^{\text{loop}}$, following Ref. [43]. According to Eq. (1.55), one would get that $\mathrm{Im}\, \mathcal{A}^{\text{loop}} \sim |\mathcal{A}^{\text{tree}}|^2$.

The main idea is that amplitudes are real in quantum field theory unless the denominators of the propagators approach zero, so that the $i\epsilon$ prescription becomes essential. In fact, it is easy to show that the imaginary part is equivalent to a discontinuity of the amplitude and has a physical origin. Consider an amplitude $\mathcal{A}(s)$ which is real below the 2-particle threshold $s = 4m^2$. Therefore for real $s < 4m^2$, $\mathcal{A}(s) = \mathcal{A}(s^*)^*$ is satisfied. The principle of analyticity states that the amplitude is analytic apart from isolated singularities, i.e. poles and branch points (which are generated by unitarity). Given that the previous equation is analytic in s, we can analytically continue it to the vicinity of the real axis for $s > 4m^2$, yielding

$$\mathrm{Re}\, \mathcal{A}(s + i\epsilon) = \mathrm{Re}\, \mathcal{A}(s - i\epsilon) \ , \quad \mathrm{Im}\, \mathcal{A}(s + i\epsilon) = -\,\mathrm{Im}\, \mathcal{A}(s - i\epsilon) \ . \tag{1.56}$$

The above expression is the so-called Schwarz reflection principle. It shows that our amplitude acquires a discontinuity after the threshold

which is proportional to its imaginary part:

$$\mathrm{Disc}\mathcal{A}(s) = 2i\,\mathrm{Im}\,\mathcal{A}(s+i\epsilon)\ . \tag{1.57}$$

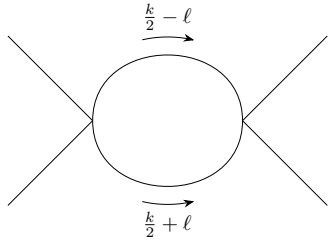

Figure 1.3: Bubble loop diagram.

To see it explicitly one can calculate the $2 \to 2$ s-channel bubble loop of Fig. 1.3:

$$i\mathcal{A}(k) = \frac{\lambda^2}{2}\int \frac{\mathrm{d}^4\ell}{(2\pi)^4}\frac{1}{\left[(k/2-\ell)^2-m^2+i\epsilon\right]}\frac{1}{\left[(k/2+\ell)^2-m^2+i\epsilon\right]}, \tag{1.58}$$

where k is the total momentum of the external states, so that $s=k^2$ and we work the CM frame, where $k_0^{\mathrm{thr}}=2m$. In particular, the discontinuity can be obtained by focusing on the zeros of the denominators. One can compute first the ℓ_0 integral by residues. In the complex ℓ_0 plane the integrand has four poles and one picks up these two: $\ell_{0\pm}=\pm k_0/2+E_{\vec{\ell}}-i\epsilon'$, with $E_{\vec{\ell}}=\sqrt{m^2+\vec{\ell}^2}$, by closing the contour below the real axis. For brevity we discuss only the ℓ_{0-} contribution, $\mathcal{A}_-$, since it is the one that will be relevant for the imaginary part (in total $\mathcal{A}=\mathcal{A}_++\mathcal{A}_-$). Then one has to compute the $\vec{\ell}$ integral

$$i\mathcal{A}_- = -2\pi i\frac{\lambda^2}{2}\int \frac{\mathrm{d}\Omega\ \mathrm{d}|\vec{l}|\ \vec{l}^2}{(2\pi)^4}\frac{1}{2E_{\vec{\ell}}}\frac{1}{\left[k_0(k_0-2E_{\vec{\ell}})+i\epsilon'\right]}\ . \tag{1.59}$$

Depending on the total energy of the external states, there will or will not be a value of $|\vec{\ell}|$ which will make the denominator approach the singularity and pick up the $i\epsilon'$. It is evident that in this case, the $|\vec{\ell}|$ goes over the singularity only if $k_0>2m$. Therefore the amplitude acquires an imaginary part for $\sqrt{k^2}>2m$, and $\sqrt{k^2}=2m$ is a branch point. In this way, we have seen that the amplitude behaves as predicted in Eq. (1.57).

One can write the discontinuity that we have discussed in the following form at $\mathcal{O}(\lambda^2)$:

$$\begin{aligned} \text{Disc}\mathcal{A}(\text{k}) &= 2i\,\text{Im}\,\mathcal{A}(k) \\ &= \frac{i}{2}\int \frac{\text{d}p_1}{(2\pi)^3}\frac{1}{2E_1}\frac{\text{d}p_2}{(2\pi)^3}\frac{1}{2E_2}\,|\mathcal{A}(k)|^2\,(2\pi)^4\delta(p_1+p_2-k)\ , \end{aligned} \tag{1.60}$$

with $p_{1,2}$ the momenta of the two propagators and $E_{1,2} = \sqrt{m^2+\vec{p}_{1,2}^{\,2}}$. The above equation is a realization of the (1.55) identity.

This kind of calculation of discontinuities is generalized to arbitrary diagrams by a procedure known as the Cutkosky rules. To compute the physical discontinuity of a given topology one can follow these steps:

1. Perform all the possible cuts to a diagram so that the cut propagators can be put on-shell.

2. For each cut propagator, make the following replacement in the integrand:

$$\frac{1}{p_a^2-m^2+i\epsilon} \to -2\pi i\delta(p_a^2-m^2)\theta(p_a^0)\ , \tag{1.61}$$

   with p_a, the momentum of each cut propagator, defined in such a way that all p_a^0 cross the cut in the same direction.

3. Sum the contributions of all possible cuts.

1.3.2 Introduction to dispersion theory: the pion vector form factor

We follow our discussion of unitarity and analyticity by reviewing the pion vector form factor (see chapter 5 of Ref. [3] for further details). This is a clear example of hadronic matrix element for which a dispersion relation (DR) proves to be useful. It also constitutes an input for our study of the electromagnetic FF in Ch. 3. We will see how to resum a particular set of diagrams (the elastic scattering ones), in order to recover unitarity, this is known as unitarization. The fact that this technique is key in the description of this form factor is illustrated in Fig. 1.4. To reproduce the pion-pion p-wave amplitude phase shift at medium energies (where ChPT does not hold), unitarization is of great help. The same applies to the pion vector form factor in the timelike region, where

the resonant contribution dominates. In the figure the inverse amplitude method (IAM) is employed, but its discussion, together with other details of the depicted curves, is postponed to the end of this section.

The pion vector form factor, F_π^{spcl}, is a real function defined trough the matrix element of the EM quark current of Eq. (1.20):

$$\left\langle \pi^+(p_2) \right| J_\mu^{\text{EM}}(0) \left| \pi^+(p_1) \right\rangle = (p_1 + p_2)_\mu F_\pi^{\text{spcl}}(q^2) \ , \tag{1.62}$$

where $q^2 = (p_2 - p_1)^2 \leq 0$, i.e. space-like region. On the other hand, the annihilation process $e^- e^+ \to \pi^- \pi^+$, corresponds to the following matrix element:

$$\left\langle \pi^-(p_1)\pi^+(p_2) \right| J_\mu^{\text{EM}}(0) \left| 0 \right\rangle = (p_2 - p_1)_\mu F_\pi^{\text{tml}}(q^2) \ , \tag{1.63}$$

with $q^2 = (p_1 + p_2)^2 \geq 4M_\pi^2$, i.e. time-like. The aforementioned analyticity of the S matrix and the fact that the form factor is related to the annihilation process by crossing symmetry implies that they are parametrized by a single function, $F_\pi(q^2)$. Such function can be defined even along the non physical region and it is continuous for $q^2 \in \mathbb{R}$,

$$F_\pi(q^2) = \begin{cases} F_\pi^{\text{spcl}}(q^2), & q^2 \leq 0 \\ F_\pi^{\text{non-phys}}(q^2), & 0 < q^2 < 4M_\pi^2 \\ F_\pi^{\text{tml}}(q^2), & q^2 \geq 4M_\pi^2 \ . \end{cases} \tag{1.64}$$

This can be explicitly shown writing the pion states in terms of the pseudoscalar current acting on the vacuum (see chapter 5 of Ref. [3]).

In the exact same way as the scattering amplitude in Eq. (1.57), $F_\pi(q^2)$ develops a discontinuity in the complex q^2 plane for $q^2 > 4M_\pi^2$. The form factor is an analytic function in the q^2 complex plane except for this cut along the real axis. Since the cut extends to the right in the standard way of displaying the complex plane (positive real part to the right), it is called right-hand cut. This information allows us to formulate a dispersive relation, useful to obtain the form factor in terms of the e^+e^- annihilation amplitude. We just apply the Cauchy integral formula:

$$F_\pi(q^2) = \frac{1}{2\pi i} \oint_C \mathrm{d}s \frac{F_\pi(s)}{s - q^2} \ , \tag{1.65}$$

and take C to be a radial contour which circumvents the discontinuity

along $q^2 > 4M_\pi^2$. Extending the contour to infinity one obtains:

$$\begin{aligned} F_\pi(q^2) &= \frac{1}{2\pi i}\int_{4M_\pi^2}^{\infty} \mathrm{d}s \lim_{\epsilon\to 0} \frac{F_\pi(s+i\epsilon) - F_\pi(s-i\epsilon)}{s-q^2} \\ &= \frac{1}{\pi}\int_{4M_\pi^2}^{\infty} \mathrm{d}s \frac{\mathrm{Im}\, F_\pi(s)}{s-q^2-i\epsilon} \ , \end{aligned} \tag{1.66}$$

where an $i\epsilon$ is included in the final term to account consistently for the imaginary part when the relation is applied for $q^2 > 4M_\pi^2$. This is the anticipated dispersion relation: for $q^2 \leq 0$ it yields the standard (space-like) pion form factor from the annihilation matrix element, and in general it describes $F_\pi(q^2)$ in the whole complex plane.

The Watson theorem and the Omnès function

We further investigate the consequences of unitarity for the pion form factor. In the first place we rewrite the optical theorem in a suitable way. The relevant T matrix element for $\gamma^* \to \pi^+\pi^-$ is, from Eq. (1.63) and the Lagrangian of Eq. (1.9):

$$T_{fi} = eA^\mu(q) F_\pi(q^2)(p_2 - p_1)_\mu \ . \tag{1.67}$$

In the optical theorem, Eq. (1.55), a sum over intermediate states appears. In the F_π case, we consider hadrons as intermediate states, $|n\rangle$. One has two general transitions, the $|n\rangle \to \pi^+\pi^-$ and the $\gamma^* \to \langle n|$ one, with the corresponding matrix elements:

$$T^*_{fn} = \left\langle \pi^-(p_1)\pi^+(p_2)\right| T \left|n\right\rangle^* \ , \quad T_{ni} = eA^\mu(q) \left\langle n\right| J^{\mathrm{EM}}_\mu \left|0\right\rangle \ . \tag{1.68}$$

The optical theorem becomes then:

$$2(p_2 - p_1)_\mu \,\mathrm{Im}\, F_\pi(q^2) = \sum\!\!\!\!\!\!\int_n \mathrm{d}\tau_N \left\langle \pi^-(p_1)\right| \pi^+(p_2) \left|n\right\rangle^* \left\langle n\right| J^{\mathrm{EM}}_\mu \left|0\right\rangle \ , \tag{1.69}$$

with $\int \mathrm{d}\tau_N$ the N-particle phase space[15]. In particular, if one focuses only on a small interval of the time-like semiaxis, the elastic region $4M_\pi^2 \leq q^2 < 16M_\pi^2$, where only $\pi^+\pi^-$ intermediate states can occur,

[15] The two body phase space is $d\tau'_{2\pi} = \delta(p_1 + p_2 - p'_1 - p'_2)\Pi_i \frac{\mathrm{d}^3 p'_i}{(2\pi)^3 p'_{i0}}$, with $i = 1, 2$.

then Eq. (1.69) reduces to

$$\begin{aligned} &2(p_2-p_1)_\mu \operatorname{Im} F_\pi^{\text{elastic}}(q^2) = \\ &= \int \mathrm{d}\tau'_{2\pi} \left\langle \pi^+(p_2)\pi^-(p_1)\right| T \left|\pi^+(p'_2)\pi^-(p'_1)\right\rangle \left\langle \pi^+(p'_2)\pi^-(p'_1)\right| J_\mu^{\text{EM}} \left|0\right\rangle \\ &= \int \mathrm{d}\tau'_{2\pi} T_{\pi\pi}(q^2,t)(p'_2-p'_1)_\mu \left(F_\pi^{\text{elastic}}(q^2)\right)^* \ . \end{aligned} \tag{1.70}$$

Here the $\pi\pi$ scattering amplitude, $T_{\pi\pi} = \langle \pi^+\pi^-| T |\pi^+\pi^-\rangle$ has been introduced, together with $t \equiv (p'_1-p_1)^2 = (p_2-p'_2)^2$, $s \equiv q^2 = (p_1+p_2)^2 = (p'_1+p'_2)^2$. Within the elastic region $T_{\pi\pi}$ has the analytic structure of the bubble of Eq. (1.58), with an $s > 4M_\pi^2$ branch cut. Equation (1.70) is a realization of the optical theorem, and for instance one could think of using it to obtain the NLO $\operatorname{Im} F_\pi^{\text{elastic}}$ just from a LO approximation of $T_{\pi\pi}$ and F_π^{elastic}. However, it turns out to be much more useful, as we will see in what follows.

One can decompose $T_{\pi\pi}$ in partial wave amplitudes (PWA) in the convention of Ref. [44] and [45][16]:

$$t_\ell(s) = \frac{1}{32\pi}\int_{-1}^{1} \mathrm{d}\cos\theta P_\ell(\cos\theta) T_{\pi\pi}(s,\cos\theta), \tag{1.71}$$

with P_ℓ the Legendre polynomials, θ defined between $\vec{p}_1$ and $\vec{p}\,'_1$ in the CM and $t_\ell(s)$ the partial wave amplitudes with δ_ℓ phases:

$$t_\ell(s) = |t_\ell(s)| \exp\left(i\delta_\ell(s)\right) \ . \tag{1.72}$$

Employing unitarity further, this time for $T_{\pi\pi}$, and taking advantage of the fact that $(p'_2-p'_1)_\mu$ in Eq. (1.70) leads to $\cos\theta' = P_1(\cos\theta')$ and the orthogonality of the P_ℓ, one arrives to the so-called Watson theorem [47] (see [3] for further details). Applied to this case, it states that, in the elastic region, the phase of the pion form factor is the same as the p-wave $\pi\pi$ amplitude:

$$F_\pi^{\text{elastic}}(s) = \left|F_\pi^{\text{elastic}}(s)\right| \exp\left(i\delta_1(s)\right) \ . \tag{1.73}$$

Notice that from now on we drop the subindex of the p-wave phase shift for simplicity.

One can take the so-called elastic approximation and neglect higher cuts beyond the 2π one, since they are less relevant in the study of the

[16] For reference, we report the leading order amplitude $t_{\ell=1} = (s-4M_\pi^2)/(96F^2)$ with the definition of [45]. This compares with the amplitudes of Ref. [46], T_ℓ^{Oller}, as $T_\ell^{\text{Oller}} = -16\pi t_\ell$.

form factor at low energies. Then the dispersive relation (1.66) becomes simpler and the results turn out to be reasonably good. In the end the entire form factor is described in terms of the $\delta(s)$ phase. The FF computed in this manner is called the Omnès function, Ω. To see how this is obtained, one starts by recalling that, since it is real below the 2π cut, F_π satisfies Schwarz's reflection principle,

$$F_\pi(s+i\epsilon) = F_\pi(s-i\epsilon)^* \ , \quad s < 4M_\pi^2 \ . \tag{1.74}$$

Expressing it in the elastic approximation, the principle reads

$$\lim_{\epsilon\to 0^+} \Omega(s \pm i\epsilon) = |\Omega(s)| \exp\left(\pm i\delta(s)\right) \ , \tag{1.75}$$

which leads to

$$\Omega(s-i\epsilon) = \Omega(s+i\epsilon) e^{-2i\delta(s)} \ , \tag{1.76}$$

and therefore

$$\mathrm{Disc}\log\left[\Omega(\mathrm{s})\right] \equiv \log\left[\Omega(\mathrm{s}+\mathrm{i}\epsilon)\right] - \log\left[\Omega(\mathrm{s}-\mathrm{i}\epsilon)\right] = 2\mathrm{i}\delta(\mathrm{s}) \ . \tag{1.77}$$

Inputting this in Eq. (1.66) one gets

$$\log\Omega(s) = \frac{1}{\pi}\int_{4M_\pi^2}^\infty \mathrm{d}s' \frac{\delta(s')}{s'-s-i\epsilon} \ . \tag{1.78}$$

To improve the convergence of the integral one subtracts the charge term, $\Omega(0)=1$:

$$\begin{aligned} \log\Omega(s) - \log\Omega(0) &= \frac{1}{\pi}\int_{4M_\pi^2}^\infty \mathrm{d}s' \ \delta(s') \left[\frac{1}{s'-s-i\epsilon} - \frac{1}{s'-i\epsilon}\right] \\ &= \frac{s}{\pi}\int_{4M_\pi^2}^\infty \mathrm{d}s' \ \frac{\delta(s')}{s'(s'-s-i\epsilon)} \ . \end{aligned} \tag{1.79}$$

In this manner, within the elastic approximation, one arrives to the so-called Muskhelishvili-Omnès[17] representation of the form factor [48, 49]:

$$F_\pi^{\mathrm{Omnes}}(s) \equiv \Omega(s) = \exp\left\{\frac{s}{\pi}\int_{4M_\pi^2}^\infty \mathrm{d}s' \frac{\delta(s')}{s'(s'-s)}\right\} \ . \tag{1.80}$$

A brief explanation of how to compute Ω is given in App. A.1. The only remaining ingredient is the p-wave phase shift. We explain how to deal with it in the next section.

[17] Finding the solution of Eq. (1.73) is called Omnès problem. The solution provided here could be multiplied by an arbitrary polynomial and would still hold. Some times the unitarity condition is stated equivalently as $\mathrm{Im}\, F_\pi(s) = F_\pi(s)\epsilon^{-i\delta(s)}\sin\delta(s)$.

Resummation: the inverse amplitude method

The discussion of dispersion theory in this thesis has been motivated by the necessity to describe the resonant beaviour present in the isovector channel of the nucleon EM form factor in Ch. 3, related to the ρ meson. In particular, a theoretical parametrization of the pion FF is needed, since it is an input required for the description of the pion mass dependence of the nucleon form factor in the dispersive approach. However, no resummation of loop contributions, necessary to obtain a resonant result, has been performed yet. This is addressed in the present section, where the approach called inverse amplitude method (IAM) [50] is introduced to calculate the $\pi\pi$ scattering amplitude. There are other manners to work with unitarized ChPT, however we restrict ourselves to the aforementioned technique which is the one that we employ in Ch. 3.

To determine $F_\pi^{\rm Omnes}(s)$ in Eq. (1.80) it is necessary to know the phase shift, $\delta(s)$, which can be extracted from $\pi\pi$ scattering. What follows is based on the book [44], and provides a didactic introduction to the problem. To begin with, we write the optical theorem for $\pi\pi$ scattering above threshold in terms of the partial waves, t_ℓ (Eq. (1.71)), and the phase space, $\sigma = \sqrt{1-4M_\pi^2/s}$, obtaining

$$\operatorname{Im} t_\ell = \sigma |t_\ell|^2 \ . \tag{1.81}$$

This is an identity to all orders in the loop expansion and we will refer to it as elastic unitarity. The idea is to use it in a dispersion relation to obtain a resonant result from ChPT input. The amplitude is decomposed as

$$t(s, M_\pi) = t_2(s, M_\pi) + t_4(s, M_\pi) + \mathcal{O}(p^6) \ , \tag{1.82}$$

where the expression applies to each PWA[18], and the subindex refers now to the ChPT order, with a real $t_2 \sim \mathcal{O}(p^2)$ and the one loop correction $t_4 \sim \mathcal{O}(p^4)$ (recall that $s, M_\pi^2 \sim \mathcal{O}(p^2)$). Applying directly elastic unitarity (1.81) gets only one loop further, for instance from tree level to 1-loop, as we saw in Eq. (1.60):

$$\begin{aligned} \operatorname{Im} t &= \operatorname{Im}(t_2 + t_4 + \mathcal{O}(\text{2-loop})) = \operatorname{Im} t_4 + \mathcal{O}(\text{2-loop}) \\ &= \sigma t_2^2 + \mathcal{O}(\text{2-loop}) \ . \end{aligned} \tag{1.83}$$

The advantage of the IAM is that applying the optical theorem to the inverse of the amplitude leads to a particular arrangement shown below,

[18] The $I = \ell = 1$ $\pi\pi$ scattering PWA is the one entering in the pion form factor.

which results in an expression valid to all loop orders. One satisfies elastic unitarity for the right hand cut to all orders (resumming the infinite intermediate bubbles). This is more precise than applying the optical theorem directly to the amplitude and leads to good agreement with experiment [46]. Therefore, one defines $G = t_2^2/t$, which has the same analytic structure as t since t_2 is real, and obtains the following for the right hand cut:

$$\mathrm{Im}\, G = t_2^2\, \mathrm{Im}\, \frac{1}{t} = t_2^2 \frac{1}{2}\left(\frac{1}{t} - \frac{1}{t^*}\right) = -t_2^2 \frac{\mathrm{Im}\, t}{|t|^2} = -t_2^2 \sigma \ , \tag{1.84}$$

which is valid to all loop orders and can be computed in ChPT.

To extract from this the real and imaginary parts of t one uses dispersion relations. Since our ChPT input goes up to $\mathcal{O}(s^2)$, growing as s^2 at large s, it is convenient to write a twice subtracted DR. In terms of the ChPT amplitudes one obtains from Eq. (1.83) the following DRs:

$$\begin{aligned} t_2 &= a_0 + a_1 s \\ t_4 &= b_0 + b_1 s + b_2 s^2 + \frac{s^3}{\pi}\int_{4M_\pi^2}^{\infty} \mathrm{d}s' \frac{\sigma(s') t_2^2(s')}{s'^3 (s' - s - i\epsilon)} \ , \end{aligned} \tag{1.85}$$

where the a_i and b_i depend on M_π. There is also a left hand cut, but we neglect it in the introduction for simplicity, given that it is subdominant. Now we write the DR for G applying Eq. (1.84)

$$G = G_0 + G_1 s + G_2 s^2 - \frac{s^3}{\pi}\int_{4M_\pi^2}^{\infty} \mathrm{d}s' \frac{\sigma(s') t_2^2(s')}{s'^3 (s' - s - i\epsilon)} \ . \tag{1.86}$$

To fix the unknown G_i, which are M_π dependent, we match to the ChPT expression writing $G = t_2^2/t \approx t_2^2/(t_2 + t_4)$ and expanding in s and M_π. In this way one finds $G_0 \approx a_0 - b_0$, $G_1 \approx a_1 - b_1$, $G_2 \approx -b_2$. From Eq. (1.85) this implies that

$$G = t_2^2/t \approx t_2 - t_4 \ , \tag{1.87}$$

and therefore

$$t = \frac{t_2^2}{t_2 - t_4} = t_2 + t_4 + \frac{t_4^2}{t_2} + \ldots \ . \tag{1.88}$$

This is the anticipated resummation and satisfies elastic unitarity (1.81) to all loop orders. It is more accurate than Eq. (1.85) which is perturbative. The desired IAM phase shift is therefore given by $\delta = \arctan(\mathrm{Im}\, t/\, \mathrm{Re}\, t)$.

Finally, to illustrate the improvement obtained by unitarization, a comparison between ChPT and the IAM is shown in Fig. 1.4. We display the p-wave phase shift and the pion vector FF, and compare results from plain ChPT with the ones from IAM. On the left panel, the dashed curve is a parametrization of experimental data [51]. In red, the NLO ChPT $\delta(s)$ from Ref. [45]. In blue, the IAM $\delta(s)$ using Eq. (1.88) and same ChPT input as previous curve; in addition our improved IAM version is shown in gray (details in Ch. 3). It is clear that the IAM is needed here to account for the ρ in the phase shift. A similar scenario is depicted on the right for the form factor. The points are data from Belle II [52]. In red, the one loop ChPT result from Eq. (15.3) of Ref. [2] is shown (even if not apparent due to the log scale, it predicts the positive s-curvature at threshold). In blue, the Omnès approximation, Ω, from Eq. (1.80), with the NLO IAM $\delta(s)$ of [45] (calculation details in App. A.1). In black and gray our improved versions of Ω and the FF respectively (explained in Ch. 3). Again, it is evident that unitarization, already in a simple approach as the Omnès approximation, is able to account for the ρ resonance, whereas ChPT is not. This is not intended as a criticism towards ChPT, but as an illustration of the necessity of unitarization in the resonance region.

As mentioned before, in Ch. 3 we seek to describe the M_π dependence of the nucleon EM form factor, and for that purpose an empirical parametrization of the pion FF is not enough, we need to predict its dependence on M_π. As detailed in Ch. 3 and App. C.1, the IAM with the NLO ChPT $\pi\pi$ scattering amplitudes provides the M_π dependence. For illustrative purposes, we display in Fig. 1.5 the pion p-wave scattering phase shift for different values of M_π. It is apparent from the figure that for $M_\pi \approx 0.45$ GeV, $m_\rho < 2M_\pi$ and the ρ width approaches zero[19]. In other words, the ρ-meson becomes a bound state. Of course, above this M_π value the formalism is not valid. On top of that, the ρ mass can be extracted from the crossing of $\delta(s)$ at $\pi/2$. As shown in Fig. C.2 of the appendix, we predict the LQCD $m_\rho(M_\pi)$ [54] very precisely. It is also in agreement with the three-flavor IAM results of Ref. [55].

With this being said, we move now to the last section of the introduction, where we comment on the topic of new physics beyond the Standard Model and its effect at low energies on hadronic processes.

[19]The ρ mass increases with M_π [53] as shown in our Fig. C.2. However, it is slower than $2M_\pi$, the threshold energy.

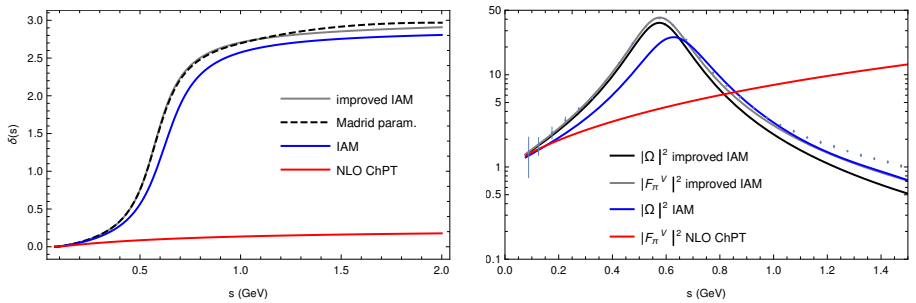

Figure 1.4: *Left panel:* two pion p-wave phase shift, $\delta(s)$. In red, determined by the NLO ChPT amplitude from Ref. [45] (LECs fitted therein). In blue, the IAM $\delta(s)$ following Eq. (1.88) and same ChPT input as previous curve. In gray the refined $\delta(s)$ from our paper (Ch. 3), which includes a Blatt-Weisskopf form factor, fitted to the Madrid parametrization of experimental data [51] (dashed black). *Right panel:* pion vector form factor and Omnès function, $\left|F_\pi^V(s)\right|^2$ and $|\Omega(s)|^2$ respectively. Points are data from Belle II [52]. In red, the one loop ChPT result from Eq. (15.3) of Ref. [2] (even if not apparent due to the log scale, it predicts the positive s-curvature at threshold). In blue, the Ω from Eq. (1.80), with the NLO IAM $\delta(s)$ of [45] (calculation details in App. A.1). In black, the improved Ω from our paper (Ch. 3). In gray, the F_π^V from Ch. 3, which includes the α_V phenomenological correction.

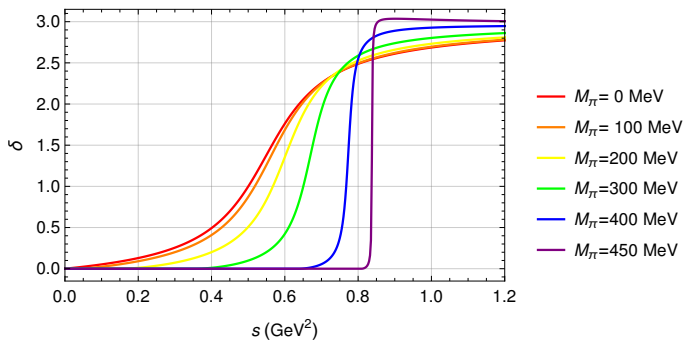

Figure 1.5: Pion p-wave scattering phase shift δ from Eq. (C.1) as a function of the Mandelstam variable s for different values of M_π.

1.4 New physics and effective field theories

The properties of hadrons are interesting not only for their content on the underlying strong and electroweak interaction, but also because they may encode information on new physics (NP) yet to be discovered. There is a huge ongoing effort dedicated to the search of these phenomena, which ideally would solve other problems of the formulation of the Standard Model.

Decays of heavy hadrons are analyzed in this context, with bottomed and charmed hadrons receiving a lot of attention [56]. In this thesis, we study a charmed one, the Λ_c baryon, characterized by $I(J^P) = 0(1/2^+)$, positive charge and $m_{\Lambda_c} \simeq 2286$ MeV. In particular we compute its weak semileptonic decay: $\Lambda_c \to \Lambda\, \ell^+ \nu_\ell$ (see Ref. [57] for a review on c decays). Recall that the Λ is the lightest baryon which contains strangeness, with $m_\Lambda \simeq 1115$ MeV and it is also $0(1/2^+)$. Partly motivated by very recent results from the BESIII collaboration [58], our study takes advantage again of existing effective field theories to analyze the decay. This leads us to briefly introduce the Standard Model Effective Field Theory (SMEFT), which parametrizes the NP fingerprints and Heavy Quark Spin Symmetry (HQSS), a useful approach to estimate heavy hadrons matrix elements.

1.4.1 Standard Model Effective Field Theory

The Standard Model Effective Field Theory constitutes a parametrization of high energy NP modes in terms of operators made of Standard Model fields. The idea is that the heavy fields are integrated out in the generating functional, which produces the appearance of new effective terms in addition to the SM Lagrangian. This approach has the advantages of an EFT: it is model-independent and has a systematic expansion in terms of power counting. The latter is based on the fact that the new operators are suppressed by inverse powers of the NP heavy scale, Λ (this happens in virtue of the Appelquist-Carazzone decoupling theorem [59]; see the introductory notes [60] and the review [61] for details[20]). The suppression is estimated as v/Λ to the respective power, where v is the Higgs vacuum expectation value [62] and represents the SM scale.

[20] It should be said that there is a more general theory than SMEFT, the so-called Electroweak EFT, which implements a chiral formalism. See Ref. [9] for an introduction.

In SMEFT one considers a generic high energy theory which is assumed to have at least the symmetries of the Standard Model. Then one works in the framework in which the heavy new physics modes have been integrated out in the generating functional, and therefore the degrees of freedom are just the SM fields. One then builds the effective Lagrangian which is Lorentz invariant, and has the $\mathrm{SU}(3)_C \otimes \mathrm{SU}(2)_L \otimes \mathrm{U}(1)_Y$ symmetry mentioned in Sec. 1.2.1. This leads to the following terms, in addition to the SM Lagrangian:

$$\mathcal{L}_{\mathrm{SMEFT}} = \mathcal{L}_{\mathrm{SM}} + \frac{1}{\Lambda}\sum_k C_k^{(5)} O_k^{(5)} + \frac{1}{\Lambda^2}\sum_k C_k^{(6)} O_k^{(6)} + \mathcal{O}\left(\frac{1}{\Lambda^3}\right) \ . \quad (1.89)$$

Here C_k and O_k are the so called Wilson coefficients and the effective operators respectively. The fields have a dimension, given by energy to a certain power. A Lagrangian has dimensions of energy to the fourth power, while the new effective operators are of higher dimension (indicated by the superindices). The Λ scale reflects the aforementioned suppression and makes the Wilson coefficients dimensionless (as the SM couplings). These constants encode the new physics that has been integrated out, playing a role analogous to the low energy constants in ChPT[21]. If a Wilson coefficient results to be nonzero, then information on the characteristics of the high energy theory beyond the Standard Model can be deduced.

In our study, we just need a subset of operators and we work below the electroweak scale, so that our Hamiltonian has a different appearance as compared to SMEFT. The only dimension-five SMEFT operator produces a Majorana mass term for the left-handed neutrino, which is beyond the reach of experiments for the Λ_c decay, given that it is suppressed by the neutrino mass. We will only consider SM left-handed neutrinos, which leads to the following dimension-six effective Hamiltonian for our quark level transition, $c \to s\,\ell^+\,\nu_l$ (see for instance Ref. [64]):

$$\begin{aligned} H_{\mathrm{eff}} \ = \ & \frac{G_F}{\sqrt{2}} V_{cs} 4 \Big[(1+\epsilon_L^\ell)\,(\bar{s}\gamma_\alpha P_L c)\ (\bar{\nu}_\ell P_R \gamma^\alpha \ell) \\ & + \epsilon_R^\ell\,(\bar{s}\gamma_\alpha P_R c)\ (\bar{\nu}_\ell P_R \gamma^\alpha \ell) + \frac{1}{2}\,\epsilon_S^\ell (\bar{s} c)\ (\bar{\nu}_\ell P_R \ell) \\ & + \frac{1}{2}\,\epsilon_P^\ell (\bar{s}\gamma_5 c)\ (\bar{\nu}_\ell P_R \ell) + \epsilon_T^\ell (\bar{s}\sigma_{\alpha\beta} P_R c)\ (\bar{\nu}_\ell \sigma^{\alpha\beta} P_R \ell) \Big] . \quad (1.90) \end{aligned}$$

[21] In SMEFT the $\mathcal{L}_{\mathrm{SM}}$ is also an effective term and the definition of couplings and masses changes, see [63].

Notice that at the decay energies, $q^2 \ll m_W^2$, the W boson can be integrated out, leading to the G_F Fermi decay constant. V_{cs} is the pertinent Cabibbo-Kobayashi-Maskawa (CKM) matrix element, while $P_{L,R} = (1 \mp \gamma_5)/2$ denotes the projectors onto left and right chiralities, respectively. The flavor (ℓ) dependent Wilson coefficients are denoted here ϵ_X^ℓ, and they have a suppression of v^2/Λ^2. Index $X = L$, R, S, P, T denotes the left-handed, right-handed, scalar, pseudoscalar and tensor structure of the corresponding $c \to s$ transition operators[22]. A tensor operator with P_L instead of P_R vanishes identically as can be shown with the help of Dirac algebra. Although these Wilson coefficients are in general complex, we adopt the CP-conserving limit and treat them as real in our work.

This formalism allows us to compute contributions to the decay from different new physics currents at the order $\epsilon \sim v^2/\Lambda^2$. However, since the process takes place within hadrons, it is still necessary to account for the hadronic matrix elements. This is challenging due to the familiar nonperturbative nature of QCD at low energies, and is assessed in the next section.

1.4.2 Heavy quark approximation

To study of the $\Lambda_c \to \Lambda\, \ell^+ \nu_\ell$ decay, the quark current has to be evaluated among the Λ and Λ_c hadronic states. This is a nonperturbative calculation, and LQCD constitutes the necessary technique to compute it. However, only the transition form factors related to the SM current have been extracted from the lattice in Ref. [65][23]. To be precise these are vector and axial form factors calculated with LQCD using gauge field configurations generated by the RBC and UKQCD collaborations with $2+1$ flavors of dynamical domain-wall fermions. Two different lattice-spacings are analyzed and the physical pion mass is reached for one ensemble. To account for all the NP currents in Eq. (1.90) we compute the additional form factors from the lattice ones under some approximations. We take advantage of the fact that the c quark has a large mass as compared with the rest of scales. Different ways of approximating the form factors are studied, in order to obtain an estimation of the size of the neglected

[22] Notice that the Wilson coefficient for the term proportional to the left-handed quark current is denoted ϵ_L^ℓ differing with the notation of Ref. [64] where it is represented as ϵ_V^ℓ.

[23] A very recent extraction of the form factors in the framework of QCD sum rules is also of interest [66].

terms.

This kind of approximation, *i. e.* taking advantage of the large value of the mass of the c and b quarks, is a common practice in the study of heavy hadrons. It is based on the small value of $\Lambda_\chi/m_h << 1$, where $h = c, b$ and $\Lambda_\chi \sim 1$ GeV. In the limit of the mass of the heavy quark $m_h \to \infty$, the system has the so called heavy quark symmetry, which is the combination of:

- heavy quark spin symmetry (HQSS): the dynamics are independent of the spin of the heavy quark confined within the hadron.

- heavy flavor symmetry: obvious invariance of the QCD Lagrangian under the interchange $c \leftrightarrow b$ if $m_h \to \infty$.

The aforementioned symmetries constitute the basis of the Heavy Quark Effective Theory (HQET), a useful framework to describe heavy hadrons (see the book [67] for an introduction). In particular, for our $\Lambda_c \to \Lambda$ matrix element, we work in the spirit of this effective theory, even though a weaker limit is considered in the first place, denoted on-shell heavy quark (OSHQ) approximation. In the following lines our approximations are discussed, and it should be noticed that they are general in the sense that they apply to any spin 1/2 heavy to light baryon transition.

Let us consider the transition between a heavy (H) and a light (L) spin 1/2 baryon induced by a general current $\bar{l}(x)\gamma h(x)$, in terms of heavy and light quark fields, h and l, and the Dirac structures $\gamma = \mathbb{1}$, γ_5, γ^μ, $\gamma^\mu\gamma_5$, $\sigma^{\mu\nu}$. Of course in the end we will make the following replacements: $H = \Lambda_c$, $L = \Lambda$, $h = c$, $l = s$. There are 12 real q^2 dependent form factors: scalar and pseudoscalar $F_{S,P}$, vector $F_{1,2,3}$, axial-vector $G_{1,2,3}$ and tensor $T_{1,2,3,4}$ for this kind of transitions. Adopting the notation of Ref. [68] and references therein, one has

$$\begin{aligned}
\langle L(p')|\bar{l}\,(1-\gamma_5)\,h|H(p)\rangle &= \bar{u}_L(p')\,(F_S-\gamma_5 F_P)\,u_H(p), \qquad (1.91)\\
\langle L(p')|\bar{l}\gamma^\alpha\,(1-\gamma_5)\,h|H(p)\rangle &= \\
&= \bar{u}_L(p')\Big\{\gamma^\alpha\,(F_1-\gamma_5 G_1)+\frac{p^\alpha}{M}\,(F_2-\gamma_5 G_2)+\frac{p'^\alpha}{m}\,(F_3-\gamma_5 G_3)\Big\}u_H(p)\,,\\
\langle L(p')|\bar{l}\sigma^{\alpha\beta}h|H(p)\rangle &= \bar{u}_L(p')\,\Big\{\,\frac{i}{M^2}\left(p^\alpha p'^\beta-p^\beta p'^\alpha\right)T_1\\
&\quad+\frac{i}{M}\left(\gamma^\alpha p^\beta-\gamma^\beta p^\alpha\right)T_2\;+\;\frac{i}{M}\left(\gamma^\alpha p'^\beta-\gamma^\beta p'^\alpha\right)T_3+\sigma^{\alpha\beta}T_4\Big\}u_H(p)\,,
\end{aligned}$$

where $M(m)$ denote the $H(L)$ mass. The translation of the form factors from the helicity basis adopted in Ref. [65] to the one adopted here is given by Eq. (E1) of Ref. [69] once the baryon masses are changed accordingly. Note that there are no additional form factors related to the matrix element of the operator $\bar{l}\sigma^{\alpha\beta}\gamma_5 h$. This is because of the relation $\sigma^{\mu\nu}\gamma_5=-\frac{i}{2}\epsilon^{\mu\nu\alpha\beta}\sigma_{\alpha\beta}$ (with $\epsilon_{0123}=1$), which allows to express the aforementioned matrix element in terms of the tensor form factors, T_i (see App. D.1.1 for details).

The first method to derive the form factors is presented below.

On-shell heavy quark approximation

The first two assumptions of this approach are:

- h can be treated as a free field obeying the Dirac equation $(i\partial\!\!\!/ - m_h)h(x)=0$, with m_h the heavy quark mass.
- $|H(s,p)\rangle$ can be factorized as $|H(s,p)\rangle = |h(\tilde{s},\tilde{p})\rangle\,|\lambda\rangle$, where $|\lambda\rangle$ is a residual light system. $\tilde{p}$ stands for the fraction of the H momentum p carried by the heavy quark, satisfying the on-shell condition $\tilde{p}^2 = m_h^2$; $\tilde{s}$ is the corresponding fraction of the spin projection s of H.

We show now how one can relate the scalar form factor to the vector ones. For the similar derivation for the pseudoscalar and tensor FFs the reader is referred to App. D.1.1. Relying on the standard second quantization decomposition of $h(x)$, the two assumptions lead to the following decomposition of the vector current, $J_V^\mu(x)=\bar{l}(x)\gamma^\mu h(x)$:

$$\langle L(s',p')|\,J_V^\mu(x)\,|H(s,p)\rangle = \langle L|\,\bar{l}(x)\gamma^\mu u(\tilde{s},\tilde{p})e^{-i\tilde{p}\cdot x}\,|0\rangle_h\,|\lambda\rangle\;. \qquad (1.92)$$

Proceeding analogously for the scalar current, $J_S = \bar{l}(x)h(x)$, one gets

$$\langle L|\, J_S(x)\,|H\rangle = \langle L|\, \bar{l}(x)u(\tilde{s},\tilde{p})e^{-i\tilde{p}\cdot x}\,|0\rangle_h\ \ |\lambda\rangle\ . \tag{1.93}$$

We finally assume that

- $\tilde{p} \approx p$ or, more specifically, that the heavy quark spinor, $u(\tilde{s},\tilde{p})$, satisfies $\not{p}u(\tilde{s},\tilde{p}) = m_h u(\tilde{s},\tilde{p})$.

In consequence, contracting with p^μ one obtains

$$\begin{aligned} p_\mu \langle L|\, J_V^\mu(x)\,|H\rangle &= \langle L|\, \bar{l}(x)\not{p}u(\tilde{s},\tilde{p})e^{-i\tilde{p}\cdot x}\,|0\rangle_h\,|\lambda\rangle \\ &= m_h \langle L|\, \bar{l}(x)u(\tilde{s},\tilde{p})e^{-i\tilde{p}\cdot x}\,|0\rangle_h\,|\lambda\rangle\ . \end{aligned} \tag{1.94}$$

This result, together with Eqs. (1.92,1.93), provides the following connection between the matrix elements of the vector and scalar currents:

$$p_\mu \langle L|\, J_V^\mu(x)\,|H\rangle = m_h \langle L|\, J_S(x)\,|H\rangle\ . \tag{1.95}$$

This leads to

$$F_S \bar{u}_L(p')u_H(p) = \frac{1}{m_h}\bar{u}_L(p')p_\mu \Gamma_V^\mu u_{H(p)}\,, \tag{1.96}$$

where

$$\Gamma_V^\mu = \gamma^\mu F_1 + \frac{p^\mu}{M}F_2 + \frac{p'^\mu}{m}F_3\,, \tag{1.97}$$

[see Eq. (1.92)]. With the help of the Dirac equations for baryons, Eq. (1.96) allows to write F_S in terms of F_{1-3}. This relation is given in the $m_h/M \to 1$ limit:

$$F_S = F_1 + F_2 + X(q^2,M,m)F_3\ , \tag{1.98}$$

with $X = (M^2 + m^2 - q^2)/(2Mm)$.

After extracting the remaining form factors as shown in App. D.1.1, the OSHQ prescription results read:

- OSHQ

$$\begin{aligned} F_S &= F_1 + F_2 + X(q^2,M,m)F_3\ , \\ F_P &= G_1 - G_2 - X(q^2,M,m)G_3\ , \\ T_1 &= -\frac{M}{m}(F_3 + G_3)\ , \\ T_2 &= F_1 - G_1 - G_3\ , \\ T_3 &= \frac{M}{m}G_3\ , \\ T_4 &= G_1 - \big[X(q^2,M,m) - 1\big]\,G_3\ . \end{aligned} \tag{1.99}$$

HQSS relations

If one implements all the consequences of having a static heavy quark with respect to the heavy hadron system, then stronger constraints are derived. Working in the leading order HQET, where HQSS is exact and the spin of the heavy quark is conserved, we follow Sec. 2.10 of Ref. [67] and approximate the matrix element as

$$\langle L(p')|\bar{l}\gamma h|H(p)\rangle \to \langle L(p')|\bar{l}\gamma h_v|H(v)\rangle = \bar{u}_L(p')\Gamma u_H(v) \ , \tag{1.100}$$

where $\not{v} u_H(v) = u_H(v)$ and $v = p/M$; $\gamma = \mathbb{1}$, γ_5, γ^μ, $\gamma^\mu\gamma_5$, $\sigma^{\mu\nu}$ while Γ denotes the corresponding representation in terms of form factors given by Eq. (1.92). In this scenario, the most general matrix element has the generic form

$$\langle L(p')|\bar{l}\gamma h_v|H(v)\rangle = \bar{u}_L(p')(\tilde{F}_1 + \tilde{F}_2\not{v})\gamma u_H(v)\,. \tag{1.101}$$

Therefore, in the HQSS limit, all form factors introduced in Eq. (1.92) can be expressed in terms of two, $\tilde{F}_{1,2}$. For instance, for $\gamma = \mathbb{1}$ one can read off

$$F_S = \tilde{F}_1 + \tilde{F}_2 \ . \tag{1.102}$$

Straightforward Dirac algebra manipulations lead to the determination of the rest (given in App. D.1.2). There is certain freedom on the choice of the two form factors in terms of which all the rest are expressed. We denote HQSSV the prescription in which all form factors are a function of $F_{1,2}$ and HQSSA the one where all depend on $G_{1,2}$:

- HQSSV

$$\begin{aligned} F_S &= F_1 + F_2 \ , & F_P &= F_1 \ , \\ T_1 &= 0 \ , & T_2 &= -F_2 \ , \\ T_3 &= 0 \ , & T_4 &= F_1 + F_2 \ . \end{aligned} \tag{1.103}$$

- HQSSA

$$\begin{aligned} F_S &= G_1 \ , & F_P &= G_1 - G_2 \ , \\ T_1 &= 0 \ , & T_2 &= -G_2 \ , \\ T_3 &= 0 \ , & T_4 &= G_1 \ . \end{aligned} \tag{1.104}$$

With this we close the general introduction to the thesis. The theoretical grounds have been established and we can move to the discussion of the different studies. We start by the pure ChPT calculation of the intriguing nucleon axial form factor at low energies. Its comparison to LQCD and the results obtained are described in detail in the next chapter.

Chapter 2

The nucleon axial form factor

2.1 Introduction

The axial form factor, F_A, has been introduced in Sect. 1.2.1 (Eq. (1.27)). It is a fundamental property of the nucleon, in particular its value at zero momentum transfer, g_A, carries information on the spin distribution within it. Given that the weak interaction is left-handed, *i. e.,* $V - A$, to describe its effect on the nucleon, not only the electromagnetic FFs are needed, which accounts for the vector term, but F_A is also required (and the pion pole dominated F_P (Eq. (1.27))). Therefore the axial form factor is a key ingredient in the analysis of weak processes.

We focus on the low energy regime, and our results are relevant for the analysis of neutrino elastic and quasielastic scattering on nucleons, important for neutrino oscillation experiments[1]. In particular, the axial radius, $\langle r_A^2 \rangle$ of Eq. (1.28) (recall that we denote the momentum transfer $q^2 = t = (p' - p)^2 = -Q^2$), connects with pion-electroproduction in the chiral limit, where $q^2 = 0$. Experimental extractions of the axial form factor are challenging, and might suffer from a certain model dependence. It can be studied in neutrino-deuteron scattering (νD) [70, 71], in pion-electroproduction (also considered in [70]) and in weak muon capture in muonic hydrogen (μH) [72]. Any extraction of the form factor

[1] As a general remark on the hot topic of neutrino oscillation experiments, the most wanted information is the mass hierarchy and CP violation in the leptonic sector. The ability to reconstruct the neutrino energy is crucial for this program, since oscillation probabilities depend on the neutrino energy E_ν. However, this is a difficult challenge indeed, since neutrinos are usually generated in broad energy fluxes.

requires a certain functional form to be fitted to the data. Different choices can be studied. Historically, the dipole parametrization has been used, which employs only one free parameter, the axial mass, M_A, even though it is not physically justified. The so-called z-expansion, which relies on the analytic structure of the FF dictated by QCD, has been also widely employed, and is considered to yield more reliable results. The z-expansion has a different number of free parameters depending on the order at which one truncates the expansion and leads to different sizes of the uncertainties. For instance in the low Q^2 regime in which we are interested, different parametrizations lead to different uncertainties for the axial radius, as one can see in Fig. 2.13. Moreover, neural networks have been used to assert this problem [73], even though the results were not completely satisfying. In the end, the main problem seems to be the lack of precise experimental data at low Q^2.

Another source of valuable information are lattice QCD simulations, which extract the form factor directly from the interactions dictated by the QCD Lagrangian. In the last ten years, the progress in this field has been significant [74], thanks to better computational resources, improved algorithms and techniques to lower systematic errors. In particular in the axial sector for baryons, the uncertainty due to excited-state contamination can be considerable, what has received a lot of recent attention [75, 76]. Unfortunately, in general several artifacts are present in LQCD computations, causing systematic errors: the lattice finite volume, L; the discretization spacing, a; the values of the light quark masses higher than the physical ones. Reaching the physical limit from simulations with the aforementioned artifacts is known as chiral continuum extrapolation, and again relies on a certain parametrization of the dependencies which is nontrivial.

Therefore, some theoretical input would be very useful in order to describe not only the Q^2 dependence of the form factor, but also the effect of the lattice artifacts. In this matter ChPT is of great help, since it is not an ad hoc parametrization, but is based on the symmetries of QCD. Once its low energy constants are fixed, it parametrizes the dependence of the axial form factor on the momentum transfer and the light quark mass, which are expansion parameters of the theory. Chiral Perturbation Theory can also account for lattice-volume and lattice-spacing corrections in a systematic way [77, 78]. It also results helpful to deal with the contamination from excited states [75, 76, 79]. It can be said that there

is a synergy between ChPT and LQCD, since the latter constrains the values of the low energy constants, some of which could be difficult to obtain from experiment. These constants appear in ChPT together with the quark mass dependence, and lattice results at nonphysical quark masses disentangle the values of the individual constants, which provide a valuable input to predict other observables.

Furthermore, the study of the light quark mass dependence is interesting in its own right because it provides theoretical insight that might not be accessible from experimental data. It discriminates between different low energy contributions such as the pion cloud and high energy terms (long-range forces mediated by Goldstone bosons as compared to standard short-range forces caused by confinement). This remains a complex subject though, elucidating the properties of confinement constitutes a difficult question and only limited insight can be obtained from these kind of analyses.

These questions have motivated us to perform a meta-analysis of a combined set of recent LQCD data using NNLO ChPT as parametrization. The main goal is to describe the axial form factor at low energies without relying on ad-hoc parametrizations. On top of that, we determine important LEC values and keep track of the truncation error of ChPT, aiming for consistent results while testing the convergence of the chiral approach.

As discussed below, past works have employed the non-relativistic approximation or have computed contributions only up to the leading loop correction, $\mathcal{O}(p^3)$ in the chiral expansion. Our aim here is to outperform the previous analyses thanks to the relativistic EOMS renormalization [39] and the explicit inclusion of the Δ up to $\mathcal{O}(p^4)$ (NNLO). In fact, the EOMS scheme guarantees that not only power counting but also analytic properties of loop functions are properly preserved. Moreover, the inclusion of $\mathcal{O}(p^4)$ leads to a better estimation of the truncation uncertainty, since it is given by differences between orders.

2.2 The nucleon axial form factor in relativistic BChPT

2.2.1 Relevant terms of the effective Lagrangian

We present now the Lagrangian, $\mathcal{L}_{\rm eff}$, needed for our computation. The Δ is introduced as an explicit degree of freedom within the aforementioned small scale expansion power counting [80, 24] (Secs. 1.2.4, 1.2.5). In total one needs

$$\mathcal{L}_{\rm eff} \supset \mathcal{L}^{(1)}_{\pi N} + \mathcal{L}^{(1)}_{\pi\Delta} + \mathcal{L}^{(1)}_{\pi N\Delta} + \mathcal{L}^{(2)}_{\pi N} + \mathcal{L}^{(2)}_{\pi N\Delta} + \mathcal{L}^{(2)}_{\pi\Delta} + \mathcal{L}^{(3)}_{\pi N} \ , \qquad (2.1)$$

where subscripts indicate the degrees of freedom and superscripts the chiral order.

We employ the $\mathcal{L}^{(1)}_{\pi N}$, $\mathcal{L}^{(1)}_{\pi\Delta}$ and $\mathcal{L}^{(1)}_{\pi N\Delta}$ discussed in Sect. 1.2.4, with $\tilde{z}=0$ in $\mathcal{L}^{(1)}_{\pi N\Delta}$. Regarding $\mathcal{L}^{(2)}_{\pi N}$, we follow Ref. [20], which denotes the required terms as

$$\begin{aligned}\mathcal{L}^{(2)}_{\pi N} \ \supset \ & \bar\Psi\Big(c_1\langle\chi_+\rangle - \frac{c_2}{8\mathring{m}^2}\left(\langle u_\mu u_\nu\rangle\{D^\mu,D^\nu\} + \text{h.c.}\right) \\ & + \frac{c_3}{2}\langle u_\mu u^\mu\rangle + \frac{ic_4}{4}[u_\mu,u_\nu]\sigma^{\mu\nu}\Big)\Psi \ . \end{aligned} \qquad (2.2)$$

If one includes only the isovector axial external fields $a^i_\mu\tau^i/2 \equiv a_\mu$, with $r_\mu = -l_\mu = a_\mu$, the building blocks of Eq. (1.45) read

$$\begin{aligned} D_\mu\Psi &= \left(\partial_\mu + \Gamma_\mu\right)\Psi \ , \\ \Gamma_\mu &= \frac{1}{2}[u^\dagger(\partial_\mu - ia_\mu)u + u(\partial_\mu + ia_\mu)u^\dagger] \ , \\ u_\mu &= i[u^\dagger(\partial_\mu - ia_\mu)u - u(\partial_\mu + ia_\mu)u^\dagger] \ ; \end{aligned} \qquad (2.3)$$

$\chi^+ = u^\dagger\chi u^\dagger + u\chi^\dagger u$ and $\chi = \text{diag}(M_\pi^2, M_\pi^2)$. In what follows we will also need $F^L_{\mu\nu} = \partial_\mu l_\nu - \partial_\nu l_\mu - i[l_\mu, l_\nu]$, $F^R_{\mu\nu} = \partial_\mu r_\nu - \partial_\nu r_\mu - i[r_\mu, r_\nu]$, with $F^\pm_{\mu\nu} = u^\dagger F^R_{\mu\nu} u \pm u F^L_{\mu\nu} u^\dagger$, and the isospin traces $F^{\pm,i}_{\mu\nu} = \frac{1}{2}\langle F^\pm_{\mu\nu}\tau^i\rangle$, $\omega^{\mu,i} = \frac{1}{2}\langle\tau^i u^\mu\rangle$.

Given the accuracy of the calculation, one needs also the NNLO Lagrangian from [20]:

$$\mathcal{L}^{(3)}_{\pi N} \supset \bar\Psi\left\{\frac{d_{16}}{2}\gamma^\mu\gamma^5\langle\chi_+\rangle u_\mu + \frac{d_{22}}{2}\gamma^\mu\gamma^5[D_\nu, F^-_{\mu\nu}]\right\}\Psi \ . \qquad (2.4)$$

The two LECs in the above Lagrangian are relevant for the M_π and q^2 dependence of the form factor at tree level.

In $\mathcal{L}^{(2)}_{\pi N\Delta}$, after redundant terms are eliminated from Eq. (67) of Ref. [81] (see also Sec. 3.1 of Ref. [82] and the Appendix of Ref. [83]) only the following monomials contribute:

$$\begin{aligned}\mathcal{L}^{(2)}_{\pi N\Delta} \;\supset\; & \bar{\Psi}^{k\alpha}\xi^{\frac{3}{2}}_{ki}\left\{-i\frac{b_1}{2}F^{+i}_{\alpha\beta}\,\gamma^5\gamma^\beta + ib_2F^{-i}_{\alpha\beta}\,\gamma^\beta\right. \\ & \left.+\frac{b_4}{2}\omega^i_\alpha\omega^j_\beta\gamma^\beta\gamma_5\tau^j + \frac{b_5}{2}\omega^j_\alpha\omega^i_\beta\gamma^\beta\gamma_5\tau^j\right\}\Psi + \text{h.c.} \qquad (2.5)\end{aligned}$$

and $\mathcal{L}^{(2)}_{\pi\Delta}$ [81],[84],

$$\mathcal{L}^{(2)}_{\pi\Delta} \supset \bar{\Psi}^i_\mu\xi^{\frac{3}{2}}_{ij}\left\{a_1\langle\chi_+\rangle\delta^{jk}g_{\mu\nu}\right\}\xi^{\frac{3}{2}}_{kl}\Psi^{l\nu}. \qquad (2.6)$$

introduces an M_π dependent correction to the Δ mass, in the same way as the term proportional to c_1 does for the nucleon mass.

2.2.2 Calculation

The diagrams that contribute to F_A are depicted in Fig. 2.1 and 2.2. The LECs that each of these diagrams introduces are listed in Table 2.1. At $\mathcal{O}(p^4)$, there are contributions from $\mathcal{O}(p^2)$ vertices but also baryon (N,Δ) mass insertions. The later are calculated perturbatively, i.e. we evaluate directly diagrams (i), (j), (l)-(n) of Fig. 2.2, avoiding Dyson resummations to all orders in the propagators. Alternative choices have been considered in Refs. [85, 86].

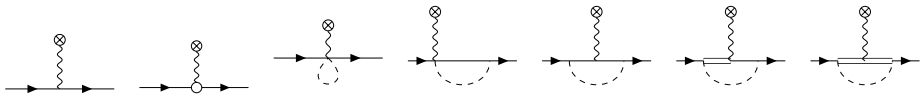

Figure 2.1: Diagrammatical contributions at orders $\mathcal{O}(p)$, (a), and $\mathcal{O}(p^3)$, (b)-(g), to the nucleon axial form factor. Dashed, solid single and double lines denote pions, nucleons and Δ resonances in that order; wiggly lines stand for external axial fields. The open circle represents an $\mathcal{O}(p^3)$ vertex, while the rest of the vertices are $\mathcal{O}(p)$. Permutations of diagrams (d) and (f) have been omitted in the figure.

Even if not depicted, the nucleon wave-function renormalization is included in the standard way. To the order of the calculation, only the

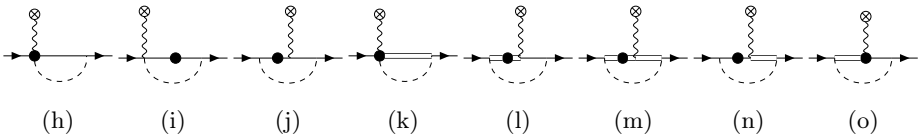

Figure 2.2: $\mathcal{O}(p^4)$ contributions to the nucleon axial form factor. Line styles are the same as in Fig. 2.1. Filled circles denote $\mathcal{O}(p^2)$ vertices. Permutations of all these diagrams are taken into account but not explicitly represented.

Table 2.1: F_A LECs introduced by Feynman diagrams in Figs. 2.1, 2.2 and by wave-function renormalization (wfr).

Diagrams	$\mathcal{O}(p)$	$\mathcal{O}(p^2)$	$\mathcal{O}(p^3)$
(a), (c), (d)	$\mathring{g}_A$	-	-
(b)	-	-	$d_{16,22}$
(e)	$\mathring{g}_A$	-	-
(f)	$\mathring{g}_A$, h_A	-	-
(g)	g_1, h_A	-	-
(h)	$\mathring{g}_A$	c_{2-4}	-
(i)	$\mathring{g}_A$	c_1	-
(j)	$\mathring{g}_A$	c_1	-
(k)	h_A	$b_{1,4,5}$	-
(l)	$\mathring{g}_A$, h_A	a_1	-
(m)	g_1, h_A	a_1	-
(n)	$\mathring{g}_A$, h_A	c_1	-
(o)	$\mathring{g}_A$, h_A	b_2	-
wfr	$\mathring{g}_A$, h_A	c_1, a_1	-

$\mathcal{O}(p)$ diagram (a), corresponding to the axial charge in the chiral limit $\mathring{g}_A$, should be multiplied by the wave-function renormalization constant Z_N, calculated from the $\mathcal{O}(p^4)$ nucleon self-energy (see App. B.1 for a

more detailed explanation),

$$Z_N \approx 1 + \left.\frac{\partial \Sigma_N^{(4)}}{\partial \not{p}}\right|_{\not{p}=m_N} . \tag{2.7}$$

Additional $\mathcal{O}(p^3)$ and $\mathcal{O}(p^4)$ contributions to g_A are generated in this way.

As commented in Sec.1.2.4, due to the presence of baryons in the loops, the power counting of such diagrams is broken. To restore it, we subtract the power counting breaking (PCB) terms by redefining the LECs. This finite renormalization, developed in Ref. [39], is called extended on mass shell (EOMS) renormalization. The LECs' shifts are lengthy, so that we provide them in the supplementary material[2]. Notice that, as in previous works [28, 87], PCB terms are identified and subtracted in an expansion in powers or M_π and t but not in δ.

Following this procedure, we obtain the axial form factor within the EOMS renormalization scheme up to $\mathcal{O}(p^4)$ with explicit Δ. Its structure is the following, with superindices indicating the chiral order and the inclusion of the Δ:

$$\begin{aligned} F_A = \; & \mathring{g}_A + 4d_{16}M_\pi^2 + d_{22}t \\ & + F_{A(\text{loop})}^{(3)\not{\Delta}}(\mathring{g}_A; M_\pi, t) + F_{A(\text{loop})}^{(3)\Delta}(\mathring{g}_A, h_A, g_1; M_\pi, t) \\ & + F_{A(\text{loop})}^{(4)\not{\Delta}}(\mathring{g}_A, c_1, c_2, c_3, c_4; M_\pi, t) \\ & + F_{A(\text{loop})}^{(4)\Delta}(\mathring{g}_A, h_A, g_1, c_1, a_1, b_1, b_2, b_4, b_5; M_\pi, t) \\ & + \mathcal{O}(p^5) \, . \end{aligned} \tag{2.8}$$

Reading this formula one might notice the following nomenclature issue: the calculation of an $\mathcal{O}(p)$ diagram such as (a) in Fig. 2.2 yields an $\mathcal{O}(p^0)$ contribution to the form factor, $\mathring{g}_A$. This is due to the fact that the external field a_μ enters in $\mathcal{L}_{\pi N}^{(1)}$ together with the partial derivative in the chiral vielbein as shown in Eqs. (1.44) and (1.45), and as a consequence the form factor has a chiral order p factorized out. When discussing the order of the calculation, the power counting of the diagram is taken as reference, and not the scaling of the contribution to the observable, in this case F_A.

[2]The Mathematica notebook with the expressions relevant for the axial form factor calculation can be found on the website shorturl.at/bAEGL (clickable link).

We do not truncate the form factor, but preserve the complete analytic structure of the loops. The $\mathcal{O}(p^3)$ part of F_A is given in Eqs. (A4-5) of Ref. [87]. The $\mathcal{O}(p^4)$ contribution from wave-function renormalization is given in Eq. (B1) of Ref. [31]. The length of the rest of the $\mathcal{O}(p^4)$ expression, which depends on several LECs, discourages us from giving it explicitly but is available in a Mathematica notebook as supplementary material [3]. We nonetheless identify that at $\mathcal{O}(p^4)$, i. e. at $\mathcal{O}(M_\pi^3)$ for g_A, c_3 and c_4 enter in the following combination $\widetilde{c}_4 = c_4 - c_3/2$, while c_2 enters only at $\mathcal{O}(p^5)$ [$\mathcal{O}(M_\pi^4)$ in g_A]. Although the rather involved contribution of diagram (k) does not, a priori, show the factorization of any mixture of b_4 and b_5 LECs, after expanding in M_π, one finds that the combination which actually enters at $\mathcal{O}(p^4)$, is $\widetilde{b}_4 = b_4 + (12/13)\, b_5$. At $\mathcal{O}(p^3)$ we reproduce the results of Eq. (A4-5) of Ref. [87], except for a global factor 36 in $\langle r_A^2 \rangle$, pointed out in Ref. [86]. However the sign of the pion tadpoles in [87] is correct, contrary to what is stated in Ref. [86]. The reason of the confusion is probably the different sign in the definitions of the integral.

At $\mathcal{O}(p^4)$ our g_A coincides with the $\not\Delta$ EOMS expressions in Ref. [85, 88] except for the different treatment of nucleon mass insertions, which in our work, do not include resummations. In consequence, $c_1 M_\pi^2$ factors appear only linearly in our computation but not at all orders. Finally, a PCB term proportional to c_4 present in Ref. [88] after the EOMS renormalization is absent in our result.

Once we have overviewed the axial form factor in ChPT, we first focus on the limit of zero momentum transfer, the axial charge. We devote the next section to analyze the quark mass dependence of the axial charge, which constitutes an interesting puzzle in itself. What follows is based on our article of Ref. [31]. Of course, the general considerations made until now hold also for g_A. In fact, the convergence of the chiral series is more easily studied in the axial charge since there is only one expansion parameter, the pion mass.

[3] See footnote 2.

2.3 The nucleon axial charge: its light quark mass dependence and pion-nucleon phenomenology

2.3.1 Introduction to the axial charge

The axial isovector charge, g_A (g_A^{u-d} to be precise), is a fundamental property of the nucleon related to the difference in the spin fractions carried by u and d quarks. It is defined as the form factor value at zero momentum, Eq. (1.28). Given that its magnitude is precisely determined from neutron β decay[4], it constitutes a benchmark for studies of Quantum Chromodynamics in the lattice (LQCD) together with other nucleon properties, such as scalar and tensor charges, electromagnetic form factors and parton distribution functions (see Ref. [91] and Sec. 10 of Ref. [74] for recent reviews).

As mentioned before, ChPT provides a systematic and model independent parametrization of the lattice results, while LQCD is useful to determine certain LECs of ChPT. This applies to the d_{16} of $\mathcal{L}_{\pi N}^{(3)}$ of Eq. (2.4). Trough a $4d_{16}M_\pi^2$ term (Eq. (2.8)), this LEC controls the slope of the quark mass dependence of the axial charge, given that m_q and M_π are related as stated after Eq. (1.43). Consequently, its determination from LQCD data at low M_π is only natural. The LEC d_{16} is considered one of the most important sources of uncertainty in the quark mass dependence of nuclear properties such as ground-state and binding energies through long-range nuclear forces [92, 93, 94].

Otherwise, LECs have been determined from experimental data[5] on various processes such as pion photo- and electroproduction [95, 96, 97, 98] but, mostly, from pion-nucleon (πN) scattering [99, 100, 101, 102, 103, 88, 40, 28, 104]. Even though d_{16} cannot be determined from πN elastic scattering, it contributes to the $\pi N \to \pi\pi N$ inelastic process. In fact, in a joint fit to elastic and inelastic πN scattering data, d_{16} has been extracted, albeit with a large uncertainty [105]. ChPT has been used to calculate the axial charge in the non-relativistic heavy-baryon [106, 107, 108, 109, 110] and relativistic [111, 85, 109, 40, 88, 87, 86] approaches both without and with the $\Delta(1232)$ as an explicit degree of freedom. In the relativistic framework, both infrared and

[4] Taking into account radiative corrections, a numerical value of $g_A = 1.2754(13)_{\rm exp}(2)_{\rm RC}$ has been recently extracted [89] from the PDG average $g_A/g_V = 1.2756(13)$ [90].

[5] Throughout this work LECs obtained from experimental data are called phenomenological or empirical to distinguish them from those extracted from LQCD simulations.

the aforementioned EOMS regularization methods have been employed. Some of these works also compute the axial form factor at low four-momentum transfers squared [111, 85, 87, 86]. In particular, the M_π dependence of the axial charge has been specifically investigated in these works [107, 108, 109, 110, 87, 86].

In the following, we study the ChPT calculation at different orders, and investigate the tension that we encounter when comparing with πN ChPT calculations without explicit Δ. Afterwards we analyze the lattice data with $\mathcal{O}(p^4)$ ChPT with Δ in EOMS, which we retain more consistent than previous analysis. As a result, we extract d_{16} and discuss the convergence of ChPT.

2.3.2 Light-quark mass dependence of the axial coupling from phenomenological input

Once the expression of the axial charge has been obtained up to a given order, one needs to assign values to the low energy constants. The strength of the effective field theory consists in the fact that these parameters relate different observables, in this case $g_A(M_\pi)$ and πN scattering. However, the higher the order in the calculation, the more LECs appear and the predictive power is weakened. In Tab. 2.2 the LECs that contribute to g_A are reported. In Ref. [105], elastic πN and $\pi N \to \pi\pi N$ scattering has been studied up to $\mathcal{O}(p^4)$ in ChPT using a modified version of the EOMS approach [104]. The LECs that enter $g_A(M_\pi)$ at $\mathcal{O}(p^4)$ in the Δ-less model were extracted, including d_{16}, thanks to the inclusion of low energy total and double differential $\pi N \to \pi\pi N$ cross section data in the combined analysis. To make a prediction of $g_A(M_\pi)$ based on this phenomenological input, we should translate the LECs from the modified EOMS of Refs. [104, 105] to the conventional one adopted here. To the order we are working at, this transformation only changes the value of d_{16} but not of c_{1-4} (see details in App. B.2). The axial charge in the chiral limit, $\mathring{g}_A$, which is not determined in Refs. [104, 105], is extracted from the experimental value, precisely known from β decay [89] as

$$g_A(M_\pi = M_{\pi(\mathrm{phys})}, \mathring{g}_A, d_{16}, c_i) = g_{A(\mathrm{phys})} = 1.2754(13)_{\mathrm{exp}}(2)_{\mathrm{RC}} \ . \quad (2.9)$$

Up to higher order corrections, the rest of chiral limit parameters have been fixed as, $F_0 \approx F_{\pi(\mathrm{phys})} = 92.2$ MeV for the pion decay constant and $\mathring{m} \approx m_{N(\mathrm{phys})} + 4c_1 M^2_{\pi(\mathrm{phys})}$, with $M_{\pi(\mathrm{phys})} = 135$ MeV and $m_{N(\mathrm{phys})} =$

939 MeV. The numerical values for d_{16}, c_{1-4} as well as $\mathring{g}_A$ and their uncertainties are summarized in Table 2.3.

Table 2.2: g_A LECs introduced by Feynman diagrams in Figs. 2.1, 2.2 and by wave-function renormalization (wfr).

Diagrams	$\mathcal{O}(p)$	$\mathcal{O}(p^2)$	$\mathcal{O}(p^3)$
(a), (c), (d)	$\mathring{g}_A$	-	-
(b)	-	-	d_{16}
(e)	$\mathring{g}_A$	-	-
(f)	$\mathring{g}_A$, h_A	-	-
(g)	g_1, h_A	-	-
(h)	$\mathring{g}_A$	c_{2-4}	-
(i)	$\mathring{g}_A$	c_1	-
(j)	$\mathring{g}_A$	c_1	-
(k)	h_A	$b_{4,5}$	-
(l)	$\mathring{g}_A$, h_A	a_1	-
(m)	g_1, h_A	a_1	-
(n)	$\mathring{g}_A$, h_A	c_1	-
wfr	$\mathring{g}_A$, h_A	c_1, a_1	-

Table 2.3: LECs employed to determine the $g_A(M_\pi)$ dependence in the $\not\Delta$ case.

	$\mathcal{O}(p^3)$	$\mathcal{O}(p^4)$
$\mathring{g}_A$	1.251 ± 0.051	1.089 ± 0.030
d_{16} (GeV^{-2})	-2.2 ± 1.1	-1.86 ± 0.80
c_1 (GeV^{-1})	-	-0.89 ± 0.06
c_2 (GeV^{-1})	-	3.38 ± 0.15
c_3 (GeV^{-1})	-	-4.59 ± 0.09
c_4 (GeV^{-1})	-	3.31 ± 0.13

Our resulting $g_A(M_\pi)$ at $\mathcal{O}(p^3)$ and $\mathcal{O}(p^4)$ are depicted in Fig. 2.3 ac-

companied by a subset of recent LQCD determinations[6]. The curves are accompanied by 1σ statistical error bands arising from the uncertainties in the LECs of Table 2.3 assuming they are Gaussian-distributed. We do not account for correlations among LECs since they are negligible because the uncertainty is strongly dominated by the d_{16} uncertainty. The

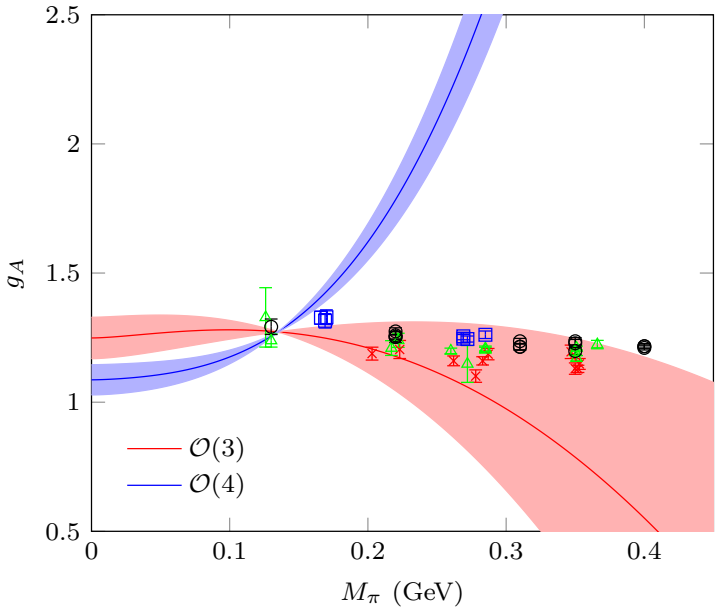

Figure 2.3: Pion-mass dependence of g_A at $\mathcal{O}(p^3)$ (red) and $\mathcal{O}(p^4)$ (blue) employing phenomenological input from Ref. [105] and 1σ error bands. The LQCD data points are from CalLat 18 [112] (black circles), Mainz 19 [113] (red crosses), RQCD 19 [79] (green triangles) and NME 21 [114] (blue squares).

$\mathcal{O}(p^3)$ result shows a partial agreement with the lattice determinations, albeit with increasing tension as M_π grows and a curvature in the central value that is absent in the LQCD points. On the other hand, it is evident that the $\mathcal{O}(p^4)$ prediction, far from improving the $\mathcal{O}(p^3)$, plainly fails to describe the M_π dependence of LQCD data. We have checked that alternative c_{1-4} extractions from earlier πN analyses using EOMS [88, 28] do not attenuate the steep increase of $g_A(M_\pi)$ at $\mathcal{O}(p^4)$. We have shown then that the inability to reconcile the light-quark mass dependence of $\mathring{g}_A$ at $\mathcal{O}(p^4)$ with phenomenology, earlier observed in non-relativistic heavy-

[6]The selection criteria for the lattice data are explained in 2.3.4

baryon ChPT [108, 109], is also an issue of the relativistic version of the theory.

This problematic $\mathcal{O}(p^4)$ result might be due to a fortuitous slow convergence of g_A in ChPT. However, one could state that additional degrees of freedom lying above the nucleons, such as the Δ [109], or even the $N(1440)$ Roper resonance, might solve the problem. A somewhat intermediate step would be the choice taken in Ref. [105], where only the Δ pole is incorporated to the theory. However, in order to predict $g_A(M_\pi)$ up to $\mathcal{O}(p^4)$ with explicit Δ, additional LECs absent in that study are necessary. For this reason we do not discuss the role of the Δ in the $g_A(M_\pi)$ dependence from purely empirical input, but delay it to Sec. 2.3.4, where our fits to recent LQCD data are presented.

In the next section we describe our procedure to fit to the lattice. In particular, we introduce an estimation of the theoretical error in the χ^2 and we correct for lattice-spacing effects.

2.3.3 General fit strategy

We will discuss now how the fit to the lattice data is performed. Given that the form factor will be analyzed later, and not only the charge, we explain the general case of the form factor fit.

First of all, we avoid model dependence by considering only data that have not been extrapolated in Q^2, M_π nor to the continuum. As we will detail later, we restrict to ensembles with a large enough volume so that size effects are negligible. When possible, we correct for the lattice-spacing, a, and to do so we introduce the following dependence:

$$F_A(t_i, M_\pi^i, a_i) = F_A(t_i, M_\pi^i) + (x_j + t_i y_j) a_i^{n_j} \ , \tag{2.10}$$

where t is the momentum transfer squared and i labels the LQCD data point. The x and y are free parameters, j is the label of the lattice action and n is the exponent of the corresponding discretization correction.

Different low energy constants appear in the form factor, some of which are well known and can be fixed, while others are left as free fitting parameters. To improve our description of the LQCD data and reduce correlations [115], we implement naturalness constraints, $\Lambda^{n-1} c_n \sim 1$,

encoded in Gaussian priors:

$$\chi^2_{\rm prior} = \sum_{\text{free LECs}} \left(\frac{\Lambda^{n-1}\, c_n}{5} \right)^2 . \tag{2.11}$$

Here, c_n stands for a generic LEC of chiral order p^n; the breakdown scale is set to $\Lambda = 1$ GeV$\sim 4\pi F_0$ [116, 1]. We foresee that a prior on $\mathring{g}_A$ is superfluous, since its value is inescapably driven to a natural one by low M_π LQCD results for g_A.

The large size of the $\mathcal{O}(p^4)$ term discussed before is a clear indication that the theoretical error associated with truncation of the chiral series should be considered. To that aim we follow the procedure of Ref. [117]. Let X be an observable with a chiral expansion

$$X = X^{(0)} + \sum_{m=1}^{\infty} \Delta X^{(m)} , \tag{2.12}$$

where $\Delta X^{(m)} = X^{(m)} - X^{(m-1)}$ refers to all the monomials that start at order m. If X is computed up to order n, $X \approx X^{(n)}$, assuming that the truncation error is dominated by order $n+1$, its contribution $\Delta X^{(n+1)}$ can be estimated in a conservative way as [117, 104]

$$|\Delta X^{(n+1)}| = \max\left\{ \epsilon^{n+1}|X^{(0)}|, \epsilon^n |\Delta X^{(1)}|, ..., \epsilon |\Delta X^{(n)}| \right\} , \tag{2.13}$$

where ϵ indicates a general chiral expansion parameter.

In the case of the axial charge, the only expansion variable ϵ is M_π/Λ, which is considered $\mathcal{O}(p)$ in ChPT. Recalling that in this case diagrammatic $\mathcal{O}(p^5)$ corresponds to $\mathcal{O}(M_\pi^4)$ at the level of $g_A(M_\pi)$, Eq. (2.13) yields for our $\mathcal{O}(p^4)$ computation:

$$\begin{aligned} \Delta g_{A\chi}^{(5)} &= \max\left\{ \left(\frac{M_\pi}{\Lambda}\right)^4 |\mathring{g}_A| , \left(\frac{M_\pi}{\Lambda}\right)^2 \left|\Delta g_A^{(3)}\right| , \frac{M_\pi}{\Lambda} |\Delta g_A^{(4)}| \right\} \\ &\sim \epsilon^4 = \mathcal{O}(p^5) . \end{aligned} \tag{2.14}$$

According to Eq. (2.8), these terms are $\Delta g_A^{(3)} = 4 d_{16} M_\pi^2 + g_{A(\rm loop)}^{(3)}$ and $\Delta g_A^{(4)} = g_{A(\rm loop)}^{(4)}$. After the discussion of Sec. 2.3.2 it is easy to anticipate that at larger M_π, $\Delta g_{A\chi}^{(5)}$ will be given by the last term in Eq. (2.14). In our $\mathcal{O}(p^3)$ fits we do not assume any prior knowledge about $\mathcal{O}(p^4)$ and, therefore, the truncation error is given by

$$\Delta g_{A\chi}^{(4)} = \max \left\{ \left(\frac{M_\pi}{\Lambda}\right)^3 |\mathring{g}_A| , \frac{M_\pi}{\Lambda} \left|\Delta g_A^{(3)}\right| \right\} \sim \epsilon^3 = \mathcal{O}(p^4) . \tag{2.15}$$

If the whole form factor is considered, one just has to take into account that there is an additional expansion parameter, the momentum transfer t, which has chiral order p^2. Therefore, for the $\mathcal{O}(p^4)$ calculation, the truncation error is given by:

$$\Delta F_{A\chi}^{(5)} = \max\left\{\epsilon^4 \mathring{g}_A, \epsilon^2 |\Delta F_A^{(3)}|, \left(\frac{M_\pi}{\Lambda}\right)|\Delta F_A^{(4)}|\right\} \sim \epsilon^4 = \mathcal{O}(p^5)\ , \quad (2.16)$$

where $\epsilon^2 \equiv \max\{M_\pi^2, -t\}/\Lambda^2$ [117].

Since we also study the agreement of the leading one loop calculation $\mathcal{O}(p^3)$, the truncation error in such fits is defined without implementing any information from the $\mathcal{O}(p^4)$ computation, and reads

$$\Delta F_{A\chi}^{(4)} = \max\left\{\left(\frac{\max\{M_\pi^3, -M_\pi t\}}{\Lambda^3}\right)\mathring{g}_A, \left(\frac{M_\pi}{\Lambda}\right)|\Delta F_A^{(3)}|\right\} \sim \epsilon^3 = \mathcal{O}(p^4)\ . \quad (2.17)$$

Altogether our χ^2 is

$$\chi^2 = \sum_i \frac{\left(F_A(t_i, M_\pi^i, a_i) - F_A^i\right)^2}{(\Delta F_A^i)^2} + \chi^2_{\text{prior}}\,. \quad (2.18)$$

Here the truncation error is added in quadrature to the LQCD one:

$$(\Delta F_A^i)^2 = (\Delta F_{A\text{LQCD}}^i)^2 + (\Delta F_{A\chi}(t_i, M_\pi^i))^2\ . \quad (2.19)$$

This procedure assigns larger uncertainties to points at high ϵ, where the convergence of the chiral expansion is poorer, therefore reducing their impact on the fit. We perform the fits iteratively, evaluating the $\Delta F_{A\chi}$ with the LECs of the previous iteration until convergence is reached ($\Delta F_{A\chi} = 0$ in the first step). With this method, truncation and LQCD errors are not independent and it is not trivial how to combine them in the error for a given quantity. In consequence, following Ref. [104], we plot them separately in the error bands for F_A, g_A and $\langle r_A^2\rangle$. On top of that, as a complementary measure of the agreement of our fit with the LQCD data, we also provide the χ_0^2 value, defined without $\Delta F_{A\chi}$ nor priors:

$$\chi_0^2 = \sum_i \frac{\left(F_A(t_i, M_\pi^i, a_i) - F_A^i\right)^2}{(\Delta F_{A\text{LQCD}}^i)^2}\,. \quad (2.20)$$

Once we have made clear our method to analyze the lattice data and the ChPT description of the form factor, we will first focus on the limit of zero momentum transfer, the axial charge.

2.3.4 Analysis of LQCD results and LEC extraction: the axial charge

Historically LQCD simulations have predicted a smaller axial charge than the experimental one (see for example Fig. 2 of Ref. [118]). However, thanks to progressive improvements, most of LQCD contemporary results agree with the empirical value at the level of a few percent [74]. Particularly significant has been the recent progress in the treatment of excited-state contamination. In consequence, we only consider data from works with an improved analysis of these effects. We study renormalized $\{g_A^i\}$ data at different $\{M_\pi^i, a_i\}$ values, where a indicates the lattice-spacing, from[7] CalLat 18 [112], Mainz 19 [113], RQCD 19 [79][8] and NME 21 [114][9]. Our analysis treats 2+1+1 (CalLat 18) and 2+1 (Mainz 19, RQCD 19, NME 21) ensembles on the same footing, assuming that the c-quark sea content plays a negligible role. As aforementioned, we discard LQCD determinations of g_A coming from Q^2, finite volume, lattice-spacing or M_π extrapolations. Since we do not account for finite volume corrections, we take only large volumes, satisfying $M_\pi L \geq 3.5$, so that the neglected extrapolation is small and can be absorbed in the uncertainties.

In order to describe the data, we perform a fit of the ChPT computation, aiming to extract the contact LECs $\mathring{g}_A$ and d_{16}. We account for lattice-spacing corrections following Eq. (2.10), which in the case of the charge reduces to

$$g_A(M_\pi^i, a_i) = g_A(M_\pi^i) + x_j a_i^{n_j} \,. \tag{2.21}$$

The free parameters x_j dictate the leading a-correction, with $j = 1, 2, 3, 4$ corresponding to points from CalLat 18, Mainz 19, RQCD 19, NME 21 respectively. This term is specific of each lattice action: $n_{1,4} = 1$, while $n_{2,3} = 2$. In any case, these corrections do not alter significantly the extracted LECs, but do reduce the χ^2/dof. All the remaining fit details and definitions of the previous section are taken to the $t \to 0$ limit in the axial charge analysis.

Finally, we have studied the convergence range of the ChPT by vary-

[7] The lattice works names follow the FLAG Review 2021 [74].

[8] From RQCD 19 [79] only the data with $m_s \sim m_{s(\text{phys})}$ is considered, the one suitable for an SU(2) ChPT study.

[9] From NME 21 [114] we consider the results from the fit method labeled as $\{4^{N\pi}, 3^*\}$, used to control excited-state contamination, averaging over the two renormalization methods Z_1 and Z_2.

ing the maximum M_π of the lattice data accepted in the fits in the range of $M_{\pi\text{cut}} \in [200, 402]$ MeV. A plateau in the χ^2 and the fitted LECs is reached towards the end of the interval. Therefore in the following fits we consider data up to $M_\pi = 402$ MeV[10]. Notice that ease the comparison between orders we use always the $M_{\pi\text{cut}}$ and Q^2_{cut} determined in the $\mathcal{O}(p^4)$ analysis with Δ. As will be discussed in Sec. 2.3.4, the theoretical uncertainty increases at higher M_π where the chiral convergence is poorer and, in consequence, the corresponding LQCD points weight less in the fits.

Now that the fit procedure has been established, we discuss the performance of the ChPT description at the different orders in the next sections.

$\not\Delta$ $\mathcal{O}(p^3)$ fit results

At $\mathcal{O}(p^3)$ without explicit Δ the only free parameters (apart from x_j controlling the a-correction) are $\mathring{g}_A$ and d_{16}. The results of the fit are shown in the upper left panel of Fig. 2.4 and the first column of Tab. 2.4. At least in appearance, this model describes the LQCD data well, with a good χ^2/dof, relatively small uncertainties and natural $\mathring{g}_A$ and d_{16} values. Comparing the first columns of Tabs. 2.3 and 2.4, the d_{16} value is slightly above the phenomenological one extracted in Ref. [105] and has a much smaller error. Instead, $\mathring{g}_A$ is in tension with the value obtained from experimental input, Eq. (2.9). In consequence $g_A(M_{\pi(\text{phys})}) = 1.205 \pm 0.010$, well below the experimental result (red filled triangle in Fig. 2.4). In truth, if one studies the results for the $\mathcal{O}(p^4)$ model described below, a large contribution from the $\mathcal{O}(p^4)$ terms at $M_\pi \gtrsim 200$ MeV is obtained, in line with the discussion of Sec. 2.3.2. The fact that these terms are considerably larger than the error band of the $\mathcal{O}(p^3)$ result implies that, in this case, the theoretical uncertainty determined from $\mathcal{O}(p)$ and $\mathcal{O}(p^3)$ terms falls short in estimating for the $\mathcal{O}(p^4)$ contribution. The fit of $g_A(M_\pi)$ at $\mathcal{O}(p^3)$ with LQCD data appears then as misleadingly good, while the errors in the LECs can be regarded as underestimated. In other words, to be realistic, an $\mathcal{O}(p^3)$ analysis should be constrained to small $M_\pi < 200$ MeV, which would be impossible due to lack of LQCD data in this interval.

[10]This limit makes possible to incorporate available data close but above $M_\pi = 400$ MeV.

$\not\Delta$ $\mathcal{O}(p^4)$ fit results

Increasing one order in the computation, including the $\mathcal{O}(p^4)$ $\not\Delta$ contribution, implies the appearance of NLO LECs c_{1-4}. They were initially allowed to evolve in the fits under the constrains set by their empirical determination [105] (second column of Table 2.3) applied as Gaussian priors. However, as these LECs are quite well determined, this procedure yields substantially the values favored by the priors. Therefore, we report here the results of a simpler fit with c_{1-4} held fixed to their central phenomenological values (second column of Table 2.4).

Anyway, as apparent from the lower left panel of Fig. 2.4 the $\mathcal{O}(p^4)$ $\not\Delta$ model fails to describe the light-quark mass dependence of g_A[11]. The small χ^2 is merely a consequence of the large theoretical error, which reduces the impact of high M_π points on the fit. Nonetheless, the poor agreement is reflected in the magnitude of χ_0^2 and also in the quite unnatural d_{16} in spite of its prior. This large d_{16} is inconsistent with its phenomenological value and nonetheless unable to correct the M_π dependence at $M_\pi \gtrsim 300$ MeV, which is largely dominated by the $\mathcal{O}(p^4)$ contribution and, consequently, very similar to the one displayed in Fig. 2.3.

The fact that the very wide theoretical error band covers the LQCD points indicates that the disagreement would be removed by a (large) contribution of $\mathcal{O}(p^5)$ compensating the $\mathcal{O}(p^4)$ ones. In fact, it has been shown within HB ChPT [108] that the curve may be *bent down* by additional contributions of orders $\mathcal{O}(p^{5,6})$ with LECs of natural size (see also Fig. 1 of Ref. [93]). We choose a different strategy and introduce the $\Delta(1232)$ explicitly as suggested in Ref. [109] based on the Adler-Weisberger sum rule [119, 120] and a HB computation for g_A.

Including the Δ explicitly: $\mathcal{O}(p^3)$ fit results

When the Δ is implemented as an explicit degree of freedom, new terms with extra LECs arise. We fix the $\mathcal{L}^{(1)}_{\pi N\Delta}$ coupling h_A to its large-N_c value, $h_A = \frac{3g_A}{2\sqrt{2}} \simeq 1.35$ [121], which is near to its empirical value [28]. For the $\mathcal{L}^{(1)}_{\pi\Delta}$ coupling g_1, whose impact on g_A is small, the large-N_c limit leads to $|g_1| = \frac{9}{5} g_A \simeq 2.29$ [24]. We can not discern its sign in our fits to g_A LQCD data and adopt $g_1 = -2.29$, preferred both by πN elastic

[11] Lattice-spacing corrections were neglected in this fit once they become unnaturally large (and uncertain) causing overfitting.

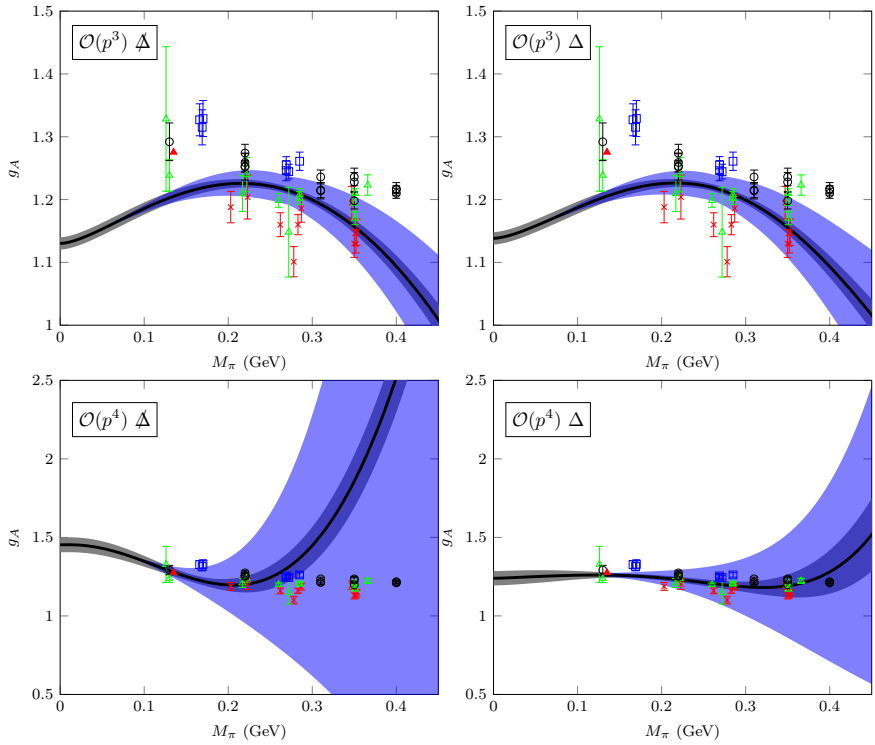

Figure 2.4: M_π dependence of g_A determined from the fits to LQCD data with $\mathcal{O}(p^3)$ and $\mathcal{O}(p^4)$ relativistic BChPT without and with $\Delta(1232)$ as explicit degree of freedom. Gray (dark) bands correspond to uncertainties determined by propagating LEC errors. Blue bands represent the estimated theoretical uncertainties $\Delta g_{A\chi}^{(4,5)}$. The LQCD points from CalLat 18 [112] (black circles), Mainz 19 [113] (red crosses), RQCD 19 [79] (green triangles) and NME 21 [114] (blue squares) are shown at their non-zero a values, *i.e.* without (small) discretization corrections. The experimental value [89] corresponds to the red filled triangle.

scattering [28] and our own studies of the nucleon axial form factor at low q^2 of the next sections. In addition, similarly to the nucleon case, $\mathring{m}_\Delta \approx m_{\Delta(\text{phys})} - 4\,a_1 M^2_{(\text{phys})}$ with $m_{\Delta(\text{phys})} = 1232$ MeV and $a_1 = 0.90$ GeV^{-1} from the LQCD M_π dependence of the Δ mass [42].

In the end, the result of this model closely resembles the $\mathcal{O}(p^3)$ $\not\Delta$ one as is evident from the upper panels of Fig. 2.3. However, the value of d_{16} changes notably, including its sign, with respect to the $\mathcal{O}(p^3)$ $\not\Delta$

Table 2.4: LEC values for g_A, both fixed and fitted to LQCD data, in the four different models under study. The χ^2/dof for each fit is given at the bottom; χ^2_0, defined in Eq. (2.20), does not include theoretical errors or naturalness priors.

	$\mathcal{O}(p^3)$ $\not\Delta$	$\mathcal{O}(p^4)$ $\not\Delta$	$\mathcal{O}(p^3)$ Δ	$\mathcal{O}(p^4)$ Δ
$\mathring{g}_A$ (free)	1.1302 ± 0.0098	1.453 ± 0.048	1.1383 ± 0.0099	1.240 ± 0.046
d_{16} (GeV^{-2}) (free)	-0.925 ± 0.055	-9.77 ± 0.87	1.224 ± 0.040	-0.88 ± 0.88
h_A	-	-	1.35	1.35
g_1	-	-	-2.29	-2.29
c_1 (GeV^{-1})	-	-0.89 ± 0.06	-	-1.15 ± 0.05
c_2 (GeV^{-1})	-	3.38 ± 0.15	-	1.57 ± 0.10
c_3 (GeV^{-1})	-	-4.59 ± 0.09	-	-2.54 ± 0.05
c_4 (GeV^{-1})	-	3.31 ± 0.13	-	2.61 ± 0.10
a_1 (GeV^{-1})	-	-	-	0.90
$\widetilde{b}_4$ (GeV^{-2}) (free)	-	-	-	-12.3 ± 1.0
x_1 (fm^{-1})	0.39 ± 0.68	-	0.38 ± 0.07	0.21 ± 0.07
x_2 (fm^{-2})	-8.10 ± 1.80	-	-8.17 ± 1.80	-7.27 ± 1.80
x_3 (fm^{-2})	2.25 ± 1.83	-	2.17 ± 1.83	3.28 ± 1.84
x_4 (fm^{-1})	0.61 ± 0.11	-	0.60 ± 0.11	0.51 ± 0.11
$\mathring{m}$ (GeV)	0.874	0.874	0.855	0.855
$\mathring{m}_\Delta$ (GeV)	-	-	1.166	1.166
χ^2/dof	$36.06/(43-6) = 0.98$	$13.31/(43-2) = 0.33$	$37.60/(43-6) = 1.02$	$11.14/(43-7) = 0.31$
χ^2_0/dof	$424.87/(43-6) = 11.48$	$122820.67/(43-2) = 2995.63$	$439.19/(43-6) = 11.87$	$501.62/(43-7) = 13.93$

one. The same feature was recognized when this LEC was extracted from LQCD results for the axial form factor at low Q^2 with $\mathcal{O}(p^3)$ relativistic BChPT [87]. The $\mathcal{O}(p^4)$ fit described in the next section produces $\mathcal{O}(p^4)$ corrections larger than the truncation uncertainty estimated here just from $\mathcal{O}(p)$ and $\mathcal{O}(p^3)$ terms (although to a lesser extent than in the $\not\Delta$ case). The extension to $\mathcal{O}(p^4)$ is in fact desirable for a more realistic determination of the LECs and their errors.

$\mathcal{O}(p^4)$ with explicit Δ fit results

In the fit of the $\mathcal{O}(p^4)$ theory with explicit Δ we fix the c_{1-4} LECs to the values extracted from πN scattering [104] (see the last column of Table 2.4). In the cited analysis the Δ pole is taken into account and results in good agreement with the combined $\pi N + \pi\pi N$ fit from Ref. [105] are obtained. In addition to $\mathring{g}_A$ and d_{16} we now have $\mathcal{O}(p^2)$ b_4 and b_5 LECs as free parameters. As mentioned in Sec. 2.2.1, these LECs appear at $\mathcal{O}(p^4)$ [more precisely, at $\mathcal{O}(M_\pi^4/\delta)$] in the combination $\widetilde{b}_4 = b_4 + (12/13)\, b_5$. Therefore we keep only $\widetilde{b}_4$ as a free parameter of the fit and neglect remaining higher order monomials proportional to b_5.

The result of the fit, shown in the lower right panel of Fig. 2.4, satisfactorily describes the trend of $g_A(M_\pi)$ as predicted by LQCD up to relatively high M_π. The theoretical error is large and rapidly increasing with M_π due to the big contribution of $\mathcal{O}(p^4)$ terms. Nevertheless, the description of LQCD data and convergence are notably improved with respect to the $\mathcal{O}(p^4)$ $\not\Delta$ model.

The obtained LECs are given in Table 2.4. The $\widetilde{b}_4$ value might seem unnatural but one should keep in mind that it is a combination of LECs. As shown in Table 2.5 the correlations among LECs are sizable; they are an indication of degeneracy among the parameters. The

Table 2.5: Correlation matrix for the $\mathcal{O}(p^4)$ Δ fit.

	$\mathring{g}_A$	d_{16}	$\widetilde{b}_4$
$\mathring{g}_A$	1	-0.97	0.79
d_{16}		1	-0.92
$\widetilde{b}_4$			1

d_{16} value obtained from this analysis, $d_{16} = -0.88 \pm 0.88$ GeV^{-2}, is in good agreement with the determination from inelastic $\pi N \to \pi\pi N$ with explicit Δ pole [105], which, transformed to standard EOMS, is $d_{16(\text{pheno})} = -1.0 \pm 1.0$ GeV^{-2}. Even though, as argued before, the M_π dependence of g_A is in principle better suited to determine d_{16} than the available experimental $\pi N \to \pi\pi N$ data, the convergence issues of the former lead to large errors, comparable to those of the phenomenological extraction. The $\mathring{g}_A$ LEC has a higher value than in the $\mathcal{O}(p^3)$ fits and with a larger uncertainty. Furthermore, at the physical point $g_A(M_{\pi(\text{phys})}) = 1.260 \pm 0.012$ is now close to the experimental value although with a much larger error.

In addition, the stability of the results for $\mathring{g}_A$ and d_{16} as a function of the maximum M_π accepted, $M_{\pi\text{cut}}$, is depicted in Fig. 2.5. It can be seen that for both quantities the numerical values and uncertainties stabilize for $M_\pi \gtrsim 300$ MeV.

Owing to the inclusion of the truncation uncertainty, the study could be extended to higher M_π, because points at higher M_π, where the convergence is worse, have a larger combined error (Eq. (2.19)) and influence less the fit.

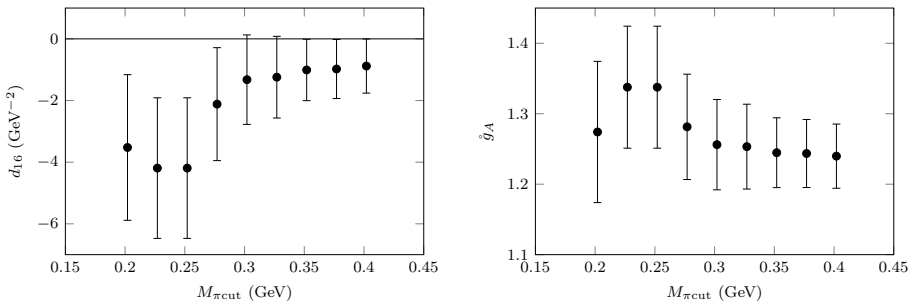

Figure 2.5: Results of the fits for the $\mathcal{O}(p^4)$ model with explicit Δ as a function of the maximum accepted pion-mass, $M_{\pi\text{cut}}$.

2.3.5 Conclusions on the axial charge light quark-mass dependence

As a result of the investigation of the M_π (or light quark-mass) dependence of the nucleon axial coupling we have drawn several conclusions regarding its description in ChPT. The axial charge has been computed up to $\mathcal{O}(p^4)$ (NNLO) in relativistic EOMS renormalization with and without explicit Δ. We have shown that up to $\mathcal{O}(p^4)$, the pion mass dependence of g_A predicted using LECs determined from phenomenological studies of pion-nucleon elastic and inelastic ($\pi N \to \pi\pi N$) scattering cannot produce the rather flat behavior predicted by recent LQCD results, if the Δ is not explicitly considered. The disagreement is evident from pion masses right above the physical one. This feature, earlier observed in non-relativistic heavy-baryon ChPT [108, 109], is therefore also present in the relativistic theory. The fact that $\mathcal{O}(p^4)$ terms become large from relatively small $M_\pi \gtrsim 200$ MeV implies that $\mathcal{O}(p^3)$ studies of $g_A(M_\pi)$ probably underestimate theoretical errors.

In line with the HB work of Ref. [109], we are able to describe satisfactorily the LQCD data for $g_A(M_\pi)$ at $\mathcal{O}(p^4)$ only after the Δ is included as an explicit degree of freedom. It must be acknowledged that, although in a much smaller degree than in the $\not\Delta$ case, a fast increase in the relative size of $\mathcal{O}(p^4)$ terms with M_π is observed and reflected by the estimate of theoretical uncertainties. This fact jeopardizes the precision of the ChPT description of $g_A(M_\pi)$ at $M_\pi \gtrsim 300$ MeV and negatively influences the extraction of LECs based on LQCD data at such M_π. Together with the sizable correlations, this feature implies that $\mathcal{O}(p^5)$ and/or heavier

resonances are required to reach a complete convergence and minimize theoretical uncertainties. The effect of setting the baryon masses in the loops to the values obtained by the LQCD simulations may be also worth exploring as suggested in Ref. [86], even though this would correspond to the resummation of baryon selfenergy insertions of higher order. To accomplish this in a consistent way, it would be relevant to have more information about the Δ pole position for the different lattice simulations.

From our most solid analysis ($\mathcal{O}(p^4)$ with Δ) of state-of-the-art LQCD data we obtain $g_A(M_{\pi(\text{phys})}) = 1.260 \pm 0.012$, closer to the experimental extraction [89] and with less error than the one from the FLAG report [74]. A $d_{16} = -0.88 \pm 0.88$ GeV^{-2}, in agreement with πN phenomenology, is obtained. As a result of the previously discussed issues, errors are still large, particularly for d_{16}, which is naturally extracted from the light-quark mass dependence of the nucleon axial coupling. New LQCD results at $M_\pi \lesssim 250$ MeV would improve the precision of the extracted LECs. In the next section we will move to the axial form factor, seeking a more integral analysis by the addition of the Q^2 dimension. This will lead not only to the acquisition of useful information on a relevant quantity such as F_A, but also to the extraction of other LECs such as d_{22}.

2.4 Analysis of LQCD results and LEC determination: the axial form factor

As anticipated, we perform a meta-analysis of a combined set of recent LQCD data. The accounted LQCD studies only partially overlap with the ones used to investigate the axial charge, but again we only consider simulations in which the excited-state contamination is taken into account. These would be RQCD [79], NME [114], "Mainz" [122], PACS [123] and, at the physical point, also ETMC [124] (see Fig. 2.7(a)).

In order to conduct the fit, we proceed as explained in Sec. 2.3.3. Different actions correspond to different lattice-spacing corrections in Eq. (2.10). The index j corresponds now to $j = \{$ Mainz, RQCD, NME$\}$ and the n_j exponent depends on the lattice action: $n = 1$ for NME, while $n = 2$ for the other two. As for g_A, we anticipate that these corrections do not affect the extracted physical quantities or LECs substantially, but only reduce the χ^2/dof. The lattice-spacing dependence from PACS and

ETMC can not be corrected because only one value of the spacing is used in the respective simulations. According to the respective publications [123, 124] (and our analysis of lattice-spacing effects of other data) the systematic uncertainty corresponding to such dependence should not be significant for our fit.

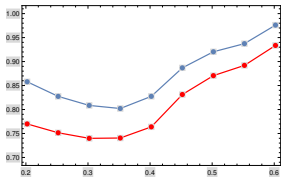

Figure 2.6: In blue, χ^2/dof vs $Q^2_{\rm cut}$ (GeV^2) in $\mathcal{O}(p^4)$ with explicit Δ. In red, the same for χ^2_0/dof of Eq. (2.20).

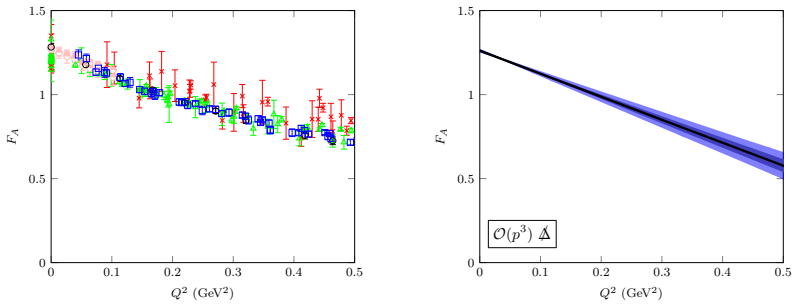

(a) (b)

Figure 2.7: *Left panel:* lattice $F_A(Q^2)$ (without continuum extrapolation and at different M_π). Red, green, pink, black and blue points correspond to "Mainz" [122], RQCD [79], PACS [123], ETMC [124] and NME [114] respectively. *Right panel:* our $F_A(Q^2)$ $\mathcal{O}(p^3)$ $\not\Delta$ fit curve at the physical point. Analogously to Fig. 2.4, gray (dark) bands correspond to uncertainties determined by propagating LEC errors. Blue bands represent the estimated theoretical uncertainties $\Delta F_{A\chi}$.

For the purpose of establishing the range in M_π and Q^2 for the analysis we search for a plateau in the χ^2/dof. The truncation error assigns a lower weight to the points at higher M_π or Q^2. Therefore the question of the fit range is connected to this uncertainty. We set $M_{\pi\rm cut} = 402$ MeV as in our analysis of g_A in Sec. 2.3.4. Regarding the momentum, we determine $Q^2_{\rm cut} = 0.36$ GeV^2 from the χ^2/dof plateau (Fig. 2.6), similarly

to Ref. [87]. As in the axial charge analysis, the cuts are determined from the analysis of the $\mathcal{O}(p^4)$ model with explicit Δ and are kept for the simpler models in order to make a straightforward comparison among them. In the following the fit results are presented, separated by chiral orders.

2.4.1 $\not\Delta$ case

$\mathcal{O}(p^3)$ fit results

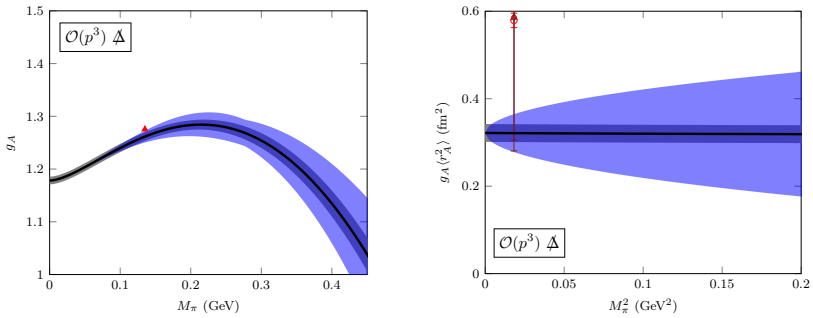

(a) (b)

Figure 2.8: Pion mass dependence of g_A (left) and of the slope at the origin, $6\,\frac{dF_A}{dt}\big|_{t=0} = g_A\langle r_A^2\rangle$, (right) both in the $\mathcal{O}(p^3)$ $\not\Delta$ scheme. The red triangle in the left panel indicates the experimental g_A value [89]. Again, gray (dark) bands correspond to uncertainties determined by propagating LEC errors, while blue bands represent the estimated theoretical uncertainties $\Delta F_{A\chi}$. In the right panel, the violet triangle (red circle) represents the empirical extraction from neutrino scattering on deuteron with a z-expansion [71] (dipole) [70] parametrization of $F_A(Q^2)$, whereas the brown diamond corresponds to the one from muon capture in muonic hydrogen [72]. These experimental determinations are also included in the rest of figures corresponding to different versions of the theory.

In the $\mathcal{O}(p^3)$ calculation without Δ there are only three free ChPT LECs: $\mathring{g}_A$, d_{16} and d_{22}. The resulting $F_A(Q^2, M_{\pi\text{phys}})$, $g_A(M_\pi)$, $g_A\langle r_A^2\rangle(M_\pi)$ (recall Eq. (1.28)) are shown in Figs. 2.7(b), 2.8(a), (b) respectively. One should notice that in this scheme $g_A\langle r_A^2\rangle$ is constant in M_π. However, in general the LQCD $F_A(Q^2)$ is steeper at $Q^2 = 0$ for ensembles with lower M_π. In this fit one can see the impact of the truncation uncertainty.

This error assigns a lower weight to the high M_π points, and therefore, the $\langle r_A^2 \rangle$ obtained with truncation error is higher than the one without it. The main issue of the $\mathcal{O}(p^3)$ description is that the fit to the data is misleadingly good, as has been shown for g_A in 2.3.4. The $\mathcal{O}(p^4)$ contributions which are unaccounted are large and therefore $\mathcal{O}(p^3)$ is not a satisfactory parametrization.

$\mathcal{O}(p^4)$ fit results

As seen before, at $\mathcal{O}(p^4)$ the c_{1-4} enter in the calculation through g_A. We proceed as in the g_A fit, fixing them to [105] (second column of our Table 2.3). However, as explained in Sec. 2.3.4, the $\mathcal{O}(p^4)$ $\not\Delta$ calculation fails to describe the light-quark mass dependence of g_A. Therefore we do not report a fit to the form factor at this order, since the result does not agree with the data.

2.4.2 Δ case

$\mathcal{O}(p^3)$ fit results

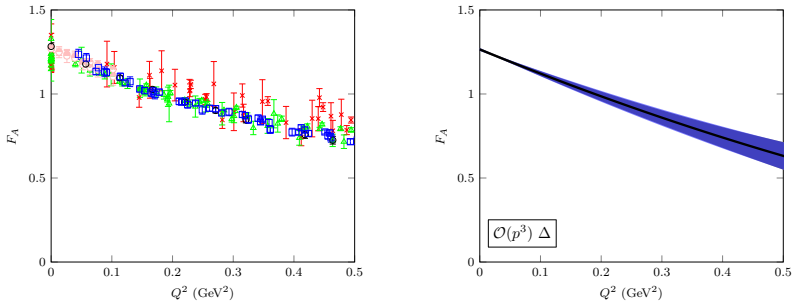

(a) (b)

Figure 2.9: *Left panel:* lattice $F_A(Q^2)$ (without continuum extrapolation and at different M_π). See caption of Fig. 2.7 for details. *Right panel:* $F_A(Q^2)$ at $\mathcal{O}(p^3)$ with explicit Δ. Notice that the χ^2 error (gray) and the pure truncation one (blue) overlap almost exactly.

At $\mathcal{O}(p^3)$ the inclusion of the Δ introduces two parameters: h_A and g_1, this is the same situation as for $g_A(M_\pi)$; the Q^2 dependence does not introduce new LECs. LEC h_A is fixed to the large-N_c value [121] as

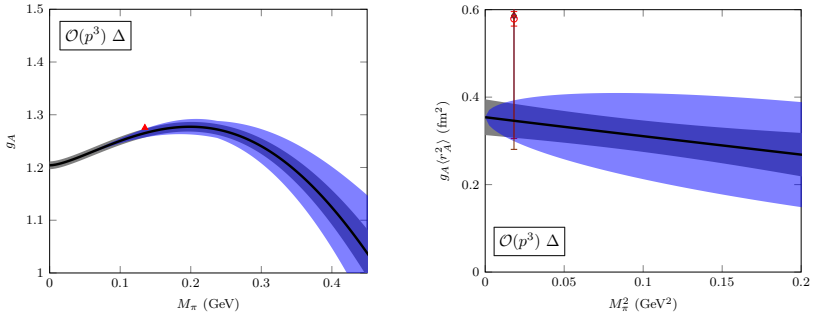

(a) (b)

Figure 2.10: Results at $\mathcal{O}(p^3)$ in the theory with explicit Δ. Same notation as in Fig. 2.8 is used.

in the g_A analysis of Sec. 2.3.4. As mentioned there, large-N_c leads to $|g_1| \simeq 2.29$ [24]. We use the large-N_c value for h_A, whereas we do not fix g_1 to any of its two a priori values. LEC g_1 appears as an important coefficient in the radius in the chiral limit, so that it is strongly correlated with d_{22}[12] (Eq. (2.8)). We can not determine exactly d_{22} and g_1 from the chiral limit radius. The main effect of leaving g_1 free is the large error of d_{22}, with which it is correlated. We choose to prioritize the extraction of the axial radius without further assumptions on the LECs. Therefore, we leave free g_1 and d_{22}, obtaining a rough estimation of their individual values, in part thanks to their naturalness priors.

The results of this fit are shown in Figs. 2.9 and 2.10. One can see in Fig. 2.10(b) that the Δ is important to account for the M_π^2 slope to the radius. However, as for the $\mathcal{O}(p^3)$ $\not\Delta$ case, the Δ $\mathcal{O}(p^3)$ fit underestimates the truncation error, especially in $g_A(M_\pi)$. Therefore the description is misleadingly accurate. That is why we focus now in the $\mathcal{O}(p^4)$ calculation with explicit Δ, which yields more realistic results.

$\mathcal{O}(p^4)$ fit results

The situation in the $\mathcal{O}(p^4)$ analysis with explicit Δ resembles the one for g_A, since many LECs only contribute to the charge. We fix the c_{1-4} LECs as in the axial charge case, to the values extracted from the πN

[12] LEC g_1 also appears with a much smaller coefficient in g_A at $\mathcal{O}(M_\pi^2)$. To be precise the g_1 impact in g_A is almost negligible so that it does not strongly affect the extraction of d_{16}.

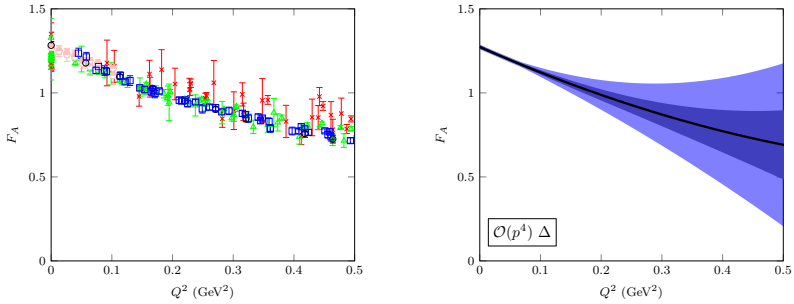

(a) (b)

Figure 2.11: *Left panel:* lattice $F_A(Q^2)$ (without continuum extrapolation and at different M_π). See caption of Fig. 2.7 for details. *Right panel:* $F_A(Q^2)$ at $\mathcal{O}(p^4)$ with explicit Δ. Same notation as in Fig. 2.7(b).

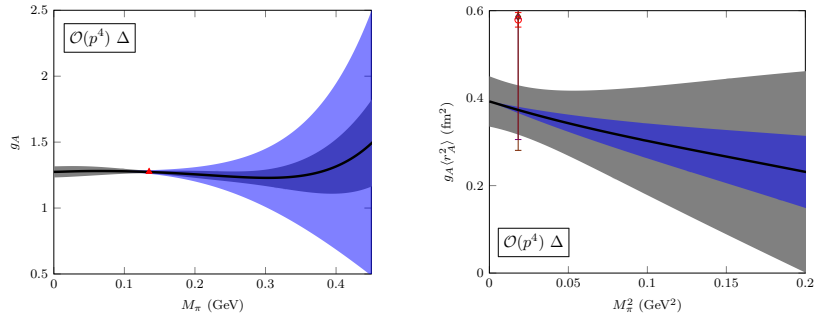

(a) (b)

Figure 2.12: Results at $\mathcal{O}(p^4)$ in the theory with explicit Δ. Same notation as in Fig. 2.8 is used. Notice that in the radius (right panel) the error propagated from the LECs dominate over the pure truncation one.

elastic scattering [104] including the Δ resonance (all fit parameters are given in the last column of our Tab. 2.6). The contribution from the Δ at this order introduces the following LECs: a_1 (fixed to the Ref. [42] value as in the g_A study), and the free b_1, b_2 and $\widetilde{b}_4$. The combination of LECs $\widetilde{b}_4$ only appears in g_A, and is necessary to compensate the $\mathcal{O}(p^4)$ $\not\Delta$ term, as has been discussed in Sec. 2.3.4. As mentioned for the $\mathcal{O}(p^3)$ calculation, the loops with internal Δ are important to describe the M_π dependence of the axial radius. The b_1 and b_2 LECs enter at $\mathcal{O}(t \times M_\pi^2)$. Their impact in the calculation is limited and we just see that the fit behaves well when they have the natural values given in Tab. 2.6.

Table 2.6: LEC values for F_A, both fixed and fitted to LQCD data, in the four different models under study. The χ^2/dof for each fit is given at the bottom; χ^2_0, defined in Eq. (2.20), does not include theoretical errors or naturalness priors.

	$\mathcal{O}(p^3)$ $\not\Delta$	$\mathcal{O}(p^3)$ Δ	$\mathcal{O}(p^4)$ Δ
$\mathring{g}_A$ (free)	1.1782 ± 0.0073	1.2041 ± 0.0074	1.274 ± 0.041
d_{16} (GeV^{-2}) (free)	-1.021 ± 0.048	0.983 ± 0.062	-1.46 ± 1.00
d_{22} (GeV^{-2}) (free)	1.275 ± 0.086	3.77 ± 1.96	0.29 ± 1.69
h_A	-	1.35	1.35
g_1 (free)	-	-0.69 ± 0.69	0.66 ± 0.56
c_1 (GeV^{-1})	-	-	-1.15 ± 0.05
c_2 (GeV^{-1})	-	-	1.57 ± 0.10
c_3 (GeV^{-1})	-	-	-2.54 ± 0.05
c_4 (GeV^{-1})	-	-	2.61 ± 0.10
a_1 (GeV^{-1})	-	-	0.90
b_1 (GeV^{-2}) (free)	-	-	-0.27 ± 4.96
b_2 (GeV^{-2}) (free)	-	-	2.27 ± 2.28
$\widetilde{b}_4$ (GeV^{-2}) (free)	-	-	-12.48 ± 1.28
x_1 (fm^{-2}) (free)	-8.4 ± 5.8	-5.6 ± 5.9	-0.25 ± 16.5
x_2 (fm^{-2}) (free)	-8.6 ± 2.6	-7.1 ± 2.6	-6.36 ± 4.20
x_3 (fm^{-1}) (free)	-0.25 ± 0.21	-0.08 ± 0.22	0.36 ± 0.47
y_1 (fm^{-2} GeV^{-2}) (free)	-100 ± 40	-76 ± 44	-64 ± 121
y_2 (fm^{-2} GeV^{-2}) (free)	-31 ± 21	-21 ± 22	-15 ± 46
y_3 (fm^{-1} GeV^{-2}) (free)	-0.63 ± 1.49	0.36 ± 1.63	2.54 ± 3.98
$\mathring{m}$ (GeV)	0.874	0.855	0.855
$\mathring{m}_\Delta$ (GeV)	-	1.166	1.166
χ^2/dof	$46.13/(127-9) = 0.391$	$39.17/(127-10) = 0.326$	$14.64/(127-13) = 0.129$
χ^2_0/dof	$857.31/(127-9) = 7.27$	$533.87/(127-10) = 4.45$	$196.58/(127-13) = 1.724$

The output of the fit is displayed in Figs. 2.11 and 2.12. The low χ^2/dof is due to the large truncation error at high M_π. In fact, by setting a lower $M_{\pi\text{cut}}$ one could obtain a higher χ^2/dof. Regarding the truncation error, one can see that it is large for the axial charge (Fig.2.12(a)), suggesting that a complete $\mathcal{O}(p^5)$ calculation is needed to achieve a full convergence in the charge. This is challenging, because at this order two loop contributions are present. The radius has a slightly decreasing slope in M_π^2, accompanied by a sizable uncertainty (Fig. 2.12(b)). In summary, we consider this calculation a good description of the form factor, especially at the physical point.

Regarding the LEC d_{16}, which governs the M_π dependence of the charge, we extract $d_{16} = -1.46 \pm 1.00$ GeV^{-2}. The large uncertainty is

due to the truncation error and reflects the slow convergence of $g_A(M_\pi)$ in ChPT. This determination is in agreement with the extraction from $\pi N \to \pi\pi N$ of Ref. [105]. Their value translated to the standard EOMS scheme is $d_{16} = -1.0 \pm 1.0$ GeV^{-2}. It is also very similar to our extraction from the axial charge fit (to other ensembles) of Sec. 2.3.4, $d_{16} = -0.88 \pm 0.88$ GeV^{-2}. In addition, the $\mathring{g}_A$ and $\widetilde{b}_4$ extracted are in good agreement with the ones determined by the g_A fit (Tab. 2.4).

Regarding d_{22}, the LEC that enters at tree level in the radius, we extract $d_{22} = 0.29 \pm 1.69$ GeV^{-2}. Since this LEC is correlated with g_1, it has a large uncertainty. The determinations of d_{22} and g_1 in Tab. 2.6 should be interpreted as a range of valid results, and one LEC value should not be adopted independently of the other. Nevertheless, d_{22} is compatible with the extraction from the $\mathcal{O}(p^3)$ analysis of π-electroproduction of Ref. [97]: $d_{22} = 0.95 \pm 0.13$ GeV^{-2}[13]. The fact that we extract LECs in line with determinations from different physical processes indicates that our calculation is assessing the ChPT series in a robust way and that the convergence is good for the different observables.

Turning now to the extraction of the physical charge and radius, we recall that the axial charge is well determined experimentally from β-decay: $g_A^{\rm exp} = 1.2754(13)_{\rm exp}(2)_{\rm RC}$ [89]. The FLAG review reports $g_A^{\rm FLAG} = 1.246 \pm 0.028$ [74]. We obtain a value, $g_A(M_{\pi{\rm phys}}) = 1.273 \pm 0.014$, in fine agreement with experiment, closer than the FLAG one. It is also compatible with our previous extraction from $Q^2 = 0$, $g_A(M_{\pi({\rm phys})}) = 1.260 \pm 0.012$. Our two g_A determinations from LQCD results have a relatively small error because the truncation uncertainty affects mostly the prediction at high M_π.

With respect to the axial radius, we extract: $\langle r_A^2 \rangle (M_{\pi{\rm phys}}) = 0.293 \pm 0.044$ fm^2 from our ChPT $\mathcal{O}(p^4)$ analysis with explicit Δ. The situation regarding the experimental and LQCD determinations of this quantity is more complex than for g_A. We dedicate the following section to the analysis of the different results.

[13] One has to be aware that in Ref. [97] the Δ is introduced only at tree level, following the so-called δ-counting.

2.5 Comparison with other $\langle r_A^2 \rangle$ determinations

The axial radius is a challenging quantity from the experimental point of view. In Fig. 2.13 we show the experimental results discussed in Sec. 2.1. In the same plot, we have reported recent LQCD determinations. One can see that the LQCD predictions are in general below the experimental extractions. The origin of this mismatch is not understood. There is a strong dependence on the Q^2 parametrization employed in both the experimental and LQCD determinations. In the experimental case, it is evident that the dipole parametrization leads to small error bars, while the z-expansion leads to very large ones. In the LQCD results this also happens, but, in addition, the central value can be substantially affected by the Q^2 parametrization.

Table 2.7: $\langle r_A^2 \rangle$ determined from our ChPT fit to LQCD compared with empirical extractions.

	$\mathcal{O}(p^4)$ fit with Δ	νD z-exp. [71]	νD dip. [70]	μH z-exp. [72]
$\langle r_A^2 \rangle$ (fm^2)	0.293 ± 0.044	0.46 ± 0.22	0.454 ± 0.013	0.46 ± 0.24

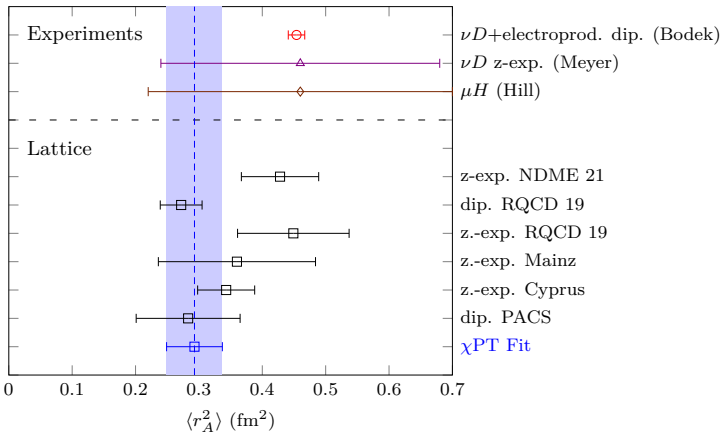

Figure 2.13: Summary of modern LQCD and empirical determinations of $\langle r_A^2 \rangle$ determinations. (Bodek), (Meyer) and (Hill) correspond to [70], [71] and [72] respectively.

Our extraction is depicted in blue in the figure. It is in line with the individual LQCD results, as it should, and illustrates the global mismatch

between LQCD and experiment. We want to emphasize the fact that we are not using any ad hoc Q^2 parametrization. Since we use ChPT our parametrization is based on the symmetries of QCD and we can estimate the theoretical uncertainty that comes with it.

2.6 Conclusions and outlook

We have investigated the nucleon axial form factor, a key quantity in the study of neutrino oscillations. We have calculated it up to $\mathcal{O}(p^4)$ in relativistic ChPT with explicit Δ. Then, we have fitted the unknown LECs to a set of different LQCD determinations, accounting also for the truncation error of ChPT. We have seen that at this order, our calculation is able to describe data up to ~ 0.6 GeV in $\sqrt{Q^2}$ and $M_\pi \sim 400$ MeV.

From our fit, we conclude that the Δ baryon is a necessary d.o.f., especially to account for the M_π dependence. From our parametrization we extract an axial charge of $g_A^{\text{phys}} = 1.273 \pm 0.014$ in good agreement with the experimental determination (more precise and closer to experiment than the one from the FLAG report [74]). We have also extracted the following important LECs of the $\mathcal{O}(p^3)$ Lagrangian: $d_{16} = -1.46 \pm 1.00$ GeV^{-2} and $d_{22} = 0.29 \pm 1.69$ GeV^{-2}, in agreement with different phenomenological determinations.

It has been shown that the slow convergence of ChPT calls for the inclusion of the higher $\mathcal{O}(p^5)$, which is difficult because two loop diagrams should be taken into account. The implementation of higher order resonances such as the $N(1440)$ Roper resonance could be a more feasible solution. Besides, we argue that a global fit of LQCD results for the axial form factor combined with pion-nucleon scattering experimental data could improve the description of both processes. In particular correlations among LECs would be reduced.

We have investigated the axial radius, a quantity which constitutes a challenge for QCD theory and experiment. From our LQCD fit we obtain $\langle r_A^2 \rangle^{\text{phys}} = 0.291 \pm 0.052$ fm^2, without using ad hoc parametrizations. The known mismatch between lattice and experimental determinations is displayed by the analysis. This motivates both sides to keep improving their studies. With respect to the experiments, there are significant systematic uncertainties related to the determination of the neutrino fluxes. New experiments with hydrogen targets would be beneficial in this regard.

Chapter 3

The nucleon electromagnetic form factor

3.1 Introduction

The electromagnetic form factor has been introduced in Sec. 1.2.1, setting the ground for the calculation reported in this section (based on our article [125]). We use ChPT improved with dispersive relations to study the EM form factor, accounting also for its light quark mass (or pion mass) dependence. The implementation of unitarity through dispersive theory is motivated by the prominence of the ρ resonance in this form factor.

Electron (or lepton) elastic scattering of nucleons is one of the simplest processes sensitive to the nucleon's inner composition [126]. In consequence, the electromagnetic form factors are fundamental quantities to understand the nucleon structure and the strong interaction itself. Even if fundamental, this form factors constitute an important challenge from the theoretical perspective due mainly to its nonperturbative nature. There are many open problems regarding it, such as whether the electric FF of the proton have a zero crossing in the spacelike region or not [127, 126]? and why does the neutron have a negative transverse charge density not only at the periphery but also at the center [128, 129]?

In recent years the most significant question was probably the one related to the so-called proton radius puzzle [130]. The form factor determination has been assessed in two different types of experiments. One

is electron-proton scattering, from which cross section one can extract the radius. The other consists in the study of the energy levels of the hydrogen atom, which are also sensitive to the proton size. The latter type of extraction, can be also performed on a muonic hydrogen atom (the muon replaces the electron in the proton's orbit). Due to the much larger muon mass, the muon sits closer to the proton and is more sensitive to its structure. The puzzle was originated by the incompatibility between the radius measured in muonic hydrogen with respect to ordinary hydrogen and electron scattering. The extraction of the radius from ep scattering led to different results, again depending on the parametrization used to extrapolate to $Q^2 = 0$, where the radius is defined [131, 132, 133]. Recent experimental results align with the muonic hydrogen measurement [130] and with determinations based on dispersion relations (see Fig. 5 of Ref. [134] and references therein), however the experimental question remains not completely clear as shown in Fig. 1 of Ref. [135].

From the QCD theory side, many LQCD groups have determined the nucleon FFs. Although results are now available even at physical quark masses [136], state-of-the-art analyses still suffer from different systematics, and the extraction of the radius is nontrivial due to the aforementioned Q^2 extrapolation. As a matter of fact, LQCD determinations are not precise enough to rule out the original electronic hydrogen data [136].

Our approach to this problem is similar to the one taken for the axial form factor. We employ ChPT to analyze the results simulated in the lattice at relatively low Q^2. Our goal is again to describe the form factor as a function of Q^2 and M_π minimizing model dependence. As aforementioned, the light-quark mass dependence is crucial in lattice determinations, and, on top of that, it is a window to deepen our insight on QCD. In addition the values of ChPT LECs are extracted (not only in our unitarized version of ChPT, but also in its plain realization).

A relativistic treatment of ChPT is performed, thanks again to the EOMS renormalization scheme, preserving covariance and the analytic properties of loop amplitudes. We work on the basis of previous ChPT studies of these form factors [137, 138, 111, 139, 22, 140, 29] and introduce the Δ explicitly in the small-scale expansion power counting (Sec. 1.2.5).

Virtual photons couple to pion pairs in a p-wave state. On the other hand, as introduced in Sec. 1.3.2, two pions in a p-wave are strongly correlated by the ρ meson. We will account for this implementing uni-

tarity, however, one might wonder if the inclusion of the ρ as an explicit d.o.f. would be satisfactory. Even if the coupling is also strong, this case is actually different from the Δ one, where the momentum scales with another small quantity. The momentum of a pion resulting from the decay of an *on shell* Δ (i.e. with an invariant mass equal to the resonance Breit-Wigner mass) to πN is proportional to δ, which is then taken as an expansion parameter of ChPT. One can picture this as the hard scale, the nucleon mass, flowing trough the baryon lines in the vertex. In the case of the ρ, the resonance mass can be considered a hard scale as well, it seems a sensible choice in view of $m_\pi \ll m_\rho \sim \Lambda_\chi$. Then what happens is that in the $\rho \to \pi\pi$ decay, a hard momentum must be provided to one or both of the pions. Therefore, it is difficult to implement the ρ meson as an explicit degree of freedom in ChPT or similar theories. Some works have investigated in this direction, for instance in Refs. [141, 142, 143], and many analyses have adopted phenomenological models to include the ρ, mainly based on the concept of vector-meson dominance [144, 145, 146, 147].

In this work, we want to conserve the virtues of EFTs: model independence, power counting and controlled errors. In terms of the effective theory, accounting for the ρ can be seen as considering terms $\sim p^2/m_\rho^2$, where p denotes some typical pion momentum (or photon virtuality). In practice, the objective is to enlarge the range of applicability concerning momenta and pion mass and improve the precision of ChPT.

The ρ dynamics can be introduced in the nucleon electromagnetic form factor by further developing the dispersive method of Sec. 1.3.2, provided one understands how the asymptotic states (here the nucleons) and the external sources (virtual photons in the present case) couple to pion pairs. This has been investigated in several studies, for instance [148, 149, 150, 133, 151]. In our case, we aim to account for the pion mass dependence, and therefore we ensure that the inputs of the dispersive calculation contain the correct pion mass parametrization.

To account for both the Q^2 and M_π dependence over a relatively large range, we combine relativistic ChPT with explicit Δ with the dispersive treatment of the two-pion (ρ) channel. This simply means that those ChPT diagrams where the photon couples to pion pairs are dispersively improved. In particular, we ensure that such modification is consistent with systematic ChPT power-counting scheme and does not create renormalization problems.

Equivalently, our calculation can be seen as an approximation of a dispersive calculation by means of ChPT. Recalling the optical theorem introduced in Eq. (1.55) of Sec. 1.3.1, the particular case of the nucleon form factor reads:

$$\mathrm{Im}\, T_{\gamma^* \to N\bar{N}} = \frac{1}{2} \sum_n (2\pi)^4 \delta(p_f - p_i) T^*_{N\bar{N}n} T_{n\gamma^*} \ . \tag{3.1}$$

Here the intermediate states n represent all possible hadronic intermediate states: 2π, 3π, 4π, ..., $K\bar{K}$, $K\bar{K}\pi$, ..., $N\bar{N}$, $N\bar{N}\pi$, ... (hadronic resonances are not included as single-particle states but are accounted by the scattering amplitudes of asymptotic states). It is known that for isovector FFs the 2π intermediate state constitutes the largest contribution at low energies $Q^2 \leq 1\,\mathrm{GeV}^2$. The basic idea of this work is therefore to treat the two-pion state via dispersion theory, relying on standard baryon ChPT for the rest. The optical theorem (3.1) relates the imaginary part of a loop diagram to the product of amplitudes, as stated by the Cutkosky cutting rules of Sec. 1.3.1. For ChPT diagrams this implies to relate one-loop FF diagrams to products of tree-level FF terms and scattering diagrams. For baryon-antibaryon intermediate states we keep just the ChPT expression, but for pion-nucleon scattering we modify the tree-level diagrams of pion-nucleon scattering and the pion vector FF. These corrections account for the pion rescattering in a unitary way. This can be understood as a resummation of multi-loop diagrams.

The work is organized as follows. In section 3.1.1 the dispersive and ChPT formalisms are described. Relying on the combined approach, we calculate the Dirac and Pauli FFs. The comparison of our results with LQCD data will be presented in section 3.2 and section 3.3 for Dirac and Pauli FF respectively, with concluding remarks summarized in Sec. 3.4.

3.1.1 The Nucleon Form Factor in dispersion theory

General expressions

Since the ρ resonance contributes only to the isovector channel, we restrict ourselves to the isovector form factor, $F = F^p - F^n$ (here we do not specify if we refer to Dirac or Pauli form factors, defined in Eq. (1.21)). Starting from perturbative QCD [152], all FFs decrease at large q^2. One can then write an unsubtracted dispersion relation identical to the pion

one (Eq. (1.66)):

$$F(q^2) = \int\limits_{4M_\pi^2}^{\infty} \frac{\mathrm{d}s}{\pi} \frac{\mathrm{Im}F(s)}{s - q^2 - i\epsilon} \,. \tag{3.2}$$

In principle, the nucleon electromagnetic FFs satisfy unsubtracted dispersion relations such as this one. However, we do not have a formula for the imaginary part that is accurate at arbitrary energies $\sqrt{s}$. ChPT applies only at low enough energies. The scattering amplitudes on the right-hand side of Eq. (3.1) are simpler the smaller the number of relevant channels. In consequence, also dispersion theory is generally restricted to low energies (or to an energy regime where perturbation theory in coupling constants suppresses many-particle states).

Typically, dispersion relations are oversubtracted [148, 149, 153, 151, 154] to strengthen the sensitivity to the low-energy regime and demote the impact of the short distance part. A once-subtracted DR for the FFs reads

$$F(q^2) = F(0) + q^2 \int\limits_{4M_\pi^2}^{\infty} \frac{\mathrm{d}s}{\pi} \frac{\mathrm{Im}F(s)}{s(s - q^2 - i\epsilon)} \,. \tag{3.3}$$

The aforementioned suppression of high energies is performed by the additional s denominator at the price of introducing a subtraction constant $F(0)$. Recall that for the Dirac and Pauli FFs, this quantity corresponds to the electric charge and anomalous magnetic moment respectively (Sec. 1.2.1).

Given that we pursue a description of the pion mass dependence of lattice data, the subtraction constant $F(0)$ has to be carefully treated. If it depends on the pion mass, we have to employ an unsubtracted dispersion relation (3.2). If not, a subtracted formula is implemented (3.3).

The isovector channel and the ρ meson

For $|q^2| \leq m_\rho^2$, the dispersion relation can be approximated by

$$F(q^2) \approx \int\limits_{4M_\pi^2}^{\Lambda^2} \frac{\mathrm{d}s}{\pi} \frac{\mathrm{Im}F_{2\pi}(s)}{s - q^2 - i\epsilon} + F_{\text{ChPT without } 2\pi \text{ cut}}(q^2) \,. \tag{3.4}$$

The first term is the dispersive one, and accounts for pion rescattering, with the cutoff $\Lambda > m_\rho$. The second stays for other diagrams without two-pion cut, and it is covered by ChPT contributions. In the rest of the section we will focus on the dispersive term, whose contributions are represented in Fig. 3.1, introducing the $NN\pi\pi$ vertex at leading order in ChPT and an explicit Δ baryon.

The 2π discontinuity is given by:

$$\mathrm{Im}F_{2\pi}(s) = F_\pi^*(s)\,\frac{p_{\rm cm}(s)^3}{12\pi\sqrt{s}}\,T(s)\ , \tag{3.5}$$

$T(s)$ are the reduced $N\bar{N} \to 2\pi$ p-wave amplitudes [153, 151], while F_π^* is the conjugate of the vector FF of the pion. Finally, $p_{\rm cm} = \sqrt{s - 4M_\pi^2}/2$ is the momentum of a pion in the frame where the two-pion system with invariant mass $\sqrt{s}$ is at rest; $p_{\rm cm}$ appears to the power of $2l + 1$.

Obviously, the left-hand side of Eq. (3.5) is real. Therefore the phases of T and F_π^* must cancel each other. This is the Watson Theorem introduced in Sec. 1.3.2 and prohibits the use of a purely perturbative calculation of the scattering amplitude T. As for the pion form factor, we use here an Omnès function to solve the problem ([155, 156, 151, 154] for further details).

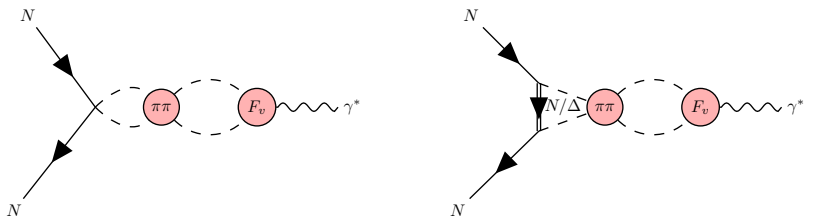

Figure 3.1: Dispersively modified diagrams with a 2π cut. Solid, dashed and wiggly lines denote nucleons, pions and virtual photons. Double solid lines stand for nucleon or Δ propagators. The "$\pi\pi$" circle represents the pion-pion scattering S-matrix, while the "F_v" circle denotes the pion vector FF.

The $N\bar{N}$ annihilation amplitude has a right and a left hand cut terms, K_R and K respectively, $T(s) = K_R(s) + K(s)$. The discontinuity along the right hand cut satisfies the unitarity relation:

$$\mathrm{Im}\,(T(s) - K(s)) = T(s)e^{-i\delta(s)}\sin\delta(s)\ , \tag{3.6}$$

with $\delta(s)$, the two pion phase shift introduced before. To solve it we introduce the following ansatz:

$$T(s) - K(s) = \Omega(s) H(s) \ , \tag{3.7}$$

with $\Omega(s)$ defined in Eq. (1.80) and $H(s)$ an arbitrary function. Therefore one has:

$$\mathrm{Im}\left(\Omega(s) H(s)\right) = \left(K(s) + \Omega(s)\right) e^{-i\delta(s)} \sin\delta(s) \ . \tag{3.8}$$

Using the fact that $\Omega(s)$ satisfies $\Omega(s) = |\Omega(s)| e^{i\delta(s)}$, one can determine from the above equation the imaginary part of $H(s)$:

$$\mathrm{Im}\, H(s) = \frac{K(s)\sin\delta(s)}{|\Omega(s)|} \ . \tag{3.9}$$

Therefore, it is possible to describe $H(s)$ by means of a dispersion relation:

$$H(s) = P + \int_{4M_\pi^2}^{\Lambda^2} \frac{\mathrm{d}s'}{\pi} \frac{\sin\delta(s')\, K(s')}{|\Omega(s')|\,(s' - s - i\epsilon)} \ , \tag{3.10}$$

with P a constant in s given by tree level ChPT. In this way, we obtain the expressions below for the annihilation amplitude. We will consider the subtracted and unsubtracted versions of the above equation, as we do for the form factors, yielding:

$$T(s) \ = \ K(s) + \Omega(s)\, P^{\mathrm{unsubtr}} + \Omega(s) \int_{4M_\pi^2}^{\Lambda^2} \frac{ds'}{\pi} \frac{\sin\delta(s')\, K(s')}{|\Omega(s')|\,(s' - s - i\epsilon)} \tag{3.11}$$

and

$$T(s) \ = \ K(s) + \Omega(s) P^{\mathrm{subtr}} + \Omega(s) s \int_{4M_\pi^2}^{\Lambda^2} \frac{\mathrm{d}s'}{\pi} \frac{\sin\delta(s')\, K(s')}{|\Omega(s')|\,(s' - s - i\epsilon)s'} \, . \tag{3.12}$$

To determine the phase shift, we rely on the IAM at NLO as explained in App. C.1. Both the $\delta(s)$ and F_π^V employed in this work are depicted in Fig. 1.4 (improved IAM curves).

Finally for the last piece in Eq. (3.5), the pion form factor, $F_\pi(s)$, we have introduced an additional term, α_V, accounting for a phenomenological correction following [157, 149, 151]:

$$F_\pi(s) = (1 + \alpha_V(M_\pi) s)\, \Omega(s) \, . \tag{3.13}$$

In particular, we need to account for the M_π dependence of α_V. This, as the pion mass dependence of the other dispersive inputs is addressed in App. C.1.

The ChPT calculation

We have calculated the Dirac and Pauli FFs in ChPT with explicit Δ up to $\mathcal{O}(p^3)$. In addition, $\mathcal{O}(p^4)$ contributions without Δ are included for F_2 because we find that $\mathcal{O}(p^3)$ ChPT yields unsatisfying results. On the other hand, it is not our ambition to go beyond state-of-the-art and provide a full-fledged $\mathcal{O}(p^4)$ calculation that includes the Δ. Therefore we make sure that we reproduce the $\mathcal{O}(p^4)$ Δ-less ($\not\Delta$) result of Ref [138][1]. In Ref. [22] the FF is calculated up to $\mathcal{O}(p^3)$ with explicit Δ and vector mesons. We reproduce the corresponding results without vector mesons. The baryon-mass difference $\delta \equiv m_\Delta - m_N$ is counted as $\mathcal{O}(p)$ (small-scale expansion [24]). This counting determines the $\mathcal{O}(p^3)$ Δ loops to be included. We proceed in the same way as for the axial form factor in Sec. 2.2.2. We work in relativistic ChPT in the EOMS renormalization and again, for the identification of the PCB terms, the δ difference is not considered as an expansion parameter.

For the $\not\Delta$ terms, we take $\mathcal{L}_2$ of Eq. (1.41) and $\mathcal{L}_{\pi N}^{(1-4)}$ from Ref. [20] with the definitions of our Sec.2.2.1:

$$\mathcal{L}_{\pi N}^{(2)} \supset \bar{\Psi}\left(\frac{ic_4}{4}[u_\mu,u_\nu]\sigma^{\mu\nu} + \frac{c_6}{8\mathring{m}}F_{\mu\nu}^{+}\sigma^{\mu\nu}\right)\Psi\ , \tag{3.14}$$

$$\mathcal{L}_{\pi N}^{(3)} \supset \bar{\Psi}\left(\frac{id_6}{2\mathring{m}}\left[D^\mu,\widetilde{F}_{\mu\nu}^{+}\right]D^\nu\ +\ \text{h.c.}\right)\Psi, \tag{3.15}$$

$$\mathcal{L}_{\pi N}^{(4)} \supset \bar{\Psi}\left(-\frac{e_{74}}{2}\left[D^\lambda,\left[D_\lambda,\widetilde{F}_{\mu\nu}^{+}\right]\right]\sigma^{\mu\nu}\ -\frac{e_{106}}{2}\widetilde{F}_{\mu\nu}^{+}\langle\chi_+\rangle\sigma^{\mu\nu}\right)\Psi, \tag{3.16}$$

with $\widetilde{F}_{\mu\nu}^{+} = F_{\mu\nu}^{+} - \langle F_{\mu\nu}^{+}\rangle/2$.

The inclusion of the Δ is important. In fact certain degree of cancellation with the nucleon has been observed [151]. For the Δ loops, we employ $\mathcal{L}_{\pi\Delta}^{(1)}$, $\mathcal{L}_{\pi N\Delta}^{(1)}$ from Sec.1.2.4 with $\tilde{z}=-1$ in $\mathcal{L}_{\pi N\Delta}^{(1)}$. The chiral limit masses $\mathring{m}=0.855$ GeV, $\mathring{m}_\Delta=1.166$ GeV are taken from our work on the

[1] Note that our c_6 LEC is $4\mathring{m}$ times the one used in Ref. [138].

axial form factor, and the chiral-limit value $F_0 = 0.0856$ GeV from [74]. We set $\mathring{g}_A = g_A^{\rm phys} = 1.2754$, given that we have seen from LQCD that it is almost M_π independent; we set $h_A \approx 3\mathring{g}_A/(2\sqrt{2}) = 1.35$ as predicted by large-N_c [121], again as in our axial form factor work.

For reference, the computed ChPT diagrams are depicted in Fig.3.2, and we report the leading ChPT terms of the isovector components of the quantities defined in Eqs. (1.23), (1.24) (in agreement with [22]):

$$\begin{aligned}\langle r_1^2\rangle^{\rm ChPT} &= -12d_6 + \frac{1}{16\pi^2 F_0^2}\Bigg\{ -2\log\left(\frac{M_\pi}{\mu}\right) - 1 \\ &\quad -\mathring{g}_A^2\left[10\log\left(\frac{M_\pi}{\mu}\right) - 12\log\left(\frac{\mathring{m}}{\mu}\right) + \frac{41}{2}\right] \\ &\quad + h_A^2\left[\frac{379}{54} - \frac{80}{27}\log\left(\frac{\mathring{m}}{\mu}\right) + \frac{80}{9}\log\left(\frac{M_\pi}{\mu}\right) - \frac{80\delta\log(X)}{9\sqrt{\delta^2 - M_\pi^2}}\right] \\ &\quad + \dots\Bigg\}, \end{aligned} \tag{3.17}$$

with $X = (\delta - \sqrt{\delta^2 - M_\pi^2})/M_\pi$; the ellipsis stands for higher orders in M_π and δ. The full expressions are given in the supplementary material of our work [125].

As already discussed, we include some $\mathcal{O}(p^4)$ diagrams in our F_2 calculation. Here we explicitly display the full tree-level but just the leading-loop isovector terms:

$$\begin{aligned}\kappa^{\rm ChPT} &= c_6 - 16e_{106}\mathring{m}M_\pi^2 + \frac{1}{4\pi^2 F_0^2}\Bigg\{ -\mathring{g}_A^2\mathring{m}M_\pi \\ &\quad + \frac{8}{9}h_A^2\mathring{m}\left[\delta\log\left(\frac{M_\pi}{2\delta}\right) - \sqrt{\delta^2 - M_\pi^2}\log(X)\right] + \dots\Bigg\}, \end{aligned} \tag{3.18}$$

$$\begin{aligned}(\kappa\langle r_2^2\rangle)^{\rm ChPT} &= 12(d_6 + 2\mathring{m}e_{74}) \\ &\quad + \frac{1}{8\pi^2 F_0^2}\left\{\frac{\pi\mathring{g}_A^2\mathring{m}}{M_\pi} - \frac{8h_A^2\mathring{m}}{9\sqrt{\delta^2 - M_\pi^2}}\log(X) + \dots\right\}. \end{aligned} \tag{3.19}$$

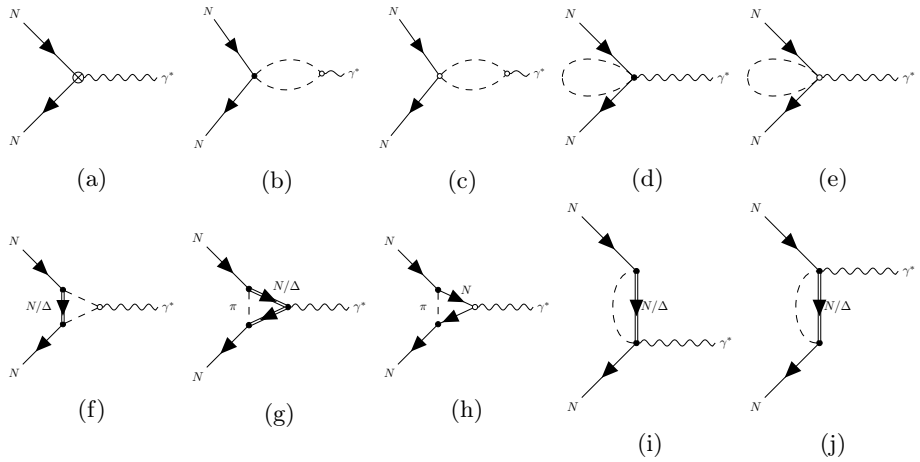

Figure 3.2: ChPT diagrams for the nucleon EM form factors. Line styles are defined as in Fig. 3.1. Diagram 3.2a represents tree level vertices up to $\mathcal{O}(p^4)$. Diagrams 3.2b-3.2j account for $\mathcal{O}(p^3)$ in a ChPT version with Δ and also $\mathcal{O}(p^4)$ in a Δ-less ($\not\Delta$) theory. The open and filled circles denote $\mathcal{O}(p^2)$ and $\mathcal{O}(p)$ vertices, respectively.

3.2 The Dirac form factor

The Dirac isovector FF at the photon point $q^2 = 0$ is given by the proton charge:

$$F_1(q^2 = 0) = 1\,. \tag{3.20}$$

Since the charge is protected by gauge invariance, it is not renormalized, and therefore does not have any M_π dependence. Consequently, this is a clear case in which it is convenient to study the subtracted form factor. Then, our dispersively improved FF reads

$$\begin{aligned} F_1(q^2) \,=\, 1 + \frac{q^2}{12\pi} \int\limits_{4M_\pi^2}^{\Lambda^2} \frac{\mathrm{d}s}{\pi}\, \frac{T_1(s)\, p_{\mathrm{cm}}^3(s)\, F_v^*(s)}{s^{3/2}\,(s - q^2 - i\epsilon)} \\ + F_1^{\text{two-baryon cut}}(q^2) - F_1^{\text{two-baryon cut}}(0) + 2q^2 d_6\ , \end{aligned} \tag{3.21}$$

where the two-pion cut is accounted by a once-subtracted dispersion relation. We also employ a subtracted annihilation amplitude:

$$T_1(s) \,=\, K_1(s) + \Omega(s)\, P_1 + \Omega(s)\, s \int\limits_{4M_\pi^2}^{\Lambda^2} \frac{\mathrm{d}s'}{\pi}\, \frac{\sin\delta(s')\, K_1(s')}{|\Omega(s')|\,(s'-s-i\epsilon)\, s'}\,. \tag{3.22}$$

Diagrams 3.2d, 3.2e, 3.2i, 3.2j of Fig. 3.2 contribute only to the charge. Diagrams 3.2b, 3.2c, 3.2f, and parts of 3.2a are covered by the dispersive integral. Diagrams 3.2g and 3.2h constitute $F_1^{\text{two-baryon cut}}$. These interrelations are further discussed in Appendix C.2.

In this work, we want a precision of at least the one-loop order, $\mathcal{O}(p^3)$, i.e. NNLO. The Dirac FF starts at leading order, but just with the trivial contribution of the charge. The next contributions appear at NNLO and all of them are proportional to q^2. Therefore, the dispersive integral in (3.21) needs only an LO input, since the q^2 factor yields an overall NNLO. Hence, in P_1 we only include the LO ChPT terms

$$\begin{aligned} P_1 &= P_1^N + P_1^\Delta + P_1^{\mathrm{WT}} \\ &= -\frac{\mathring{g}_A^2}{F^2} + \frac{2h_A^2(\mathring{m}_\Delta + \mathring{m})^2}{9F^2\mathring{m}_\Delta^2} + \frac{1}{F^2}\,, \end{aligned} \tag{3.23}$$

where P_1^N, P_1^Δ, and P_1^{WT} come from the nucleon exchange, the Δ exchange and from the Weinberg-Tomozawa term [158, 159], respectively. Correspondingly, K_1 is obtained from the parts of the nucleon- and Δ-exchange diagrams where a propagator appears (after partial-fraction decomposition) as explicitly covered in Refs. [153, 151]. Details on the expressions are given in App. C.3.

Corrections to LO P_1 are proportional to s or M_π^2, and therefore two orders higher than what is strictly necessary for us. This can be deduced from the results in Ref. [19] using a Ward identity that relates diagrams where one photon line is replaced by two pion lines.

To be precise, it should be noticed that since the $N\bar{N}$ annihilation amplitude is once-subtracted, the integral in Eq. (3.22) is nominally of higher order. However it is kept to respect Watson's theorem. Finally, regarding the specific interrelation with ChPT, we have checked that the once-subtracted DR for F_1 reproduces the non-analyticity of the ChPT 2π cut at $\mathcal{O}(p^3)$.

3.2.1 Comparison to LQCD results with fixed parameters

We have explored how different theories describe the LQCD results for the isovector Dirac form factor, F_1. In the present subsection we discuss results where all parameters are previously determined from experimental data, so that the FF is a prediction (no LEC is fitted here to the lattice simulations). The following approaches are tested:

- A purely dispersive calculation where we neglect the contributions with a two-baryon cut and set $d_6 = 0$ in (3.21). We denote this version as "disp".
- A plain $\mathcal{O}(p^3)$ ChPT computation without dispersive modifications [in this case the radius $\langle r_1^2 \rangle$ is given by Eq. (3.17)]. Two alternatives are considered:
  - retaining the higher order contributions to the loops, i.e. without a further expansion in small parameters. This approach is denoted "full ChPT".
  - truncating the 2Δ diagram in Fig. 3.2g keeping only $\mathcal{O}(p^3)$. We label this just "ChPT".
- Dispersion theory supplemented with ChPT two-baryon loops and the d_6 $\mathcal{O}(p^3)$ contact term; this is the full version of Eq. (3.21). We test again two versions:
  - "disp+full ChPT" includes the full 2Δ loop.
  - "disp+ChPT" contains the 2Δ diagram truncated up to $\mathcal{O}(p^3)$.

The purely dispersive calculation, "disp", yields a prediction for F_1 without further input, whereas all the other choices depend on the LEC

Table 3.1: LEC d_6 values obtained from the experimental Dirac radius quoted by the Particle Data Group (PDG) [5] within the various approaches (see text). In addition, the dependence on the renormalization point is illustrated by showing the numbers for two typical scales. For our plots we have taken $\mu = m_\rho$.

	ChPT (truncated)	full ChPT	disp+ChPT (truncated)	disp+full ChPT
$d_6^{\rm exp}(\mu = m_\rho)$ (GeV^{-2})	-0.385	-0.353	0.216	0.248
$d_6^{\rm exp}(\mu = m_N)$ (GeV^{-2})	-0.733	-0.701	-0.045	-0.013

d_6. In any case, this LEC can be pinned down from the experimental value of $\langle r_1^2 \rangle$ (see Table 3.1). We compare to the LQCD determinations of Ref. [136]. We study only these data, and no other recent simulations such as [114], because the former have a smaller dependence on lattice artifacts. Accounting for these additional dependencies would complicate the analysis and is beyond the purpose of the present work.

$F_1(Q^2)$ is shown in Fig. 3.3 at the low M_π values of different ensembles from Ref. [136]. Whereas the M_π dependence of $\langle r_1^2 \rangle$ is shown in a corresponding figure, 3.4(a). These plots show that the purely dispersive scheme ("disp") is close to the LQCD data in both the Q^2 and M_π variables. The nonperturbative treatment is responsible for the generation of a realistic Q^2 curvature. The M_π dependence of the radius is also well described up to $M_\pi \sim 400$ MeV. As aforementioned, the $\log M_\pi$ divergence of $\langle r_1^2 \rangle$ at $M_\pi \to 0$ predicted by ChPT is also obtained from the dispersive integral.

Looking now at the ChPT curves, one can see in Fig. 3.3 that none of the two alternatives ("ChPT" and "full ChPT") describes the Q^2 behavior of F_1 in the different ensembles beyond $Q^2 \gtrsim 0.3\,\mathrm{GeV}^2$. The obtained curvature is insufficient. In particular, we notice that the experimental FF also has a significant Q^2 curvature, as apparent from the dashed orange curve in Fig. 3.7(a), which corresponds to the Kelly empirical parametrization [160]. In Fig. 3.4(a) it is also shown that the M_π dependence of the radius is described better by the computation with the truncated Δ contribution.

In comparison to the ChPT versions, the scheme "disp+ChPT" improves the Q^2 behavior of the Dirac FF, though the curvature is still underpredicted. By contrast, the scheme "disp+full ChPT" (dispersive result combined with untruncated ChPT) produces an excessive curvature in Q^2. In both versions, the combination of the dispersive approach and ChPT does not cause a change in the M_π dependence of $\langle r_1^2 \rangle$. Indeed, the curves for "ChPT" and "disp+ChPT" overlap in Fig. 3.4 and so do the "full ChPT" and "disp+full ChPT" ones.

These comparisons display that the higher order contributions from the loop with two Δ propagators lead to a worse description of LQCD results at higher Q^2 and M_π. In consequence, we have decided to retain from the loop with two Δ propagators only the part that is strictly $\mathcal{O}(p^3)$. To further support our prescription, we note that the relativistic Δ prop-

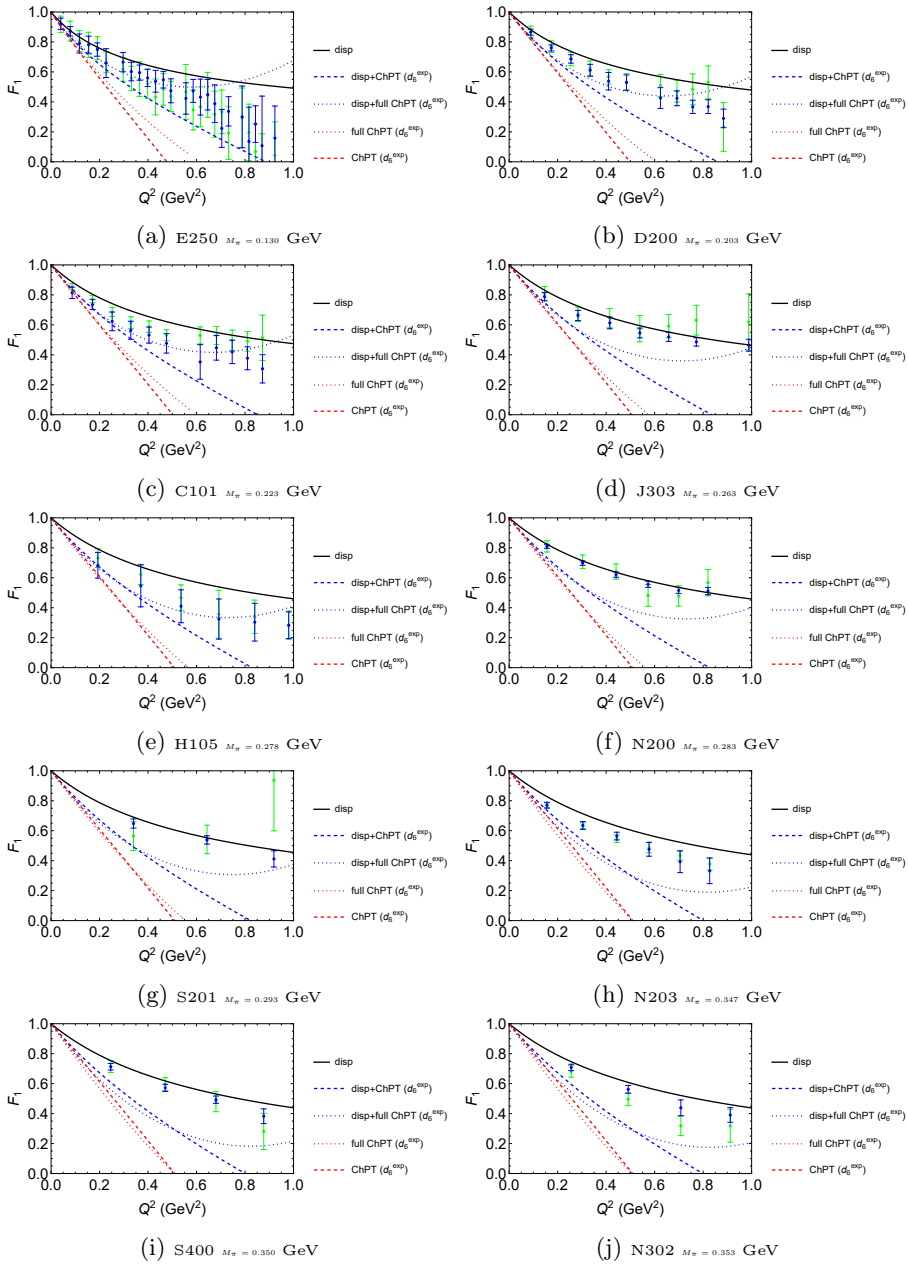

(a) E250 $M_\pi = 0.130$ GeV (b) D200 $M_\pi = 0.203$ GeV

(c) C101 $M_\pi = 0.223$ GeV (d) J303 $M_\pi = 0.263$ GeV

(e) H105 $M_\pi = 0.278$ GeV (f) N200 $M_\pi = 0.283$ GeV

(g) S201 $M_\pi = 0.293$ GeV (h) N203 $M_\pi = 0.347$ GeV

(i) S400 $M_\pi = 0.350$ GeV (j) N302 $M_\pi = 0.353$ GeV

Figure 3.3: $F_1(Q^2)$ for different M_π, corresponding to the LQCD ensembles of [136] (belonging to summation and two-state method in green and blue resp.). The curves are the approaches described in the text (when present d_6 is fixed from the experimental value for the Dirac radius [5]).

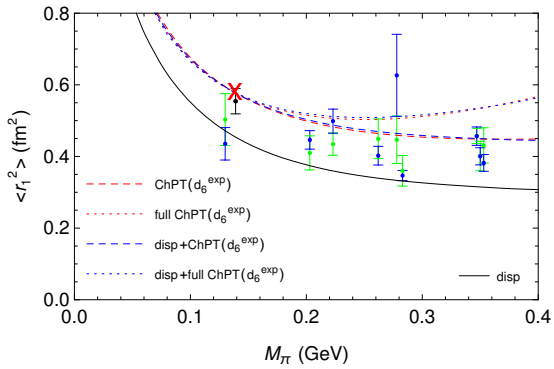

(a)

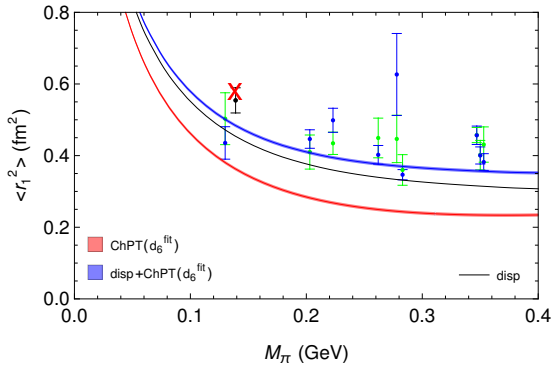

(b)

Figure 3.4: The Dirac radius $\langle r_1^2 \rangle$ as a function of M_π. LQCD points in green (summation method) and in blue (two-particle method) were obtained in Ref. [136] using the z-expansion to parametrize the Q^2 dependence of F_1. The black point is the $\langle r_1^2 \rangle$ value at the physical M_π obtained in Ref. [136] employing Heavy Baryon ChPT to extrapolate LQCD results for F_1 in M_π and Q^2. The red cross (with negligibly small error bars) corresponds to the experimental value quoted by PDG [5]. *Top panel:* results obtained with the five strategies introduced in Sec. 3.2.1, fixing d_6 at the physical M_π with the experimental value quoted in Ref. [5] for $\langle r_1^2 \rangle$. *Bottom panel:* results obtained by fitting d_6 to the LQCD values of Ref. [136] for $F_1(Q^2, M_\pi)$ with "ChPT" and "disp+ChPT" versions, as discussed in the text. The bands account only for the statistical error. The "disp" (black) curve is the same in both panels.

agators contain unphysical spin-1/2 contributions. In principle, those must be absorbed by LECs [36]. But for the two-Δ contributions beyond $\mathcal{O}(p^3)$, we have not included the aforementioned LECs. Eventually, a justification for our choice can only come from a complete calculation at $\mathcal{O}(p^4)$, which is beyond our scope here.

3.2.2 Fit to LQCD

In the previous section, by fixing d_6 from the experimental $\langle r_1^2 \rangle$, compatibility between the LQCD results and experiment has been implicitly assumed. It is worthwhile to remove this constraint and attempt to fit F_1 with our theory (a χ^2 fit), considering d_6 as a free parameter. On the basis of the results obtained so far we regard the dispersive calculation combined with truncated ChPT ("disp+ChPT") as the most promising scheme for this exercise. We also fit (truncated) "ChPT" as a reference for comparison.

With the purpose to avoid correlations, we limit our fit to the LQCD results obtained with one of the methods, the summation one. We however disregard possible correlations among different data points, conceding that this might slightly distort our analysis. After studying the variation of χ^2 with the accepted range of Q^2 and M_π, we find it reasonable to include data with $Q^2 < 0.6\,\mathrm{GeV}^2$. We fit to all available ensembles, so that we reach $M_\pi \simeq 350\,\mathrm{MeV}$. Regarding the M_π dimension, the χ^2/dof value vs the variation of the largest M_π included is shown in Fig. 3.5 for reference, keeping the maximum Q^2 set to $0.6\,\mathrm{GeV}^2$.

The results using "disp+ChPT" and "ChPT" are presented in Fig. 3.7 for the Dirac FF at different M_π (Fig. 3.6 shows the evaluation at $M_\pi \sim M_\pi^{\mathrm{phys}}$). The parameter-free purely dispersive prediction, "disp", is also displayed for reference. The band widths correspond to a 1σ uncertainty in d_6. We regard our errors to be underestimated, since they do not account for theoretical uncertainty, in particular for the truncation error of the chiral series. However, a reliable estimation would require implementing one additional order in ChPT, which goes beyond our scope here. We prefer to focus on describing the main features of the LQCD data. The results of the three schemes for d_6, χ^2, and $\langle r_1^2 \rangle_{\mathrm{phys}}$ are reported in Tab. 3.2.

Comparing Figs. 3.3 and 3.7 we distinguish a clear improvement when

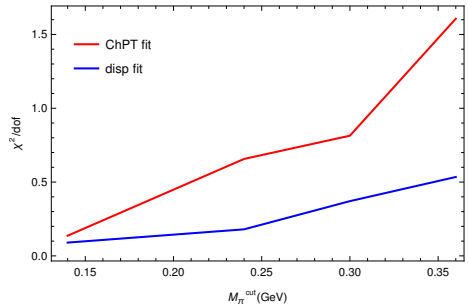

Figure 3.5: The value for χ^2/dof as a function of the largest pion mass $M_\pi^{\rm cut}$ included in the fit. The two schemes are "ChPT" (red) and "disp+ChPT" (blue). For both we use $Q^2_{\rm cut} = 0.6\,\text{GeV}^2$ as the largest included value.

Table 3.2: Results from the $F_1(Q^2, M_\pi)$ fit to LQCD.

	disp (prediction)	ChPT	disp+ChPT	HB from [136]	exp. (PDG [5])
$d_6(\mu = m_\rho)$ (GeV^{-2})	-	0.074 ± 0.010	0.416 ± 0.010		
$d_6(\mu = m_N)$ (GeV^{-2})	-	-0.422 ± 0.010	0.155 ± 0.010		
χ^2/dof	$108.9/47 = 2.32$	$73.9/(47-1) = 1.61$	$24.6/(47-1) = 0.53$		
$\langle r_1^2\rangle_{\rm phys}$ (fm^2)	0.4541	0.3626 ± 0.0047	0.4838 ± 0.0047	0.554 ± 0.035	0.577 ± 0.0018

d_6 is fitted to the LQCD results rather than to the experimental value of the radius. It is apparent in Fig. 3.7 that both "disp+ChPT" and "ChPT" are in good agreement with the LQCD data, especially, but not only, in the $Q^2 < 0.6\,\text{GeV}^2$ regime where data was fitted. However, it should be noticed that fitting the plain "ChPT" computation to Q^2 values as high as 0.6 GeV^2 does not make the most of the theory. The region $Q^2 \in [0.4, 0.6]$ GeV^2 is beyond the reach of $\mathcal{O}(p^3)$ ChPT but we keep the same cut as for the dispersively modified scheme to simplify the comparison. The previous ChPT result with $d_6^{\rm exp}(m_\rho) = -0.385$ GeV^{-2} fixed to experiment (Tab. 3.1) is better to rate the ChPT performance. The use of this LEC value is indeed advised for plain ChPT. In fact, to compensate the lack of Q^2 curvature in the ChPT fit, one extracts a d_6 which yields a too small radius.

In the dispersively modified approach, one should first recall that the pure dispersive calculation is already quite good a result. The main benefit of supplementing it with ChPT contributions is the possibility to increase the radius. The added ChPT term mostly corresponds to a shift of the radius, $\langle r_1^2\rangle^{\rm disp} \to \langle r_1^2\rangle^{\rm disp} - 12 d_6 + \langle r_1^2\rangle^{\text{2-baryon loops}}$ as shown

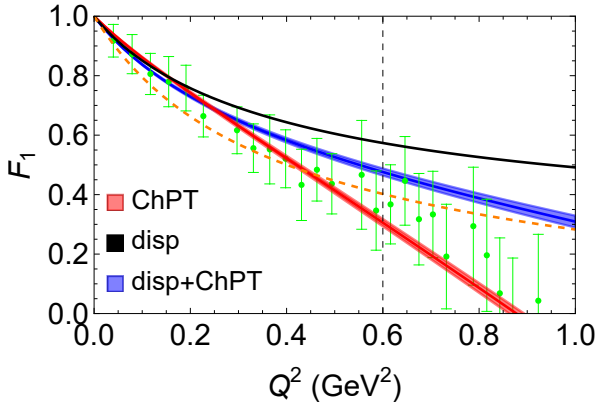

Figure 3.6: $F_1(Q^2)$ for $M_\pi = 0.130 \sim M_\pi^{\rm phys}$, corresponding to the LQCD ensemble E250 of Ref. [136]. Line and point styles match the ones in Fig. 3.3 but, in contrast, the "ChPT" and "disp+ChPT" curves have been obtained with a global fit of the d_6 LEC to the LQCD points of all the ensembles. The vertical dashed line is the maximum Q^2 adopted in the fits. The dashed orange curve is the Kelly empirical parametrization of F_1 [160].

in Fig. 3.4(b), (a specific discussion is reported below). In addition, regarding now the F_1 Q^2-curvature, it remains essentially the same as the pure dispersive. That is to say, the "disp+ChPT" $F_1(Q^2)$ and the "disp" curves are approximately obtained from each other by rotations around the photon point. It should be noticed that the Q^2 dependence of the LQCD results is well described with "disp+ChPT" up to Q^2 values even larger than $Q^2_{\rm cut} = 0.6\,{\rm GeV}^2$. In fact, this scheme outperforms "ChPT" and "disp", yielding a smaller χ^2 as shown in Tab. 3.2. In addition, at the physical M_π the "disp+ChPT" curve is close to the empirical Kelly parametrization, as shown by Fig. 3.7(a).

On top of this, the M_π dependence of $\langle r_1^2 \rangle$ for the fitted d_6 values is displayed in Fig. 3.4(b). Both schemes yield the same shape but the "disp+ChPT" curve is closer to the results of the extrapolations of the LQCD points to $Q^2 = 0$ performed in Ref. [136] employing the z expansion. At the physical point, $\langle r_1^2 \rangle_{\rm phys}^{\rm disp+ChPT} = 0.4838 \pm 0.0047\,{\rm fm}^2$ also agrees better to the PDG value and to the HB ChPT extrapolation of Ref. [136] ($\langle r_1^2 \rangle^{\rm HB} = 0.554 \pm 0.035\,{\rm fm}^2$) but falls short by $\sim 20\%$. This disagreement could be due to the lack of a more realistic theoretical error

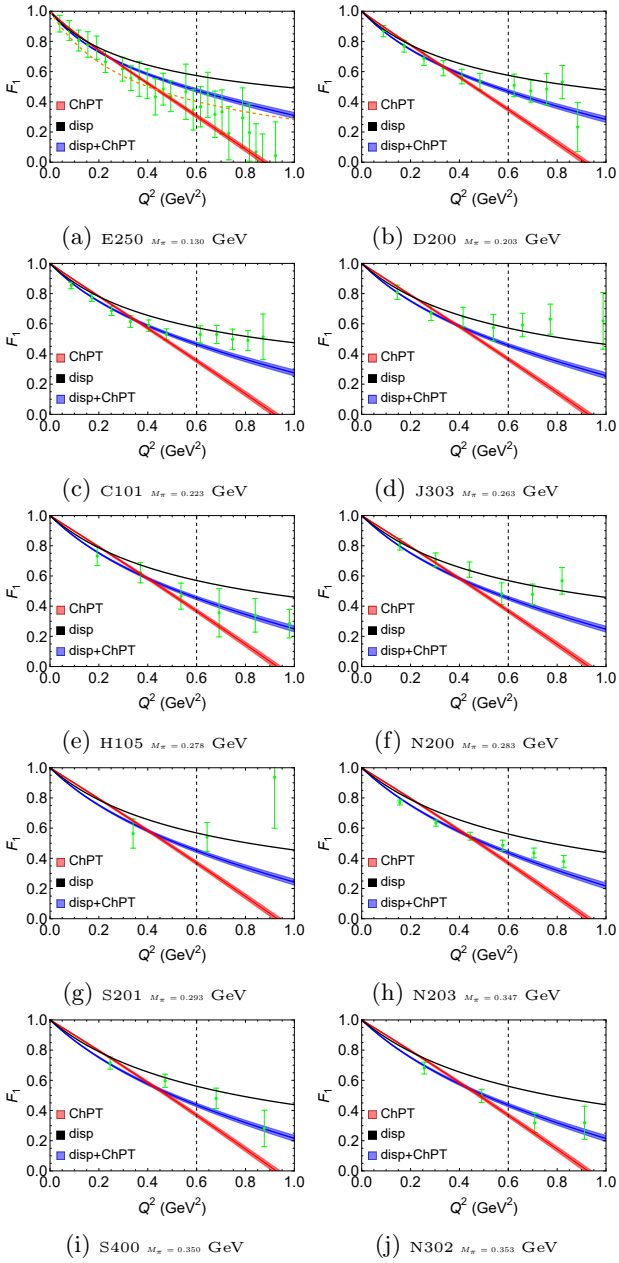

Figure 3.7: Same as in Fig. 3.6, showing now all the LQCD ensembles of Ref. [136].

in our computation. Our results for $\langle r_1^2 \rangle$ together with other reference values are summarized in Tab. 3.2.

Finally, we would like to briefly discuss the d_6 LEC. As usual, it depends on μ, the scale of the ChPT dimensional regularization. It also appears in the disp+ChPT calculation, although in this case its running comes only from the 2Δ loop. In general, d_6 is of the same order of magnitude in "ChPT" and in "disp+ChPT". In addition, it has always a relatively small value, $|d_6(\mu)| < 2$ GeV^{-2} for $\mu \in [0.5, 2]$ GeV, in both schemes. The μ dependence of d_6 is explicitly reported in App. C.4.

3.3 The Pauli form factor

3.3.1 Selection of diagrams

Turning now to the Pauli FF, given that its value at $Q^2 = 0$ is nontrivial and has an M_π dependence which we want to assess, we do not perform any subtraction. An unsubtracted dispersion relation, both for the form factor

$$\begin{aligned} F_2(q^2) &= \frac{1}{12\pi} \int\limits_{4M_\pi^2}^{\Lambda^2} \frac{\mathrm{d}s}{\pi} \frac{T_2(s)\, p_{\mathrm{cm}}^3(s)\, F_v^*(s)}{s^{1/2}\,(s - q^2 - i\epsilon)} \\ &\quad + F_2^{\text{ChPT without } 2\pi \text{ cut}}(q^2) \end{aligned} \tag{3.24}$$

and the annihilation amplitude

$$T_2(s) = K_2(s) + \Omega(s)\, P_2 + \Omega(s) \int\limits_{4M_\pi^2}^{\Lambda^2} \frac{\mathrm{d}s'}{\pi} \frac{\sin\delta(s')\, K_2(s')}{|\Omega(s')|\,(s' - s - i\epsilon)} \tag{3.25}$$

is employed.

We aim to obtain a form factor with at least the accuracy of the $\mathcal{O}(p^3)$ ChPT diagrams, *i. e.,* NNLO in the ChPT diagrammatic power counting. According to the ChPT counting, the LO and NLO terms of the polynomial P_2 are required for our accuracy, as discussed below:

$$\begin{aligned} P_2 &= P_2^N + P_2^\Delta + P_2^{\mathrm{NLO}} + \mathcal{O}(p^2) \\ &= 0 + \frac{4h_A^2 \mathring{m}(3\mathring{m} + 4\mathring{m}_\Delta)}{9F^2 \mathring{m}_\Delta^2} + \frac{4c_4 \mathring{m}}{F^2} + \mathcal{O}(p^2)\,, \end{aligned} \tag{3.26}$$

with c_4 the already familiar constant from $\mathcal{L}^{(2)}_{\pi N}$ of Eq. (3.14).

The leading contribution to the Pauli FF in ChPT appears one order higher than the dominant term of F_1; it is NLO, proportional to the NLO LEC from $\mathcal{L}^{(2)}_{\pi N}$. In particular it is the c_6 term in Eq. (3.18), which contributes to the chiral limit anomalous magnetic moment [19]. Corrections at NNLO are of the form $\sim M_\pi$ and $\sim Q^2/M_\pi$. As aforementioned, M_π is proportional to the light quark mass squared, and therefore even the first term is not analytic in the quark mass. Such contributions originate from loops and can not be reproduced by subtraction constants. By employing a subtracted dispersion relation for F_2, one would lose part of the NNLO contributions. The same applies to Eq. (3.25): by using a subtracted dispersive integral one would miss part of the (non-analytic) terms, which are needed to achieve the required NNLO precision in F_2 (Eq. (3.24))[2].

The use of an unsubtracted dispersion relation implies no demotion for the high energy part of the integral. Therefore one might worry about having more cutoff dependence than for the Dirac FF. In any case, if s is large, then any integrand can be expanded in powers of M_π^2/s. This region of integration does not produce any non-analyticity in the quark mass. In consequence cutoff dependence can be compensated by changes in the LECs. In particular, F_2 has a constant contribution from c_6, Eq. (3.18). Additional LECs accompanied by powers of q^2 or M_π^2 would contribute beyond the desired NNLO accuracy.

Regarding now the annihilation amplitude, T_2, one can discuss its unsubtracted nature with analogous arguments. In Eq. (3.25), K_2 is taken from the tree-level nucleon- and Δ-exchange diagrams of pion-nucleon scattering. One-loop diagrams with left-hand cuts yield two-loop diagrams for the FF. This is beyond our accuracy goal. On the other hand, P_2 gets contributions from LO pion-nucleon scattering amplitudes. These are the nucleon- and Δ-exchange diagrams, given that they contain parts without propagators (after a partial-fraction decomposition). Looking in detail to these terms, first, these contributions to P_2 are actually NLO; second, the nucleon contribution cancels, and, third, the Δ-exchange term depends on the details of how the Δ-N-π interaction vertex is constructed [153, 151]. In any case, there is a contact term with a LEC appearing at NLO for pion-nucleon scattering and contributes with a

[2]The relation between the power counting and the dispersive integration has been examined in App. C.2.

constant to P_2. This four-point interaction term, proportional to c_4 in Eq. (3.26), absorbs the ambiguities from the three-point Δ-N-π vertex [36, 153, 151]. Therefore we can use P_2 (or c_4) as a fit parameter of our scheme. Besides, the dominant part of the cutoff dependence of the unsubtracted T_2 dispersive integral can be compensated by a shift in P_2.

In principle, we need LO, NLO, and NNLO terms for T_2, but we have already argued why a tree-level approximation for K_2 is sufficient. What is not covered by K_2 are polynomials (in s and M_π^2) and loop contributions without two-pion cuts. Formally at NNLO, the latter are obtained from diagrams 3.2d, 3.2g, 3.2i, 3.2j in Fig. 3.2 by replacing the photon line by two pion lines. Again, one can use the Ward identity in Eq. (A.10) of Ref. [19] and the explicit results at the end of Sec. 3.1.1 to show that in the end such diagrams do not contribute to T_2 at NNLO.

The last remark concerning the dispersive approach is about P_2 in Eq. (3.26). The nominal LO contribution is in practice NLO. LEC c_4 from the pion-nucleon NLO contact interaction contributes also with a constant. Given that NNLO terms are one order higher and therefore can not be analytic in s or M_π^2, they cannot contribute to P_2. In consequence, we restrict P_2 to a fit constant in our analysis. It is equivalent to use as fit parameter P_2 or c_4, but it might be more informative to employ a LEC that appears in the ChPT Lagrangian instead of a subtraction constant of a dispersive integral.[3] A meaningful purely dispersive approach ("disp") starts from Eq. (3.24), but contains only c_6 instead of the full $F_2^{\text{ChPT without } 2\pi \text{ cut}}$.

On the plain ChPT side, we now show that the $\mathcal{O}(p^3)$ calculation does not describe the LQCD data well. In Fig. 3.10 the $\mathcal{O}(p^3)$ ChPT F_2 is depicted. As can be concluded from the mismatch at zero Q^2 for different M_π ensembles, $\mathcal{O}(p^3)$ ChPT predicts a too steep slope for $F_2(0, M_\pi) \equiv \kappa(M_\pi)$. Moreover the Q^2 dependence does not agree with the lattice. This result motivates us to include the $\not{\Delta}$ contributions of $\mathcal{O}(p^4)$. In particular, in the ChPT term we truncate the Δ contribution at pure $\mathcal{O}(p^3)$ following the same criterion as for F_1. For this reason, the only Δ contribution to F_2 comes from diagram 3.2f of Fig. 3.2 (recall that the leading plain ChPT κ and $\langle r_2^2 \rangle$ are given by Eqs. (3.18), (3.19)).

Like for the Dirac, we improve the ChPT Pauli form factor combining it with the dispersive 2π cut. In practice, for the combined approach,

[3] There is no straightforward argument to implement other LECs in this scheme without 2-baryon loops, so we do not include them.

Table 3.3: ChPT input for F_2 from the respective diagrams of Fig. 3.2 that we take include (✓) or not (×). We implement all $\mathcal{O}(p^3)$ and all Delta-less $\mathcal{O}(p^4)$ diagrams. Therefore we exclude all Δ diagrams that de facto start at $\mathcal{O}(p^4)$. Δ denotes diagrams with Δ propagators in the loop; $\not\Delta$ indicates Delta-less contributions; "wfr" stands for wave-function renormalization.

diagrams	ChPT	disp+ChPT	reason to include/exclude from the (disp+)ChPT scheme
3.2a	✓	✓	LECs
nucleon 3.2g	✓	✓	2-nucleon cut diagram
3.2d	-	-	it is zero (only contributes to $F_1(0)$)
nucleon 3.2i, 3.2j	-	-	it is zero (only contributes to $F_1(0)$)
nucleon 3.2f	✓	×	generated dispersively
3.2b	-	-	it is zero (only contributes to $F_1(0)$)
nucleon 3.2h	✓	✓	$\mathcal{O}(p^4)$ 2-nucleon cut diagram
3.2e (c_6)	✓	✓	$\not\Delta\mathcal{O}(p^4)$ without cut
3.2c (c_4)	✓	×	$\not\Delta\mathcal{O}(p^4)$ generated dispersively
Δ 3.2i, 3.2j	×	×	de facto $\Delta\mathcal{O}(p^4)$
Δ 3.2g	×	×	de facto $\Delta\mathcal{O}(p^4)$
Δ 3.2f	✓	×	generated dispersively
wfr $\not\Delta\mathcal{O}(p^3) \times c_6$	✓	✓	de facto $\not\Delta\mathcal{O}(p^4)$ without cut
wfr $\Delta\mathcal{O}(p^3) \times c_6$	×	×	de facto $\mathcal{O}(p^4)$ with Δ
wfr $\not\Delta\mathcal{O}(p^4) \times c_6$	×	×	de facto $\not\Delta\mathcal{O}(p^5)$

we supplement the dispersive F_2 with the addition of $\not\Delta$ diagrams 3.2a, 3.2g, 3.2h and 3.2e and the $\mathcal{O}(p^3)$ $\not\Delta$ wave function renormalization (see Tab. 3.3). For F_2, our truncation criterion implies that no Δ contributions are added from the ChPT side to the disp+ChPT calculation. Also notice that diagram 3.2f of Fig. 3.2 is covered by the dispersion relation. Now that the computation has been clarified, we can finally discuss how well the different schemes describe the LQCD data of Ref. [136] (the same procedure as for the Dirac case).

3.3.2 Fit results for F_2, anomalous magnetic moment and Pauli radius

The three schemes considered are:

- the purely dispersive approach (implementing the c_6 contact term), denoted "disp+c_6". It contains LECs c_4 and c_6 as free parameters.
- plain "ChPT" including diagrams up to $\mathcal{O}(p^4)$. This includes five LECs beyond LO (d_6, c_6, e_{74}, e_{106} and c_4) in Eqs. (3.18), (3.19). However d_6 is fixed from the corresponding "ChPT" fit to the Dirac FF.
- the combined "disp+ChPT", which includes the same number of fit parameters as "ChPT".

All fits are performed in the same range as for for F_1, meaning $Q^2 < 0.6$ GeV^2 and covering all M_π ensembles, i.e. $M_\pi \leq 0.350\,\text{GeV}$.

There is a conceptual difference between LECs d_6, c_6, e_{74}, e_{106} as compared to c_4. The latter is inherited from pion-nucleon scattering, while the others are directly tied to the electromagnetic FFs (tree-level contributions to magnetic moment and radii). Given this and the large number of free parameters, we implement a Gaussian prior on c_4, accounting for the present information from πN scattering:

$$\chi^2 = \chi_0^2 + \frac{(c_4 - c_4^{\text{prior}})^2}{\Delta c_4^{\text{prior}}} \,, \tag{3.27}$$

whit χ_0^2, the standard χ^2. For dispersive approaches, in order to determine this prior, we study the values of c_4 for which our reduced scattering amplitude T_2 agrees well with the results obtained by solving Roy–Steiner equations for pion-nucleon scattering [103]. The T_2 curves are shown in Fig. 3.8. in consequence, we set $c_4^{\text{prior}} = c_4^{\text{Roy}} = -0.402$ GeV^{-1} and $\Delta c_4^{\text{prior}} = \Delta c_4^{\text{Roy}} = 0.075$ GeV^{-1} in Eq. (3.27). Similarly, we put a prior to c_4 in plain ChPT as well. In this case we use the πN scattering analysis of Ref. [28] and take $c_4^{\text{prior}} = c_4^{\pi N} = 1.200$ GeV^{-1}, $\Delta c_4^{\text{prior}} = \Delta c_4^{\pi N} = 0.045$ GeV^{-1}.[4]

We outline now the quality of the three fits:

- "disp+c_6":
  From Fig. 3.10 (Fig. 3.9 for $M_\pi \sim M_\pi^{\text{phys}}$) and from the χ^2 value in Table 3.4 it is apparent that dispersion theory reproduces well the Q^2 and M_π dependence of the LQCD data. There is a large correlation between c_4 and c_6 because both of them appear in $\kappa(M_\pi =$

[4] We take the value from [28] for $c_4^{\pi N}$ even if it corresponds to a different off-shell parameter $\tilde{z}$. Furthermore, the μ running is neglected.

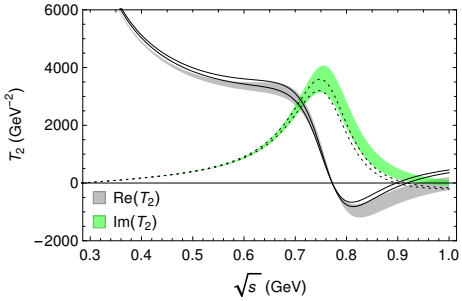

Figure 3.8: Reduced annihilation amplitude, T_2, in the unphysical region. The bands correspond to the real and imaginary parts of T_2 as obtained from a Roy-Steiner analysis of pion-nucleon scattering [103, 149] in gray and green, respectively. The curves represent our T_2, binding the region covered by the assumed prior knowledge of c_4. The real and imaginary parts are represented by solid and dashed lines respectively.

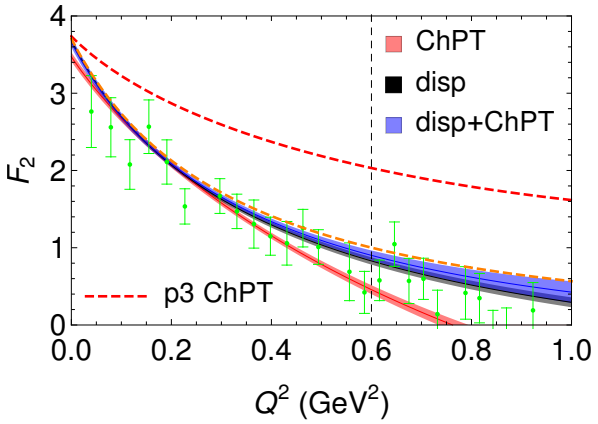

Figure 3.9: $F_2(Q^2)$ for $M_\pi = 0.130 \sim M_\pi^{\rm phys}$, corresponding to the LQCD ensemble E250 of Ref. [136]. LQCD points obtained with the summation method are shown. Red, black and blue bands are the results for the "ChPT", "disp+c_6", and "disp+ChPT" schemes, respectively. Band widths show the 1σ statistical errors. The dashed red curve represents the $\mathcal{O}(p^3)$ ChPT result. As in Fig. 3.7, the vertical dashed line indicates the maximum Q^2 adopted in the fits (fits are global, *i. e.* to all the LQCD ensembles simultaneously). The dashed orange curve in panel is the Kelly empirical parametrization of F_2 [160].

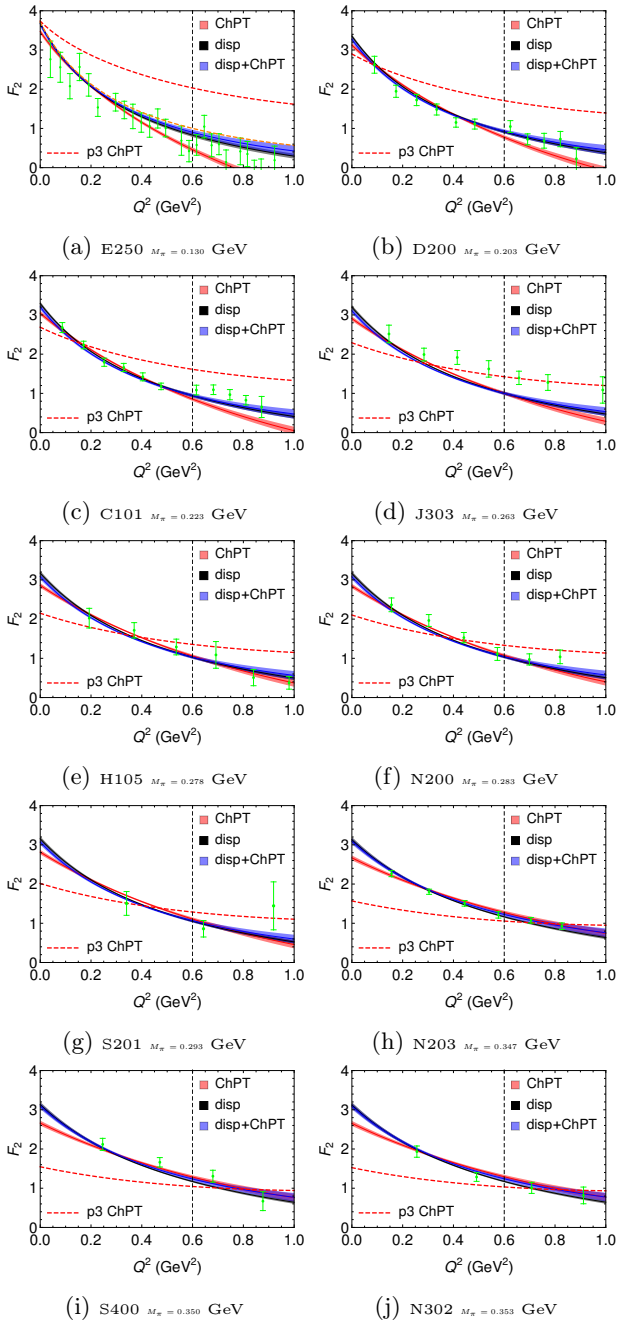

Figure 3.10: Same as in Fig. 3.9, showing now all the LQCD ensembles of Ref. [136].

Table 3.4: Results from our fit to the $F_2(Q^2, M_\pi)$ LQCD data of Ref. [136]. The HB column contains the heavy-baryon extrapolation from Ref. [136]. The experimental values [5] are also reported.

	disp+c_6	ChPT	disp+ChPT	HB	exp. (PDG)
χ^2/dof	$\frac{49.95}{47-2} = 1.110$	$\frac{44.18}{47-4} = 1.027$	$\frac{56.08}{47-4} = 1.304$		
χ^2_0/dof	1.09	1.027	1.283		
$\kappa_{\rm phys}$	3.632 ± 0.037	3.423 ± 0.059	3.605 ± 0.067	3.71 ± 0.17	3.706
$\langle r_2^2\rangle_{\rm phys}$ (fm^2)	0.792 ± 0.011	0.61885 ± 0.0069	0.788 ± 0.015	0.690 ± 0.042	0.7754 ± 0.0080

0). Actually, the LQCD data constrain κ in the chiral limit more strongly than other quantities such as $\langle r_2^2\rangle$. Such a mismatch among errors drives the correlation towards -1. A fit with free c_4 obtains $c_4 = -0.600 \pm 0.031$ GeV^{-1}, which is close but below the Roy-Steiner value ($c_4^{\rm Roy} = -0.402 \pm 0.075$ GeV^{-1}).

- "ChPT": The theory agrees well with the data, even with better χ^2 than the dispersive approaches. in particular, LEC c_4 yields the prior value without causing tensions in the fit.

- "disp+ChPT": As can be seen in Fig. 3.10, this curve is almost identical to the "disp+c_6" one. We believe that the slight χ^2 increase as compared to the other schemes (see Table 3.4) has no deeper meaning, since the differences are negligible. More interesting is the behavior close to $Q^2 = 0$, where there are no LQCD data. The larger curvature of the "disp+c_6" and "disp+ChPT" theories increments the slope of the corresponding curves at $Q^2 = 0$ compared to "ChPT". This leads to the prediction of a larger radius as one can see in Tab. 3.4. At the physical point, the dispersive descriptions happen to be closer to the empirical Kelly parametrization than the ChPT curve, describing better both the trend of the empirical curve and the LQCD points beyond the Q^2 cut [see Fig. 3.9]. Finally, we regard the combined "disp+ChPT" scheme as the best one because it is more solid from the theoretical point of view if one aims at describing the FF up to rather large $Q^2 \approx 0.6\,$GeV^2.

The extracted LECs are reported in Tab. 3.5. The "ChPT" and "disp+ChPT" LEC values are different, as expected, since they are related to the renormalization performed. ChPT dimensional renormalization is not the same as the dispersive approach where the influence of

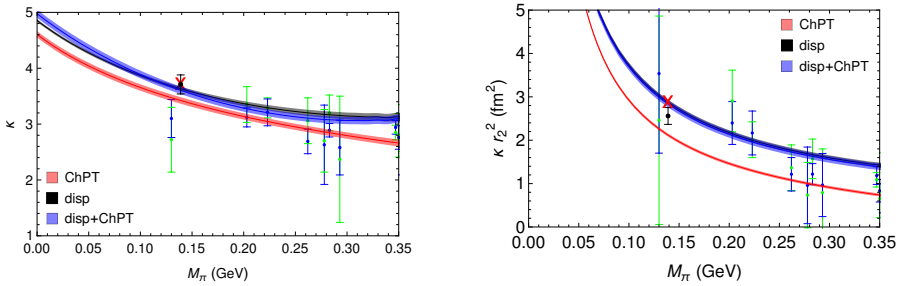

Figure 3.11: $F_2(Q^2 = 0) = \kappa$ (left) and its slope $\kappa\langle r_2^2\rangle$ (right) as a function of M_π. Red, black and blue bands are the results for the "ChPT", "disp+c_6", and "disp+ChPT" approaches, respectively. Band widths denote 1σ statistical errors. As in Fig. 3.4, LQCD points in green (summation method) and in blue (two-particle method) were obtained in Ref. [136] using the z-expansion to parametrize the Q^2 dependence of F_2. The black points are the values at the physical M_π obtained in Ref. [136] using Heavy Baryon ChPT to extrapolate LQCD results for F_2 in M_π and Q^2. The red crosses correspond to the experimental values quoted by PDG [5].

Table 3.5: Resulting values for the fitted LECs for $\mu = m_\rho$ and $\mu = m_N$ (purely dispersive scheme is μ independent).

	disp+c_6	ChPT ($\mu = m_\rho$)	disp+ChPT ($\mu = m_\rho$)
c_4 (GeV^{-1}) (with prior)	-0.600 ± 0.031	1.194 ± 0.045	-0.479 ± 0.072
c_6	-0.27 ± 0.12	4.606 ± 0.057	-0.88 ± 0.26
d_6 (GeV^{-2}) (fixed)	-	-0.385	0.416
e_{74} (GeV^{-3})	-	0.178 ± 0.042	-0.293 ± 0.075
e_{106} (GeV^{-3})	-	0.170 ± 0.050	-0.361 ± 0.054
χ^2/dof	1.110	1.027	1.304
		ChPT ($\mu = m_N$)	disp+ChPT ($\mu = m_N$)
c_4 (GeV^{-1}) (with prior)		1.194 ± 0.045	-0.477 ± 0.072
c_6		4.606 ± 0.057	-0.88 ± 0.26
d_6 (GeV^{-2}) (fixed)		-0.733	0.155
e_{74} (GeV^{-3})		0.252 ± 0.042	-0.140 ± 0.075
e_{106} (GeV^{-3})		0.151 ± 0.052	-0.4046 ± 0.060
χ^2/dof		1.027	1.291

intermediate energies is demoted by the Omnès function at the scale of the ρ-meson mass while the influence of larger energies is cut off by Λ. In any case, we see that the results do not depend strongly on μ. In fact, the overall ChPT loop contribution to the radius in the "disp+ChPT" scheme is negligible. Finally, we observe that in the "disp+ChPT" the fit yields a c_4 consistent with the Roy-Steiner one: $c_4 = -0.479 \pm 0.072\,\mathrm{GeV}^{-1}$, compared to $c_4^{\mathrm{Roy}} = -0.402 \pm 0.075\,\mathrm{GeV}^{-1}$.

We also report in Fig. 3.11 $F_2(0) = \kappa$ and the FF slope at the photon point, $\kappa\langle r_2^2\rangle$, as a function of M_π according to the fits for the three schemes. The "disp+c_6" and "disp+ChPT" schemes yield a $\kappa(M_\pi^{\mathrm{phys}})$ close to the experimental point. Our results are also in agreement with the HB extrapolation performed in Ref. [136]. However, the "ChPT" curve stays slightly below the other ones. For $\langle r_2^2\rangle$ the dispersive results at the physical M_π are compatible with the experimental value. Again the ChPT computation is slightly below, whereas the HB result lies in between.

3.4 Conclusions

We have analyzed the nucleon electromagnetic FFs, fundamental quantities which contain information on the nucleon structure and the underlying QCD dynamics. We calculated the isovector electromagnetic FFs combining dispersion theory and relativistic ChPT, both with explicit Δ baryons. In particular, we assess the M_π dependence: the non-analyticities are given by ChPT, while the dispersive integral reproduces the leading ChPT non-analyticities coming from the 2π cut.

In a second step, we have studied how well we describe the LQCD data from Ref. [136], considering three different approaches, namely (a) a purely dispersive approach that only implements the two-pion intermediate state; (b) plain ChPT, and (c) our combined scheme. For the Dirac FF, we realize that even the purely dispersive calculation is able to predict the FF well. This nonperturbative calculation provides sufficient curvature to the FF, accounting for the ρ-meson dynamics. Later, we have tested how well $\mathcal{O}(p^3)$ ChPT and the combined method describe the lattice results, fitting the d_6 LEC. We observe that the combined dispersive and ChPT scheme outperforms the ChPT fit and the purely dispersive approach. The calculation describes well the data for

$Q^2 < 0.6\,\mathrm{GeV}^2$ and all the LQCD ensembles, *i. e.,* $M_\pi \leq 350$ MeV. The value of $\langle r_1^2 \rangle_{\mathrm{phys}}^{\mathrm{disp+ChPT}} = 0.4838 \pm 0.0047$ fm^2 for the Dirac radius, is extracted from the combined computation, slightly below the experimental determination.

Next, we have considered the Pauli FF. Being a higher-order quantity, higher-order LECs were included. We account for LECs and ChPT $\not\Delta$ loops of $\mathcal{O}(p^4)$. This leads to a good description of the LQCD data by both the dispersive and the ChPT computations, in the same range of Q^2 and M_π as for the Dirac case. Combining both theories leads mainly to the same results as the purely dispersive description. Interestingly, both the dispersive and the combined results are quite close to the experimental parametrization, even beyond the $Q^2 = 0.6\,\mathrm{GeV}^2$ fit cut. Between these two schemes, we regard the combined version a more solid result from a theoretical perspective.

We have extracted $\kappa_{\mathrm{phys}}^{\mathrm{disp+ChPT}} = 3.605 \pm 0.067$, which is close to the empirical value, and $\langle r_2^2 \rangle_{\mathrm{phys}}^{\mathrm{disp+ChPT}} = 0.788 \pm 0.015$ fm^2, in agreement with experiment. In addition, the values of several LECs have been determined, which are useful for future calculations. For this first exploration of the combined scheme, we did not attempt to estimate the theoretical uncertainty. The reported errors are only statistical and therefore underestimated.

In summary, the isovector component of the Dirac and Pauli FFs are successfully described accounting not only for the Q^2, but also for the M_π dependence in the aforementioned range, obtaining a good agreement with lattice and experiment. We demonstrate that in the Dirac case the dispersively modified ChPT outperforms both the dispersive method where only the 2π channel is considered and the plain ChPT one. The modified ChPT improves the Q^2 description with a good parametrization of the M_π dependence.

Turning now to possible extensions of this work, a straightforward one would be to compute Δ form factors or $\Delta - N$ transition FFs. The objective would be to improve the Q^2 parametrization relative to plain ChPT while the M_π dependence is still described well. The Δ baryon represents complementary information on QCD, since they differ from nucleons just by the flip of one of the valence quark spins. It is also conceivable to address strangeness aspects, either along the lines of [153, 154] where only the two-pion channel is treated dispersively, or by a complete

three-flavor calculation. In this manner one would investigate the structure of hyperons as well as the strangeness content of the nucleon.

Regarding the pions and other mesons, it is well known that they dictate the strong interaction at low energies. However, their own structure is also an important subject. In this study we have obtained as a by-product the quark-mass dependence of the pion p-wave phase shift and the pion vector FF. We employ a Blatt-Weisskopf improved IAM and an extension of the Omnès function that account for corrections beyond the two-pion channel in the pion vector FF. Such effects are small, but observable at low energies. We predict well the lattice results for the M_π dependence of the mass of the ρ meson. Of course, this approach could be applied to other mesons and could be further scrutinized by comparison to phase shifts and meson FFs simulated in the lattice.

This relates to the self-consistency of the comparison to LQCD, in view of the lattice intrinsic systematics of continuum-limit and infinite-volume extrapolations. For a more consistent comparison of the effective theory to lattice data, it might be advisable to employ directly lattice input (instead of ChPT or IAM) for the quantities that enter our calculations (mesonic input and pion-nucleon scattering amplitudes).

Finally, with respect to the plain ChPT calculation of nucleon FFs, we have restricted ourselves mostly to $\mathcal{O}(p^3)$ calculations, at least when including the Δ. Full $\mathcal{O}(p^4)$ calculations in ChPT are in a development phase. Partly, this is due to the excessively increasing number of LECs. Moreover, the Δ role is not so clear at this order, as we have also seen in the present work where only a restriction of the two-Δ diagram to its pure $\mathcal{O}(p^3)$ part leads to a reasonable curvature for the Dirac FF. It is possible that the dispersive perspective adds some information in this matter, since the Δ is an elastic πN resonance. Therefore, one might think of the inclusion of *one* Δ line in a ChPT one-loop diagram as an important resummation of two- and (higher-)loop effects. However, the implementation of *two* Δ propagators constitutes already a three-loop effect of ordinary Δ-less ChPT. We have not investigated this and in particular the specific consequences for the power counting. In any case, what should be clear is that a reasonable $\mathcal{O}(p^4)$ calculation combined with dispersion theory should improve the precision of the calculations, and also help to estimate the theoretical uncertainty as we did in the study of the axial FF.

Chapter 4

The Λ_c semileptonic decay with new physics

4.1 Introduction

Here we analyze the impact of possible new physics (NP) signals in the Λ_c semileptonic decay as motivated in Sec. 1.4. In this work we use the general framework to study any hadron semileptonic decay for including NP contributions introduced in Ref. [69]. The scheme is based on the Standard Model Effective Field Theory (SMEFT) of Refs. [62, 161], and allows to analyze any decay driven by a $q \to q'\, l\, \bar{\nu}_l$ quark level CC process involving massless left-handed neutrinos. We analyze CP-even (real Wilson coefficients) scalar, pseudo-scalar, right-handed and tensor NP terms, as well as corrections to the SM left contribution. The hadronic inputcan be parametrized in terms of the hadronic structure functions ($W's$), given by the matrix elements of the operators involved. The structure functions are written in terms of the transition form factors, and depend on the masses of the initial and final particles and on the invariant mass of the outgoing lepton pair. The specific expressions needed are detailed in App. D.2 including formally complex (CP-violating) Wilson coefficients.

In this work, we will focus on the μ channel and disregard the e one. This is in line with the assumption of the standard flavor hierarchy, in which the Wilson coefficient is larger the heavier the lepton. In addition, the (pseudo)scalar and tensor NP contributions are $\mathcal{O}(m_\ell)$ suppressed, what complicates their detection in the e channel.

4.2 The $\Lambda_c \to \Lambda\, \ell^+ \nu_\ell$ weak decay including new physics

4.2.1 Observables

For the $\Lambda_c^+(p) \to \Lambda(p')\, \ell^+(k')\, \nu_l(k)$ the double-differential branching ratio $\mathcal{B} \equiv \Gamma/\Gamma_{\rm tot}$, in terms of $q^2 = (k+k')^2$ and the angle θ between the Λ and ℓ^+ three-momenta in the leptonic rest frame, where $q = (\sqrt{q^2}, \vec{0})$, can be cast as [162, 64, 69]

$$\frac{\mathrm{d}^2\mathcal{B}}{\mathrm{d}q^2 \mathrm{d}\cos\theta} = |V_{cs}|^2 \left[c_0^\ell(q^2) + c_1^\ell(q^2)\cos\theta + c_2^\ell(q^2)\cos^2\theta\right] , \tag{4.1}$$

where $|V_{cs}|^2$ has been factorized for convenience. The full Λ_c width Λ_c width $\Gamma_{\rm tot} = (3.252 \pm 0.050)\cdot 10^{-12}$ GeV has been obtained from its mean live $\tau = (202.4 \pm 3.1) 10^{-15}$ s [90]. Functions $c_i(q^2)$ entirely characterize the decay and can be extracted from experimentally measurable quantities. For example, as shown in Eqs. (D.17)-(D.19), they can be obtained from the single-differential width $\mathrm{d}\Gamma/\mathrm{d}q^2$, the forward-backward asymmetry, $\mathcal{A}_{\rm FB}$, and the convexity, $\mathcal{A}_{\pi/3}$. Our analysis of NP contributions is performed in terms of $c_{0-2}^\ell(q^2)$. For this purpose we take advantage of the general framework developed in Ref. [69] for the study of hadron semileptonic decays in presence of NP. Appendix D.2 discloses how the formalism of Ref. [69] is adapted to the present case.

In order to reduce the theoretical and experimental uncertainties, it is useful to consider lepton flavor universality (LFU) ratios. In our case

$$R_i \equiv \frac{c_i(m_\mu, q^2, \epsilon^\mu)}{c_i(m_e, q^2, \epsilon^e)} = \frac{c_i^\mu(q^2, \epsilon^\mu)}{c_i^{\rm eSM}(q^2)} + \mathcal{O}(\epsilon^e) \underbrace{\simeq}_{\text{if } \epsilon^e \ll \epsilon^\mu} 1 + \mathcal{O}(m_\mu^2) + \mathcal{O}(\epsilon^\mu)\,. \tag{4.2}$$

The common assumption $\epsilon^e \ll \epsilon^\mu$ arises, for example, in many NP models which explain the fermion mass hierarchy [163, 164]. In these ratios, not only $V_{\rm CKM}$ cancels out. An important advantage resides on the fact that in the SM the deviation from unity enters at $\mathcal{O}(m_\mu^2)$ (recall that $m_\mu \simeq 105.7$ MeV) and so does the SM uncertainty. There is hence a significant improvement in the sensitivity to NP in the μ channel, $\mathcal{O}(\epsilon^\mu)$.

4.2.2 QCD input

Functions $c_{0-2}(q^2)$ depend on the NP Wilson coefficients introduced above and om purely hadronic structure functions which are themselves given in terms of transition form factors (see Appendix E of Ref. [69]). For the $\Lambda_c \to \Lambda$ transition, the relevant form factors have been defined in Eq. (1.92) and add up to 12: scalar and pseudoscalar $F_{S,P}$, vector $F_{1,2,3}$, axial-vector $G_{1,2,3}$ and tensor $T_{1,2,3,4}$. As detailed in the introduction (Sec. 1.4.2), the vector and axial form factors have been calculated in the lattice [65]. Using these form factors, in agreement with Ref. [65] we obtain:

$$\begin{aligned} \frac{\Gamma(\Lambda_c \to \Lambda e^+ \nu_e)}{|V_{cs}|^2} &= 0.2008(71)^{\rm LQCD}_{\rm stat}\ {\rm ps}^{-1}, \\ \frac{\Gamma(\Lambda_c \to \Lambda \mu^+ \nu_\mu)}{|V_{cs}|^2} &= 0.1945(69)^{\rm LQCD}_{\rm stat}\ {\rm ps}^{-1}, \end{aligned} \tag{4.3}$$

yielding the lepton flavor universality (LFU) ratio

$$R^{\rm SM} = \frac{\Gamma(\Lambda_c \to \Lambda \mu^+ \nu_\mu)}{\Gamma(\Lambda_c \to \Lambda e^+ \nu_e)} = 0.96884(61)^{\rm LQCD}_{\rm stat}\ . \tag{4.4}$$

We notice the difference between this SM ratio and the value of 0.974(1) reported by Ref. [165] although both are consistent with the experimental result of $R^{\rm exp} = 0.98(5)_{\rm stat}(3)_{\rm syst}$ of Ref. [58] owing to its large error.

Ideally one would also take the rest of form factors from the lattice, relying in this way on an accurate parametrization of the QCD structure. However this input is not yet available. Therefore, we express the scalar, pseudoscalar and tensor form factors in terms of the vector and axial ones employing approximations based on the fact that the charm quark mass is considerably larger than the masses of the light ones: $m_c \gg m_{s,u,d}$ (and higher than the QCD scale Λ_χ). There is some freedom in the way one exploits this condition. The resulting differences are used to estimate the systematic uncertainty of the approximations. As discussed in the Sec. 1.4.2 of the introduction, HQSS for a heavy-light quark transition implies that at leading order in $1/m_c$ all possible form factors can be given in terms of only two independent functions. For this purpose we choose either $F_{1,2}$ or $G_{1,2}$ ($F_3 = G_3 = 0$ in the HQSS limit). We refer to these prescriptions as HQSSV and HQSSA respectively. A less stringent choice arises from the assumption that the c quark is on-shell. Then, in the $m_c/M \to 1$ limit, one obtains a consistent set of equations which allow to

relate all (pseudo)scalar and tensor form factors to $F_{1,2,3}$ and $G_{1,2,3}$. This solution, labeled OSHQ (for On-Shell Heavy Quark), is consistent with HQSS in the $F_3 = G_3 = 0$ limit. The three form factors corresponding to the three prescriptions are given in Eqs.(1.103), (1.104) and (1.99) of Sec. 1.4.2.

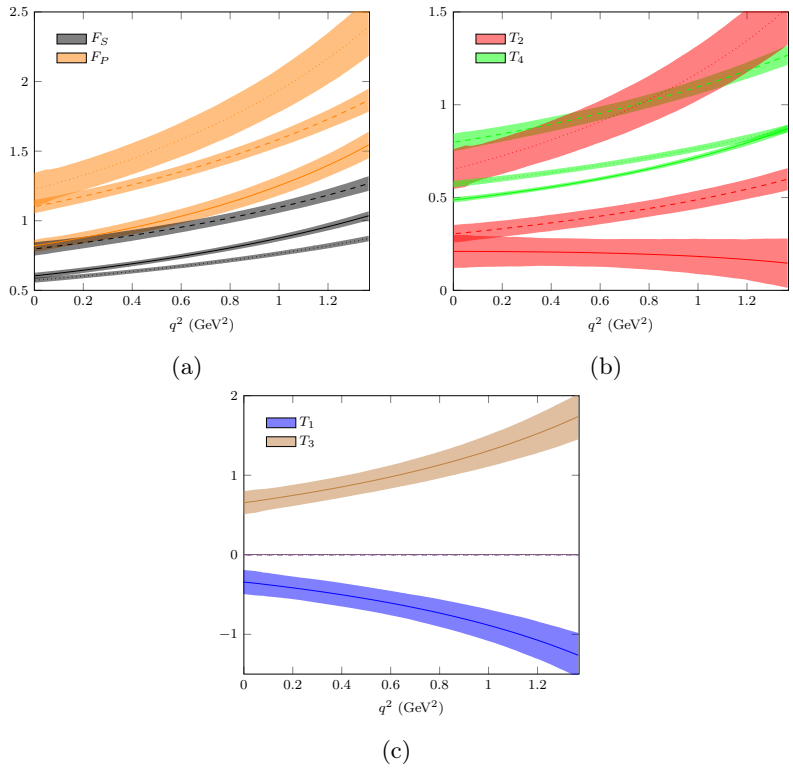

Figure 4.1: Scalar, pseudoscalar and tensor form factors obtained from the vector and axial ones using HQSS approximations. The continuous, dashed and dotted lines are obtained with OSHQ, HQSSV and HQSSA prescriptions, respectively. Notice that $T_1 = T_3 = 0$ within HQSSV and HQSSA.

Figure 4.1 displays $F_{P,S}$ and T_{1-4} in terms of F_{1-3} and G_{1-3} from LQCD [65] in the q^2 range of relevance for the Λ_c decay using the three prescriptions. In the following, our theoretical error bands for each of these form factors cover the results of all three prescriptions including the LQCD errors given by the bands in Fig. 4.1. This defines a conservative estimate of the QCD uncertainty.

4.2.3 New physics contributions

In order to analyze individual new physics contributions to c_{0-3}^{ℓ} we introduce

$$c_i^{\ell}(q^2, \epsilon_X^{\ell}) \equiv c_i^{\ell}(q^2, \epsilon_X^{\ell}, \epsilon_{Y\neq X}^{\ell} = 0)\,, \qquad X, Y = L, R, S, P, T\,,\; i = 0 - 2\,, \tag{4.5}$$

which can be cast as

$$\begin{aligned} c_i(\epsilon_X) &= c_i^{\rm SM} + \epsilon_X c_i^{X\rm l} + \epsilon_X^2 c_i^{X\rm q} \\ &= c_i^{\rm SM} + \epsilon_X \left(c_i^{X\rm l} + \epsilon_X c_i^{X\rm q} \right) \equiv c_i^{\rm SM} + \epsilon_X c_i^{X}(\epsilon_X)\,. \end{aligned} \tag{4.6}$$

Lepton index and q^2 dependence are implicit. The NP part has terms linear and quadratic in ϵ_X. The leading linear part $\epsilon_X c_i^{X\rm l}$ arises from the interference between SM and NP terms in the decay amplitude squared. On the other hand, one has to keep in mind that the subleading $\epsilon_X^2 c_i^{X\rm q}$ provide an incomplete account of the $\mathcal{O}(\epsilon^2)$ order. It also receives contributions from the interference between the SM and terms from a higher order (ϵ^2) SMEFT computation, including additional Wilson coefficients [166].

The structure of the NP perturbation of the SM values is therefore encoded in $c_i^X(\epsilon_X)$, which are depicted in Fig. 4.2 for $\ell = \mu$. Propagated QCD uncertainties from LQCD and HQSS prescriptions discussed in Sec. 4.2.2 give rise to the bands. The dashed lines denote the linear $c_i^{X\rm l}$ terms that contribute at $\mathcal{O}(1/\Lambda^2)$. Although for $X = S, P, T$ these interference terms are suppressed by the muon mass, the tensor contribution turns out to be comparable or larger than $X = L, R$ ones for c_0 and c_1 observables.

To account for the residual ϵ_X dependence of $c_i^X(\epsilon_X)$, we choose as indicative the central ϵ_X values extracted in Ref. [162] from leptonic and semileptonic decays of pseudoscalar mesons. These ϵ_X values and the correspondence with the notation of Ref. [162] are given in Appendix D.3. The smallness of the quadratic terms is apparent from the difference between the dashed and the central solid lines, which can hardly be discerned except for $c_{0,2}^T$. Indeed, $\epsilon_T c_0^{T\rm q}$ is relatively large at a typical $\epsilon_T = 1.2 \times 10^{-2}$. The tensor contribution to c_2 is purely quadratic ($c_2^{T\rm l} \equiv 0$) and quite large. The central value of ϵ_P is one order of magnitude lower than the rest of the Wilson coefficients, but we have verified that $\epsilon_P c_0^{P\rm q}$ remains negligible for an $\epsilon_P \sim \mathcal{O}(10^{-2})$; c_0 is the only observable with a quadratic scalar and pseudoscalar contribution, $c_{1,2}^{S\rm q}$ and $c_{1,2}^{P\rm q}$ are exactly zero.

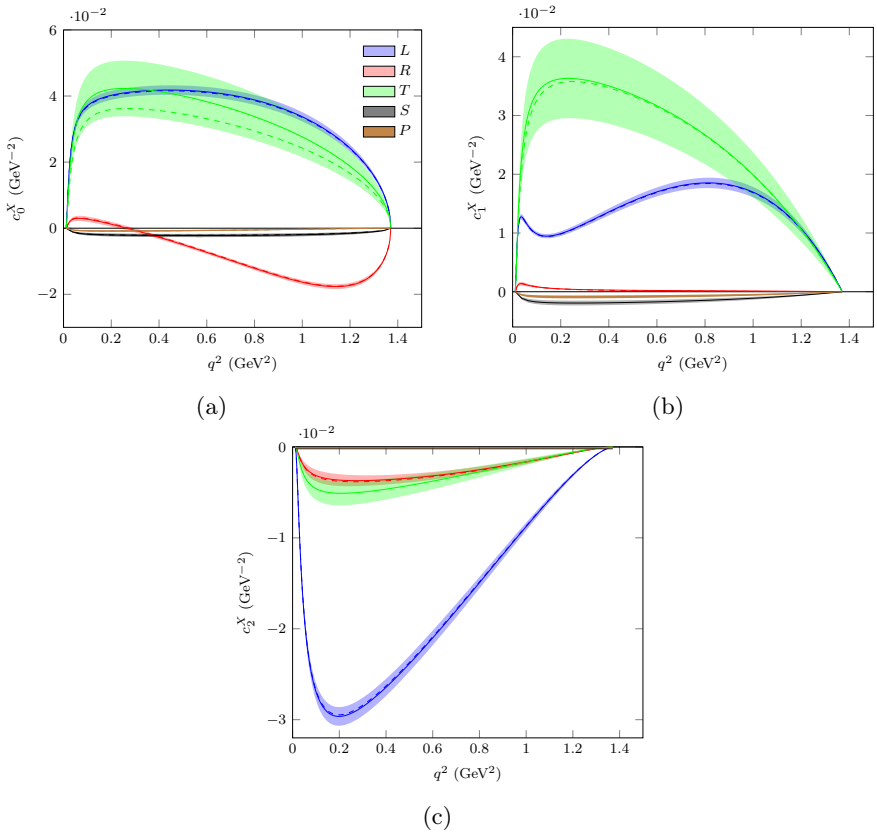

Figure 4.2: q^2 dependence of the NP individual perturbations $c_i^X = c_i^{X\mathrm{l}} + \epsilon_X c_i^{X\mathrm{q}}$, Eq. (4.6) ($i = 0, 1, 2$ from left to right). Colors denote the type of interaction $X = L$ (blue), R (red), S (black), P (brown) and T (green). Wilson coefficients are set to the central values of Ref. [162] (see also Appendix D.3). The dashed lines originate from the linear terms $c_i^{X\mathrm{l}}$. The bands represent the QCD uncertainty from the transition form factors.

The plots of Fig. 4.2 show the magnitude and shape of the individual contributions. They allow us to identify the NP perturbations that are in principle more easily revealed in an experiment. The sensitivity to these NP contributions is carefully studied in Sect. 4.3. To assess the results of Fig. 4.2 from this perspective it is useful to bear in mind that $c_i^{\mathrm{SM}} = c_i^{L\mathrm{l}}/2$. For c_0 [Fig. 4.2 (a)], tensor and left-handed contributions prevail, while the right-handed one is also sizable and changes sign. In

c_1 [Fig. 4.2 (b)] the tensor interaction is the largest, peaking in the q^2 region where the SM has a local minimum. Since the SM relative error is quite constant in q^2, a minimum in the SM magnitude corresponds to a minimum in the SM error (see the width of the c_1^L band). Therefore one can expect a good sensitivity to tensor NP at low q^2 in c_1. Finally, in c_2 [Fig 4.2 (c)] the left-handed term dominates, having a maximum in its absolute value at low q^2. The suppression of all contributions with respect to the left-handed one implies that the latter is the only potentially relevant NP mechanism in c_2. It is also worth noting that scalar and pseudoscalar contributions are small in $c_{0,1}$ and exactly zero in c_2.

4.2.4 Phenomenological constraints

In the first row of Fig. 4.4 the c_i values allowed by the aforementioned phenomenological constraints to the Wilsons from Ref. [162] for the μ channel are depicted. We have varied the ϵ_X values in the given ranges approximating their distributions by Gaussians and neglecting correlations. The LQCD errors of the vector form factors have been propagated in the same way, while all three prescriptions of the HQSS form factors in $c_i^{S,P,T}$ are covered by the band (in this case the HQSSV choice practically covers the bands of the other two prescriptions). Given that the Wilsons studied are compatible with zero, the SM and NP band would overlap, even if no additional uncertainty would have been included. However one can already see where the possible NP contribution is more prominent. Fig. 4.4 (b) reflects that the SM local minimum is a good place to look for a NP (tensor) signal: one can see that in the local minimum the central values are more separated than anywhere else.

Under the assumption of the standard hierarchy, $\epsilon_X^\mu \gg \epsilon_X^e$, one would expect to observe deviations from the SM only in the muon channel. The comparison of the differential width in the SM scenario with LQCD input to the BESIII data of Refs. [167, 58] shown in Fig. 4.3 reveals tensions not only in the $\ell = \mu$ channel but also in the $\ell = e$ one. Moreover, the SM fits performed in Refs. [167] produce form factors that clearly differ from those of Ref. [65], as can be seen in Fig. 3 of Ref. [167]. We have also obtained that this tension cannot be accommodated by natural $\epsilon_X^e \neq 0$. Therefore, the extraction of allowed ranges on e_X^μ under the assumption of $\epsilon^e \ll \epsilon^\mu$ directly from the present data on $\Lambda_c \to \Lambda \mu^+ \nu_\mu$ [58] would be

undermined by these discrepancies in the $\ell = e$ channel that cast doubts about the QCD input.

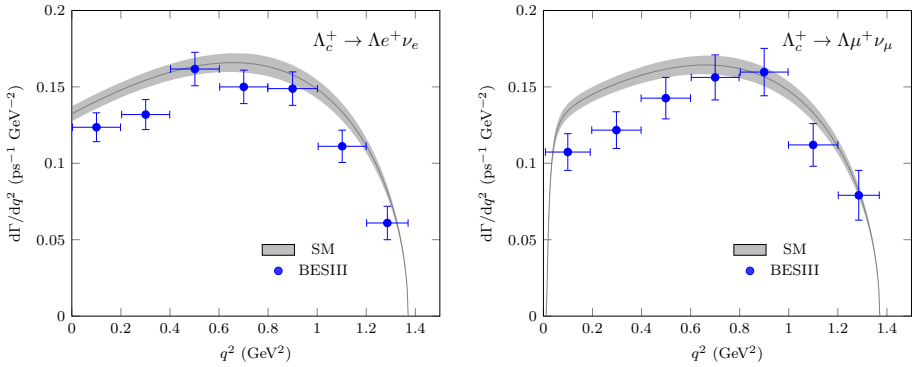

Figure 4.3: Differential decay width for $\Lambda_c^+ \to \Lambda e^+ \nu_e$ (left panel) and $\Lambda_c^+ \to \Lambda \mu^+ \nu_\mu$ (right panel). The grey band is the SM prediction with 1σ errors from the LQCD form factors (neglecting 1% error in V_{cs}). The blue points are the experimental data from BESIII [167, 58].

Turning now to the LFU ratios, they are defined according to the $\cos\theta$ separation in c_i, $i = 0 - 2$:

$$R_i(\epsilon_X^\mu) = \frac{c_i(\Lambda_c \to \Lambda \mu^+ \nu_\mu, \epsilon_X^\mu)}{c_i^{\rm SM}(\Lambda_c \to \Lambda e^+ \nu_e)} \ , \tag{4.7}$$

and depend on all ϵ_X^μ and implicitly on q^2. They are shown in the second row of Fig. 4.4 with the values of ϵ_X^μ ranging the phenomenological constraints from Ref. [162]. The case of all Wilsons set to zero, *i. e.* the Standard Model, is also depicted. In fact, the reduction of the SM uncertainty is evident here: the SM error bands become negligible compared with the ϵ_X^μ range of values. This provides a much higher sensitivity to NP.

4.3 Sensitivity to new physics in the μ channel: LFU ratios

We have posed ourselves the question of how large should be a new physics signal in order to be classified as such in this framework. We focus on the μ channel, assuming $\epsilon^\mu \gg \epsilon^e \simeq 0$ and studying ratios to

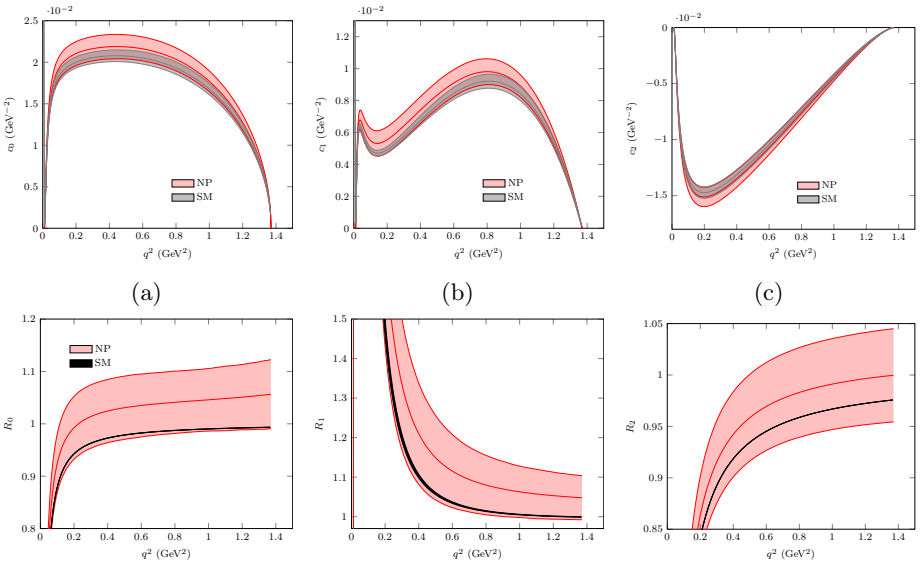

Figure 4.4: q^2 dependence of c_i^μ and LFU ratios R_i in the SM and in presence of NP (with the empirical values obtained in Ref. [162]). The SM bands (grey) include errors in the LQCD vector form factors. The NP bands (red) arise from both the uncertainties in all form factors and in the Wilson coefficients.

reduce the uncertainty. We define the signals to which we are sensitive as the ones that do not overlap with the SM prediction including the errors. In other words, if a Wilson coefficient had a given true value, ϵ_X, we would be sensitive to it at a certain q^2 only if its magnitude is large enough to completely separate the one-σ NP band from the SM one. This condition has some degree of arbitrariness and would still be insufficient to claim a discovery in an experiment but serves the purpose of getting an idea of the discovery potential for each of the LFU ratios, R_i, as functions of q^2. We define ϵ_X^{sens} as the minimum ϵ_X in magnitude which satisfies this condition and calculate their values, one by one, setting the rest of the Wilson coefficients to zero. Recalling the notation of Eq. (4.7) we define ϵ_X^{sens} as the one that satisfies

$$\left|R_i(\epsilon_X) - R_i^{\text{SM}}\right| > \Delta R_i(\epsilon_X) + \Delta R_i^{\text{SM}} \tag{4.8}$$

with a minimal $|\epsilon_X|$. Here ΔR_i^{SM} and $\Delta R_i(\epsilon_X)$ denote the one-σ errors of R_i^{SM} and $R_i(\epsilon_X)$, which includes NP. It is clear that the larger the ϵ_X,

the more promising the observable would be to detect a given NP signal. However, the SMEFT calculation has a worse convergence for larger ϵ_X. We take this into account by introducing a SMEFT truncation error within $\Delta R_i(\epsilon_X)$, which is defined below.

We explore the condition of Eq. (4.8) for positive and negative ϵ_X separately. In general we do not obtain the same absolute value in both cases due to quadratic corrections. Quadratic terms in SMEFT are briefly discussed in Ref. [168], while the theoretical uncertainty of SMEFT is addressed in Sect. 2.7.6 of Ref. [169]. According to this reference, to properly account for the truncation error one should calculate to one-loop order. It is also argued that an estimate can be given without such a computation, but including Wilson coefficients of the dimension-eight Lagrangian (Eq. (2.79) therein). Such studies are beyond the scope of the present work. We content ourselves with a simpler approach, relying on a common truncation error estimate given by the difference between linearization and quadratization of the matrix element squared, and define the following uncertainty for c_i (Eq. (4.6)),

$$\Delta c_i^{\mathrm{SMEFT}}(\epsilon_X) = \epsilon_X^2 \max\{|c_i^{SM}|, |c_i^{X\mathrm{l}}|, |c_i^{X\mathrm{q}}|\} \ . \tag{4.9}$$

It estimates the size of the unaccounted $\mathcal{O}(\epsilon^2)$ contributions, only with information from $\mathcal{L}_{\mathrm{SM}}$ and $\mathcal{L}_6$. To simplify the notation, index $\ell = \mu$ has been omitted throughout this section. Correspondingly,

$$\Delta R_i^{\mathrm{SMEFT}}(\epsilon_X) = \frac{\Delta c_i^{\mathrm{SMEFT}}(\epsilon_X)}{c_i^{e\mathrm{SM}}} \ . \tag{4.10}$$

We do not claim this is a very precise truncation error determination, but we retain it clear and conservative.

In order to obtain $\epsilon_X^{\mathrm{sens}}$ from Eq. (4.8) we sum in quadratures the error propagated from the LQCD vector form factors, $\Delta R_i^{\mathrm{LQCD}}$, with the truncation one, yielding

$$(\Delta R_i(\epsilon_X))^2 = \left(\Delta R_i^{\mathrm{LQCD}}(\epsilon_X)\right)^2 + \left(\Delta R_i^{\mathrm{SMEFT}}(\epsilon_X)\right)^2 \ . \tag{4.11}$$

In addition, the HQSS uncertainty in $c_i^{S,P,T}$ is taken into account by covering all three versions of the form factors as in Sect. 4.2.4. In this case, this reduces to taking the least favorable choice, meaning the HQSS prescription associated with the minimum perturbation to the SM and therefore maximizing $|\epsilon_X^{\mathrm{sens}}|$.

First of all, we study the ratio of integrated widths, *i. e.* we introduce NP contributions in the numerator of Eq. (4.4). In this observable, $|\epsilon_L^{\text{sens}}| = 6.3 \times 10^{-4}$, $|\epsilon_R^{\text{sens}}| = 2.1 \times 10^{-3}$, $|\epsilon_T^{\text{sens}}| = 8.0 \times 10^{-4}$, $|\epsilon_S^{\text{sens}}| = 8.9 \times 10^{-3}$, but we are not sensitive to ϵ_P. This is a very good sensitivity, beyond the multi-TeV scale. Indeed, the ϵ value corresponding approximately to a NP scale Λ of 1 TeV is estimated by a naive power counting to be $|\epsilon| = v^2/\Lambda^2 \simeq 0.0625$, with $v \approx 250$ GeV (see Sec. 2.1 of Ref. [169]).

Next, we analyze the LFU ratios defined in Eq. (4.7). The first thing to notice is that in the SM R_2 is independent of the form factors. Therefore $\Delta R_2^{\text{SM}} = 0$. Applying the criterion of Eq. (4.8), we are sensitive to arbitrarily small NP $\epsilon_{L,R,T}$, which are the ones that contribute to c_2. This has to be understood as a result neglecting $\mathcal{O}(\epsilon^2)$ and SM one loop corrections (and disregarding the experimental uncertainty). Nevertheless, this result clearly indicates that R_2 is a very sensitive observable. The drawback is that it might be difficult to measure, because c_2 is related to the angular asymmetry $\mathcal{A}_{\pi/3}$, Eq. (D.19).

We have also observed that R_0 is more sensitive than R_1. In consequence we put the focus on R_0 in the following, which is dominated by the ratio of decay widths. In Fig. 4.5 we study the sensitivity of R_0 to NP signals of different chirality, ϵ_X, as a function of q^2. The $\epsilon_X^{\text{sens}}(q^2)$ are reported; they set the boundaries of the sensitive to ϵ_X regions. Red lines denote the Wilson coefficient values corresponding to a NP scale of 2 (dashed) and 10 TeV (solid). The plots reveal an excellent sensitivity to ϵ_L and ϵ_T (upper panels). For ϵ_R, the sensitivity is higher in the region of medium to high q^2 (lower left panel). We are also sensitive to quite small ϵ_S (lower right panel). The only current to which this ratio is not sensitive is the pseudoscalar one. In this case the ϵ_P signal is too small to be discerned from the SM, taking into account the $\mathcal{O}(\epsilon_P^2)$ theoretical error.

Finally, from our analysis we conclude that the main obstacle to resolve a NP signal from the theoretical point of view is the LQCD error of the (axial)vector form factors, prevailing over the HQSS errors that accompany some NP contributions, and the SMEFT uncertainty, which can be sizable for relatively large ϵ_X.

One may also wonder about the experimental uncertainty and therefore about the real sensitivity in practice. At the present day the exper-

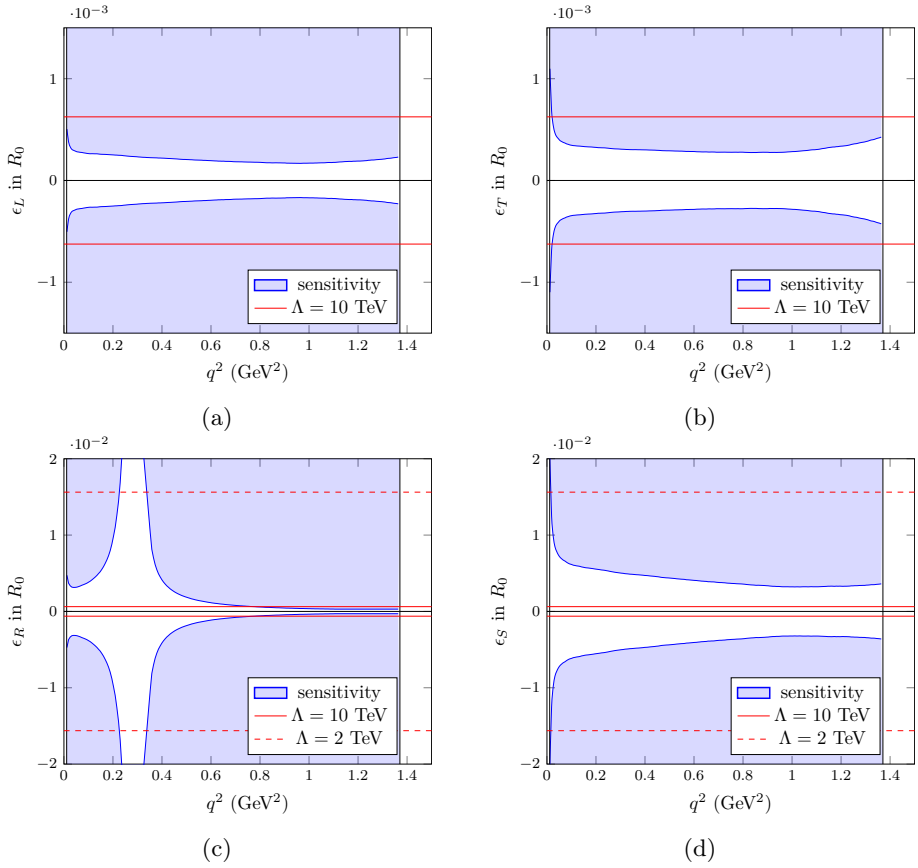

Figure 4.5: The q^2 dependence of the ϵ_X to which we are sensitive in R_0 is depicted (light blue regions). The blue line represents ϵ_X^{sens} defined in Eq. (4.8). Currents of chirality L, T, R and S are studied in (a), (b), (c) and (d) respectively. Notice that the axis scale changes by row. The red continuous (dashed) lines represent the Wilson value for a $\Lambda = 10$ TeV ($\Lambda = 2$ TeV) in the naive power counting. Black vertical lines delimit the phase space. In R_0 We are sensitive to Wilsons smaller than the central values obtained by Ref. [162].

imental error is much larger than the theoretical one. To illustrate this, we study the integrated ratio R (defined in Eq. (4.4) for the SM case). For instance, to be sensitive to an $\epsilon_L = 1.2 \times 10^{-2}$ as the one given by the central value extracted in Ref. [162] one would need the experimen-

tal error to be reduced to the 10% of its current size[1]. As discussed in Sec. 4.2.4, the tensions that arise in the description of $\Lambda_c \to \Lambda e^+ \nu_e$ with SM LQCD input compromise the extraction of ϵ_X^μ from $\Lambda_c \to \Lambda \mu^+ \nu_\mu$ data alone. On the other hand, recalling the aforementioned $\mathcal{O}(m_\mu^2)$ suppression of the form factor uncertainty in the SM contribution to LFU ratios, we find that these ratios are more reliable in order to look for NP deviations, because systematic differences in the SM form factor largely cancel out. In Fig. 4.6 we report the LFU ratio for the differential width, defined in analogy with Eq. (4.7) as

$$R_\Gamma(\epsilon_X^\mu) = \frac{d\Gamma/dq^2(\Lambda_c \to \Lambda \mu^+ \nu_\mu, \epsilon_X^\mu)}{d\Gamma/dq^{2\,\mathrm{SM}}(\Lambda_c \to \Lambda e^+ \nu_e)} \,, \tag{4.12}$$

compared to the corresponding experimental result from BESIII [58]. The theoretical result carries a black 1σ SM band from LQCD and a red one accounting for the allowed range in the Wilson coefficients from Ref. [162]. In line with the previous comments about the ratio of integrated widths, the present experimental uncertainty is still insufficient to put competitive bounds on the ϵ_μ Wilson coefficients.

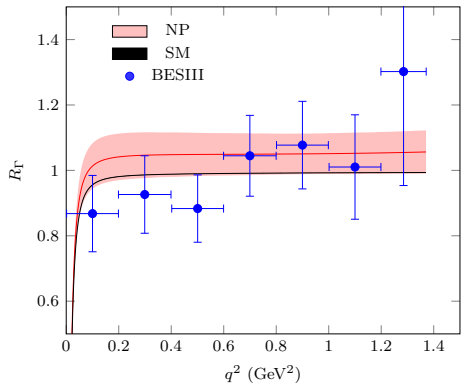

Figure 4.6: μ/e LFU ratio for the differential decay width $\mathrm{d}\Gamma/\mathrm{d}q^2$ as a function of q^2. The black band denotes the SM prediction from 1σ errors in the LQCD form factors. The red band corresponds to the inclusion of NP with the empirical bounds obtained in Ref. [162]. The blue points are the experimental data from BESIII [58].

[1]Recall that we set all the $\epsilon_{X \neq L} = 0$ and account for the theoretical uncertainties.

4.4 Sensitivity to new physics in the μ channel: c_i^μ functions

Here we report an analysis similar to the one performed for LFU ratios but at the level of the $c_i^\mu(q^2)$ functions. It is free of assumptions on the flavor hierarchy of Wilson coefficients. Furthermore, $c_i^\mu(q^2)$ would not receive any contribution from the statistical experimental error in the $\Lambda_c \to \Lambda e^+ \nu_e$ decay. Unfortunately, the sensitivity is considerably reduced in comparison with the one expected for the LFU ratios explored in the previous section. We present only the cases where the NP perturbation was found to be relatively large in Sec. 4.2.3 (see Fig. 4.2). In consequence, we do not take into account (pseudo)scalar terms.

The left-handed contributions are studied in Figures 4.7 (a)-(c). In this case the truncation error is governed by $\epsilon_L^2 c_i^{Ll} = 2\epsilon_L^2 c_i^{\rm SM}$ and the convergence is good, from the point of view of the uncertainty that we have defined. The error is dominated by the one of the LQCD vector form factors, even at high ϵ_L. The plots show that the study of c_{0-2} for the present process is mostly insensitive to the ϵ_L range constrained by pseudoscalar meson decays in Ref. [162].

The right-handed contributions are in general modest, being more prominent in c_0 than in $c_{1,2}$. We show the sensitivity to ϵ_R in c_0 in Fig. 4.7 (d). It is much poorer than in the other displayed cases. Indeed this observable is only sensitive to quite low Λ (below the TeV) in the naive power counting estimation[2]. At low q^2, c_0 is not sensitive to ϵ_R at all. In other words, the condition (4.8) is not satisfied. Actually, due to the small magnitude of c_0^R at low q^2, ϵ_R needs to be large to be distinguishable. However, at such values of ϵ_R the truncation error becomes large enough to make Eq. (4.8) impossible to satisfy. The difference between positive and negative $\epsilon_R^{\rm sens}$ is caused by the $\epsilon_R^2 c_0^{R\rm q}$ term, which is important at high ϵ_R. A similar scenario is encountered for the tensor contribution to c_0 studied in Fig. 4.7 (e). Now the decay under study is not sensitive to negative ϵ_T. This is due to the twofold impact of the quadratic term in Eq. (4.8), which is relatively large: not only does it notably increase $\Delta c_0(\epsilon_T)$, it also conspires to cancel the linear contribution to $c_0(\epsilon_T)$, having the opposite sign. As argued in the previous section, the quadratic contribution is not complete. Hence, the fact that

[2] Approaching the electroweak scale, less new physics models survive that have not been ruled out empirically.

$e^2_{R,T}$ are large implies that our sensitivity estimates are less solid in these cases. This is partially accounted by the truncation error. In all the other c_i^X analyzed in Fig. 4.7, $\Delta c_i^{\rm SMEFT}$ is negligible for low values of ϵ_X ($\epsilon_X \leq 0.1$).

The most promising analysis turns out to be the study of ϵ_T in c_1, Fig. 4.7 (f). As anticipated in Sec. 4.2.3, the maximum in the tensor perturbation coincides with a SM minimum (Fig. 4.2 (b)). This leads to a good sensitivity in the low-medium q^2 region as can be seen in Fig. 4.7 (f). The quadratic coefficient $c_1^{T\rm q}$ is small and the truncation error is negligible (it is given by $\epsilon_T^2 c_1^{T\rm l}$). The critical uncertainty in this scenario is actually the one of the LQCD vector form factors $\Delta c_1^{\rm LQCD}$. In this case, the $\Lambda_c \to \Lambda \mu^+ \nu_\mu$ decay is sensitive to a part of the band allowed by pseudoscalar meson decays [162] without resorting to ratios. Finally, the tensor contribution to c_2 is not discussed because there is no linear term in ϵ_T.

As a final remark, we stress that the key uncertainties to asses in order to gain sensitivity to NP with the Λ_c semileptonic decay are the ones of the LQCD vector form factors because they appear in the leading SM term. In the case of the tensor contribution to c_0, this error competes with the truncation one. In this sense, a more precise estimate of the SMEFT uncertainty, taking into account all terms at $\mathcal{O}(1/\Lambda^4)$ would be very useful as well. In addition, it is clear that a reliable determination of the truncation error would provide more consistency to the analysis in general, including the left and right-handed contributions. In the tensor term the HQSS uncertainty is not so critical, since it is part of the NP correction (hence it is multiplied by ϵ_T) and is therefore small.

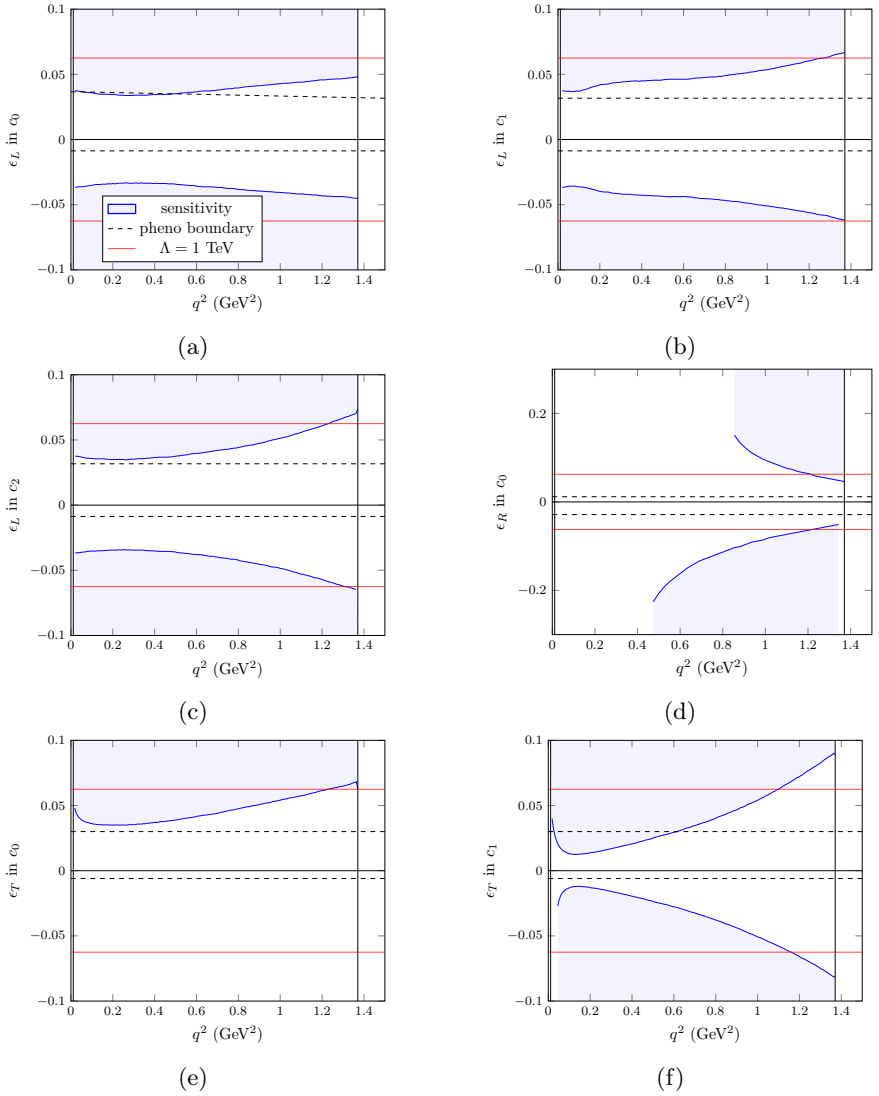

Figure 4.7: The sensitivity regions to ϵ_X in selected c_i is represented by the light blue regions. The solid blue line denotes ϵ_X^{sens} defined in Eq. (4.8). Panels (a), (b) and (c) show the sensitivity to ϵ_L in c_0, c_1 and c_2, respectively. The (d) panel reports the poor sensitivity to the right-handed contribution in c_0 (note the different scale). The (e) and (f) panels display the sensitivity to ϵ_T in c_0 and c_1 respectively. The dashed lines encompass the allowed region obtained in Ref. [162] from pseudoscalar meson decays. The red lines represent the values of Wilson coefficients for a $\Lambda = 1$ TeV in the naive power counting. Black vertical lines delimit the phase space.

4.5 Conclusions and outlook

We have studied the $\Lambda_c \to \Lambda \ell^+ \nu_\ell$ decay, investigating the impact of new physics currents in the $\ell = \mu$ channel. To accomplish this task, an effective Hamiltonian for $c \to s\ell^+\nu_\ell$, based on SMEFT has been employed. We have also relied on the LQCD results for the axial and vector $\Lambda_c \to \Lambda$ form factors obtained in Ref. [65]. The form factors required to describe the $\Lambda_c \to \Lambda$ transitions driven by scalar, pseudoscalar and tensor operators have been expressed in terms of the axial and vector ones by taking advantage of the large c-quark mass. Differences arising from alternative approximations to implement this connection among form factors are treated as a theoretical uncertainty.

The NP analyses is performed in terms of the $c_i(q^2)$ functions that drive the dependence on the angle between the Λ and the μ^+ in the leptonic rest frame. We have first obtained the q^2 shapes of the NP contributions to c_i, with their QCD uncertainty bands. Lepton flavor universality ratios received special attention. In the first place, owing to the LQCD form factor input, a SM ratio $\Gamma(\Lambda_c \to \Lambda \mu^+ \nu_\mu)/\Gamma(\Lambda_c \to \Lambda e^+ \nu_e) = 0.96884(61)^{\text{LQCD}}_{\text{stat}}$ is obtained, differing from the one reported in Ref. [165]. These ratios are particularly advantageous in the search for NP due to the $\mathcal{O}(m_\mu^2)$ suppression of the SM uncertainty. This is apparent in the reported $R_i = c_i^\mu / c_i^e$, $i = 0 - 2$.

We have then studied the theoretical sensitivity to a potential NP current of a certain chirality in the μ channel, accounting also for the theoretical uncertainty in the SMEFT truncation. Assuming a $\epsilon^\mu \gg \epsilon^e$ hierarchy, we have analyzed different LFU ratios. In the ratio of integrated widths the sensitivity is already very high, probing the multi-TeV scale, except for the pseudoscalar interaction. However, to realize this theoretical expectation, the experimental uncertainty should be reduced as explained in the work. In addition, we have shown that the ratios R_0 and R_2 have an excellent sensitivity to NP of any type but the pseudoscalar one. Finally, an analogous a sensitivity analysis has been performed on the c_i^μ observables themselves, which are free of the flavor hierarchy assumption. In this case the sensitivity varies notably depending on the NP chirality. In particular, the NP tensor contribution to c_1 displays a promising discovery potential.

We have identified the LQCD uncertainty of the axial and vector form factors as the most important one when it comes to improving the

sensitivity to NP. Besides, we have also seen that a better estimation of the SMEFT uncertainty would substantially improve the precision of this kind of analysis.

As a future development, the inclusion of right-handed neutrinos in the analysis would be interesting, since they are present in a large variety of NP models and can be implemented in a straightforward way.

Chapter 5

Conclusions

In this thesis the low energy properties of hadrons have been analyzed with effective field theory techniques. We have investigated the axial and electromagnetic isovector form factors of the nucleon for small transfer of momentum (Chs. 2 and 3 respectively), which contain information relevant for hadron and neutrino physics. In addition, the Λ_c semileptonic decay, $\Lambda_c^+ \to \Lambda\, \ell^+\, \nu_l$, has been studied in order to analyze the possible impact of beyond the Standard Model signals (Ch. 4).

Regarding the axial structure of the nucleon, we have computed the axial isovector form factor in relativistic Chiral Perturbation Theory up to NNLO with the explicit inclusion of the Δ baryon. In a first work, we have focused on the axial charge ($F_A(0) = g_A$) and the corresponding lattice QCD results. There, we have studied the compatibility between the phenomenological analyses of $\pi N \to \pi N$ and $\pi N \to \pi\pi N$ compared to the pion mass dependence of g_A obtained in the lattice. If the Δ baryon is not explicitly introduced, the low energy constants fixed by πN scattering predict $g_A(M_\pi)$ up to NNLO. However, we have seen that the obtained dependence does not agree with the LQCD simulations. We have then performed fits to a combined set of LQCD results, and a satisfactory description at $\mathcal{O}(p^4)$ is only achieved after the Δ is included as an explicit degree of freedom. The fact that we include several orders allows us to implement in the fit a conservative estimation of the theoretical uncertainty of ChPT. In this way, the d_{16} LEC has been extracted, albeit with a relatively large error, coming from the slow convergence of the chiral series.

Next, we have considered the form factor, performing a meta analysis of the results of recent lattice collaborations. For this purpose we obtain a model independent representation of the axial form factor at $Q^2 \geq 0$ using ChPT and fit the unknown low-energy constants to the lattice data. fitting our ChPT FF. At $\mathcal{O}(p^4)$ with explicit Δ we are able to describe data for $\sqrt{Q^2} \lesssim 0.6$ GeV and $M_\pi \lesssim 400$ MeV. In this manner, we obtain the following LEC values, $d_{16} = -1.46 \pm 1.00$ GeV^{-2} and $d_{22} = 0.29 \pm 1.69$ GeV^{-2}, in agreement with different phenomenological estimations. The first one is important to determine the quark mass dependence of nuclear properties such as ground-state and binding energies through long-range nuclear forces, whereas the second one is relevant for the axial radius and for pion electroproduction. From our parametrization we obtain an axial charge of $g_A^{\text{phys}} = 1.273 \pm 0.014$ in good agreement with the experimental determination (more precise and closer to experiment than the one from the FLAG report [74]). The axial radius is also extracted, $\langle r_A^2 \rangle^{\text{phys}} = 0.291 \pm 0.052$ fm^2. This result does not come from an ad hoc parametrization, on the contrary, relativistic ChPT has been used, and its uncertainty, together with different lattice effects, has been taken into account. This value reflects the general situation of lattice results, which predict an axial radius slightly lower than the experimental estimations. Besides, we argue that a combined fit of LQCD results for the axial form factor together with pion-nucleon scattering experimental data could improve the description of both processes.

Moving now to the electromagnetic form factor, we have computed the isovector component of this fundamental quantity combining relativistic ChPT with dispersion relations. In this way, the important contributions of $\pi\pi$ elastic rescattering in the partial wave dominated by the ρ meson are implemented. The idea here was to compare the Q^2 and M_π dependence with LQCD results, and extract nucleon electromagnetic properties as well as LECs. We have shown how three schemes describe the lattice data: (a) a purely dispersive calculation accounting only for the 2π intermediate state in terms of an Omnès function; (b) plain relativistic ChPT with explicit Δ; (c) our combined scheme. In particular, we have performed fits of the Dirac and Pauli FFs.

On the one hand, for the Dirac FF, we have observed that the combined theory outperforms the other two, describing well the data in the relatively large range $\sqrt{Q^2} \lesssim 0.77$ GeV and all the simulated M_π ($M_\pi \lesssim 350$ MeV). From this fit, the value $\langle r_1^2 \rangle_{\text{phys}}^{\text{disp+ChPT}} = 0.4838 \pm 0.0047$

fm^2 is extracted, slightly below the experimental determination.

On the other hand, we have analyzed the somewhat more challenging Pauli FF. Given that the leading term of this quantity is of higher order in ChPT as compared to the Dirac case, we have observed that an $\mathcal{O}(p^3)$ calculation was not sufficient to describe it. Therefore we have added $\mathcal{O}(p^4)$ contributions without Δ to the ChPT term, resulting in a good fit of the LQCD data in plain ChPT, in the same range as for the Dirac FF. Given that the purely dispersive approach also leads to a good agreement with the data, the combined theory does not particularly improve the result. In any case we regard the latter to be a more complete description, corresponding to a Q^2 dependence of the FF which is remarkably close to the experimental parametrization at the physical point, even beyond the fit cut, $\sqrt{Q^2} = 0.77$ GeV. From the combined theory we have obtained $\kappa_{\text{phys}}^{\text{disp+ChPT}} = 3.605 \pm 0.067$, which is close to the experimental value, and $\langle r_2^2 \rangle_{\text{phys}}^{\text{disp+ChPT}} = 0.788 \pm 0.015$ fm^2, in agreement with the empirical determination. In addition, the values of several LECs have been extracted, which are useful for future computations.

Since it was required for our dispersive study of the nucleon form factors, we have computed the M_π dependence of the pion p-wave phase shift and the pion vector FF. We calculate the phase shift with the IAM and implementing a Blatt-Weisskopf form factor. For the pion FF the Omnès function is used, including an additional phenomenological parameter. We predict well the LQCD results for the M_π dependence of the mass of the ρ meson. In the future, this method could be applied to other mesons and could be further tested by comparison to phase shifts and meson FFs from the lattice.

Another interesting future development would be to employ the dispersively improved ChPT technique to compute $\Delta - N$ transition form factors. On top of that, the inclusion of the strange quark flavor, shifting our focus to the structure of hyperons would be another fruitful way to employ the techniques developed in these analyses.

In the light of our works on nucleon form factors, we think that a combined fit to several observables in baryon ChPT could be of great use. This would take the most out of the EFT, in analogy with what has been already done in the mesonic sector in the last decades. For instance one could fit pion electroproduction and πN scattering data, together with experimental (or LQCD) data of the electromagnetic FF. In this

way the correlations among LECs and the theoretical accuracy could be assessed in greater detail.

Finally, we have also undertaken the analysis of new physics signals in hadron phenomenology. Given that there are still several open problems in the Standard Model, it seems that the latter is in reality an EFT of some ultraviolet theory, whose fingerprints could be determined in the existing and future experimental data. Motivated by recent measurements of BESIII [58], we have focused on the specific case of the $\Lambda_c \to \Lambda \nu \ell^+$ decay. We have studied the possible impact of beyond the SM signals in the framework of the low energy limit of SMEFT. For the QCD input we rely, once more, on LQCD data for the (transition) form factors. In this computation, the large value of the charm quark as compared with the rest of scales is exploited to express some of the required form factors in terms of those determined with LQCD. There is a certain arbitrariness in the way in which one applies the aforementioned heavy quark approximations. This leads us to take the difference between prescriptions as an estimate of the error of the approximation.

We study lepton flavor universality violation ratios and show the large cancellation of theoretical uncertainties that they produce. After analyzing the SM case, the standard hierarchy $\epsilon^\mu \gg \epsilon^e$ has been considered. Therefore, we begin by reporting results on the different angular amplitudes, c_{0-2} (Eq. (4.1)), of the μ channel without taking ratios, and relying on the Wilson coefficients from Ref. [162]. Here the separation in c_i proves to be useful, showing the particular discovery potential of the c_1 amplitude.

Next, we study the sensitivity to different NP currents in the c_i amplitudes, finding that the tensor contribution to c_1 displays a promising discovery potential. Afterwards, we study LFU ratios, so that we approximate the BSM contributions to lie only on the muon and not on the electron channel. The theoretical sensitivity achieved here, disregarding experimental uncertainties, is very high, probing the multi-TeV scale, even if the SMEFT error is considered.

As the experimental results are becoming more precise, we have identified the LQCD uncertainty in the (axial-)vector FFs as the main source of theoretical error (even though the SMEFT one is also important in certain regimes).

There are still several hadronic decays to which this kind of analysis

could be performed, including combined studies of different types of decays, such as baryonic and mesonic ones, which would prove the same quark transitions. On top of that, the inclusion of right-handed neutrinos in the theory would be a simple extension of the work, with implications for many new physics models.

Resumen en español

Introducción

La Cromodinámica Cuántica (QCD), la teoría que describe la interacción fuerte, gobierna la dinámica de los quarks y gluones, ligándolos en hadrones. Las propiedades de estos son sumamente interesantes, no solo para investigar la interacción fuerte subyacente, sino también porque son omnipresentes en los procesos de física de partículas, siendo esenciales en cualquier análisis experimental.

Como partículas compuestas, los hadrones son cuerpos extensos con estructura. Su composición puede ser investigada experimentalmente, y en este sentido, los nucleones, es decir, protones y neutrones, son especiales. El protón es el único hadrón estable (dentro de los límites experimentales) y el neutrón es el segundo más estable, con una vida media de aproximadamente 15 minutos. Esto convierte al nucleón en el objetivo más adecuado para experimentos de dispersión, que es la forma más directa de sondear la estructura interna. En particular, la dispersión elástica electrón-nucleón es sensible a la distribución de carga eléctrica dentro de este hadrón, así como a sus propiedades magnéticas. Por otro lado, experimentos como la dispersión cuasi-elástica de neutrinos en nucleones, un proceso débil, dan acceso a la llamada estructura axial del nucleón. Esta está relacionada con la distribución de espín dentro del nucleón y es un elemento clave para el análisis de la física de neutrinos. En general, las secciones eficaces de estos procesos se descomponen en funciones del momento transferido, llamadas factores de forma (FF), que portan la información sobre la estructura del hadrón.

Buena parte de esta tesis se centra en el estudio de los factores de forma a bajas energías, con la consiguiente información sobre las

propiedades del nucleón. Sin embargo, existe una complicación intrínseca a QCD: a bajas energías el acoplo fuerte es relativamente grande, por lo que no se puede calcular perturbativamente en este régimen. Una forma de superar este obstáculo consiste en formular la teoría en un espacio tiempo discretizado, lo que se conoce como lattice (retículo) QCD (LQCD). El reciente progreso en LQCD es una de las principales motivaciones de esta tesis, aunque esta valiosa fuente de información teórica sufre de algunos efectos artificiales e incertidumbres sistemáticas. Nuestro enfoque es emplear teorías de campos efectivas (EFT) y otras herramientas teóricas para obtener resultados de QCD en el régimen no perturbativo, que posteriormente son utilizados en el análisis de datos de lattice y experimentales. Una teoría efectiva es aquella que se vale de aspectos de la teoría fundamental (por ejemplo QCD) tales como simetrías o diferencias entre escalas, para calcular cantidades que en general no son computables en la teoría original. Además, una EFT es en lo posible independiente de modelos y la precisión de sus resultados se puede mejorar de manera sistemática.

En particular, en los capítulos sobre los factores de forma del nucleón, la EFT que hemos empleado se conoce como Teoría Quiral de Perturbaciones (ChPT), un formalismo idóneo para estudiar QCD a bajas energías. Ésta se basa en aprovechar una simetría aproximada de QCD, relacionada con el sabor de los quarks ligeros (u, d y s), para construir una teoría cuántica de campos perturbativa, donde los grados de libertad corresponden a los hadrones ligeros. Esta teoría tiene un historial de éxitos en la descripción de la física de hadrones y puede emplearse también para estudiar efectos específicos de LQCD. De hecho, en el centro de esta tesis está el uso de ChPT para analizar la dependencia en la masa de pión que presentan las simulaciones en el retículo. Además, ChPT resulta útil para el tratamiento de otros efectos de lattice, tales como la dependencia en el volumen finito del retículo y en la separación entre puntos del mismo.

Una teoría complementaria a ChPT es la Teoría Dispersiva o las relaciones de dispersión. Esta herramienta explota la unitariedad y analiticidad de las amplitudes para obtener resultados no perturbativos. En particular, hemos empleado relaciones de dispersión en combinación con ChPT para estudiar el factor de forma electromagnético del nucleón, donde la resumación del estado intermedio de dos piones es fundamental.

Por otro lado, el enfoque efectivo ha sido empleado en un problema distinto en esta tesis, en concreto para considerar posibles señales de nueva física más allá del Modelo Estándar. Dicho modelo describe las interacciones entre partículas fundamentales con gran precisión, sin embargo presenta varios problemas que indican que no se trata de la teoría definitiva de la naturaleza. Para parametrizar posibles desviaciones del Modelo Estándar, es conveniente utilizar la Teoría Efectiva del Modelo Estándar (SMEFT). Este formalismo permite estudiar de forma sistemática y relativamente general dichas desviaciones sin asumir modelos específicos de nueva física. Con este formalismo, se ha estudiado el decaimiento semileptónico de la resonancia Λ_c, $\Lambda_c \to \Lambda \nu \ell^+$, con la motivación de nuevos datos de BESIII [58]. Además, para dicho trabajo se emplea también otra aproximación en la línea de las teorías efectivas, como es la aproximación de quark pesado (HQ). En este caso se utiliza dicha simplificación para obtener elementos de matriz hadrónicos a partir de otros extraídos de lattice. Los resultados obtenidos para este y el resto de problemas tratados se resumen a continuación. Esta tesis está organizada de forma que los estudios sobre el factor de forma axial y electromagnético se exponen en los capítulos 2 y 3 respectivamente, mientras que el análisis del decaimiento semileptónico de la Λ_c se presenta en el capítulo 4.

Factor de forma axial del nucleón

El factor de forma axial es una cantidad fundamental del nucleón. En particular, su valor a $Q^2 = 0$ contiene información sobre la distribución de espín en su interior. Además, puesto que la interacción débil es de tipo "left", el factor de forma axial contribuye junto con el electromagnético (vectorial). Por lo tanto el FF axial es un ingrediente clave en el análisis de procesos débiles. Nosotros nos centramos en el régimen de baja energía, útil para el estudio de la dispersión elástica y cuasielástica de neutrinos en nucleones que se da en los experimentos de oscilaciones.

En cuanto a las extracciones experimentales hay que decir que son difíciles, de hecho no están exentas de cierta dependencia del modelo. Al margen de otras cuestiones, cualquier extracción del factor de forma requiere que se ajuste una cierta forma funcional a los datos. La llamada expansión z, se ha utilizado ampliamente, pero no se ha llegado a un resultado plenamente satisfactorio. Además, no hay datos experimentales

lo suficientemente precisos a bajo Q^2 para determinar con precisión el factor de forma.

Esto nos ha llevado a realizar un cálculo de la componente isovectorial del factor de forma axial a bajas energías en ChPT y a estudiar a continuación su ajuste a un conjunto de resultados de LQCD de distintas colaboraciones recientes. El hecho de emplear ChPT permite parametrizar la dependencia en Q^2 y masa de quark de los datos de lattice sin basarnos en ninguna función ad hoc, sino valiéndonos en las simetrías de QCD. En nuestro cálculo, vamos más allá de los estudios anteriores, puesto que utilizamos la renormalización EOMS relativista e incluimos explícitamente la resonancia Δ hasta $\mathcal{O}(p^4)$ (NNLO). El esquema EOMS garantiza que no solo el conteo de potencia, sino también las propiedades analíticas de las funciones de bucle se preserven correctamente. Además, la inclusión de $\mathcal{O}(p^4)$ conduce a una mejor estimación de la incertidumbre de truncado, ya que está dada por diferencias entre órdenes.

En una primera fase analizamos la dependencia en masa de quark (o de pión) de la carga axial, g_A. Así, mostramos que hasta $\mathcal{O}(p^4)$, la dependencia de la masa del pión de g_A predicha usando LECs determinadas a partir de estudios fenomenológicos de dispersión elástica e inelástica pión-nucleón ($\pi N \to \pi\pi N$) no puede producir el comportamiento plano predicho por los resultados de distintos trabajos de LQCD ([112], [113], [79], [114]), si no se considera explícitamente la Δ. Una vez incluida la Δ, realizamos un ajuste satisfactorio de los datos de LQCD hasta masas pión de 400 MeV. Extraemos una carga axial en el punto físico más precisa que la determinación del informe del FLAG [74]. Hay que reconocer, sin embargo, que la convergencia de la serie quiral parece ser lenta, pues el $\mathcal{O}(p^4)$ es considerable, lo que repercute en el error de truncado y por tanto en las distintas LECs extraídas. Junto con las correlaciones significativas, esta característica implica que se requieren resonancias de $\mathcal{O}(p^5)$ y/o más pesadas para alcanzar una convergencia completa y minimizar las incertidumbres teóricas.

A continuación, estudiamos el factor de forma axial a momentos bajos, ajustando nuestro cálculo a otro conjunto de resultados recientes de lattice ([79], [114], [122], [123], [124]) que tienen en cuenta la contaminación por estados excitados. Observamos pues que a orden $\mathcal{O}(p^4)$ con Δ explícita, nuestro cálculo es capaz de describir los datos hasta aproximadamente 0.6 GeV en $\sqrt{Q^2}$ y $M_\pi \sim 400$ MeV. De nuestro ajuste concluimos que el barión Δ es un grado de libertad necesario, especial-

mente para tener en cuenta la dependencia de M_π. A partir de nuestra parametrización, extraemos una carga axial física de $g_A = 1.273 \pm 0.014$, concordando bien con la determinación experimental. Extraemos también las LECs del Lagrangiano $\mathcal{O}(p^3)$: $d_{16} = -1.46 \pm 1.00$ GeV^{-2} y $d_{22} = 0.29 \pm 1.69$ GeV$^-2$, consistentes con diferentes determinaciones fenomenológicas. La primera constante es importante para determinar la dependencia en masa de quark de propiedades nucleares como la energía del estado fundamental y de ligadura debidas a fuerzas nucleares de largo alcance. La segunda es relevante para el radio axial del nucleón así como para el proceso de electroproducción de pión.

En el estudio del factor de forma axial, mostramos que como en el de g_A, la lenta convergencia de ChPT requiere la inclusión de términos de orden superior $\mathcal{O}(p^5)$, con las posibles soluciones antes mencionadas. Por otro lado, entendemos que un ajuste combinado de los resultados de LQCD para el factor de forma axial junto con los puntos experimentales de dispersión pión-nucleón podría mejorar la descripción de ambos procesos. En particular, las correlaciones entre LECs estarían más bajo control.

Por último, discutimos el radio axial, una cantidad que constituye un desafío que abarca la teoría y el experimento de la QCD. A partir de nuestro ajuste de diferentes resultados de LQCD, obtenemos $\langle r_A^2 \rangle = 0.291 \pm 0.052$ fm^2. Consideramos ChPT relativista una parametrización óptima a bajas energías, mejor que funciones ad hoc. El conocido hecho de que el $\langle r_A^2 \rangle$ de lattice (incluido el nuestro) y extracciones empíricas no estén del todo alineados ha quedado patente en este trabajo. Esto motiva a ambas partes a seguir mejorando sus estudios.

Factor de forma electromagnético del nucleón

El scattering nucleón-leptón es uno de los procesos observables más simples sensibles a la estructura interna del nucleón. Por tanto, los factores de forma electromagnéticos son fundamentales en el estudio de la estructura del nucleón y de la subyacente interacción fuerte. Estos FFs suscitan interés por distintos motivos, siendo particularmente notorio el problema del radio eléctrico del protón en los últimos años ("proton radius puzzle"). Desde el punto de vista teórico, se han realizado distintos estudios de los factores de forma electromagnéticos en LQCD en los úl-

timos años con cada vez mayor precisión. Aunque los resultados ahora están disponibles incluso a masas de quarks físicas, los análisis de última generación aún sufren de diferentes errores sistemáticos, y por ejemplo la extracción de distintas propiedades como el radio se ve dificultada debido a la mencionada parametrización del Q^2.

En el caso de los factores de forma electromagnéticos, nos centramos en la componente isovectorial y combinamos ChPT con relaciones de dispersión, para después comprobar si la descripción de datos de lattice es satisfactoria. La implementación de la unitariedad a través de la teoría dispersiva está motivada por la prominencia del "rescattering" de dos piones (en el canal de la resonancia ρ) en este factor de forma y busca aumentar el rango de aplicabilidad de la teoría. Nuestra idea fundamental es implementar el corte de dos piones dispersivamente (incluyendo el formalismo de la función de Omnès) y aproximar el resto de contribuciones con ChPT relativista con Δ explícita. Esta estrategia se resumiría a grandes rasgos en la siguiente fórmula, donde el primer término es el dispersivo y el segundo es la contribución complementaria de ChPT:

$$F(q^2) \approx \int_{4M_\pi^2}^{\Lambda^2} \frac{\mathrm{d}s}{\pi} \frac{\mathrm{Im}F_{2\pi}(s)}{s - q^2 - i\epsilon} + F_{\text{ChPT without } 2\pi \text{ cut}}(q^2)\,. \tag{5.1}$$

En particular se presta mucha atención a la descripción de la dependencia en la masa de pión, tanto en el término de simple ChPT como en la parte dispersiva. En lo que respecta a ésta última, se utiliza como input la amplitud de $\pi\pi$ scattering del método de la amplitud inversa a segundo orden (NLO IAM). Además se ha implementado un FF de Blatt-Weiskopf para corregir el comportamiento a altas energías. Una vez que comprobado que la dependencia en M_π del input dispersivo está de acuerdo con datos de LQCD , lo implementamos en los FFs electromagnéticos. En particular, al factor de forma de Dirac, F_1, se le realiza una sustracción para mejorar la convergencia de la integral dispersiva, mientras que el de Pauli, F_2, no se substrae, para preservar así su dependencia no trivial en M_π a $Q^2 = 0$. Respecto a la dependencia de M_π de los FFs y comprobamos que las no-analiticidades principales de ChPT asociadas a los diagramas con corte de dos piones son reproducidas por la integral dispersiva.

A continuación comparamos nuestros resultados con datos de lattice a distintas M_π que muestran un buen control de los efectos de dis-

cretización [136]. Consideramos tres enfoques diferentes: (a) un cálculo puramente dispersivo que solo implementa el estado intermedio de dos piones; (b) simple ChPT, y (c) nuestro esquema combinado. Para el FF de Dirac, observamos que incluso el esquema puramente dispersivo es capaz de predecir razonablemente bien el FF. Este cálculo no perturbativo proporciona suficiente curvatura al FF, teniendo en cuenta la dinámica de la ρ. A continuación observamos que el esquema combinado dispersivo y ChPT supera al ajuste de ChPT y al enfoque puramente dispersivo. El cálculo describe bien los datos para $\sqrt{Q^2} < 0.77$ GeV y todos los conjuntos de LQCD, es decir, $M_\pi \leq 350$ MeV. El valor de $\langle r_1^2 \rangle_{\text{phys}}^{\text{disp+ChPT}} = 0.4838 \pm 0.0047$ fm^2 para el radio de Dirac, se extrae de la versión combinado, ligeramente por debajo de la determinación experimental.

Posteriormente consideramos el FF de Pauli. Siendo una cantidad de orden superior, se incluyen LECs de orden mayor. Necesitamos por tanto incorporar las LECs y los loops de ChPT $\not\Delta$ de $\mathcal{O}(p^4)$. Esto lleva a una buena descripción de los datos de LQCD tanto por los cálculos dispersivos como por los de ChPT, en el mismo rango de Q^2 y M_π que para el caso de Dirac. Combinar ambas teorías lleva principalmente a los mismos resultados que la descripción puramente dispersiva. Curiosamente, tanto los resultados dispersivos como los combinados están bastante cerca de la parametrización experimental, incluso más allá del corte del ajuste, $\sqrt{Q^2} = 0.77$ GeV. Entre estos dos esquemas, consideramos que la versión combinada es un resultado más sólido desde un punto de vista teórico. De esta descripción, extraemos $\kappa_{\text{phys}}^{\text{disp+ChPT}} = 3.605 \pm 0.067$, que está cerca del valor empírico, y $\langle r_2^2 \rangle_{\text{phys}}^{\text{disp+ChPT}} = 0.788 \pm 0.015$ fm^2, que concuerda con el experimento. Además, se han determinado los valores de varias LECs, que son útiles para futuros cálculos. Para esta primera exploración del esquema combinado, no intentamos estimar la incertidumbre teórica. Los errores reportados son sólo estadísticos y, por lo tanto, están subestimados.

En la tesis se discuten posibles mejoras de este cálculo, así como otros observables en el que el esquema aquí desarrollado sería de gran utilidad. En particular el cálculo factores de forma de transición $N - \Delta$ se podría beneficiar del método propuesto, así como aplicarse a bariones con extrañeza.

Nueva física en el decaimiento semileptónico de la Λ_c

Los hadrones no sólo son interesantes por sus propiedades relativas a QCD y a la interacción débil, sino que también pueden revelar información sobre nueva física más allá del Modelo Estándar. De hecho distintas áreas de la física de partículas están trabajando conjuntamente para encontrar pruebas de dichos fenómenos, que podrían dar respuesta a problemas del Modelo Estándar. Los decaimientos de hadrones pesados se analizan en este contexto y han recibido especial atención en los últimos años. En esta tesis, estudiamos un hadrón con quark c, el barión Λ_c, caracterizado por $I(J^P) = 0(1/2^+)$. En particular, calculamos su decaimiento semileptónico débil: $\Lambda_c \to \Lambda, \ell^+\nu_\ell$. Motivados en parte por resultados muy recientes de la colaboración BESIII[58], nuestro estudio aprovecha nuevamente las teorías efectivas existentes para analizar el proceso.

A nivel de la transición de quarks, consideramos posibles corrientes de nueva física $\mathcal{O}(1/\Lambda^2)$ en SMEFT utilizando un Hamiltoniano efectivo de bajas energías, en el que no sólo las partículas de NP, sino también los bosones débiles han sido integrados en el funcional generador. Esto permite parametrizar el impacto de cada corriente en el correspondiente coeficiente de Wilson. Además, se tiene en cuenta una estimación de los órdenes superiores despreciados, como parte de la incertidumbre en el análisis. En cuanto al elemento de matriz hadrónico, existen resultados para los factores de forma de transición axial y vector [65]. Para obtener los factores de forma del resto de quiralidades utilizamos distintas formas de aproximación de quark pesado. De esta manera, la diferencia entre las distintas aproximaciones se emplea como estimación del error cometido.

Una vez calculada la amplitud para los canales e y μ, computamos ratios de violación de universalidad del sabor leptónico (LFU), que cancelan distintos errores teóricos. En concreto para las anchuras integradas en el SM obtenemos

$$R^{\rm SM} = \Gamma(\Lambda_c \to \Lambda\mu^+\nu_\mu)/\Gamma(\Lambda_c \to \Lambda e^+\nu_e) = 0.96884(61)^{\rm LQCD}_{\rm stat} \ ,$$

diferente al de [165] y consistente con la extracción experimental $R^{\rm exp} = 0.98(5)(3)$ [58], que arrastra una incertidumbre notable.

Pasando al análisis de la nueva física, discutimos la estructura de las distintas contribuciones de las correientes más allá del SM en las

amplitudes angulares $c_{0,1,2}$. En el análisis nos concentramos en el canal μ, de acuerdo con la jerarquía estándar, en la que los Wilsons de los leptones más pesados son mayores. Seguidamente mostramos las $c_{0,1,2}$ con los Wilsons evaluados en los rangos obtenidos en la Ref. [162] a partir de decaimientos de mesones pseudoescalares. Con los mismos Wilsons para el canal μ, también se discuten ratios de LFU donde los Wilsons del canal e se toman como nulos. En este contexto se observa que c_1 tiene más potencial como señal de nueva física.

Posteriormente estudiamos la sensibilidad a una posible corriente de NP de cierta quiralidad en el canal μ, teniendo en cuenta también la incertidumbre teórica de SMEFT. Primero analizamos diferentes cocientes de LFU. Ya en el cociente de anchuras integradas, la sensibilidad es muy alta, sondeando la escala multi-TeV, excepto para el pseudoescalar (se desprecia la actual gran incertidumbre experimental). Además, demostramos que los cocientes $R_0 = c_0^\mu/c_0^e$ y $R_2 = c_2^\mu/c_2^e$ en función de q^2 tienen una excelente sensibilidad a cualquier tipo de NP excepto el pseudoescalar.

Finalmente, se ha realizamos un análisis análogo de la sensibilidad en las c_i del canal μ, por lo tanto libre de la suposición de jerarquía. Aquí, la sensibilidad varía notablemente dependiendo de la quiralidad de la NP. En particular, se muestra que la contribución tensorial de NP a c_1 es muy accesible desde el punto de vista teórico.

Tras este trabajo, identificamos la incertidumbre de LQCD de los factores de forma axiales y vectoriales como la más importante cuando se trata de estudiar la sensibilidad a NP, pues aparecen en el término del Modelo Estándar. Además, hemos visto que una estimación más precisa de la incertidumbre de SMEFT mejoraría sustancialmente la precisión de este tipo de análisis. Por último, como desarrollo futuro, consideramos que la inclusión de neutrinos "right" en el análisis sería interesante, ya que están presentes en una gran variedad de modelos de nueva física y pueden implementarse de manera directa.

Acknowledgements

I write this page right before the submission of the manuscript, when the paperwork has drained my energy. I apologize if I forget to include someone. I have tried to be thankful in person to everyone who has accompanied me in this long and exciting roller coaster.

Primero de todo, estoy muy agradecido a mi tutor, Luis. Aprecio mucho que me hayas transmitido una fracción de tu amplio conocimiento y que hayas tenido en cuenta mi opinión en las discusiones científicas. Has resultado un guía fantástico, compartiendo tu experiencia, me has ayudado a sortear diversos escollos a lo largo de mi vida predoctoral.

A lot of good came out of my Swedish stay. I am really grateful to Stefan. I learned so much from your expertise. You are a great collaborator and an even better person. From that time, I also want to thank my colleagues and friends from the ChPT gang, Nora (birra al Palermo?), An Di and Kees.

Por supuesto, quiero agradecer a los excelentes investigadores con los que he compartido grupo en el IFIC. Los doctores primero: Manuel Vicente, Juan Nieves, Raquel Molina, Miguel Albaladejo, Eulogio Oset, Albert Feijoo, Alessandro Giachino, Pan Pan Shi, Jing Song, Menglin Du (*thank you for letting me try the Sichuan spicy food*), Natsumi Ikeno y Juan Manuel Franco. A continuación, muchas gracias a los que conocí como predocs, que están en primera línea de batalla en la física y en la vida: Don Gustavo (∞ gracias por la ayuda y namasté), Fer (lo que pasa en París se queda en París...), Víctor(o) (unos baos?), Yulius (qué versículo de la Biblia es este?), Neus (maestra, muchas gracias por la ayuda final), Zejian, María, Edu, Pedro, Rafa, Vinicius, Asia y Amador.

Estoy agradecido a muchos otros compañeros del IFIC que me han apoyado de maneras diversas, voy a citar una muestra no exhaustiva,

lo siento: Alberto (mi discípulo de salsa), Marc (quedáte tranquilo!), Gustavo Alcalá (el más pillo de Caracas), Giorgia (nos vemos mañana), Stefan, Simone y Baibhab, entre otros. También a Mariluz de la entrada, a Luis Claramunt y Jose Pérez de secretaría y a los informáticos, se llamen o no Ximo, muchas gracias, sois los pilares del IFIC.

Por último, estoy muy agradecido a mis amigos no corpusculares, que me habéis apoyado en esta travesía. Saludo a un subconjunto con el que he tenido más contacto durante el doctorado: por aquí cerca a Aurora, desde más lejos a Fran y a Tomás (y a Yuri, por ser mi colaboradora eterna).

Appendix A

Theoretical remarks

A.1 On the computation of the Omnès function

In order to compute the Omnès function one needs to calculate the integral in Eq. (1.80). First of all one has to remember that the $i\epsilon$ appears in the denominator in order to evaluate the expression above the real axis in the complex plane. In short, one needs to employ the principal value (PV), as follows [3]

$$\frac{1}{x - x_0 - i\epsilon} = \mathrm{PV}\frac{1}{x - x_0} + i\pi\delta(x - x_0) \ , \tag{A.1}$$

with δ the Dirac δ function and PV for a singularity at $x = b$ defined as:

$$\mathrm{PV}\int_a^c \mathrm{d}x f(x) = \lim_{\Delta\to 0}\left(\int_a^{b-\Delta} \mathrm{d}x f(x) + \int_{b-\Delta}^c \mathrm{d}x f(x)\right) \ . \tag{A.2}$$

Therefore one has in general

$$\int_{-\infty}^{\infty} \mathrm{d}x \frac{f(x)}{x - x_0 - i\epsilon} = \mathrm{PV}\int_{-\infty}^{\infty} \mathrm{d}x \frac{f(x)}{x - x_0} + i\pi f(x_0) \ . \tag{A.3}$$

Applying this to Eq.(1.80), $f(x)$ would be $\delta(s')/s'$[1]. In general it is easier to integrate numerically, and to that end one can rearrange the calculation so that the singularity at $s = s'$ is integrated analytically. It is enough to add and subtract $\delta(s)$ in the numerator of the integrand in Eq.(1.80). We write the aforementioned integral defining u, $\Omega(s) \equiv$

[1] To integrate precisely in the $(-\infty, \infty)$ interval, one should write $f(x) = \theta(s' - 4M_\pi^2)\delta(s')/s'$.

$\exp u(s)$,

$$\begin{aligned} u(s+i\epsilon) &= \frac{s}{\pi}\int_{4M_\pi^2}^{\infty} \mathrm{d}s' \frac{\delta(s')}{s'(s'-s-i\epsilon)} \\ &= \underbrace{\frac{s}{\pi}\int_{4M_\pi^2}^{\infty} \mathrm{d}s' \frac{\delta(s')-\delta(s)}{s'(s'-s)}}_{\equiv u_{\mathrm{num}}} + \underbrace{\frac{s\delta(s)}{\pi}\int_{4M_\pi^2}^{\infty} \mathrm{d}s' \frac{1}{s'(s'-s-i\epsilon)}}_{\equiv u_{\mathrm{anal}}} \end{aligned} \tag{A.4}$$

Now one computes u_{num} numerically for any $\delta(s)$, and uses Eq. (A.3) with $f(x) = 1/s'$ to analytically integrate the singularity:

$$\begin{aligned} u_{\mathrm{anal}} &= \frac{s\delta(s)}{\pi}\mathrm{PV}\int_{4M_\pi^2}^{\infty} \mathrm{d}s' \frac{1}{s'(s'-s)} + i\delta(s) \\ &= \frac{s\delta(s)}{\pi}\lim_{\Delta\to 0}\frac{1}{s}\left\{\left[\log\left|\frac{s'-s}{s'}\right|\right]_{4M_\pi^2}^{s-\Delta} + \left[\log\left|\frac{s'-s}{s'}\right|\right]_{s+\Delta}^{\infty}\right\} + i\delta(s) \\ &= \frac{\delta(s)}{\pi}\log\left|\frac{4M_\pi^2}{4M_\pi^2-s}\right| + i\delta(s)\ . \end{aligned} \tag{A.5}$$

Appendix B

Details of the axial form factor calculation

B.1 Mass and wave-function renormalization of the nucleon

As stated in Ref. [43], the Fourier transform of the two point function omitting the multiparticle branch cut:

$$\int \mathrm{d}^4x \, \langle\Omega| \, T\Psi(x)\bar{\Psi}(0) \, |\Omega\rangle \, e^{ipx} = \frac{iZ(\not{p} + m_N)}{\not{p} - m_N + i\epsilon}, \tag{B.1}$$

which defines the renormalized mass, m_N, and the wave-function renormalization constant, Z, for the nucleon case. It is given by the sum infinite 1PI two point amplitude called selfenergy, $\Sigma(\not{p})$, with chiral limit propagators

$$\begin{aligned} &\int \mathrm{d}^4x \, \langle\Omega| \, T\Psi(x)\bar{\Psi}(0) \, |\Omega\rangle \, e^{ipx} \\ &= \frac{i}{\not{p} - \mathring{m}} + \frac{i}{\not{p} - \mathring{m}} \left(\frac{\Sigma(\not{p})}{\not{p} - \mathring{m}}\right) + \frac{i}{\not{p} - \mathring{m}} \left(\frac{\Sigma(\not{p})}{\not{p} - \mathring{m}}\right)^2 + ... \\ &= \frac{i}{\not{p} - \mathring{m} - \Sigma(\not{p})} \, . \end{aligned} \tag{B.2}$$

After the resummation, the renormalized mass m_N is defined by the pole position:

$$\not{p} - \mathring{m} - \Sigma(\not{p})|_{\not{p}=m_N} = 0 \, . \tag{B.3}$$

Expanding Σ around $\not{p} = \mathring{m}$ ($\not{p} - \mathring{m}$ counts as a small quantity $\mathcal{O}(p)$ off-shell) one obtains

$$\begin{aligned}\Sigma(\not{p}) &= \Sigma(\mathring{m}) + (\not{p} - \mathring{m})\Sigma'(\mathring{m}) + \frac{1}{2}(\not{p} - \mathring{m})^2\Sigma''(\mathring{m}) + ... \\ &\equiv \Sigma(\mathring{m}) + (\not{p} - \mathring{m})\Sigma'(\mathring{m}) + R(\not{p}),\end{aligned} \tag{B.4}$$

where the tilde stays for derivative with respect to $\not{p}$ and R is defined by the higher orders. Thus, one can express the propagator as:

$$\frac{1}{\not{p} - \mathring{m} - \Sigma(\not{p})} = \frac{1}{\not{p} - \mathring{m} - \frac{\Sigma(\mathring{m})}{1-\Sigma'(\mathring{m})} - \frac{R(\not{p})}{1-\Sigma'(\mathring{m})}} \frac{1}{1 - \Sigma'(\mathring{m})} \ . \tag{B.5}$$

The pole satisfies then

$$m_N = \mathring{m} + Z\Sigma(\mathring{m}) + ZR(m_N) \ , \tag{B.6}$$

where Z is the residue

$$Z = \frac{1}{1 - \Sigma'(\mathring{m})} \ . \tag{B.7}$$

As in Ref. [42] we calculate the nucleon selfenergy up to $\mathcal{O}(p^4)$. Separating in chiral orders it reads

$$\Sigma = \Sigma^{(2)} + \Sigma^{(3)} + \Sigma^{(4)} \ , \tag{B.8}$$

with the tree level

$$\Sigma^{(2)} = -4c_1 M_\pi^2 \ , \tag{B.9}$$

and the rest given as supplementary material in the Mathematica notebook on the website shorturl.at/bAEGL (clickable link). Expanding the pole in Eq (B.4) around $\mathring{m}$, the renormalized mass is given by

$$m_N = \mathring{m} + \Sigma(\mathring{m}) + \Sigma^{(2)}\Sigma^{(3)}(\mathring{m}) + \mathcal{O}(p^5) \ , \tag{B.10}$$

neglecting $\mathcal{O}(p^5)$. This yields a better convergence than just taking the first recursive solution from tree level, $m_N = m + \Sigma(\not{p} = \mathring{m} + \Sigma^{(2)})$. It corresponds to a minimal inclusion of c_1 insertions, just at lineal order. Including higher c_1 orders might be troublesome if not performed together with the addition of other diagrams.

For the wave-function renormalization constant, we expand Eq. (B.7) as

$$Z \equiv 1 + \delta Z = 1 + \Sigma'(\mathring{m}) \ . \tag{B.11}$$

Then we perform an analogous expansion as for the mass:

$$\delta Z = \Sigma'(\mathring{m}) + \Sigma^{(2)}\Sigma^{(3)\prime\prime}(\mathring{m}) + \mathcal{O}(p^5) \tag{B.12}$$

neglecting $\mathcal{O}(p^5)$. This corresponds again to a minimal inclusion of c_1 mass insertions.

B.2 LEC conversion

The covariant renormalization prescription adopted in Refs. [104, 105] differs from EOMS. In EOMS only power-counting breaking terms are subtracted by a shift in the LECs. To obtain an equivalence between covariant and heavy-baryon results, the method of Ref. [104] also subtracts infrared-regular terms at the order of the calculation, as well as terms proportional to $\log\left(M_\pi^2/m_N^2\right)$. After setting $\bar{\lambda} = 0$ and $\mu = m_N$ in Eq. (21) of Ref. [104] one is left with a dimensionally regularized LEC, x_r:

$$\begin{aligned} x_r &= \bar{x}^{\text{cov}} + \frac{1}{F_\pi^2}\left(\delta\bar{x}_f^{(3)} + \delta\bar{x}_f^{(4)}\right) + \frac{\beta_x}{32\pi^2 F_\pi^2}\log\left(\frac{M_{\pi(\text{phys})}^2}{m_{N(\text{phys})}^2}\right) \\ &= x^{\text{EOMS}} + \delta x_f^{\text{EOMS}}\,, \end{aligned} \tag{B.13}$$

which makes possible to write the renormalized EOMS LECs x^{EOMS} in terms of the corresponding ones, $\bar{x}^{\text{cov}}$, from Refs. [104, 105]. The β-functions β_x needed to cancel the mesonic tadpole terms are reported in Appendix B of Ref. [104] together with the finite shifts $\delta\bar{x}_f^{(3,4)}$. Our EOMS finite shifts δx_f^{EOMS} are provided in the supplementary material of our work [31] as well as on the website shorturl.at/bAEGL (clickable link). In particular, for the relevant LECs in this study we obtain that

$$d_{16}^{\text{EOMS}} = d_{16}^{\text{cov}} + \frac{1}{F_0^2}\delta\bar{d}_{16f}^{(3)} + \frac{\beta_{d_{16}}}{32\pi^2 F_0^2}\log\left(\frac{M_{\pi(\text{phys})}^2}{m_{N(\text{phys})}^2}\right), \tag{B.14}$$

with

$$\delta\bar{d}_{16f}^{(3)} = \frac{1}{32\pi^2}(\mathring{g}_A + \mathring{g}_A^3) \;\text{ and }\; \beta_{d_{16}} = \frac{\mathring{g}_A}{2} + \mathring{g}_A^3 \tag{B.15}$$

because, in this case, $\delta\bar{d}_{16f}^{(4)} = \delta d_{16f}^{\text{EOMS}}$. Additionally,

$$c_{1-4}^{\text{EOMS}} = c_{1-4}^{\text{cov}}\,, \tag{B.16}$$

once $\beta_{c_{1-4}} = 0$ [104], and the finite shifts coincide with those in EOMS. Equations B.14-B.16 are derived for the $\not\Delta$ case but hold also for the model with the Δ pole of Ref. [104] since it does not include additional renormalizations.

Appendix C

Details of the EM form factor calculation

C.1 Pion-mass dependence of mesonic quantities

In order to compare dispersively modified ChPT to LQCD results, it is necessary to know the pion-mass dependence of the pion vector form factor, $F_v(s, M_\pi)$, and the pion-pion (p-wave) scattering phase shift, $\delta(s, M_\pi)$.

For the phase shift, we employ the IAM, using to some extent the PWAs of Ref. [45]. However, at next-to-leading order (NLO) the p-wave phase shifts $\delta^{\rm NLO}_{\rm IAM}(s)$ do not approach π asymptotically as they should. [170, 171]. This problem is remedied at two-loop order by the next-to-next-to leading order (NNLO IAM) phase shifts. Unfortunately, at physical pion masses, the ρ-meson peak is not so well reproduced by the NNLO IAM fit to LQCD data [45]. For this reason, in the present work, we use NLO IAM, but instead of smoothly extrapolating the phase shift to π [171], we modify the LO ChPT $\pi\pi$ amplitude $t_2(s)$ with a Blatt-Weisskopf form factor [172]:

$$\tilde{t}_2(s) = t_2(s)\frac{1}{1+r^2p^2_{\rm cm}} = \frac{s\sigma^2}{96\pi F_0^2}\frac{1}{1+r^2p^2_{\rm cm}}\ , \tag{C.1}$$

with the velocity of the pions $\sigma(s) \equiv \sqrt{1-4M_\pi^2/s}$. The range parameter r characterizes the scale that we do not resolve by our effective theory, i.e. we expect $r \sim 1/\Lambda$. The modified IAM amplitude $t^{\rm BW}_{\rm IAM}$ is then given

as

$$\frac{1}{t_{\rm IAM}^{\rm BW}} = \frac{\tilde{t}_2 - \tilde{t}_4}{\tilde{t}_2^2} = \frac{\tilde{t}_2 - {\rm Re}\, t_4}{\tilde{t}_2^2} - i\sigma\,, \tag{C.2}$$

where

$${\rm Re}\, t_4 = \sum_{i=0}^{2} b_i(s)\,[L(s)]^i + \sum_{i=1}^{2} b_{l_i}(s) l_i^r\ , \tag{C.3}$$

with $L(s)$ defined as

$$L(s) \equiv \log\frac{1+\sigma(s)}{1-\sigma(s)}\,. \tag{C.4}$$

The coefficient functions are [45]

$$\begin{aligned}
b_{l_1}(s) &= -2b_{l_2}(s) = \frac{s\left(4M_\pi^2 - s\right)}{48\pi F_0^4}\,,\\
b_0(s) &= -\frac{120M_\pi^6 - 197M_\pi^4 s + 61M_\pi^2 s^2 - 2s^3}{27648\pi^3 F_0^4\,(s-4M_\pi^2)},\\
b_1(s) &= -\frac{64M_\pi^8 - 55M_\pi^6 s + 6M_\pi^4 s^2}{2304\pi^3 F_0^4 s\,\sigma(s)\,(s-4M_\pi^2)}\,,\\
b_2(s) &= -\frac{M_\pi^4\left(6M_\pi^4 + 13M_\pi^2 s - 3s^2\right)}{1536\pi^3 F_0^4\,(s-4M_\pi^2)^2}\,.
\end{aligned} \tag{C.5}$$

It is easy to check that phase shifts $\delta(s, M_\pi)$ extracted from $t_{\rm IAM}^{\rm BW}$ approach π smoothly. At NLO, the combination of LECs, $l_2^r - 2l_1^r$, appears in t_4. In Ref. [45], it is found that this combination is roughly in the range $0.009 < l_2^r - 2l_1^r < 0.019$. For physical pion masses, we fit $\delta(s, M_\pi = 0.139\,{\rm GeV})$ in the interval $s \in (4M_\pi^2, 1.5\,{\rm GeV}^2)$ to the phase shifts extracted from the dispersive analysis of Ref. [51]. We find that the best-fit values are $l_2^r - 2l_1^r = 0.01$ and $r = 0.12\,{\rm fm} = 1/(1.6\,{\rm GeV})$.

The resulting $\delta(s, M_\pi = 0.139\,{\rm GeV})$ is compared to the corresponding function from Ref. [51]. Figure C.1b shows the phase shifts at different pion masses. It is apparent from the figure that for $M_\pi \approx 0.45$ GeV, $m_\rho < 2M_\pi$ and the ρ width approaches zero. In other words, the ρ-meson becomes a bound state. Of course, above this M_π value the formalism is not valid.

The ρ mass can be extracted from the crossing of $\delta(s)$ at $\pi/2$. As shown in Fig. C.2, with the parameters r and $l_2^r - 2l_1^r$ obtained at the physical pion mass, we predict the LQCD $m_\rho(M_\pi)$ [54] very precisely. It is also in agreement with the three-flavor IAM results of Ref. [55].

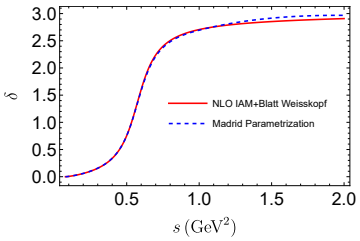

(a) $\delta(s)$ at the physical M_π

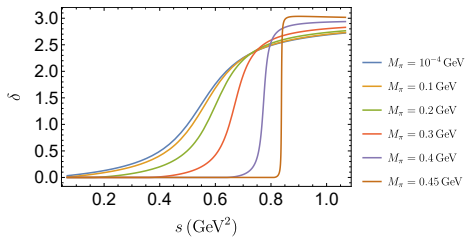

(b) $\delta(s)$ for different values of M_π

Figure C.1: Pion p-wave scattering phase shift δ from Eq. (C.1) as a function of the Mandelstam variable s.

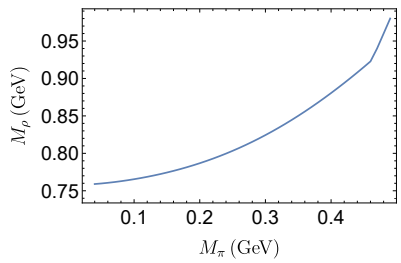

(a) m_ρ as a function of M_π.

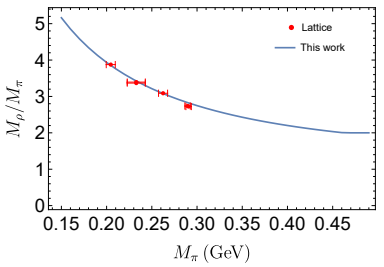

(b) m_ρ/M_π as a function of M_π.

Figure C.2: M_π dependence of the ρ-meson mass m_ρ. The lattice data are taken from Ref. [54].

Regarding the pion-vector FF, Eq. (3.13)

$$F_\pi(s, M_\pi) = [1 + \alpha_V(M_\pi)s]\,\Omega(s, M_\pi)\,, \tag{C.6}$$

we compute the Omnès function from $\delta(s, M_\pi)$ with Eq. (1.80). The correction $\alpha_V(M_\pi)$ has been introduced on phenomenological grounds to improve the description of the experimental data for $F_\pi(s)$ [157, 149, 151] and its physical value can be predicted from the pion charge radius. To determine $\alpha_V(M_\pi)$, we study the pion radius in NLO ChPT [2]:

$$\langle r_\pi^2\rangle = \frac{1}{16\pi^2 F_0^2}\left(\bar{l}_6 - 1\right) =: \frac{1}{16\pi^2 F_0^2}\left[\widetilde{l}_6(\mu^2) - 1 - \log\!\left(M_\pi^2/\mu^2\right)\right]. \tag{C.7}$$

Notice that, contrary to $\bar{l}_6$, LEC $\widetilde{l}_6$ is M_π independent but depends on the renormalization scale [2]. Using the experimental value $\langle r_\pi^2\rangle = 0.434\,\mathrm{fm}^2$, we find $\widetilde{l}_6 = 14.26$ for $\mu = 0.770$ GeV. On the other hand, the pion charge radius is defined via the pion vector FF in the usual way, cf. Eq. (1.24).

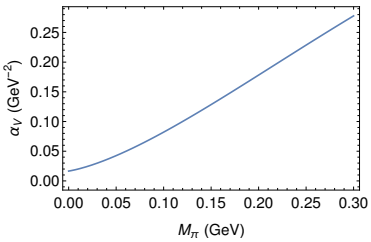

Figure C.3: The dependence of the phenomenological parameter α_V on the pion mass.

From Eq. (C.6) one obtains

$$\alpha_V(M_\pi) = \frac{\langle r_\pi^2 \rangle}{6} - \dot{\Omega}(0, M_\pi) \ , \tag{C.8}$$

with

$$\dot{\Omega}(0, M_\pi) = \frac{1}{\pi} \int_{4M_\pi^2}^{\infty} \frac{\delta(s, M_\pi)}{s^2} \, \mathrm{d}s \, . \tag{C.9}$$

In this way we determine the numerical $\alpha_V(M_\pi)$ dependence, displayed in Fig. C.3. Note that the logarithmic pion-mass dependence in (C.7) is compensated by a corresponding logarithm emerging from (C.9). Therefore α_V has no logarithmic divergence at $M_\pi = 0$. As a cross-check, in Fig. C.4 we also present the resulting $F_\pi(s)$ at the physical pion mass. It is displayed together with data from Belle [52]. We observe an excel-

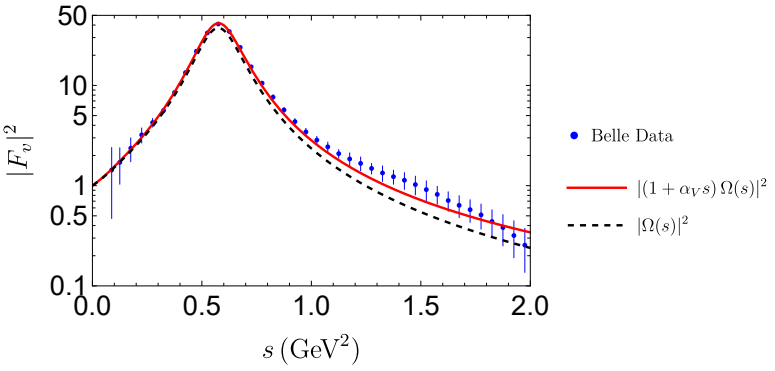

Figure C.4: Our prediction for the pion vector FF $F_v(s)$ at the physical pion mass. The data are obtained from the process $\tau^- \to \pi^-\pi^0\nu_\tau$ as measured by the Belle experiment [52].

lent agreement with data up to energies of about 1 GeV. A pure Omnès function ($\alpha_V = 0$) yields a less satisfying description.

In summary, we have obtained reasonable parametrizations of the pion p-wave scattering phase shift, checking its M_π dependence with LQCD m_ρ data. From $\delta(s, M_\pi)$ we determine the pion vector FF as a function of M_π, which we have checked that reproduces well physical data.

C.2 Diagrams generated by dispersive integrals

In this section, the relation among dispersive and ChPT contributions is discussed. From the optical theorem (1.55) one could naively think that a dispersive integral produces only one-loop diagrams from tree-level amplitudes (also two-loop diagrams from one-loop and tree-level input and so on). From a purely perturbative perspective (ChPT regime) this is true. However, this idea would not explain how the whole FF (including tree level) is generated by the Cauchy integral of Eq. (3.2). In fact, a careful look at the integration region of the dispersive integrals is necessary. We distinguish the low-energy region of ChPT, the resonance region of the ρ meson, and the high-energy region that is actually cut away by the cutoff Λ (but might leave a Λ dependence). We introduce a second cutoff Λ_L that distinguishes the first two regions, i.e.

$$\begin{aligned} 4M_\pi^2 \leq s, s' < \Lambda_L^2 \qquad & \text{ChPT region,} \\ \Lambda_L^2 \leq s, s', m_\rho^2 < \Lambda^2 \qquad & \text{resonance region,} \\ \Lambda^2 \leq s, s' \qquad & \text{high-energy region.} \end{aligned} \tag{C.10}$$

In the following semi-quantitative discussion it is enough to cover the resonance region considering the ρ as a narrow resonance. This means that in the intermediate region the pion p-wave phase shift $\delta(s)$ changes rather suddenly from about 0 to π, crossing $\pi/2$ at $s = m_\rho^2$. Therefore, we approximate

$$\begin{aligned} F_v(s) \approx \Omega(s) \approx \frac{m_\rho^2}{m_\rho^2 - s - i\epsilon} \approx \frac{m_\rho^2}{m_\rho^2 - s - i m_\rho \Gamma_\rho} \,, \\ \Omega(s)\, F_v^*(s) \approx |\Omega(s)|^2 \approx \frac{\pi m_\rho^3}{\Gamma_\rho}\, \delta(s - m_\rho^2) \,, \end{aligned} \tag{C.11}$$

with Γ_ρ the ρ width. In addition, we consider the reduced scattering amplitude T from Eqs. (3.11, 3.12) generically as

$$T(s) \equiv K(s) + \Omega(s)\, R(s)\,. \tag{C.12}$$

This relation defines R as the sum of the polynomial P and the Omnès integral.

With this at hand, one can decompose the dispersive integral of Eq. (3.4) as

$$\begin{aligned}\int\limits_{4M_\pi^2}^{\Lambda^2} \frac{\mathrm{d}s}{\pi} \frac{\mathrm{Im}F_{2\pi}(s)}{s-q^2-i\epsilon} &\approx \int\limits_{4M_\pi^2}^{\Lambda^2} \frac{\mathrm{d}s}{12\pi^2} \frac{K(s) p_{\mathrm{cm}}^3 \Omega^*(s)}{\sqrt{s}(s-q^2-i\epsilon)} + \int\limits_{4M_\pi^2}^{\Lambda^2} \frac{\mathrm{d}s}{12\pi^2} \frac{R(s) p_{\mathrm{cm}}^3 |\Omega(s)|^2}{\sqrt{s}(s-q^2-i\epsilon)} \\ &\approx \int\limits_{4M_\pi^2}^{\Lambda^2} \frac{\mathrm{d}s}{12\pi^2} \frac{K(s) p_{\mathrm{cm}}^3 \Omega^*(s)}{\sqrt{s}(s-q^2-i\epsilon)} + \int\limits_{4M_\pi^2}^{\Lambda_L^2} \frac{\mathrm{d}s}{12\pi^2} \frac{R(s) p_{\mathrm{cm}}^3}{\sqrt{s}(s-q^2-i\epsilon)} \\ &\quad + \frac{m_\rho^2}{12\pi\Gamma_\rho} \frac{R(m_\rho^2) p_{\mathrm{cm}}^3(m_\rho^2)}{m_\rho^2-q^2-i\epsilon}.\end{aligned} \tag{C.13}$$

Now we comment on the last three terms individually. Starting by the first one, for large s, both the left-hand-cut component K and the Omnès function Ω decrease. Either K drops so fast that the first integral is most sensitive to the ChPT region or one needs Ω to cut off the s-integration at

$$\int\limits_{4M_\pi^2}^{\Lambda^2} \frac{\mathrm{d}s}{12\pi^2} \frac{K(s)\, p_{\mathrm{cm}}^3\, \Omega^*(s)}{\sqrt{s}(s-q^2-i\epsilon)}\,. \tag{C.14}$$

In any case, a tree-level input for K is related to the one-loop diagram 3.2f of Fig. 3.2. If K drops fast enough, this triangle diagram is not very sensitive to m_ρ or Λ. In ChPT, the result of the integral will not depend on the renormalization scale μ. The results (dispersive and ChPT) will approximately agree. If K does not drop rapidly enough, the dispersive expression is effectively renormalized at a scale m_ρ while the ChPT diagram calculated in the standard way is renormalized at μ. Then, differences between the dispersive and pure ChPT treatments can be compensated by readjusting counter terms (LECs), cf. also Appendix C.4. At low values of s, one has $\Omega(s) \approx 1 + \mathcal{O}(p^2)$. If K is of order $\mathcal{O}(p^n)$ in the chiral counting then the integral (C.14) is of order $\mathcal{O}(p^{n+2})$. This

matches the usual expectation from ChPT: LO vertices lead to NNLO one-loop diagrams.

We can then move to the term

$$\int_{4M_\pi^2}^{\Lambda_L^2} \frac{\mathrm{d}s}{12\pi^2} \frac{R(s)\, p_{\mathrm{cm}}^3}{\sqrt{s}(s-q^2-i\epsilon)} \,, \tag{C.15}$$

which corresponds to the ChPT diagrams 3.2b and 3.2c of Fig. 3.2 and higher-loop diagrams. It is sensitive to the cutoff Λ_L, however this can be compensated by changes of LECs again.

Until now, we have seen that tree-level input for the scattering amplitudes leads to one-loop contributions for the FF. The most interesting aspects are related to the last term of (C.13). The clear peak structure of Ω has motivated the term

$$\frac{m_\rho^2}{12\pi\Gamma_\rho} \frac{R(m_\rho^2)\, p_{\mathrm{cm}}^3(m_\rho^2)}{m_\rho^2-q^2-i\epsilon} \,. \tag{C.16}$$

The polynomial contributions, P, of Eqs. (3.11,3.12) produce polynomial terms in ChPT when one expands (C.16) in powers of q^2/m_ρ^2. More generally, tree-level input for the scattering amplitudes leads to tree-level contributions to the FF. One-loop input leads to one-loop contributions and so forth.

This has consequences for the power counting and the accuracy of the inputs employed. In general, this forces one to have an accuracy of $\mathcal{O}(p^n)$ in the reduced scattering amplitudes to reach an $\mathcal{O}(p^n)$ precision for the FF. As explained before, this complication is circumvented for F_1 by using a subtracted dispersion relation. For F_2, however, we require input beyond LO. We actually cover a significant part of the one-loop contributions involving an NLO vertex and, in particular diagram 3.2c of Fig. 3.2. To achieve a fair comparison of pure ChPT and dispersion theory, we also include ChPT p^4 loop diagrams. The details are reported in Sec. 3.3.

C.3 The left-hand cut structures $K_{1,2}$

We report here how to obtain the $K_{1,2}$ amplitudes of Eq. (3.11):

$$\begin{aligned} K_1(q^2) &= \frac{8m_N^2}{4m_N^2 - q^2}\left(K_E(q^2) - \frac{q^2}{4m_N^2}K_M(q^2)\right), \\ K_2(q^2) &= \frac{8m_N^2}{q^2 - 4m_N^2}(K_E(q^2) - K_M(q^2)). \end{aligned} \tag{C.17}$$

The explicit formulas for the nucleon and Δ contribution to $K_{E,M}$ can be extracted from [151, 153]. The polynomials P_1 and P_2 are computed in the exact same way as in Eq. (C.17).

C.4 The renormalization-group running of d_6

Here the dependence of d_6 with the dimensional renormalization scale, μ, is reported:

$$d_6(\mu) = d_6(m_\rho) - \frac{1}{12}\frac{\beta_{d6}}{(4\pi F_\pi)^2}\log\left(\frac{m_\rho}{\mu}\right), \tag{C.18}$$

where in ChPT $\beta_{d6} = \beta_{d6}^{\mathrm{no}\Delta\Delta} + \beta_{d6}^{\Delta\Delta}$, while in disp+ChPT the running is given just by the loop with two Δ, $\beta_{d6} = \beta_{d6}^{\Delta\Delta}$. The β functions read

$$\begin{aligned} \beta_{d6}^{\mathrm{no}\Delta\Delta} &= 2 - 2\mathring{g}_A^2 + 4h_A^2\frac{\left(\mathring{m}^2 + 2\mathring{m}\mathring{m}_\Delta - 8\mathring{m}_\Delta^2\right)}{9\mathring{m}_\Delta^2}, \\ \beta_{d6}^{\Delta\Delta} &= 10h_A^2\frac{\left(7\mathring{m}^4 + 6\mathring{m}^3\mathring{m}_\Delta + 9\mathring{m}^2\mathring{m}_\Delta^2 + 16\mathring{m}\mathring{m}_\Delta^3 - 48\mathring{m}_\Delta^4\right)}{27\mathring{m}_\Delta^4}. \end{aligned} \tag{C.19}$$

The origin of the difference in the runnings in the two schemes is the fact that the dispersively treated loop diagrams do not require an explicit renormalization. Instead, the Omnès function cuts off the integrals approximately at $s = m_\rho^2$.

Appendix D

Details of the Λ_c semileptonic decay calculation

D.1 Heavy quark transition form factors

D.1.1 On-shell heavy quark approximation

Here the pseudoscalar and tensor form factors are related to the (axial)vector ones following the OSHQ prescription. One follows the same procedure as in Sec. 1.4.2, replacing $J_V(x)$ by the axial current, $J_A^\mu(x) = \bar{l}(x)\gamma^\mu\gamma_5 h(x)$, and $J_S(x)$ by the pseudoscalar one, $J_P = \bar{l}(x)\gamma_5 h(x)$. Therefore one obtains

$$F_P \bar{u}_L(p')\gamma_5 u_H(p) = -\frac{1}{m_h}\bar{u}_L(p')p_\mu \Gamma_A^\mu u_{H(p)}\,, \tag{D.1}$$

with

$$\Gamma_A^\mu = \left(\gamma^\mu G_1 + \frac{p^\mu}{M}G_2 + \frac{p'^\mu}{m}G_3\right)\gamma_5\,. \tag{D.2}$$

The resulting expression for F_P in terms of axial form factors G_{1-3} is also given in Eq. (1.99).

Next we repeat the procedure with tensor currents $J_T^{\mu\nu}(x) = \bar{l}(x)\sigma^{\mu\nu}h(x)$ and $J_{TA}^{\mu\nu}(x) = \bar{l}(x)\sigma^{\mu\nu}\gamma_5 h(x)$ and obtain

$$\bar{u}_L(p')\left[(p_\alpha\Gamma_V^\alpha)p^\mu - m_h^2\Gamma_V^\mu\right]u_H(p) = im_h\bar{u}_L(p')\Gamma^{\mu\nu}p_\nu u_H(p), \tag{D.3}$$

$$\bar{u}_L(p')\left[(p_\alpha\Gamma_A^\alpha)p^\mu - m_h^2\Gamma_A^\mu\right]u_H(p) = -im_h\bar{u}_L(p')\Gamma_A^{\mu\nu}p_\nu u_H(p), \tag{D.4}$$

where ($\epsilon_{0123} = 1$)

$$\Gamma_A^{\mu\nu} = -\frac{i}{2}\epsilon^{\mu\nu\alpha\beta}\Gamma_{\alpha\beta} \,, \tag{D.5}$$

thanks to the relation

$$\sigma^{\mu\nu}\gamma_5 = -\frac{i}{2}\epsilon^{\mu\nu\alpha\beta}\sigma_{\alpha\beta} \,, \tag{D.6}$$

and

$$\begin{aligned}\Gamma^{\alpha\beta} \;=\; & \frac{i}{M^2}\left(p^\alpha p'^\beta - p^\beta p'^\alpha\right) T_1 + \frac{i}{M}\left(\gamma^\alpha p^\beta - \gamma^\beta p^\alpha\right) T_2 \\ & + \frac{i}{M}\left(\gamma^\alpha p'^\beta - \gamma^\beta p'^\alpha\right) T_3 + \sigma^{\alpha\beta} T_4 \,. \end{aligned} \tag{D.7}$$

In the $m_h/M \to 1$ limit, Eqs. (D.3,D.4) lead to a consistent and independent set of four equations for T_{1-4} in terms of $F_{1,3}$ and $G_{1,3}$, completing the OSHQ prescription of Eq. (1.99).

D.1.2 Heavy quark spin symmetry approximation

Here the transition form factors are given as a function of the HQSS ones, $\tilde{F}_{1,2}$, from Sec. 1.4.2. It is a straightforward result from Eq. (1.101):

$\gamma = \mathbb{1}$**:** $F_S = \tilde{F}_1 + \tilde{F}_2$

$\gamma = \gamma_5$**:** $F_P = \tilde{F}_1 - \tilde{F}_2$

$\gamma = \gamma^\mu$**:** $F_1 = \tilde{F}_1 - \tilde{F}_2$, $F_2 = 2\tilde{F}_2$, $F_3 = 0$

$\gamma = \gamma^\mu\gamma_5$**:** $G_1 = \tilde{F}_1 + \tilde{F}_2$, $G_2 = -2\tilde{G}_2$, $G_3 = 0$

$\gamma = \sigma^{\mu\nu}$**:** $T_1 = T_3 = 0$, $T_2 = -2\tilde{F}_2$, $T_4 = \tilde{F}_1 + \tilde{F}_2$.

D.2 General framework and observables

With the aim of taking advantage of the general analytic results derived in Ref. [173], we rewrite the Hamiltonian of Eq. (1.90) as

$$\begin{aligned} H_{\text{eff}} = \; & \tfrac{4G_F V_{cs}}{\sqrt{2}} \quad \left[C_{LR}^V \mathcal{O}_{LR}^V + C_{RR}^V \mathcal{O}_{RR}^V + C_{LR}^S \mathcal{O}_{LR}^S \right. \\ & \left. + C_{RR}^S \mathcal{O}_{RR}^S + C_{RR}^T \mathcal{O}_{RR}^T \right] , \end{aligned} \tag{D.8}$$

where

$$\begin{aligned}
\mathcal{O}^V_{(L,R)R} &= (\bar{s}\gamma_\alpha P_{L,R}\, c)(\bar{\ell}^c\gamma^\alpha P_R\nu^c_\ell)\ , \\
\mathcal{O}^S_{(L,R)R} &= (\bar{s}\, P_{L,R}\, c)(\bar{\ell}^c\, P_R\nu^c_\ell)\ , \\
\mathcal{O}^T_{RR} &= (\bar{s}\,\sigma_{\alpha\beta}P_R\, c)(\bar{\ell}^c\sigma^{\alpha\beta} P_R\nu^c_\ell)\ ;
\end{aligned} \tag{D.9}$$

ℓ^c, ν^c_ℓ are the charge-conjugated lepton fields. Taking into account that

$$\bar{\nu}_\ell P_R\Gamma\ell \equiv -\bar{\ell}^c C\Gamma^T C^\dagger P_R\nu^c_\ell, \tag{D.10}$$

and

$$C\Gamma^T C^\dagger = (-1)^n\Gamma\ ;\ \begin{cases} n=0 & ,\Gamma = I \\ n=1 & ,\Gamma = \gamma_\alpha, \sigma_{\alpha\beta} \end{cases}\ , \tag{D.11}$$

where $C = i\gamma^2\gamma^0$ denotes the charge conjugation matrix, we identify

$$\begin{aligned}
C^V_{LR} &= 1+\epsilon^\ell_V\ , \qquad C^V_{RR} = \epsilon^\ell_R, \\
C^S_{LR} &= -\frac{\epsilon^\ell_S - \epsilon^\ell_P}{2}\ , \quad C^S_{RR} = -\frac{\epsilon^\ell_S + \epsilon^\ell_P}{2}\ , \\
C^T_{RR} &= \epsilon^\ell_T\ .
\end{aligned} \tag{D.12}$$

Once the charge conjugated fields play for antiparticles the same role as the original fields for particles, all the expressions derived in Ref. [173] for $b\to c\ell^-\bar{\nu}_\ell$ are directly applicable.

In particular, one can write the differential decay width as

$$\frac{\mathrm{d}^2\Gamma}{\mathrm{d}\omega\mathrm{d}s_{13}} = \frac{G_F^2|V_{cs}|^2 Mm^2}{16\pi^3}\Big[\mathcal{A}(\omega) + \mathcal{B}(\omega)\frac{k\cdot p}{M^2} + \mathcal{C}(\omega)\frac{(k\cdot p)^2}{M^4}\Big]\,. \tag{D.13}$$

M and m are the masses of the initial and final hadrons, respectively; $s_{13}\equiv (p-k)^2 = M^2 - 2k\cdot p$; $\omega \equiv p\cdot p'/(Mm)$ is the product of the hadron four-velocities. It is related to $q^2 = M^2+m^2-2Mm\omega$. Functions $\mathcal{A}(\omega)$, $\mathcal{B}(\omega)$ and $\mathcal{C}(\omega)$ are given in Appendix D of Ref. [173] as a combination of Wilson coefficients[1] and purely hadronic structure functions. The latter are given in terms of transition form factors: in the case of $1/2^+\to 1/2^+$ transitions, as the one under study here, explicit expressions can be found in Ref. [69].

[1] It is useful to bear in mind that from the definitions of Appendix A of Ref. [173] and Eq. (D.12) follows that $C^V_R = 1+\epsilon^\ell_V+\epsilon^\ell_R$, $C^A_R = -(1+\epsilon^\ell_V-\epsilon^\ell_R)$, $C^S_R = -\epsilon^\ell_S$, $C^P_R = -\epsilon^\ell_P$, $C^T_R = \epsilon^\ell_T$.

The $k \cdot p$ product can be written as

$$k \cdot p = \frac{M}{2}\Big(1 - \frac{m_\ell^2}{q^2}\Big)(M_\omega + m\sqrt{\omega^2-1}\cos\theta) \ , \tag{D.14}$$

with $M_\omega = M - m\omega$. Accordingly,

$$\begin{aligned}\frac{\mathrm{d}^2\Gamma}{\mathrm{d}\omega \mathrm{d}\cos\theta} &= \frac{G_F^2 |V_{cs}|^2 M^2 m^3}{16\pi^3}\sqrt{\omega^2-1}\left(1-\frac{m_\ell^2}{q^2}\right)^2 \\ &\quad \times [a_0(\omega) + a_1(\omega)\cos\theta + a_2(\omega)\cos^2\theta] \, , \end{aligned} \tag{D.15}$$

where $a_{0,1,2}(\omega)$ are linear combinations of $\mathcal{A}(\omega)$, $\mathcal{B}(\omega)$ and $\mathcal{C}(\omega)$ (see Eq. (18) of Ref. [69]). Finally, the c_i functions introduced in Eq. (4.1) correspond to a_i up to a normalization:

$$c_i = \frac{G_F^2 M m^2}{32\pi^3}\sqrt{\omega^2-1}\left(1-\frac{m_\ell^2}{q^2}\right)^2 \frac{a_i}{\Gamma_{\rm tot}}. \tag{D.16}$$

The c_i functions can be extracted from measurable quantities: the differential width, $d\Gamma/dq^2$, forward-backward asymmetry, $\mathcal{A}_{\rm FB}$, and convexity, $\mathcal{A}_{\pi/3}$. They are related as follows [162, 64, 69],

$$\frac{1}{\Gamma_{\rm tot}}\frac{\mathrm{d}\Gamma}{\mathrm{d}q^2} = |V_{cs}|^2 \, 2(c_0 + c_2/3) \ , \tag{D.17}$$

$$\begin{aligned}\mathcal{A}_{\rm FB} &\equiv \left(\frac{\mathrm{d}\Gamma}{\mathrm{d}q^2}\right)^{-1}\left[\int_0^1 \mathrm{d}\cos\theta \frac{\mathrm{d}^2\Gamma}{\mathrm{d}q^2\mathrm{d}\cos\theta} - \int_{-1}^0 \mathrm{d}\cos\theta \frac{\mathrm{d}^2\Gamma}{\mathrm{d}q^2\mathrm{d}\cos\theta}\right] \\ &= \frac{c_1}{2(c_0+c_2/3)} \\ &= c_1 \, |V_{cs}|^2 \left(\frac{\mathrm{d}\mathcal{B}}{\mathrm{d}q^2}\right)^{-1} \ , \end{aligned} \tag{D.18}$$

$$\begin{aligned}\mathcal{A}_{\pi/3} &\equiv \left(\frac{\mathrm{d}\Gamma}{\mathrm{d}q^2}\right)^{-1}\left[\int_{1/2}^1 \mathrm{d}\cos\theta \frac{\mathrm{d}^2\Gamma}{\mathrm{d}q^2\mathrm{d}\cos\theta} - \int_{-1/2}^{1/2} \mathrm{d}\cos\theta \frac{\mathrm{d}^2\Gamma}{\mathrm{d}q^2\mathrm{d}\cos\theta} \right. \\ &\qquad \left. + \int_{-1}^{-1/2} \mathrm{d}\cos\theta \frac{\mathrm{d}^2\Gamma}{\mathrm{d}q^2\mathrm{d}\cos\theta}\right] \\ &= \frac{c_2}{4(c_0+c_2/3)} \\ &= \frac{1}{2}\, c_2 \, |V_{cs}|^2 \left(\frac{\mathrm{d}\mathcal{B}}{\mathrm{d}q^2}\right)^{-1} \ . \end{aligned} \tag{D.19}$$

D.3 Wilson coefficients conversion

In Fig. 4.4 we show the prediction employing the values of the Wilson coefficients extracted in Ref. [162]. It is worth mentioning that the values used in Ref. [64] contain mistakes. The relation between the Wilsons in [162] and the ones in this work is, assuming only real component:

$$\epsilon_{L,R} = \frac{g_V \mp g_A}{2} = g_{V_{L,R}}, \quad \epsilon_{S,P,T} = g_{S,P,T}. \tag{D.20}$$

These ranges are: $\epsilon_L = (1.2 \pm 2.0) \times 10^{-2}$, $\epsilon_R = (-0.9 \pm 2.0) \times 10^{-2}$, $\epsilon_S = (-1 \pm 2) \times 10^{-2}$, $\epsilon_P = (0.7 \pm 1.4) \times 10^{-3}$, $\epsilon_T = (1.2 \pm 1.8) \times 10^{-2}$.

Bibliography

[1] S. Scherer and M.R. Schindler, *A Primer for Chiral Perturbation Theory*, vol. 830 (2012), 10.1007/978-3-642-19254-8.

[2] J. Gasser and H. Leutwyler, *Chiral Perturbation Theory to One Loop*, *Annals Phys.* **158** (1984) 142.

[3] A. Khodjamirian, *Hadron Form Factors: From Basic Phenomenology to QCD Sum Rules*, CRC Press, Taylor & Francis Group, Boca Raton, FL, USA (2020).

[4] J.F. Donoghue, E. Golowich and B.R. Holstein, *Dynamics of the Standard Model: Second edition*, Cambridge University Press (11, 2022), 10.1017/9781009291033.

[5] Particle Data Group collaboration, *Review of Particle Physics*, *PTEP* **2022** (2022) 083C01.

[6] M. Nowakowski, E.A. Paschos and J.M. Rodriguez, *All electromagnetic form-factors*, *Eur. J. Phys.* **26** (2005) 545 [physics/0402058].

[7] J. Goldstone*Nuovo Cim.* **19** (1960) 154.

[8] J. Goldstone, A. Salam and S. Weinberg*Phys. Rev.* **127** (1962) 965.

[9] A. Pich, *Effective Field Theory with Nambu-Goldstone Modes*, 1804.05664.

[10] G. Eichmann, *Lecture notes: QCD and Hadron Physics* (http://cftp.ist.utl.pt/ gernot.eichmann/lecture-notes).

[11] R. Haag, *Quantum field theories with composite particles and asymptotic conditions*, *Phys. Rev.* **112** (1958) 669.

[12] S.R. Coleman, J. Wess and B. Zumino, *Structure of phenomenological Lagrangians. 1.*, *Phys. Rev.* **177** (1969) 2239.

[13] C.G. Callan, Jr., S.R. Coleman, J. Wess and B. Zumino, *Structure of phenomenological Lagrangians. 2.*, *Phys. Rev.* **177** (1969) 2247.

[14] J. Zinn-Justin, *Strong interactions dynamics with padéapproximants*, *Physics Reports* **1** (1971) 55.

[15] S. Weinberg, *The quantum theory of fields. Vol. 2: Modern applications*, Cambridge University Press (8, 2013), 10.1017/CBO9781139644174.

[16] S. Weinberg, *Nonlinear realizations of chiral symmetry*, *Phys. Rev.* **166** (1968) 1568.

[17] R.F. Dashen and M. Weinstein, *Soft pions, chiral symmetry, and phenomenological lagrangians*, *Phys. Rev.* **183** (1969) 1261.

[18] S. Weinberg, *Phenomenological Lagrangians*, *Physica A* **96** (1979) 327.

[19] J. Gasser, M.E. Sainio and A. Svarc, *Nucleons with Chiral Loops*, *Nucl. Phys. B* **307** (1988) 779.

[20] N. Fettes, U.-G. Meissner, M. Mojzis and S. Steininger, *The Chiral effective pion nucleon Lagrangian of order p**4*, *Annals Phys.* **283** (2000) 273 [hep-ph/0001308].

[21] H. Georgi, *Weak Interactions and Modern Particle Theory* (1984).

[22] T. Bauer, J.C. Bernauer and S. Scherer, *Electromagnetic form factors of the nucleon in effective field theory*, *Phys. Rev. C* **86** (2012) 065206 [1209.3872].

[23] E.E. Jenkins and A.V. Manohar, *Chiral corrections to the baryon axial currents*, *Phys. Lett. B* **259** (1991) 353.

[24] T.R. Hemmert, B.R. Holstein and J. Kambor, *Chiral Lagrangians and Delta(1232) interactions: Formalism*, *J. Phys. G* **24** (1998) 1831 [hep-ph/9712496].

[25] V. Pascalutsa and D.R. Phillips, *Effective theory of the delta(1232) in Compton scattering off the nucleon*, *Phys. Rev. C* **67** (2003) 055202 [nucl-th/0212024].

[26] V. Bernard, T.R. Hemmert and U.-G. Meissner, *Infrared regularization with spin 3/2 fields*, *Phys. Lett. B* **565** (2003) 137 [hep-ph/0303198].

[27] C. Hacker, N. Wies, J. Gegelia and S. Scherer, *Including the Delta(1232) resonance in baryon chiral perturbation theory*, *Phys. Rev. C* **72** (2005) 055203 [hep-ph/0505043].

[28] D.-L. Yao, D. Siemens, V. Bernard, E. Epelbaum, A.M. Gasparyan, J. Gegelia et al., *Pion-nucleon scattering in covariant baryon chiral perturbation theory with explicit Delta resonances*, *JHEP* **05** (2016) 038 [1603.03638].

[29] A.N. Hiller Blin, *Systematic study of octet-baryon electromagnetic form factors in covariant chiral perturbation theory*, *Phys. Rev. D* **96** (2017) 093008 [1707.02255].

[30] M. Thürmann, E. Epelbaum, A.M. Gasparyan and H. Krebs, *Nucleon polarizabilities in covariant baryon chiral perturbation theory with explicit Δ degrees of freedom*, *Phys. Rev. C* **103** (2021) 035201 [2007.08438].

[31] F. Alvarado and L. Alvarez-Ruso, *Light-quark mass dependence of the nucleon axial charge and pion-nucleon scattering phenomenology*, *Phys. Rev. D* **105** (2022) 074001 [2112.14076].

[32] W. Rarita and J. Schwinger, *On a theory of particles with half integral spin*, *Phys. Rev.* **60** (1941) 61.

[33] N. Wies, J. Gegelia and S. Scherer, *Consistency of the pi Delta interaction in chiral perturbation theory*, *Phys. Rev. D* **73** (2006) 094012 [hep-ph/0602073].

[34] V. Pascalutsa, M. Vanderhaeghen and S.N. Yang, *Electromagnetic excitation of the Delta(1232)-resonance*, *Phys. Rept.* **437** (2007) 125 [hep-ph/0609004].

[35] R.D. Peccei, *Chiral lagrangian calculation of pion-nucleon scattering lengths*, *Phys. Rev.* **176** (1968) 1812.

[36] V. Pascalutsa, *Correspondence of consistent and inconsistent spin - 3/2 couplings via the equivalence theorem*, *Phys. Lett. B* **503** (2001) 85 [hep-ph/0008026].

[37] G. Ecker, *Chiral perturbation theory*, *Prog. Part. Nucl. Phys.* **35** (1995) 1 [hep-ph/9501357].

[38] E.E. Jenkins and A.V. Manohar, *Baryon chiral perturbation theory using a heavy fermion Lagrangian*, *Phys. Lett. B* **255** (1991) 558.

[39] T. Fuchs, J. Gegelia, G. Japaridze and S. Scherer, *Renormalization of relativistic baryon chiral perturbation theory and power counting*, *Phys. Rev. D* **68** (2003) 056005 [hep-ph/0302117].

[40] J.M. Alarcon, J. Martin Camalich and J.A. Oller, *Improved description of the πN-scattering phenomenology in covariant baryon chiral perturbation theory*, *Annals Phys.* **336** (2013) 413 [1210.4450].

[41] L.S. Geng, J. Martin Camalich, L. Alvarez-Ruso and M.J. Vicente Vacas, *Leading SU(3)-breaking corrections to the baryon magnetic moments in Chiral Perturbation Theory*, *Phys. Rev. Lett.* **101** (2008) 222002 [0805.1419].

[42] L. Alvarez-Ruso, T. Ledwig, J. Martin Camalich and M.J. Vicente-Vacas, *Nucleon mass and pion-nucleon sigma term from a chiral analysis of lattice QCD data*, *Phys. Rev. D* **88** (2013) 054507 [1304.0483].

[43] M.E. Peskin and D.V. Schroeder, *An Introduction to quantum field theory*, Addison-Wesley, Reading, USA (1995).

[44] A. Dobado, A. Gomez-Nicola, A.L. Maroto and J.R. Pelaez, *Effective lagrangians for the standard model* (1997).

[45] M. Niehus, M. Hoferichter, B. Kubis and J. Ruiz de Elvira, *Two-Loop Analysis of the Pion Mass Dependence of the ρ Meson*, *Phys. Rev. Lett.* **126** (2021) 102002 [2009.04479].

[46] J.A. Oller, E. Oset and J.R. Pelaez, *Meson meson interaction in a nonperturbative chiral approach*, *Phys. Rev. D* **59** (1999) 074001 [hep-ph/9804209].

[47] K.M. Watson, *Some general relations between the photoproduction and scattering of pi mesons*, *Phys. Rev.* **95** (1954) 228.

[48] N. Muskhelishvili, *Singular integral equations: Boundary problems of function theory and their application to mathematical physics*, Springer (1958).

[49] R. Omnes, *On the Solution of certain singular integral equations of quantum field theory*, *Nuovo Cim.* **8** (1958) 316.

[50] T.N. Truong, *Chiral Perturbation Theory and Final State Theorem*, *Phys. Rev. Lett.* **61** (1988) 2526.

[51] R. Garcia-Martin, R. Kaminski, J.R. Pelaez, J. Ruiz de Elvira and F.J. Yndurain, *The Pion-pion scattering amplitude. IV: Improved analysis with once subtracted Roy-like equations up to 1100 MeV*, *Phys. Rev. D* **83** (2011) 074004 [1102.2183].

[52] Belle collaboration, *High-Statistics Study of the tau- —> pi- pi0 nu(tau) Decay*, *Phys. Rev. D* **78** (2008) 072006 [0805.3773].

[53] P.C. Bruns and U.-G. Meissner, *Infrared regularization for spin-1 fields*, *Eur. Phys. J. C* **40** (2005) 97 [hep-ph/0411223].

[54] C. Andersen, J. Bulava, B. Hörz and C. Morningstar, *The $I = 1$ pion-pion scattering amplitude and timelike pion form factor from $N_{\rm f} = 2 + 1$ lattice QCD*, *Nucl. Phys. B* **939** (2019) 145 [1808.05007].

[55] R. Molina and J. Ruiz de Elvira, *Light- and strange-quark mass dependence of the $\rho(770)$ meson revisited*, *JHEP* **11** (2020) 017 [2005.13584].

[56] W. Altmannshofer and F. Archilli, *Rare decays of b and c hadrons*, in *Snowmass 2021*, 6, 2022 [2206.11331].

[57] H.-B. Li and X.-R. Lyu, *Study of the standard model with weak decays of charmed hadrons at BESIII*, *Natl. Sci. Rev.* **8** (2021) nwab181 [2103.00908].

[58] BESIII collaboration, *Study of $\Lambda_c^+ \to \Lambda\mu^+\nu_\mu$ and test of lepton flavor universality with $\Lambda_c^+ \to \Lambda\ell^+\nu_\ell$ decays*, *Phys. Rev. D* **108** (2023) L031105.

[59] T. Appelquist and J. Carazzone, *Infrared Singularities and Massive Fields*, *Phys. Rev. D* **11** (1975) 2856.

[60] A.V. Manohar, *Introduction to Effective Field Theories*, 1804.05863.

[61] I. Brivio and M. Trott, *The Standard Model as an Effective Field Theory*, *Phys. Rept.* **793** (2019) 1 [1706.08945].

[62] W. Buchmuller and D. Wyler, *CP Violation and R Invariance in Supersymmetric Models of Strong and Electroweak Interactions*, *Phys. Lett. B* **121** (1983) 321.

[63] L. Berthier and M. Trott, *Towards consistent Electroweak Precision Data constraints in the SMEFT*, *JHEP* **05** (2015) 024 [1502.02570].

[64] P. Colangelo, F. De Fazio and F. Loparco, *Role of $B_c^+ \to B_{s,d}^{(*)} \bar{\ell}\, \nu_\ell$ in the Standard Model and in the search for BSM signals*, *Phys. Rev. D* **103** (2021) 075019 [2102.05365].

[65] S. Meinel, *$\Lambda_c \to \Lambda l^+ \nu_l$ form factors and decay rates from lattice QCD with physical quark masses*, *Phys. Rev. Lett.* **118** (2017) 082001 [1611.09696].

[66] S.-Q. Zhang and C.-F. Qiao, *Λc semileptonic decays*, *Phys. Rev. D* **108** (2023) 074017 [2307.05019].

[67] A.V. Manohar and M.B. Wise, *Heavy quark physics*, vol. 10 (2000).

[68] N. Penalva, E. Hernández and J. Nieves, *$\bar{B}_c \to \eta_c$, $\bar{B}_c \to J/\psi$ and $\bar{B} \to D^{(*)}$ semileptonic decays including new physics*, *Phys. Rev. D* **102** (2020) 096016 [2007.12590].

[69] N. Penalva, E. Hernández and J. Nieves, *Hadron and lepton tensors in semileptonic decays including new physics*, *Phys. Rev. D* **101** (2020) 113004 [2004.08253].

[70] A. Bodek, S. Avvakumov, R. Bradford and H.S. Budd, *Vector and Axial Nucleon Form Factors:A Duality Constrained Parameterization*, *Eur. Phys. J. C* **53** (2008) 349 [0708.1946].

[71] A.S. Meyer, M. Betancourt, R. Gran and R.J. Hill, *Deuterium target data for precision neutrino-nucleus cross sections*, *Phys. Rev. D* **93** (2016) 113015 [1603.03048].

[72] R.J. Hill, P. Kammel, W.J. Marciano and A. Sirlin, *Nucleon Axial Radius and Muonic Hydrogen — A New Analysis and Review*, *Rept. Prog. Phys.* **81** (2018) 096301 [1708.08462].

[73] L. Alvarez-Ruso, K.M. Graczyk and E. Saul-Sala, *Nucleon axial form factor from a Bayesian neural-network analysis of neutrino-scattering data*, *Phys. Rev. C* **99** (2019) 025204 [1805.00905].

[74] Y. Aoki et al., *FLAG Review 2021*, 2111.09849.

[75] B.C. Tiburzi, *Time Dependence of Nucleon Correlation Functions in Chiral Perturbation Theory*, *Phys. Rev. D* **80** (2009) 014002 [0901.0657].

[76] O. Bar, *Chiral perturbation theory and nucleon–pion-state contaminations in lattice QCD*, *Int. J. Mod. Phys. A* **32** (2017) 1730011 [1705.02806].

[77] S.R. Beane and M.J. Savage, *Nucleon properties at finite lattice spacing in chiral perturbation theory*, *Phys. Rev. D* **68** (2003) 114502 [hep-lat/0306036].

[78] S.R. Beane and M.J. Savage, *Baryon axial charge in a finite volume*, *Phys. Rev. D* **70** (2004) 074029 [hep-ph/0404131].

[79] RQCD collaboration, *Nucleon axial structure from lattice QCD*, *JHEP* **05** (2020) 126 [1911.13150].

[80] T.R. Hemmert, B.R. Holstein and J. Kambor, *Systematic 1/M expansion for spin 3/2 particles in baryon chiral perturbation theory*, *Phys. Lett. B* **395** (1997) 89 [hep-ph/9606456].

[81] S.-Z. Jiang, Y.-R. Liu and H.-Q. Wang, *Chiral Lagrangians with* $\Delta(1232)$ *to one loop*, *Phys. Rev. D* **97** (2018) 014002 [1707.09690].

[82] M. Holmberg and S. Leupold, *The relativistic chiral Lagrangian for decuplet and octet baryons at next-to-leading order*, *Eur. Phys. J. A* **54** (2018) 103 [1802.05168].

[83] Y. Ünal, A. Küçükarslan and S. Scherer, *Axial-vector nucleon-to-delta transition form factors using the complex-mass renormalization scheme*, *Phys. Rev. D* **104** (2021) 094014 [2104.03125].

[84] D. Siemens, *Elastic pion-nucleon scattering in chiral perturbation theory: Explicit $\Delta(1232)$ degrees of freedom*, 2001.03906.

[85] S.-i. Ando and H.W. Fearing, *Ordinary muon capture on a proton in manifestly Lorentz invariant baryon chiral perturbation theory*, *Phys. Rev. D* **75** (2007) 014025 [hep-ph/0608195].

[86] M.F.M. Lutz, U. Sauerwein and R.G.E. Timmermans, *On the axial-vector form factor of the nucleon and chiral symmetry*, *Eur. Phys. J. C* **80** (2020) 844 [2003.10158].

[87] D.-L. Yao, L. Alvarez-Ruso and M.J. Vicente-Vacas, *Extraction of nucleon axial charge and radius from lattice QCD results using baryon chiral perturbation theory*, *Phys. Rev. D* **96** (2017) 116022 [1708.08776].

[88] Y.-H. Chen, D.-L. Yao and H.Q. Zheng, *Analyses of pion-nucleon elastic scattering amplitudes up to $O(p^4)$ in extended-on-mass-shell subtraction scheme*, *Phys. Rev. D* **87** (2013) 054019 [1212.1893].

[89] M. Gorchtein and C.-Y. Seng, *Dispersion relation analysis of the radiative corrections to g_A in the neutron β-decay*, *JHEP* **10** (2021) 053 [2106.09185].

[90] Particle Data Group collaboration, *Review of Particle Physics*, *PTEP* **2020** (2020) 083C01.

[91] H.-W. Lin, *Frontiers in lattice nucleon structure*, *Int. J. Mod. Phys. A* **35** (2020) 2030006.

[92] S.R. Beane and M.J. Savage, *The Quark mass dependence of two nucleon systems*, *Nucl. Phys. A* **717** (2003) 91 [nucl-th/0208021].

[93] J.C. Berengut, E. Epelbaum, V.V. Flambaum, C. Hanhart, U.G. Meissner, J. Nebreda et al., *Varying the light quark mass: impact on the nuclear force and Big Bang nucleosynthesis*, *Phys. Rev. D* **87** (2013) 085018 [1301.1738].

[94] E. Epelbaum, H. Krebs, T.A. Lähde, D. Lee and U.-G. Meißner, *Dependence of the triple-alpha process on the fundamental constants of nature*, *Eur. Phys. J. A* **49** (2013) 82 [1303.4856].

[95] V. Bernard, N. Kaiser, T.S.H. Lee and U.-G. Meissner, *Threshold pion electroproduction in chiral perturbation theory*, *Phys. Rept.* **246** (1994) 315 [hep-ph/9310329].

[96] M. Hilt, B.C. Lehnhart, S. Scherer and L. Tiator, *Pion photo- and electroproduction in relativistic baryon chiral perturbation theory and the chiral MAID interface*, *Phys. Rev. C* **88** (2013) 055207 [1309.3385].

[97] G.H. Guerrero Navarro and M.J. Vicente Vacas, *Threshold pion electro- and photoproduction off nucleons in covariant chiral perturbation theory*, *Phys. Rev. D* **102** (2020) 113016 [2008.04244].

[98] N. Rijneveen, A.M. Gasparyan, H. Krebs and E. Epelbaum, *Pion photoproduction in chiral perturbation theory with explicit treatment of the* $\Delta(1232)$ *resonance*, 2108.01619.

[99] M. Mojzis, *Elastic pi N scattering to O(p**3) in heavy baryon chiral perturbation theory*, *Eur. Phys. J. C* **2** (1998) 181 [hep-ph/9704415].

[100] N. Fettes and U.-G. Meissner, *Pion nucleon scattering in chiral perturbation theory. 2.: Fourth order calculation*, *Nucl. Phys. A* **676** (2000) 311 [hep-ph/0002162].

[101] N. Fettes and U.G. Meissner, *Pion - nucleon scattering in an effective chiral field theory with explicit spin 3/2 fields*, *Nucl. Phys. A* **679** (2001) 629 [hep-ph/0006299].

[102] K. Torikoshi and P.J. Ellis, *Low-energy pion nucleon scattering in the heavy baryon and infrared schemes*, *Phys. Rev. C* **67** (2003) 015208 [nucl-th/0208049].

[103] M. Hoferichter, J. Ruiz de Elvira, B. Kubis and U.-G. Meißner, *Roy–Steiner-equation analysis of pion–nucleon scattering*, *Phys. Rept.* **625** (2016) 1 [1510.06039].

[104] D. Siemens, V. Bernard, E. Epelbaum, A. Gasparyan, H. Krebs and U.-G. Meißner, *Elastic pion-nucleon scattering in chiral perturbation theory: A fresh look*, *Phys. Rev. C* **94** (2016) 014620 [1602.02640].

[105] D. Siemens, V. Bernard, E. Epelbaum, A.M. Gasparyan, H. Krebs and U.-G. Meißner, *Elastic and inelastic pion-nucleon scattering to fourth order in chiral perturbation theory*, *Phys. Rev. C* **96** (2017) 055205 [1704.08988].

[106] J. Kambor and M. Mojzis, *Field redefinitions and wave function renormalization to O(p**4) in heavy baryon chiral perturbation theory*, *JHEP* **04** (1999) 031 [hep-ph/9901235].

[107] T.R. Hemmert, M. Procura and W. Weise, *Quark mass dependence of the nucleon axial vector coupling constant*, *Phys. Rev. D* **68** (2003) 075009 [hep-lat/0303002].

[108] V. Bernard and U.-G. Meissner, *The Nucleon axial-vector coupling beyond one loop*, *Phys. Lett. B* **639** (2006) 278 [hep-lat/0605010].

[109] M. Procura, B.U. Musch, T.R. Hemmert and W. Weise, *Chiral extrapolation of g(A) with explicit Delta(1232) degrees of freedom*, *Phys. Rev. D* **75** (2007) 014503 [hep-lat/0610105].

[110] A. Calle Cordon and J.L. Goity, *Baryon Masses and Axial Couplings in the Combined $1/N_c$ and Chiral Expansions*, *Phys. Rev. D* **87** (2013) 016019 [1210.2364].

[111] M.R. Schindler, T. Fuchs, J. Gegelia and S. Scherer, *Axial, induced pseudoscalar, and pion-nucleon form-factors in manifestly Lorentz-invariant chiral perturbation theory*, *Phys. Rev. C* **75** (2007) 025202 [nucl-th/0611083].

[112] C.C. Chang et al., *A per-cent-level determination of the nucleon axial coupling from quantum chromodynamics*, *Nature* **558** (2018) 91 [1805.12130].

[113] T. Harris, G. von Hippel, P. Junnarkar, H.B. Meyer, K. Ottnad, J. Wilhelm et al., *Nucleon isovector charges and twist-2 matrix elements with $N_f = 2 + 1$ dynamical Wilson quarks*, *Phys. Rev. D* **100** (2019) 034513 [1905.01291].

[114] Nucleon Matrix Elements (NME) collaboration, *Precision Nucleon Charges and Form Factors Using 2+1-flavor Lattice QCD*, 2103.05599.

[115] S. Wesolowski, N. Klco, R.J. Furnstahl, D.R. Phillips and A. Thapaliya, *Bayesian parameter estimation for effective field theories*, *J. Phys. G* **43** (2016) 074001 [1511.03618].

[116] A. Manohar and H. Georgi, *Chiral Quarks and the Nonrelativistic Quark Model*, *Nucl. Phys. B* **234** (1984) 189.

[117] E. Epelbaum, H. Krebs and U.G. Meißner, *Improved chiral nucleon-nucleon potential up to next-to-next-to-next-to-leading order*, *Eur. Phys. J. A* **51** (2015) 53 [1412.0142].

[118] M. Constantinou, *Lattice Generalized Parton Distributions and Form Factors of the Nucleon*, in *22nd International Symposium on Spin Physics*, 1, 2017 [1701.02855].

[119] S.L. Adler, *Calculation of the axial vector coupling constant renormalization in beta decay*, *Phys. Rev. Lett.* **14** (1965) 1051.

[120] W.I. Weisberger, *Renormalization of the Weak Axial Vector Coupling Constant*, *Phys. Rev. Lett.* **14** (1965) 1047.

[121] V. Pascalutsa and M. Vanderhaeghen, *The Nucleon and delta-resonance masses in relativistic chiral effective-field theory*, *Phys. Lett. B* **636** (2006) 31 [hep-ph/0511261].

[122] S. Capitani, M. Della Morte, D. Djukanovic, G.M. von Hippel, J. Hua, B. Jäger et al., *Isovector axial form factors of the nucleon in two-flavor lattice QCD*, *Int. J. Mod. Phys. A* **34** (2019) 1950009 [1705.06186].

[123] E. Shintani, K.-I. Ishikawa, Y. Kuramashi, S. Sasaki and T. Yamazaki, *Nucleon form factors and root-mean-square radii on a (10.8 fm)^4 lattice at the physical point*, *Phys. Rev. D* **99** (2019) 014510 [1811.07292].

[124] C. Alexandrou et al., *Nucleon axial and pseudoscalar form factors from lattice QCD at the physical point*, *Phys. Rev. D* **103** (2021) 034509 [2011.13342].

[125] F. Alvarado, D. An, L. Alvarez-Ruso and S. Leupold, *Light quark mass dependence of nucleon electromagnetic form factors in dispersively modified chiral perturbation theory*, *Phys. Rev. D* **108** (2023) 114021 [2310.07796].

[126] F. Gross et al., *50 Years of Quantum Chromodynamics*, 2212.11107.

[127] V. Punjabi, C.F. Perdrisat, M.K. Jones, E.J. Brash and C.E. Carlson, *The Structure of the Nucleon: Elastic Electromagnetic Form Factors*, *Eur. Phys. J. A* **51** (2015) 79 [1503.01452].

[128] G.A. Miller, *Charge Density of the Neutron*, *Phys. Rev. Lett.* **99** (2007) 112001 [0705.2409].

[129] C.E. Carlson and M. Vanderhaeghen, *Empirical transverse charge densities in the nucleon and the nucleon-to-Delta transition*, *Phys. Rev. Lett.* **100** (2008) 032004 [0710.0835].

[130] R. Pohl et al., *The size of the proton*, *Nature* **466** (2010) 213.

[131] M.A. Belushkin, H.W. Hammer and U.G. Meissner, *Dispersion analysis of the nucleon form-factors including meson continua*, *Phys. Rev. C* **75** (2007) 035202 [hep-ph/0608337].

[132] I. Sick and D. Trautmann, *Proton rms-radii from low-q power expansions*, *Phys. Rev. C* **95** (2017) 012501 [1701.01809].

[133] J.M. Alarcón and C. Weiss, *Nucleon form factors in dispersively improved Chiral Effective Field Theory II: Electromagnetic form factors*, *Phys. Rev.* **C97** (2018) 055203 [1710.06430].

[134] U.-G. Meißner, *The proton radius and its relatives – much ado about nothing?*, in *28th International Nuclear Physics Conference*, 11, 2022 [2211.05419].

[135] W. Xiong and C. Peng, *Proton Electric Charge Radius from Lepton Scattering*, *Universe* **9** (2023) 182 [2302.13818].

[136] D. Djukanovic, T. Harris, G. von Hippel, P.M. Junnarkar, H.B. Meyer, D. Mohler et al., *Isovector electromagnetic form factors of the nucleon from lattice QCD and the proton radius puzzle*, *Phys. Rev. D* **103** (2021) 094522 [2102.07460].

[137] B. Kubis and U.-G. Meissner, *Low-energy analysis of the nucleon electromagnetic form-factors*, *Nucl. Phys. A* **679** (2001) 698 [hep-ph/0007056].

[138] T. Fuchs, J. Gegelia and S. Scherer, *Electromagnetic form-factors of the nucleon in relativistic baryon chiral perturbation theory*, *J. Phys. G* **30** (2004) 1407 [nucl-th/0305070].

[139] T. Ledwig, J. Martin-Camalich, V. Pascalutsa and M. Vanderhaeghen, *Nucleon and $\Delta(1232)$ form factors at low momentum transfer and small pion masses*, *Phys. Rev.* **D85** (2012) 034013 [1108.2523].

[140] R. Flores-Mendieta and M.A. Rivera-Ruiz, *Dirac form factors and electric charge radii of baryons in the combined chiral and $1/N_c$ expansions*, *Phys. Rev. D* **92** (2015) 094026 [1511.02932].

[141] D. Djukanovic, J. Gegelia, A. Keller and S. Scherer, *Complex-mass renormalization in chiral effective field theory*, *Phys. Lett. B* **680** (2009) 235 [0902.4347].

[142] C. Terschlüsen, S. Leupold and M.F.M. Lutz, *Electromagnetic Transitions in an Effective Chiral Lagrangian with the η' and Light Vector Mesons*, *Eur. Phys. J. A* **48** (2012) 190 [1204.4125].

[143] C. Terschlüsen and S. Leupold, *Renormalization of the low-energy constants of chiral perturbation theory from loops with dynamical vector mesons*, *Phys. Rev. D* **94** (2016) 014021 [1603.05524].

[144] G.J. Gounaris and J.J. Sakurai, *Finite width corrections to the vector meson dominance prediction for $\rho \to e^+e^-$*, *Phys. Rev. Lett.* **21** (1968) 244.

[145] R.P. Feynman, *Photon-Hadron Interactions*, CRC Press, Taylor and Francis, Boca Raton, Florida, USA (1972).

[146] L.G. Landsberg, *Electromagnetic Decays of Light Mesons*, *Phys. Rept.* **128** (1985) 301.

[147] *MesonNet Workshop on Meson Transition Form Factors*, 7, 2012.

[148] S.P. Schneider, B. Kubis and F. Niecknig, *The $\omega \to \pi^0\gamma^*$ and $\phi \to \pi^0\gamma^*$ transition form factors in dispersion theory*, *Phys. Rev.* **D86** (2012) 054013 [1206.3098].

[149] M. Hoferichter, B. Kubis, J. Ruiz de Elvira, H.W. Hammer and U.G. Meißner, *On the $\pi\pi$ continuum in the nucleon form factors and the proton radius puzzle*, *Eur. Phys. J. A* **52** (2016) 331 [1609.06722].

[150] J.M. Alarcón, A.N. Hiller Blin, M.J. Vicente Vacas and C. Weiss, *Peripheral transverse densities of the baryon octet from chiral effective field theory and dispersion analysis*, *Nucl. Phys.* **A964** (2017) 18 [1703.04534].

[151] S. Leupold, *The nucleon as a test case to calculate vector-isovector form factors at low energies*, *Eur. Phys. J. A* **54** (2018) 1 [1707.09210].

[152] G.P. Lepage and S.J. Brodsky, *Exclusive Processes in Perturbative Quantum Chromodynamics*, *Phys. Rev. D* **22** (1980) 2157.

[153] C. Granados, S. Leupold and E. Perotti, *The electromagnetic Sigma-to-Lambda hyperon transition form factors at low energies*, *Eur. Phys. J. A* **53** (2017) 117 [1701.09130].

[154] O. Junker, S. Leupold, E. Perotti and T. Vitos, *Electromagnetic form factors of the transition from the spin-3/2 Σ to the Λ hyperon*, *Phys. Rev. C* **101** (2020) 015206 [1910.07396].

[155] R. Garcia-Martin and B. Moussallam, *MO analysis of the high statistics Belle results on $\gamma\gamma \to \pi^+\pi^-, \pi^0\pi^0$ with chiral constraints*, *Eur. Phys. J.* **C70** (2010) 155 [1006.5373].

[156] X.-W. Kang, B. Kubis, C. Hanhart and U.-G. Meißner, *B_{l4} decays and the extraction of $|V_{ub}|$*, *Phys. Rev.* **D89** (2014) 053015 [1312.1193].

[157] C. Hanhart, *A New Parameterization for the Pion Vector Form Factor*, *Phys. Lett. B* **715** (2012) 170 [1203.6839].

[158] S. Weinberg, *Pion scattering lengths*, *Phys. Rev. Lett.* **17** (1966) 616.

[159] Y. Tomozawa, *Axial vector coupling renormalization and the meson baryon scattering lengths*, *Nuovo Cim. A* **46** (1966) 707.

[160] J.J. Kelly, *Simple parametrization of nucleon form factors*, *Phys. Rev. C* **70** (2004) 068202.

[161] B. Grzadkowski, M. Iskrzynski, M. Misiak and J. Rosiek, *Dimension-Six Terms in the Standard Model Lagrangian*, *JHEP* **10** (2010) 085 [1008.4884].

[162] D. Bečirević, F. Jaffredo, A. Peñuelas and O. Sumensari, *New Physics effects in leptonic and semileptonic decays*, *JHEP* **05** (2021) 175 [2012.09872].

[163] R. Barbieri, G. Isidori, J. Jones-Perez, P. Lodone and D.M. Straub, $U(2)$ *and Minimal Flavour Violation in Supersymmetry*, *Eur. Phys. J. C* **71** (2011) 1725 [1105.2296].

[164] R. Alonso, B. Grinstein and J. Martin Camalich, *Lifetime of* B_c^- *Constrains Explanations for Anomalies in* $B \to D^{(*)}\tau\nu$, *Phys. Rev. Lett.* **118** (2017) 081802 [1611.06676].

[165] D. Bečirević and F. Jaffredo, *Looking for the effects of New Physics in the* $\Lambda_b \longrightarrow \Lambda_c(\to \Lambda\pi)\ell\nu$ *decay mode*, 2209.13409.

[166] C.W. Murphy, *Dimension-8 operators in the Standard Model Eective Field Theory*, *JHEP* **10** (2020) 174 [2005.00059].

[167] BESIII collaboration, *Study of the Semileptonic Decay* $\Lambda_c \to \lambda e^+ \nu_e$, *Phys. Rev. Lett.* **129** (2022) 231803 [2207.14149].

[168] T. Corbett, *The one-loop tadpole in the geoSMEFT*, 2106.10284.

[169] G. Passarino and M. Trott, *The Standard Model Effective Field Theory and Next to Leading Order*, 1610.08356.

[170] J. Nebreda, J.R. Pelaez and G. Rios, *Chiral extrapolation of pion-pion scattering phase shifts within standard and unitarized Chiral Perturbation Theory*, *Phys. Rev. D* **83** (2011) 094011 [1101.2171].

[171] M. Dax, T. Isken and B. Kubis, *Quark-mass dependence in* $\omega \to 3\pi$ *decays*, *Eur. Phys. J. C* **78** (2018) 859 [1808.08957].

[172] J.M. Blatt and V.F. Weisskopf, *Theoretical nuclear physics*, Springer, New York (1979), 10.1007/978-1-4612-9959-2.

[173] N. Penalva, E. Hernández and J. Nieves, *The role of right-handed neutrinos in* $b \to c\tau\bar{\nu}_\tau$ *from visible final-state kinematics*, *JHEP* **10** (2021) 122 [2107.13406].